2010

Optically stimulated luminescence (OSL) and its applications in radiation therapy dosimetry

Bin Hu
University of Wollongong

OPTICALLY STIMULATED LUMINESCENCE (OSL) AND ITS APPLICATIONS IN RADIATION THERAPY DOSIMETRY

A thesis submitted in fulfilment of the requirements for the award of the degree

DOCTOR OF PHILOSOPHY
FROM THE
UNIVERSITY OF WOLLONGONG

BIN HU
ENGINEERING PHYSICS
2010

CERTIFICATION

I, Bin Hu, declare that this thesis, submitted in partial fulfilment of the requirements for an award of Doctor of Philosophy in the Department of Biological Sciences, University of Wollongong, is wholly my own work unless otherwise referenced or acknowledged. The document has not been submitted for qualifications at any other academic institution.

Bin Hu

18 October 2010

ACKNOWLEDGEMENTS

I would like to express the deepest appreciation to Professor Yang Wang, for promoting my research project and supporting the experimental work. I would also like to give my greatest thanks to Professor William Zealey, for his valuable advice and guidance. They have provided strong support; their supervision and leadership helped me tremendously.

My thanks also to all the staff of the Radiation Oncology Associated (ROA) at St. Vincent's Private, Sydney, for providing me the opportunity to undertake this research project and to complete my thesis.

I would like to acknowledge a scholarship from the School of Engineering Physics, University of Wollongong, Australia.

I give my grateful thanks to my parents, my dad, Yimin Hu, for offering his knowledge for phantom design, thesis review, and for helping me accomplish this project; my mother, Xilan Han, for taking care of my son. Without their support and their constant love I could not have started or completed this project.

I give a special thank to one who doesn't want to be mentioned, but he knows who he is and what he did for me.

Abstract

Optically stimulated luminescence (OSL) was studied using a commercial OSL dosimetry system developed by Landauer (Landauer Inc.,USA) to analyse the possibility of using OSL dosimetry for external beam radiotherapy planning checks and in-vivo dosimetry. Experiments were performed to determine signal sensitivity, dose response range, beam type and energy dependency, reproducibility and linearity. Optical annealing processes to test OSL material reusability were also studied. OSL clinical usability was assessed by verifying IMRT dose distributions in a phantom and measuring exit doses for in-vivo dosimetry.

Experimental results show that OSL dosimetry provides a wide dose response range as well as good linearity and reproducibility for doses up to 600cGy, and up to 800cGy shows a 2.0% maximum deviation from linearity. The standard deviation in the response of screened dosimeters was 2.0%. As this needs to be taken into account when OSLDs are used clinically, multiple readings of each irradiated OSLD are recommended. OSLDs can be reused when an optical annealing process is applied, which can restore the OSLD to its original state. After optical annealing using incandescent light, the readout intensity decreased by approximately 98% in the first 30 minutes, decreasing further after repeated optical annealing according to the power law, $I \propto t^{-1.3}$, where I is the light intensity.

Quantitative comparisons were made between treatment planning system (TPS) calculated dose and OSL measurement points dose using a custom-designed spherical phantom. Three clinical IMRT cases were used: Nasopharynx, Prostate and Lung. Although quantitative comparisons are highly dependent on the calibration accuracy and dose range of OSLDs, experimental results showed that the OSL dose is within 3% of the TPS calculated dose with careful calibration**.** Quantitative comparisons were made between various bactscatter material conditions when performing exit

dosimetry. OSLD dose was 5.7% lower when no backscatter material was added compared to full backscatter. Adding 0.5cm to 1.0cm water equivalent material reduced the dose by 2%. The reduction in dose may vary due to the density of the tissue in the primary beam path. These measurements demonstrated the importance of adding appropriate backscatter material to improve the accuracy of the readings.

One made quantitative comparisons between OSL measurements and the depth dose data from linear accelerator commissioning and those of a Markus ion chamber by using a custom-designed heterogeneous phantom. Compared to the depth dose data, OSL dose is 1% lower in the full backscatter condition, 2% with a 1cm backscatter and there is a maximum of 6% reduction with no additional backscatter added. Compared to the Markus ion chamber OSL readings show an insignificantly lower dose. Added backscatter thickness, field size, energy, tissue or a tumour's size and density along the primary beam path-length, as well as the control/calibration dose will all affect OSL response in in-vivo dosimetry.

The research work shows that OSL dosimetry can be an alternative dosimetry technique for use in radiotherapy, especially for patient specific Quality Assurance (QA) including skin dose measurement, IMRT plan checks, and linear accelerator QA. In conclusion, OSL dosimetry can provide an alternative dosimetry technique for use in radiotherapy if rigorous measurement protocols are established.

TABLE OF CONTENTS

ACKNOWLEDGEMENTS

ABSTRACT……..I

TABLE OF CONTENTS……III

LIST OF FIGURES……XII

LIST OF TABLES……XVIII

Part One: Overview and Literature

Chapter 1 General Overview…….……..1

1.1 Optically Stimulated Luminescence…….....1

1.2 Historical development of OSL dosimetry and its applications ……..……1

1.3 Sturcture of this thesis…….…….. 6

1.4 Summary of this study……8

Chapter 2 Physical Aspects of Optically Stimulated Luminescence……13

2.1 Luminescence theory……12

2.2 Stimulated relaxation phenomena (SRP) ……..14

2.3 The energy transition of luminescence process…….....15

2.4 Mathematical description of OSL……16

2.5 Photoionisation cross-section…….....18

2.6 Three main OSL modes ……19

2.6.1 Continuous wave OSL (CW-OSL) ……..20

2.6.1.1 Mechanism and process……..21

2.6.1.2 Temperature influence……....22

2.6.1.3 Theoretical explanation of the temperature dependence of OSL……..23

2.6.1.4 Excitation power ……..25

2.6.1.5 Dose effect…….....25

2.6.2 Linear modulated OSL (LM-OSL) ……..25

2.6.2.1 Mechanism and process……..25

2.6.2.2 Characteristic of LM-OSL curves……..26

2.6.2.3 Relationship between LM-OSL and CW-OSL……27
2.6.2.4 Advantages of LM-OSL technique……28
2.6.3 Pulsed OSL (POSL) ……28
2.6.3.1 Mechanism and process……28
2.6.3.2 Characteristic of POSL curve……29
2.6.3.3 Relationship between POSL and CW-OSL……30
2.6.3.4 Advantages of POSL technique……31
2.7 Summary……31
Chapter 3 OSL Properties of Al_2O_3:C……32
3.1 Introduction……33
3.2 Historical overview of Al_2O_3:C development……34
3.3 Crystal structure of Al_2O_3:C ……35
3.4 Characteristics of Al_2O_3:C ……36
3.4.1 Al_2O_3:C stimulation and emission characteristics……36
3.4.1.1 Stimulation ……36
3.4.1.2 Luminescence ……38
3.4.2 The OSL response of Al_2O_3:C to radiation exposure……40
3.4.2.1 Good response linearity over wide dose range ……40
3.4.2.2 Reusability ……41
3.4.3 Temperature dependence of Al_2O_3:C OSL……42
3.4.4 OSL signal zeroing from Al_2O_3:C……46
3.4.4.1 Thermal annealing……46
3.4.4.2 Bleaching with stimulation light……47
3.5 Summary……47
Chapter 4 Literature review of Al_2O_3:C based OSL measurement technologies in medical dosimetry……49
4.1 Introduction……49
4.2 Risø TL/OSL reader……50
4.3 OSL real-time optical fibre dosimetry technique (Standard Risø TL/OSL measurement system) ……52
4.3.1 Introduction……52

4.3.2. Al_2O_3:C OSL fibres in in-vivo dosimetry……..53

4.3.3 Main components of the OSL fibre reader……..55

4.3.4 Measurement procedures and data processing algorithms……..56

4.3.4.1 RL and post-irradiation OSL measurement procedure ….....56

4.3.4.2 Periodic OSL stimulation…….....56

4.3.5 OSL fibre system dosimetry characteristics…….....57

4.3.5.1 Reproducibility……...57

4.3.5.2 Energy dependence……..58

4.3.5.3 Dose-rate dependence……..58

4.3.5.4 Angular dependence……..58

4.3.6 OSL fibre system clinical applications and performances in radiotherapy……58

4.3.6.1 For measurements of depth dose and off-axis dose distributions ……58

4.3.6.2 *In-vivo* measurements in head and neck IMRT plan……58

4.4 Summary…….....59

Chapter 5 Literature review of the tools and techniques used in in-vivo dosimetry in radiation therapy ……61

5.1 Introduction…..……61

5.2 Definition and concept of in-vivo dosimetry……63

5.3 The requirement for clinical accuracy and consistency……64

5.4 Diode dosimeters in in-vivo dosimetry……65

5.4.1 History of diodes for in-vivo dosimetry…….....65

5.4.2 Diode detectors and electrometers……...66

5.4.3 Characteristics of diodes used in in-vivo dosimetry……66

5.4.4 QA of diodes for in-vivo dosimetry……..67

5.4.5 Clinical application of diodes for in-vivo dosimetry ….....68

5.5 Thermoluminescence detectors (TLDs) in in-vivo dosimetry……..68

5.5.1 History of TLDs for in-vivo dosimetry…….....68

5.5.2 TL dosimeters and readout systems of TLD ……..……68

5.5.2.1 TL dosimeters……..……68

5.5.2.2 TL readers……..……69

5.5.3 Characteristics of TLDs for in vivo dosimetry…….....70

5.5.4 QA of TLDs for clinical in-vivo dosimetry …….....71

5.5.5 Clinical applications of TLDs in in-vivo dosimetry ……72

5.6 Electronic portal imaging devices (EPIDs) for in vivo dosimetry……72

5.7 Metal oxide semiconductor field-effect transistors (MOSFETs) in *in-vivo* dosimetry ……...72

5.8 Summary…....74

Part Two: Experiments

Chapter 6 Evaluation of Landauer's microStar™ system and OSL dosimeters for radiotherapy……75

6.1 Introduction…….....75

6.2 Instrumentation……75

6.2.1 InLight OSL Dosimeter (OSLD) ……75

6.2.2 InLight™ manual microStar™ reader system…….....77

6.3 Methodology…….....78

6.3.1 Establishing a standard baseline for reader performance……..…….78

6.3.2 Reader reproducibility / stability with OSL dosimeters……..79

6.3.3 Random fluctuations of repeated readings ……79

6.3.4 Random orientation error of dot dosimeter ……80

6.4 Results and discussion…….....80

6.4.1 Reader performance test……..…….80

6.4.2 Reader reproducibility / stability with OSL dosimeters…….....81

6.4.3 Random fluctuations of repeated readings……..…….85

6.4.4 Random orientation error of dot dosimeter evaluation……..85

6.5 Summary……..……...86

6.6 Conclusion……...87

Chapter 7 Performance of Al_2O_3:C Optical Luminescent Dosimeters (and specifically, Landauer's InLight™ Dosimeter) for Clinical Radiation Therapy Applications ……..…89

7.1 Introduction……...89

7.2 Instrumentation……92
7.2.1 OSL Dosimeters and reader system……92
7.2.2 Irradiation equipment ……92
7.2.2.1 Radiation source……92
7.2.2.2 Solid slab square phantom……92
7.2.2.3 Solid sphere phantom……93
7.2.3 Annealing light source……94
7.3 Methodology……94
7.3.1 Irradiation setup……94
7.3.2 Sensitivity……97
7.3.2.1 Variation of sensitivity……97
7.3.2.2 Sensitivity factor ……97
7.3.2.3 Dose and beam energy dependence……98
7.3.3 Dose-response curve linearity, dynamic range and dependence on beam quality ……98
7.3.4 Directional / angular dependence……99
7.3.5 Incremental exposure characteristic……100
7.3.6 Post-irradiation readout time dependence……100
7.3.7 Reciprocity effects affecting OSL materials……100
7.3.8 Optical annealing……101
7.3.9 OSL signal fading and re-use possibility……101
7.4 Results……101
7.4.1 Sensitivity……101
7.4.1.1 Sensitivity factor……101
7.4.1.2 Sensitivity curve vs. dose and beam energy……103
7.4.2 Dose-response linearity and dynamic range……102
7.4.3 Beam quality dependence……106
7.4.4 Directional / Angular dependence ……109
7.4.5 Incremental exposure /Accumulated dose……109
7.4.6 Post-irradiation readout time dependence……111
7.4.7 Reciprocity……113

7.4.8 Optical Annealing…..……..……..114

7.4.9 Fading and reuse ability ……..……..……...116

7.5 Summary……..……..……..117

7.6 Conclusion……..……..……..119

Chapter 8 Preliminary Study of OSL use for Patient Dose Verification in Intensity-Modulated Radiation Therapy (IMRT)……121

8.1 Introduction……..……..……..121

8.2 Instrumentation……..……..……125

8.2.1 OSLdosimeters and reader system ……..……...125

8.2.2 The spherical phantom used in OSL calibration and IMRT dose verification planning……..……..……125

8.2.3 Irradiation source ……..……126

8.2.4 CT scanner and TPS system……..……..……126

8.3 Methodology……..……..……..127

8.3.1 Calibration of OSL dosimeters……..……127

8.3.2 Patient's IMRT cases……..……..……127

8.3.3 IMRT plan dose verification procedure……..……128

8.3.4 OSL measurement data analysis……..……130

8.3.5 Setup uncertainty evaluation from TPS……..……..……134

8.4 OSL measurement results……..……..……..134

8.4.1 Nasopharynx IMRT plan dose verification……..……134

8.4.2 Prostate IMRT plan dose verification……..……...136

8.4.3 Lung IMRT plan dose verification……..……..……137

8.4.4 Setup uncertainty evaluation……..……..……..……137

8.4.4.1 Nasopharynx IMRT case ……..……..……..……...138

8.4.4.2 Prostate IMRT case……..……..……....139

8.4.4.3 Lung IMRT case……..……..……..……..…139

8.5 Summary and discussion……..……140

8.6 Conclusion ……..……..……..141

Chapter 9 Preliminary Study of OSL Used for Patient Skin Exit Dose Dosimetry in Megavoltage X-ray beams……143

9.1 Introduction……143

9.2 Instrumentation……145

9.2.1 Standard electron density phantom……145

9.2.2 In-house made phantom ……145

9.2.3 Computer Tomography (CT) Scanner……146

9.2.4 Radiation source……146

9.2.5 PTW-Freiburg Advanced Markus Ion-Chamber and Fluke Electrometer ……147

9.2.6 Optical Stimulated Luminescent (OSL) dosimetry system ……148

9.3 Experiment preparation: Converting CT number to density……148

9.3.1 Methodology……150

9.3.2 Results……150

9.4 Effective path-length (EPL) correction……151

9.5 Verification in-house phantom using PTW Markus Ion-Chamber ……153

9.5.1 PDD, TPR, an TMR……153

9.5.2 Methodology……154

9.5.3 Results……155

9.6 Verification an OSL dosimetry system in in-house phantom……156

9.6.1 Methodology……156

9.6.2 Results……157

9.7 Summary of experiment……160

9.8 Exit dose Dosimetry using Markus Ion-chamber ……160

9.9 Effect of back scatter thickness on the dose variations……162

9.9.1 Markus Experiment 1: Measurement performed at isocentre in in-house homogenous phantom…… ……162

9.9.1.1 Methodology……162

9.9.1.2 Results……163

9.9.2 Markus Experiment 2: Measurement point set on the exit surface in a homogeneous phantom……165

9.9.2.1 Methodology……165
9.9.2.2 Results……167
9.10 Markus Experiment 3: Exit dose vs. Field Size……173
9.10.1 Methodology……173
9.10.2 Results……174
9.11 Markus Experiment 4: Exit dose vs. Energy influence……175
9.11.1 Methodology……175
9.11.2 Results……176
9.12 Markus Experiment 5: Verification Markus ion-chamber measurement data ……177
9.12.1 Methodology ……177
9.12.2 Results……178
9.13 Markus Experiment 6: Exit Dose variation vs. the size of tissue equivalent materials inserts……181
9.13.1 Methodology……181
9.13.2 Results……182
9.14 Summary for exit dose dosimetry using Markus ion-chamber ……184
9.15 Exit dosimetry using OSLD……185
9.16 Calibration of OSLDs……186
9.17 OSL Experiment 1: Measurement performed at isocentre in homogeneous phantom……188
9.17.1 Methodology……188
9.17.2 Results……189
9.18 OSL Experiment 2: Measurement performed at isocentre in a heterogeneous phantom ……191
9.18.1 Methodology……191
9.18.2 Results……193
9.19 Summary of section 9.17~9.18……195
9.20 OSL Experiment 3: Verification Markus ion-chamber measurement data ……196
9.20.1 Methodology……196
9.20.2 Results……197

9.21 OSL Experiment 4: Measurement point set on the exit surface on the beam axis in heterogeneous phantom……205

9.21.1 Methodology……..…..…..205

9.21.2 Results…….....…..206

9.22 OSL Experiment 5: Comparison of OSL measurement data to clinical TMR data and Markus ion chamber data……209

9.22.1 Methodology……..…..…..209

9.22.2 Results…….....…..210

9.23 OSL Experiment 6: Exit dose vs. Field Size……..217

9.23.1 Methodology……..…..…..217

9.23.2 Results…….....…..218

9.24 Discussion on the factors influenced the exit dose measurements……219

9.25 Conclusion……219

Chapter 10 Conclusions and recommendations…….....…...223

Reference…….……..229

Appendix A Guide for OSL Dosimetry Radiotherapy Protocol Design….253

Appendix B Original data for the figure in the thesis …….....257

LIST OF FIGURES

Figure 2.1 Simplified illustrations of luminescence excitation and emission in crystals

Figure 2.2 Schematic energy band diagram of stimulated phenomena

Figure 2.3 Occupancy of forbidden gap states

Figure 2.4 A schematic of the possible optical absorption transitions in an insulator.

Figure 2.5 Schematic diagrams of three main OSL stimulation methods: CW-OSL, LM-OSL, and POSL

Figure 2.6 A model combing all the possible traps in an OSL sample

Figure 2.7 OSL decay curves.

Figure 2.8 Schematic representation of the processes that my give rise to a temperature dependence for OSL production

Figure 2.9 Experimental LM-OSL curves from Al_2O_3:C.

Figure 2.10 Stimulated LM-OSL curves for first-order kinetics, using three different values of the product σγ.

Figure 2.11 Comparison between CW-OSL, transformed Pseudo-LM-OSL and experimental LM-OSL curves from a Na-feldspar sample.

Figure 2.12 OSL decay curves acquired after a stimulation pulse from a laser at 25˚C

Figure 2.13 Schematic illustrating the variation in the ratio of the light emitted during a pulse to that emitted after the pulse as the pulse width changes for fixed stimulation energy per pulse.

Figure 2.14 Ratio, represents the efficiency, of the luminescence emitted after the pulse to that emitted during the pulse

Figure 3.1 Crystal structure of Al_2O_3

Figure 3.2 Excitation spectra for OSL from Al_2O_3:C (TLD-500)

Figure 3.3 Decay curve of OSL from Al_2O_3:C (TLD-500)

Figure 3.4 Isometric plot of the stimulation spectra (200 ~ 320 nm) emission spectra (360 ~ 580 nm) from an irradiated 0.1% Mg-doped Al_2O_3:C sample.

Figure 3.5 Comparison of OSL stimulation spectra (solid line) with photoconductivity after Al_2O_3:C irradiated 300 Gy by a ^{60}Co source.

Figure 3.6 Dose response for Al_2O_3:C powder.

Figure 3.7 Dose responses for α- Al_2O_3:C using POSL.

Figure 3.8 Repeated single aliquot regeneration OSL measurements of Al_2O_3:C after exposed to the same dose of 4 μGy 60Co gamma radiation.

Figure 3.9 Dose reassessments for five repeated POSL measurement for the initial dose from 3x10.4 Gy to 2 Gy

Figure 3.10 Time-resolved OSL from α- Al_2O_3:C following irradiation at room temperature with a dose of 0.04 Gy 90Sr/90Y.

Figure 3.11 Arrhenius plot of the variation of the lifetime of the slow component as a function of temperature.

Figure 3.12 Glow curves from (1) POST-quality, (2) TLD-quality, (3) DOSL-quality Al_2O_3:C samples irradiated at 200 K and heated at 0.5 K/s.

Figure 3.13 Thermo-optical luminescence (TOL) characteristics of Al_2O_3:C after 1 Gy $^{90}Sr/^{90}Y$ beta dose irradiation at room temperature and heated at 2˚C/s.

Figure 3.14 Plots of OSL signals against pre-heat temperature for Al_2O_3:C chips irradiated 1 Gy(dot), 110 mGy(square) and 100 μGy(triangle), respectively, using a $^{90}Sr/^{90}Y$ beta source and measured at room temperature

Figure 3.15 OSL decay curves from Al_2O_3:C dosimeters exposed over 15 and 72 hrs to the natural environmental radiation representing evaluated integrated doses of 0.98 and 5.10 μGy, respectively, compared to that from 43.5 μGy 60Co gamma calibration dose

Figure 3.16 OSL decay curve from Al_2O_3:C exposed to 110 mGy and 100 μGy beta radiation at room temperature, respectively

Figure 4.1 Schematic drawing of Risø TL/OSL reader

Figure 4.2 Schematic diagrams of the combined blue LED cluster and IR laser diode OSL unit

Figure 4.3 Al_2O_3:C fibers at different stages of production

Figure 4.4 Diagram of RL/OSL reader

Figure 4.5 Two measurement techniques of OSL fibre readers.

Figure 5.1 A typical glow curve of LiF:Mg,Ti(TLD-100) following ^{60}Co irradiation to a dose level of 100 Gy taken at a heating rate of $1K/s^{-1}$.

Figure 6.1 The InLight™ OSL dosimeter

Figure 6.2 The InLight™ dot dosimeter

Figure 6.3 Images of microStar™ reader

Figure 6.4 Stability of the microStar reader for multiple CAL and LED counts.

Figure 7.1 Schematic of standard $30x30cm^2$ solid water slabs (Computerized Imaging Reference System, Norfolk, VA, USA)

Figure 7.2 A diagram of the spherical phantom including a template and other modifications for Dot OSL dosimeters.

Figure 7.3a SSD irradiation setup for OSL detectors in a solid slab phantom to build two different equivalent depths: dmax of various beam qualities (were calculated to the depth of 2mm beyond the peak value of maximum PDDs) and 5 cm (for energy dependence experiments). The 10cm thickness below the OSL detector is for the back scatter.

Figure 7.3b SAD irradiation setup for Stability and reproducibility experiment in a solid slab phantom

Figure 7.4a Irradiation setup for OSL dosimeters in the spherical phantom with an additional mount for OSL placement. The isocentre was set to the centre of OSLD, as well as the centre of the phantom.

Figure 7.4b The spherical phantom with additional components and OSL dot placement.

Figure 7.5 The directional dependence experiment image

Figure 7.6 OSL response comparisons over different energies.

Figure 7.7a Dose-response curves for a 6MV photon beam with the dose range from 50cGy to 800cGy in solid slab phantom with build-up depth and 10 cm thickness back scatter depth.

Figure 7.7b Partial dose-response curve for a 6MV photon beam with original data derived from Figure 7.7a.

Figure 7.8 Dose-response curves for a 10MV photon beam with a dose range from 50cGy to 800cGy in solid slab phantom with a build-up depth and a 10 cm thickness back scatter depth.

Figure 7.9 Energy dependence of OSL detectors for photon beams of 6 MV and 10 MV and electron beams with energies from 5MeV to 14 MeV.

Figure 7.10 Response of OSL dosimeters under an incremental dose in cGy for 6MV Linear Accelerator irradiation

Figure 7.11 Response of OSL dosimeters under an incremental dose (in cGy) for 6MV Linear Accelerator irradiation.

Figure 7.12 Response of OSL dosimeters under an incremental dose (in cGy) for 6MV Linear Accelerator irradiation.

Figure 7.13 Readout time dependencies with measurement reading differences after this group of OSL dosimeters was irradiated with a 500cGy calibrated dose.

Figure 7.14 Reproducibility comparisons of 6 OSL dosimeters irradiated incrementally from 10cGy to 800cGy in a water with a 5cm build-up and 10cm back scatter

Figure 7.15 Annealing Efficiency analysis with six OSLs irradiated to 500cGy with the annealed measurement readings acquired after the annealing process

Figure 7.16 OSL re-use ability analysis.

Figure 8.1 Schematic of a Setup of a spherical phantom.

Figure 8.2 Schematic of OSL detectors in a spherical Phantom.

Figure 8.3 The setup of spherical phantom with OSL inserted on CT table

Figure 8.4 Schematic of setup of spherical phantom on Linear Accelerator for IMRT dose verification using OSLDs.

Figure 8.5 Nasopharynx IMRT treatment plan dose distribution

Figure 8.6 Prostate IMRT treatment plan dose distribution

Figure 8.7 Lung IMRT treatment plan dose distribution

Figure 8.8 Nasopharynx IMRT case: TPS calculated doses for 8 measurement points when the isocentre is shifted ±2.0mm and ±1.0mm in three directions in cross-sections (X: lateral, Y: longitudinal, Z: vertical)

Figure 8.9 Prostate IMRT case: TPS calculated doses for 8 measurement points when the isocentre shifted ±2.0mm and ±1.0mm in three directions in cross-sections (X: lateral, Y: longitudinal, Z: vertical)

Figure 8.10 Lung IMRT case: TPS calculated doses for 8 measurement points when the isocenter is shifted ±2.0mm and ±1.0mm in three directions cross-sections (X: lateral, Y: longitudinal, Z: vertical)

Figure 8.11 IMRT plan dose distribution verification experiement setup with a spherical phantom

Figure 9.1 CT image of the CIRS Phantom

Figure 9.2 Coronal view of the in-house phantom (a) without insert and PTW Markus ion-chamber placement; (b) with inserts and OSL placement

Figure 9.3 PTW Advanced Markus ion chamber

Figure 9.4 CT-to-mass density curve and CT-to-electron density curve of a standard CIRS M062 phantom with associated tissue equivalent inserts (dark blue) and an in-house phantom (red) associated with three samples (in different colours with labels on) through interpolation

Figure 9.5 Schematic of PTW Markus Ion-chamber calibrations

Figure 9.6 Schematic of OSL dosimeter calibration

Figure 9.7 Schematic setup of PTW Markus for back scatter thickness measurements with an effective measurement point at isocentre

Figure 9.8 Markus ion-chamber Experiment 1 results (1)

Figure 9.9 Markus ion-chamber Experiment 1 results (2)

Figure 9.10 Schematic of the setup for back scatter thickness influence measurements in a

Homogeneous phantom 1 for Markus ion-chamber Experiment 2

Figure 9.11 Schematic of the setup for back scatter thickness influence measurements for a phantom with tissue equivalent material inserted, phantom 2 to phantom 4 of the Markus ion-chamber Experiment 1.

Figure 9.12 Markus ion-chamber Experiment 2 results (1)

Figure 9.13 Markus ion-chamber Experiment 2 results (2)

Figure 9.14 Markus ion-chamber Experiment 2 results (3)

Figure 9.15 Markus ion-chamber Experiment 2 results (4)

Figure 9.16 Markus ion-chamber Experiment 2 results (5)

Figure 9.17 Markus ion-chamber Experiment 2 results (6)

Figure 9.18 Markus ion-chamber Experiment 2 results (7)

Figure 9.19 Markus ion-chamber Experiment 2 results (8)

Figure 9.20 Markus ion-chamber Experiment 2 results (9)

Figure 9.21 Schematic of setup for back scatter thickness influence measurements for a phantom with tissue equivalent material inserted for Markus ion-chamber Experiment 3

Figure 9.22 Markus ion-chamber Experiment 3 results (1)

Figure 9.23 Markus ion-chamber Experiment 3 results (2)

Figure 9.24 Markus ion-chamber Experiment 4 results (1)

Figure 9.25 Markus ion-chamber Experiment 4 results (2)

Figure 9.26 Markus ion-chamber Experiment 5 results (1)

Figure 9.27 Markus ion-chamber Experiment 5 results (2)

Figure 9.28 Markus ion-chamber Experiment 5 results (3)

Figure 9.29 Markus ion-chamber Experiment 6 results (1):

Figure 9.30 Markus ion-chamber Experiment 6 results (2):

Figure 9.31 Markus ion-chamber Experiment 6 results (3):

Figure 9.32 Schematic of OSL setup to assess the influence of back scatter thickness with the effective measurement point at isocentre in the homogeneous phantom used in OSL Experiment 1.

Figure 9.33 OSL Experiment 1 results (1)

Figure 9.34 OSL Experiment 1 results (2)

Figure 9.35 Schematic of OSL setup to assess the influence of back scatter thickness with

the effective measurement point at isocentre in a homogeneous phantom for OSL Experiment 2.

Figure 9.36 Experiment Exit Dose OSL Two results (1):

Figure 9.37 OSL Experiment 2 results (2)

Figure 9.38 OSL Experiment 3, verification and comparison of OSL measurement results (1)

Figure 9.39 OSL Experiment 3, verification of OSL measurement result (2):

Figure 9.40 OSL Experiment 3 results (3):

Figure 9.41 Schematic of a setup to assess how back scatter thickness influence measurements with an effective measurement point at the exit surface on in a homogeneous phantom using the same tissue equivalent materials inserts as in OSL Experiment 4.

Figure 9.42 OSL Experiment 4 results (1):

Figure 9.43 OSL Experiment 4 results (2):

Figure 9.44 OSL Experiment 5 results: verification and comparison of OSL measurement vs. TMR values (1)

Figure 9.45 OSL Experiment 5 results: verification of OSL measurement results (2):

LIST OF TABLES

Table 1.1 Historical development of OSL dosimetry

Table 3.1 Historical Overview of Al2O3:C Development

Table 6.1 MicroStar Reader reproducibility test using a calibrated InLight™ Dot dosimeter from Landauer

Table 6.2 MicroStar Reader reproducibility test on calibrated InLIght™ dosimeter from Landauer

Table 6.3 MicroStar Reader reproducibility test on a single exposure under 6MV Linear Accelerator (single detector pellicles, Inlight™ Dot Dosimeter) using doses of 50, 100, 200, 300, 400, 500, 600, 700 and 800 cGy, respectively

Table 6.4 MicroStar Reader reproducibility test on a single exposure under a 6MV Linear Accelerator (Cartridges of 4 detector pellicles, Inlight™ dosimeter)

Table 6.5 Error analysis due to wrong orientation of a Dot dosimeter

Table 7.1 Sensitivity of 20 unscreened OSL dosimeters.

Table 7.2 Sensitivity of 7 screened dot OSLDs with irradiation 100 cGy. The OSLDs were put in a 30cm x 30cm slab phantom at a SAD of 100cm with 10 cm build-up.

Table 7.3. The raw readings for beam quality dependence with different OSL dosimeter groups irradiated by 6 MV photons using doses ranging from 50cGy to 800cGy.

Table 7.4 Beam quality dependence for 6MV and 10MV photon and 5,7,9,10,12 and 15 electron beams with irradiated dose range from 50cGy to 600cGy. The OSL response are normalized to the mean value of all the energies

Table 7.5 Beam quality dependence for 6MV and 10MV photon beams with an irradiated dose range from 50cGy to 800cGy. The OSL responses are normalized to the mean value of all the energies.

Table 7.6 Beam quality dependence for 5,7,9,10,12 and 14 electron beams with an irradiated dose range from 50cGy to 600cGy. The OSL responses are normalized to the mean value of all the energies.

Table 7.7 Raw measurement readings of the directional dependence of OSLD

Table 7.8 Post-Irradiation reading time dependence

Table 7.9 Comparison of 4 OSL dosimeters irradiated incrementally from 10cGy to 800cGy in slab water phantom with a build-up depth and a 10cm back scatter depth. The readings were taken 5 times for each OSLs of each exposure. The difference between consecutive readouts were calculated and normalized to 1cGy dose.

Table 7.10 Annealing efficiency comparing the ratio of measurement reading changes between two different light sources, fluorescent (white) and Incandescent (yellow), by given 2 hours annealing. The ratio indicated a significant difference. Average readings were based on 8 OSL dosimeters of each group.

Table 7.11 Fading and reusability

Table 8.1 CT scan Protocols for IMRT cases

Table 8.2 OSL Point measurement verification results for the nasopharynx IMRT case. SD represents the standard deviation of averages of 5 readouts. *ΔD* represents the difference of OSLDs measured dose to that of TPS calculated. σ represents setup uncertainty (2mm). *Diff (%)* represents the percentage difference of OSLDs measured dose to that of TPS calculated.

Table 8.3 OSL Point measurement verification result for the nasopharynx IMRT case. SD represents the standard deviation of averages of 5 readouts. *ΔD* represents the difference of OSLDs measured dose to that of TPS calculated. σ represents setup uncertainty(2mm). *Diff (%)* represents the percentage difference of OSLD measured dose to that which was calculated using a TPS.

Table 8.4 OSL Point measurement verification results for the nasopharynx IMRT case. SD represents the standard deviation of the averages of 5 readouts. *ΔD* represents the difference of OSLDs measured dose to that of TPS calculated. σ represents setup uncertainty (2mm). *Diff (%)* represents the percentage difference of OSLDs measured dose to that of TPS calculated.

Table 9.1 CT numbers of various typical tissues or materials

Table 9.2 CT HU value (120kV, 200mA) vs. Mass Density and Electron Density

Table 9.3 Calculated equivalent thicknesses of phantom and tissue equivalent inserts

Table 9.4 Measurement data for the Verification and Calibration of a PTW Markus Ion-Chamber.

Table 9.5 Measurement data for the Verification and Calibration of OSL dosimeters (1).

Table 9.6 Measurement data for the Verification and Calibration of OSL dosimeters (2).

Table 9.7 Measurement data for Verification and Calibration of OSL dosimeters (3).

Table 9.8 Measurement data for Verification and Calibration of OSL dosimeters (4).

Table 9.9 Summary of the Verification and Calibration of OSLDs.

Table 9.10 Dose calibration of OSL dosimeters for exit dose measurement.

Table 9.11 OSL Experiment 1 result (1)

Table 9.12 OSL Experiment 1 result (2)

Table 9.13 OSL Experiment 2 results

Table 9.14 OSL Experiment 3 results

Table 9.15 OSL Experiment 4 results

Table 9.16 OSL Experiment 5 results

Table 9.17 OSL Experiment 6 results

Chapter 1 General Overview

Optically stimulated luminescence (OSL) dosimetry research was conducted as part of a Doctor of Philosophy program at the University of Wollongong Australia (UOW) and in association with Radiation Oncology Associates (ROA), Sydney Australia. This research was part of collaborative effort with the University of Wollongong Department of Physics.

1.1 Optically Stimulated Luminescence

OSL is a radiation measurement technique that uses the ability of OSL materials like Al_2O_3:C to store absorbed dose and then release it as light when stimulated with another light source having the appropriate wavelength. In this study the radiation sensitivity and dose response linearity of OSL dosimeters was measured by exposing OSL samples to a known radiation field followed by reading the OSL values.

Optically Stimulated Luminescence (OSL) commonly refers to the luminescence of an irradiated insulator or semiconductor when exposed to light. OSL is similar to thermo-stimulated-luminescence in that electrons trapped in defects in the material can be stimulated to generate luminescent emission by laser light rather than by thermal means.

OSL offers some advantages over thermoluminescence (TL) dosimetry. It is normally used at room temperature and can be stored in a dark environment for two years without fading (Akselrod *et al*., 1990). Its sensitivity is potentially higher than TL and it does not need thermal quenching. This makes OSL materials potentially more sensitive and more reliable than TL. OSL dose can be read repeatedly several times with the same dosimeter and can be corrected by using a pre-determined decay constant (Duller 1993; Murray and Wintle 1998). A single grain of an OSL can be read using a focused laser beam (Duller *et al*, 1999). OSL responds to a similar range of radiation energies to TL (Bøtter-Jensen *et al*., 1991; Murry *et al*., 1997) but is more sensitive to visible light than a TLD.

1.2 Historical development of OSL dosimetry and its applications

Many crystal materials have luminescent ability and can be used as OSL materials.

Aluminium oxide was one of the first materials recognized as having the required characteristics and was used as a thermoluminescent dosimeter (TLD) in the 1950's. In 1990, Akselrod *et al*. (1990) found that if oxygen vacancies were included in the Al_2O_3:C structure this would give the material a higher OSL sensitivity. This was the first published paper introducing Al_2O_3:C as an OSL material. In 1995 using Al_2O_3:C as an OSL luminescent material was validated by McKeever *et al.* (1995) after they had compared it with other crystalline materials.

Antonov-Romanovskii *et al.(*1956) developed a method of using infra-red light to stimulate luminescence from strontium sulphide and found that the phosphor had a linear response over a wider irradiation dose range with a fading effect that was dependent on the exposed dose. Relatively few luminescent materials are suitable for dosimetry. The requirements are: a high sensitivity to radiation, high optical stimulation efficiency, low effective atomic number and good fading characteristics. Few papers were published reporting the use of OSL in radiation dosimetry for many years until the late 1980's when the Riso laboratory took advantage of its existing TL measurement platform to develop a new reader based on OSL techniques.

OSL was first suggested for dosimetric purposes by Antonov-Romanovskii *et al.* (1956), Braunlich *et al*.,(1967) and Sanboren *et al*.(1967) in the 1950's and 1960's. The OSL characteristics based on photo-transferred thermoluminescence of Al_2O_3:C were first investigated by Miller in 1988. Single crystals of anion-deficient Al_2O_3:C were developed originally as a highly sensitive TL material (Akselrod *et al*., 1990) and as they appeared to be satisfactory for OSL use became widely used as an OSL detector.

In the 1980s, Al_2O_3:C film material was developed as a commercial OSL dosimetry system for radiation protection by the Battelle Pacific Northwest National Laboratory. This material, integrated with the development of the InLight™ dosimetry system (Perks *et al.*, 2007) by Landauer, OSL, has become widely used in radiation dosimetry.

Many methods of stimulating and measuring the luminescence of OSL materials were developed and the most common ones are: "continuous-wave-OSL (CW-OSL)", "linear-modulation OSL" (LM-OSL) and "pulsed OSL" (POSL). In the CW-OSL method, the stimulation light intensity is kept constant and the OSL signal is monitored continuously throughout the stimulation period. In the LM-OSL method, the stimulation intensity is ramped linearly while the OSL is collected. For the POSL

method, the stimulation source is pulsed and the OSL is collected only between pulses.

Table 1.1 Historical development of OSL dosimetry

	Year	Person	Contribution
Optically Stimulated Luminescence	1921	Przibram	First to observe and describe the effect of light emission of illuminated irradiated substances as radio-photoluminescence.
	1992	Przibram & Kara-Michailova	Demonstrated that photo- phosphorescent intensity depends on the excitation wavelength
	1926	Urbach	Used red light to stimulate a luminescence from irradiated CsBr and KCI.
	1930	Urbach & Schwarz	Demonstrated the light bleaching mechanisms in irradiated rock-salt.
Material	1956	Antonov-Romanovskii *et al.*	Stimulated luminescence from strontium sulphide.
	1959	Schulman	Demonstrated that OSL capable materials have the potential to serve as radiation dosimeters
	1967 1967 1984	Braulnlich *et al.* Sanborn & Beard Rao *et al.*	First generation of phosphors, including Ce(cerium),Sm (samarium) and Eu(Europium) suggested for OSL dosimetry applications
	1969 1970	Tochilin *et al.* Rhyner & Miller	BeO
	1974	Bernhardt & Herforth	CaF_2:Mn
	1998 2001	Dusseau *et al.* Polge *et al.*	MgS
	1977 1981	Pradhan & Ayyanger Pardhan & Bhatt	$CaSO_4$:Dy
	1990 1995 1996	Akselrod *et al.* Markey *et al.* McKeever *et al.*	Al_2O_3:C
Stimulated Luminescence Light Source	1956	Antonov-Romanovskii *et al.*	First to develop infrared light to stimulate luminescence from strontium sulfide.
	1985	Huntley *et al.*	First OSL measurements with quartz and feldspar using argon ion laser.
	1988	Huntley *et al.*	Stimulated feldspars using near infra-red wavelengths around 880nm
	1990	Spooner *et al.*	Used infra-red stimulated luminescence (IRSL) with clusters of diodes (IR LED array).
	1992	Bøtter-Jensen & Duller	Used green light from filtered halogen lamps with quartz.
	1999	Bøtter-Jensen *et al.*	Blue (470nm) L.E.D's
	2000	Duller & Murray	Stimulation using a focused solid-state laser for sedimentary deposits

Table 1.1 Historical development of OSL dosimetry (cont'd)

	Year	Person	Contribution
Readout mode and technique (approach)	1972 1990	Regulla Miller & Endres	Radio-photoluminescence (RPL) for alkali halides.
	1990, 1993	Piesch *et al.*	RPL for phosphate glasses
	1985	Huntley *et al.*	First investigation of a continuous- wave OSL (CW-OSL) method.
	1991 1994 2000	Fain J, *et al.* Bailiff *et al.* Mkeever	Developed CW-OSL on ESR dating.
	1996	Bulur	First introduction of the LM-OSL method.
	1997	Bulur and Goksu	First application of a LM-OSL technique to OSL from ZnS and SrS; storage phosphors that can be stimulated by Infrared light.
	1997	Bulur and Goksu	Applied the LM-OSL technique to OSL from ZnS and SrS (storage phosphors that can be stimulated by Infrared light).
	1997	Yoder & Salasky	Delayed OSL (DOSL)
	1994	Sanderson and Clark	First to develop pulse OSL (POSL) using light-emitting diode (LED) arrays, laser diodes and a pulsed dye laser
	1995 1996 1999	Markey *et al.* McKeever *et al.* Akselrod *et al.*	Pulse OSL (POSL)
	2000	Akselrod *et al.*	Pulse OSL (POSL) for imaging the dose distribution over large area detectors
	1969 1970	Tochilin *et al.* Rhyner & Miller	First to study DOSL from BeO and suggested the DOSL technique in dosimetry
	1997	Yoder & Salasky	Named DOSL for delayed OSL and study DOSL from Al_2O_3:C.
Dose calculation protocol	1997	Murray *et al.*	Dose calculation method for single aliquots of quartz using filtered lamp system
	2000	Murray & Wintle	Single aliquot regenerative dose (SAR) protocol used in dating and accident dosimetry
	2000 2002	Duller *et al.* Murray and Olley	Applied SAR protocol for quartz

Table 1.1 Historical development of OSL dosimetry (cont'd)

	Year	Person	Contribution
Application	1956 1967 1967	Antonow-Romanovskii *et al.* Braunlich *et al*. Sanborn & Beard	Personal monitoring dosimetry using OSL material.
	1995	Bøtter-Jensen & Thompson	Environmental monitoring using OSL material.
	1988 1993 1998	Wheeler Wintle Aitken	Retrospective dosimetry (1) -Dating of geological and archaeological materials
Application (cont'd)	1997 1999 1999	Bailiff Banerijee et al. Bøtter-Jensen et al.	Retrospective dosimetry (2) - Accident dosimetry
	2001 2002 2002 2002	Huston et al. Polf et al. Ranchoux et al. Huston et al.	Medical dosimetry (1) -Real-time optical fibre
	1998 - 2001	Dusseau et al. Dusseau	Medical dosimetry (2) -Dose mapping

One class of measurements, known as stimulated phenomena, optically stimulated luminescence (OSL) have been used for many areas in radiation dosimetry, including: personal monitoring (Antonov-Romanovskii *et al*., 1956; Braulich *et al*., 1967; McKeever *et al*.,1995), environmental monitoring (Huntley *et al.*, 1985; Bøtter-Jensen *et al*., 1997), space dosimetry (Benton and Benton, 2001), UV dosimetry(Bulur 1996; Mckeever et al.,1996), medical dosimetry (Akselrod and Mckeever, 1999; Duesseau *et al*., 1998; 1999; Aznar *et al.*, 2004; Juristic 2007) and retrospective dosimetry (Bøtter-Jensen *et al*., 1996b). The first reported use of OSL as a dosimetry tool for radiation dose measurement in radiotherapy was in 2001 by Huston *et al* (2001). An Al_2O_3:C based dual-probe optical fibre dosimeter system was successfully used in-vivo for checking head and neck IMRT treatment and in a solid phantom for the measurements of central axis depth dose of a radiation field (Aznar *et al*., 2004).

Table 1.1 Illustrates the history of OSL dosimetry development in terms of readout modes/approaches, stimulated luminescence light sources, dose calculation methods, OSL materials and applications in radiation dosimetry.

1.3 Structure of this thesis

This study focused on analysing and evaluating the characteristics of a Al_2O_3:C based Optically Stimulated Luminescence (OSL) system and its potential applications to radiation therapy dosimetry. A commercial OSL dosimetry system developed by Landauer (Landauer Inc., Glenwood, IL) was used for this study. This OSL system includes Al_2O_3:C based InLight™ dosimeters (OSLDs) (quad detectors or single detector) and InLight™ MicroStar™ reader system. The first part of this study covers a technical assessment of OSL dosimeters, as well as the dose characteristics of this specific Al_2O_3:C based OSL system, which allow them to be used in radiation therapy dosimetry including evaluating the stability and reliability of this specific OSL system and evaluating its dosimetry characteristic and technical performance when used with megavoltage radiotherapy beams. The second part of this study explores the possibilities of this specific OSL system as a dosimetry tool to verify point dose and dose distributions for clinical Intensity-Modulated Radiation Therapy(IMRT) dose deliveries, in particular exploring OSL use as a dosimetry tool for skin exit dose measurements (exit dosimetry) in homogeneous and heterogeneous phantoms.

The evaluation of the stability and reliability of the specific OSL system in this research work includes testing the reader performance, the reproducibility of OSL dosimeters, random fluctuations in repeated readings, and random orientation errors of OSL dosimeters.

The evaluation of this OSL system in terms of dosimetric characteristics and technical performance in megavoltage radiotherapy beams in this research work includes: sensitivity of individual OSLD for various beam qualities, dose-response curve linearity, dose dynamic range, beam quality dependence, directional/angular dependence, incremental exposure dose characteristics, reproducibility, read out time dependence, post-irradiation dependence, and annealing characteristics (optimum annealing process, optical source, fading and re-using ability).

The use of this OSL system as a dosimetry tool to verify point dose and dose distributions of clinical IMRT plans was performed using a custom spherical phantom and IMRT plans for three different clinical sites(nasopharynx, prostate and lung).

Exploring of the possibilities of this specific OSL system as a dosimetry tool for skin

exit dose measurements (exit dosimetry) in this research work includes three parts: 1) Markus ion-chamber measurement to investigate the factors that may affect the skin exit dose measurement; 2) OSLD measurement following similar experiment set up and at similar depths to those of the Markus ion-chamber measurements; and 3) comparison of measurement results from OSLD and to Markus ion chamber results.

This thesis consists of 10 chapters:

Chapter 1 introduces the physical principles of OSL, the characteristics of OSL when used for radiation dosimetry, the historical development of OSL dosimetry and the possible applications of OSL dosimetry to radiation therapy.

Chapter 2 describes the theory of OSL.

Chapter 3 describes the properties of OSL materials and OSL measurement technologies.

Chapter 4 discusses the applications of using OSL technology in medical dosimetry.

Chapter 5 discusses the various tools and techniques used in in-vivo dosimetry in radiotherapy.

Chapter 6 provides a detailed evaluation of Landauer's InLight^{TM} Personal Dosimetry System which was used for the experiments in this study.

Chapter 7 assesses the dosimetric characteristics of OSL dosimeters.

Chapter 8 demonstrates the techniques for the application of OSLD to radiation therapy dosimetry by using selected clinical examples and illustrating its potential use for the dose verification of IMRT planned dose deliveries.

Chapter 9 discusses the possibility of using OSLDs for skin exit dose measurements. OSL measurement results were compared with the percentage depth dose measurements from a parallel-plate chamber (Markus ion chamber).

Chapter 10 includes conclusions and recommendations for using OSL in radiotherapy dosimetry.

1.4 Summary of this study

Previous publications describe some of the properties of Al_2O_3:C as a material for OSL dosimetry. These properties make Al_2O_3:C a good candidate for various applications in radiation dosimetry, including personal monitoring, environment monitoring, space dosimetry, UV dosimetry, retrospective dosimetry and medical dosimetry.

Compared with other dosimetric techniques such as TLDs, Semiconductors, Films, and Ionization chambers, the OSL dosimetric technique is unique in that it can: take the form of a flexible film which then can be cut into different shapes or sizes to conform to the measurement conditions. OSL permits a simple operation process, allows the readout to be repeated several times for a single radiation exposure and provides a low degree of uncertainty between repeated readings. Furthermore OSL material can be re-used by overlaying subsequent radiation doses over previous ones without the need for optical annealing until the saturation dose (before departure from the linearity or saturation in dose response) is reached. The maximum accumulation dose in this study was shown to be 800cGy, which is typically less than the maximum dose per fraction used for most clinical treatments. The results from these experiments show that the OSL material may be reused by using a carefully managed optical annealing process even if the repeated overlaid exposures exceed 800cGy, although there are indications that the repeatability of measurements diminishes rapidly after five or more annealing cycles. Further research should be carried out in this area.

Based on the dosimetric characteristics discussed in some recent studies, the intention of this research was to evaluate the use of OSL dosimetry techniques in two ways, the first is a technical assessment of OSL dosimeters as they apply to radiation therapy dosimetry, and the second is an assessment of their clinical use.

In detail:

1: To investigate the dose characteristics of the OSL dosimeters (OSLDs) and the commercially available readout systems, with a special focus on the Landauer's InLight™ Personal Dosimetry System, that need to be considered in its possible applications to radiation therapy dosimetry. In particular, the study assessed OSL signal sensitivity per unit dose, dose response range and dose linearity, beam

type/energy dependency, directional dependency, reproducibility, as well as the possibilities of reuse after annealing the detector.

The experimental results show that in terms of these characteristics the OSL Dosimeter is suitable as a clinical dosimetry tool for both online or offline dosimetry, treatment plan checks, as well as quality assurance (QA) and quality control (QC). The study of OSLD dose-response with accumulated dose shows that OSL dosimetry provides a wide dose response range, good dose linearity and reproducibility for doses up to 600cGy. Doses above 600-800cGy show a 2% maximum deviation from linearity. Doses over 800cGy were not investigated for a linear dose response. The standard deviation in the dose response of 20 unscreened dosimeters with a varied irradiation history was 3.0%. As this needs to be taken into account when OSLDs are used for clinical trials, multiple readings for each irradiation are recommended.

OSLDs can be reused when an optical annealing process is applied by using light, which can restore an OSL to its original state. After optical annealing using incandescent light, the readout intensity decreased by approximately 98% in the first 30 minutes, decreasing further after repeated optical annealing according to the power law, $I \propto t^{-1.3}$, where I is the light intensity.

In the test of OSLD dose response vs. radiation beam energies to asses their use as a tool for both online or offline dosimetry, one found that a similar linear dose-response for both electron and photon beams at different energy levels exists, with only a 2.0% maximum difference between 6 and 10MV x-rays and 5.0% for 6 to 14MeV electrons. When OSLDs were used for the exit dose measurements, the results show that, with a back scatter thickness of 0.5cm, there is no significant difference between 6MV and 10MV x-ray data as the overall dose difference for both energies is within -1.0%. This demonstrates that there is a little energy dependence in OSLDs. The same experiment also demonstrated that the directional dependence of OSLDs was less than ±0.7% for gantry angles from 0 to 90 degrees, as well as demonstrating that OSLDs had little fading effect and good reusability.

2. To verify the IMRT dose distribution in a phantom and to measure exit dose in in-vivo dosimetry using OSL dot dosimeters. For IMRT treatments one made quantitative comparisons of the dose distributions calculated by treatment planning systems (TPS) to those from the measurements by OSL at various points in the custom-designed spherical phantom. Three clinical IMRT plan cases: Nasopharynx,

Prostate and Lung, were used. For in-vivo dosimetry the quantitative comparisons with various backscatter conditions (thicknesses) were performed ranging from an additional 5.0cm thickness back scatter material down to no additional back scatter material added. Secondly the quantitative comparisons with the OSL measurement data to the theoretical data from linear accelerator commissioning data and to the data measured by Markus ion chamber in a custom-designed heterogeneous phantom were performed. Based on the comparisons, recommendations were made for OSL protocols to guide OSL usage in radiotherapy dosimetry.

Based on this experimental data compared with the data from TPS, the study was extended to use OSLD for IMRT plan dose verifications in a phantom. Based on the experimental data compared with the data from percentage depth dose at the same conditions and the data from Markus ion chamber measurement, the study to use OSLD for skin exit dose measurements in a phantom was extended and in virtual patients (simulated by using a phantom with tissue equivalent material inserts). The results, compared with those taken using a Markus chamber and with those from linear accelerator percentage depth dose tables, show that OSLD can be used for skin exit dose measurements with results not significantly different to the Markus chamber. With a 0.5cm~1.0cm back scatter thickness added, compared to that at the full backscatter condition, the accuracy of OSLD is within 2% for normal soft tissue inserts, and is around 4% for high density tissue inserts. The OSLD can also be used in air alone with accuracy of 3.5% for normal soft tissue inserts, and of around 6% for high density tissue inserts. These measurements demonstrated the importance of adding appropriate back scatter material to improve reading accuracy.

Quantitative comparisons were carried out between the dose calculated by TPS and the dose measured by OSLDs in a custom-designed spherical phantom. Three clinical IMRT cases were used for the comparisons: Nasopharynx, Prostate and Lung. Although the quantitative comparisons are highly dependent on the calibration accuracy, the experimental results showed that the dose measured by OSLD was within 3% of that calculated by a TPS when the OSLDs were carefully calibrated**.**

Clinical measurements were performed by using OSLDs to verify the dose distributions and the exit dose using a phantom. These quantitative comparisons were highly dependent on the control dose (or calibration) of the OSLD. OSL can be used to measure the dose distributions in the high dose gradient area, but OSLDs has certain limitations as a point dosimetry tool.

As mentioned above, the results from this study show that OSL dosimetry can be

used for radiotherapy dosimetry, when combined with other dosimetry techniques, as an alternative technology for treatment plan dose measurement and verification as well as for sensitive tissue's dose monitoring. Some factors however must be considered such as backscatter (back scatter thickness), field size, energy, tissue / tumour size and density as these may influence the measured results.

In conclusion, OSL dosimetry can provide an alternative dosimetry technique for use in radiotherapy if rigorous measurement protocols are established. The calibration (control dose) of the OSL dosimeter is extremely important. A practical guide designed for using the Landauer OSLD dosimetry system for radiotherapy dosimetry is summarised in Appendix A.

Chapter 2 Physical Aspects of Optically Stimulated Luminescence

2.1 Luminescence theory

Luminescence is a phenomenon in which the crystalline and/or semi-conductor materials store energy when receiving radiation. This energy may be released as photons when the materials are stimulated by an external thermal or light source (normally in the visible light range with difference wavelength).

The luminescence process can be explained in terms of the band structure of a semiconductor: There are two kinds of energy bands in a material:

- An upper conduction band - which may be empty in the case of an insulator or partially filled in conductors and semiconductors
- Lower valence bands - these lie below the conduction band- which may be filled in insulators and conductors or partially filled in a semiconductor.

When an insulator or semiconductor absorbs thermal or photon energy, electrons may be promoted from the filled valence band to the conduction band, leaving holes in the valence band. The electrons trapped in the conduction band act as mobile charge carriers as do the holes in the valence band. When pairs of charge carriers (electrons and holes) are formed they can move freely within the conduction and valence band respectively increasing the material's conductance.

Most crystals and semi-conductors contain lattice defects or impurities that form intermediate energy levels or traps between the conductive and valence bands. The charge carriers (electrons and holes) may be promoted by the absorption of energy from ionizing radiation sources and trapped in these electron traps as "long –lived" levels (metastable). The crystal may be stimulated by an external thermal or light source to make it return to its equilibrium state. When the luminescence centres (called F+ centres in Figure 2.1) formed are stimulated light is emitted. The stimulating energy source commonly uses ultra-violet, visible or infra-red light in OSL applications. The storage lifetime of exposed radiation energy for a particular crystal is dependent on the energy depth of the electron traps.

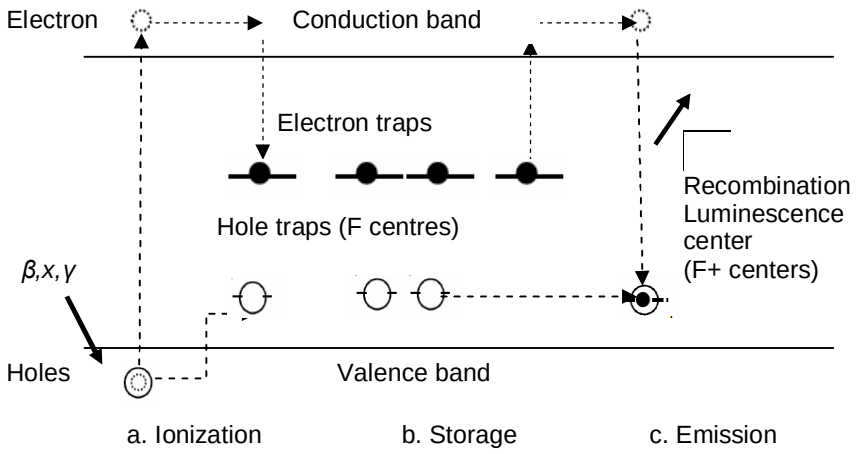

Figure 2.1 Simplified illustration of luminescence excitation and emission in crystals

2.2 Stimulated relaxation phenomena (SRP)

Figure 2.2 shows schematically the energy band of stimulated relaxation phenomena covering the thermally stimulated phenomena (TSP) and optically stimulated phenomena (OSP). The form of perturbation may differ with the property being monitored during the stimulation. In the technique of thermoluminescence (TL) the luminescence is stimulated thermally by warming the sample at a prescribed rate after radiation absorption.

TL and OSL phenomena have perhaps the commonest form of stimulated relaxation phenomena (SRP).

Thermally stimulated conductivity (TSC) or photoconductivity (PC), may also be used to detect ionizing radiation. Instead of measuring the stimulated photon emission the electrical conductivity of the detector can also be monitored.

Thermally stimulated exo-electron emission (TSEE) or optically stimulated exo-electron emission (OSEE) monitors the exo-emission of electrons from near the surface of the material after the stimulation process. In the case of deep level transient spectroscopy (DLTS) or thermally stimulated capacitance (TSCap), the capacitance changes across a semiconductor pn-junction is monitored.

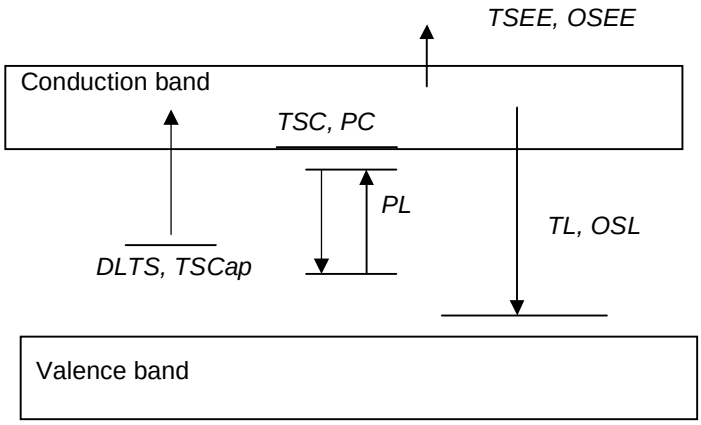

Figure 2.2 Schematic energy band diagram of stimulated phenomena (Bøtter-Jensen *et al,* 2003)

In case of OSL, the intensity of the stimulated relaxation is related to the rate at which the crystal returns to equilibrium. The rate at which the equilibrium is re-established is a function of the concentration of trapped (meta-stable) charge, and the rate in the simplest case is linearly proportional to the trapped charge concentration. Normally the intensity of the luminescence as a function of time is monitored resulting in a characteristic luminescence-versus-time curve.

The use of OSL in radiation dosimetry is based on the fact that the integrated luminescence is proportional to the trapped charge which is proportional to the absorbed radiation dose.

2.3 The energy transition of luminescence process

Bøtter-Jensen *et* al. (2003) and Braunlich (1979) used “filling diagrams“ to represent the energy transition process of different states during an optically stimulated relaxation experiment. As indicated in Figure 2.3: E_C is the energy of conduction band, E_V is the energy of valence band, E_f is the energy of a Fermi level (assumed to be approximately at the mid-way between the top of E_V and bottom of E_C), *f(E)* is the filled energy states and *N(E)* is the normal distributions of energy states, one for electron and one for hole traps.

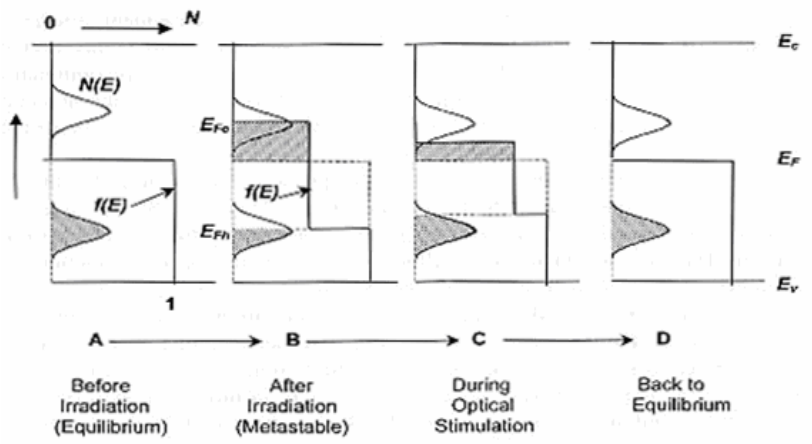

Figure 2.3 Occupancy of forbidden gap states, represented by Bøtter-Jensen *et al.* (2003). The details are described by the text below.

The whole process of energy transition can be represented by four steps including original equilibrium state (before irradiation), meta-stable state (after irradiation), during optical stimulation, and back to the equilibrium state:

A. Before irradiation, the system is at its equilibrium state. All electron traps above E_f are empty, all hole traps below E_f are full. The filled energy state below the Fermi level are full, $f(E) = 1$. All states above the Fermi level are empty.

B. After perturbation by radiation some electron traps are filled by electrons of an energy above the Fermi level E_f, and an equal concentration are trapped in holes below the Fermi level E_f. Two quasi-Fermi levels, one for electrons E_{fe} and one for holes E_{fh} can be defined. These are useful means for describing the non-equilibrium state, which follows the perturbation in terms of equilibrium statistics by making the assumption that the trapped electron and hole population are in thermal equilibrium over their available energy level.

C. During stimulated relaxation, namely during illumination of the irradiated sample with UV, visible and IR light, the filling function $f(E)$ gradually returns to its pre-perturbation state. During this process, the quasi-Fermi levels gradually move back towards the equilibrium Fermi level as the trapped charge concentrations decay back to their equilibrium values.

D. And finally all states return to their original equilibrium occupancies.

2.4 Mathematical description of OSL

The total concentration of occupied metastable stages is a function depending on time and dose as it increases during irradiation and decreases during stimulation. Time *t* may be represented by

$$\mu(t) = \int_{\gamma_1}\int_{\gamma_2}\cdots\int_{\gamma_m} n(\gamma_1,\gamma_2,\cdots\gamma_n,t)d\gamma_1 d\gamma_2\cdots d\gamma_m \qquad (2.1)$$

where the parameters represent:

- $n(\bar{\gamma}_1,\gamma_2, \gamma_3.....\gamma_m, t)$: occupied state
- $\bar{\gamma}_1,\gamma_2, \gamma_3.....\gamma_m$: state parameters dictate the stability of the meta-stable state under the prevailing conditions of temperature and illumination intensity.
- $n(\bar{\gamma}_1,\gamma_2, \gamma_3.....\gamma_m, t)$: a weighting function or distribution, expressing the concentration of occupied states possessing the parameters $\bar{\gamma}_1,\gamma_2, \gamma_3.....\gamma_m$.
- In general, $n(\bar{\gamma})=N(\bar{\gamma})f(\bar{\gamma},t)$. Where, $n(\bar{\gamma})$ is the concentration of occupied states, $N(\bar{\gamma})$ is the concentration of available states, and $f(\bar{\gamma})$ is the occupancy of the state ($f=1$ when a state is full and $f=0$ when a state is empty). Both $n(\bar{\gamma})$ and $f(\bar{\gamma})$ are time-dependent functions.

The equation 2.1 is a time- and dose-dependent function as it increases during irradiation and decreases during stimulation.

In stimulated luminescence measurements the intensity of the emitted luminescence during the return of the system to equilibrium is monitored and represented by a characteristic luminescence-versus-time curve. The integral of this curve represents the trapped charge concentration and reflects the proportion to the initial dose of the absorbed radiation. The luminescence intensity is proportional to the rate at which the meta-stable states decay and is represented by a time-dependent probability. The form of probability depends on the stimulation method. For optical stimulation, the probability depends on the optical stimulation intensity, the threshold optical stimulation energy required for charge release and return to equilibrium and the photoionisation cross-section for interaction of the meta-stable state with an incident photon.

In stimulated luminescence measurements, the intensity of the emitted

luminescence during the return of the system to equilibrium is monitored and represented by a characteristic luminescence-versus-time curve. The integral of the luminescence-versus-time curve represents the trapped charge concentration and reflects the proportion to the initial dose of the absorbed radiation. The luminescence intensity I is proportional to the rate at which the meta-stable states decay and is represented by a time-dependent probability $p(\gamma_1, \gamma_2, \gamma_3 \ldots \gamma_m, t)$.

$$I(t) = \left| \frac{d\mu(t)}{dt} \right| = \int_{\gamma_1} \int_{\gamma_2} \cdots \int_{y_m} n(\gamma_1, \gamma_2, \cdots \gamma_m, t) p(\gamma_1, \gamma_2, \cdots \gamma_m, t) d\gamma_1 d\gamma_2 \cdots d\gamma_m \qquad (2.2)$$

The form of probability p depends on the stimulation method. For optical stimulation, p can be representing by:

$$p(E_0) = \Phi \sigma(E_0) \qquad (2.3)$$

where the parameters represent:

- Φ: the optical stimulation intensity, here it is a fixed value independent of time.

- E_0: the threshold optical stimulation energy required for charge release and return to equilibrium.

- $\sigma(E_0)$: the photoionisation cross-section for interaction of the meta-stable state with an incident photon.

- $m=1$ and $\gamma_t = E_0$ for OSL.

2.5 Photoionisation cross-section

Bøtter-Jensen *et al.* (2003) summarized five possible optical absorption transitions which are important to dosimetry (Figure 2.4): (1) band-to-band optical transition; (2) excitation formation; (3) defect ionization; (4) trap ionization, and (5) internal intra-centre transition. However, only the transition 4 in Figure 2.4 comes from an initial localization of charge by traps during irradiation and results in OSL emission. Thus, the subsequent luminescence light is a function of the initial dose of radiation absorbed,

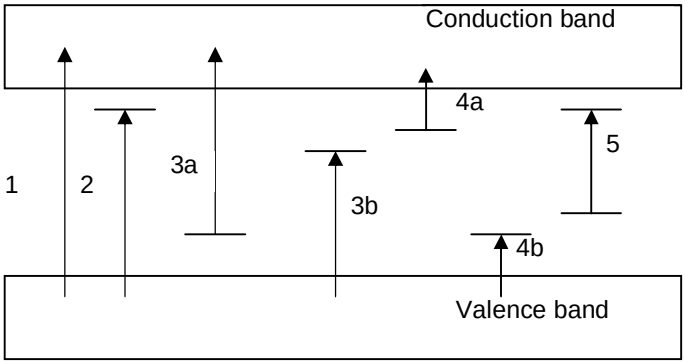

Figure 2.4 A schematic of the possible optical absorption transitions in an insulator.(1) ionisation (2) exciton formation transition, (3) defect ionisation,(4) trap ionisation, (5) internal intra-centre. (From Bøtter-Jensen et al.,2003)

and the intensity, wavelength and duration of the optical stimulation light (Bøtter-Jensen *et al.*, 2003).

The photoionisation cross-section is an important parameter associated with the traps' ionization transition. It dictates the stability of a particular trap during optical stimulation. It is wavelength dependent and represented by optical stimulation energy. To determine the photoionisation cross-section, several expressions were derived by previous researchers such as Lucovsky (1964), Blakmore and Rahimi (1984), Grimmeiss and Ledebo (1975a,b), Banks et al. (1980), Ridley (1988), and Landsberg (1991).

The photoionisation cross-section can also be obtained experimentally through various methods, demonstrated respectively by Ditlefsen and Huntley (1994), Whitely & McKeever (2000) and Bøtter-Jensen *et al*.(2003). Nevertheless, these technologies can only produce relative values for the photoionisation cross-sections rather than its absolute ones. In fact, the absolute values of photoionisation cross-sections can be obtained from LM-OSL with a fixed wavelength or from the ratio of the slope of CW-OSL decay curve against the CW-OSL intensity (Huntly *et al.*, 1996).

2.6 Three main OSL modes

As described above, the optical stimulation intensity depends on the method of

optical stimulation. Three popular optical stimulation schemes are illustrated in Figure 2.5:

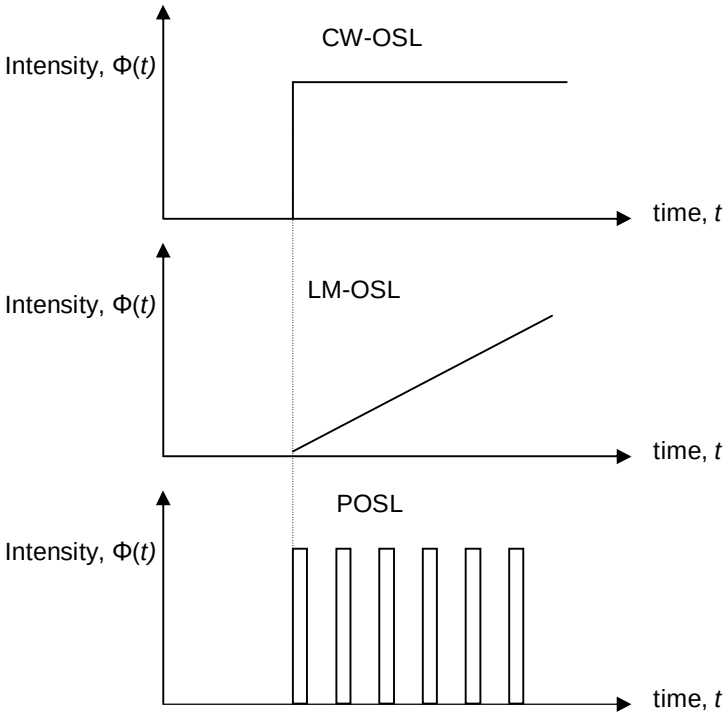

Figure 2.5 Schematic diagrams of three main OSL stimulation methods: CW-OSL, LM-OSL, and POSL. (From Bøtter-Jensen *et al.*,2003)

1. When a fixed wavelength and steady stimulation intensity are used to empty the traps, the optical luminescence is recorded as a continuous wave OSL (CW-OSL).
2. When a fixed wavelength is used and the scanned stimulation intensity rises with time, the optical luminescence is recorded as a linear modulation OSL (LM-OSL).
3. When pulsed with pulse width ($\Delta\tau$) and pulse period (τ) stimulation is used, the optical stimulation is called pulsed OSL (POSL).

2.6.1 Continuous wave OSL (CW-OSL)

The continuous wave OSL (CW-OSL) using a fixed wavelength and a steady stimulation intensity to empty the traps and to record the luminescence as a function

of illumination time is named the luminescence-versus-time curve.

The optical excitation light source in a continuous wave mode is either from a laser or from a high power arc lamp with monochromator / filter system.

Huntley *et al.* (1985) used 514.5 nm light from an-argon laser to irradiate an OSL sample at room temperature and demonstrated a luminescence-versus-time curve, which is also named as OSL decay curve.

2.6.1.1 Mechanism and process

McKeever *et al.* (1997a) summarized various mechanisms and processes that can be used for CW-OSL based on feldspar and quartz. They introduced a combined model (Figure 2.6) which encompassed many trap possibilities and might be a more accurate real-world model of OSL materials. This model includes five level typical traps: a shallow trap, a dosimetry trap, a deep trap, a radiative recombination centre, and a non-radiative recombination centre.

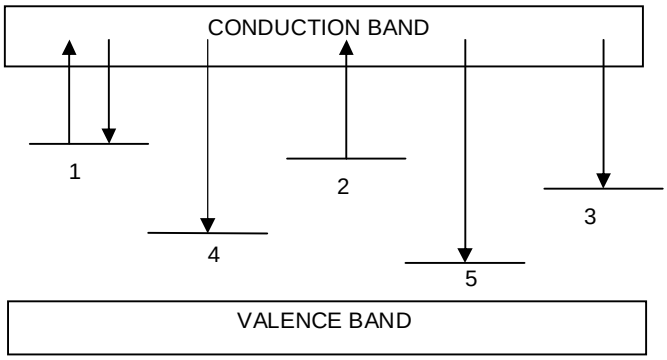

Figure 2.6 A model combing all the possible traps in an OSL sample. Including: (1) a shallow trap; (2) a dosimetry trap (a optically active trap); (3) a deep trap; (4) a radiative recombination centre; and (5) a non-radiative recombination centre. (From McKeever *et al.,* 1997a)

Level 1. Shallow trap: electrons are either trapped ones during optical stimulation in the shallow trap (downward arrow) or thermally or optically released ones from the shallow trap (upward arrow).

Level 2. Dosimetry trap: electrons are optically stimulated from the dosimetry trap.

Level 3. Deep trap: electrons are trapped into the deep trap and remain localized once trapped.

Level 4. Radiative recombination centre: in which electrons are recombined with trapped holes with producing an OSL photon.

Level 5. Non-radiative recombination centre: in which electrons are recombined without producing any OSL photon.

In general, the shape of decay curve is dependent upon the OSL sample, the absorbed dose, the illumination intensity and the temperature (Bøtter-Jensen *et al*., 1994; Spooner, 1994; McKeever *et al.*, 1997a; Whitley and McKeever, 2000).

In practice, the decay curves show a wide variety of curve shapes, non-exponential and with a long "tail" of decay at long illumination times, temperature-dependence and a clear peak at an intermediate temperature, with excitation power and absorbed dose influences.

Based on the model described in Figure 2.6 McKeever *et al*. (1997b) experimentally demonstrated the various factors influencing on OSL decay curves that includes a variety of temperatures (in units of K), excitation rate f (in units of s^{-1}), and different absorbed dose (in units of dose unit). Figure 2.7 shows the results excluding thermally assisted transitions.

2.6.1.2 Temperature influence

Temperature dependence effects play an important role in CW-OSL technique. At low temperatures (Figure 2.7a), the half-life of the charge in the shallow traps is much longer than the decay time for the CW-OSL signal, the OSL signal is reduced due to the released charge coming from competing traps into the shallow traps. At high temperatures, where the half-time of the charge is much shorter compared to the decay time for the CW-OSL signal, a higher OSL intensity is obtained. After an initial increase in the curve after the illumination applied, OSL decay curves show a roughly exponential change followed by a longer period of non-exponential decay. Non-exponential OSL decay is contributed to by charges re-trapped into the shallow traps, dosimetric traps, deep traps, and non-radiative recombination centres.

The decay is a convolution of simple decay due to the depletion. It firstly increases and then decreases at a rate governed by the thermal stability of the shallow traps (Bøtter-Jensen *et al*., 2003). At a higher temperature, the effect of the shallow traps is negligible. Meanwhile, at a lower temperature, the charge in the shallow traps is stable and does not contributes to the luminescence (McKeever *et al*., 1997a). At

intermediate temperature, a peak is observed on the CW-OSL curves as the trapping and thermal de-trapping of the charge are mostly from the shallow traps.

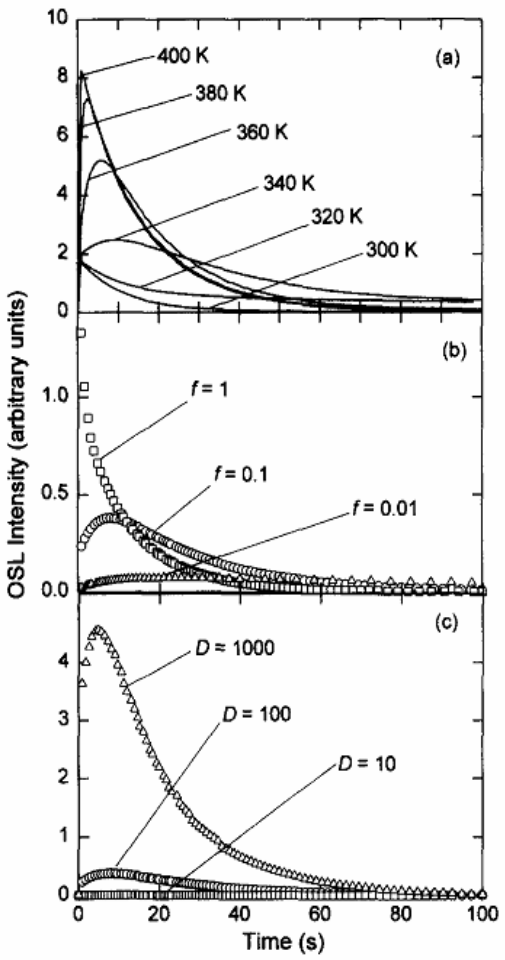

Figure 2.7 OSL decay curves. *D* represents dose with dose unit 10, 100, and 1000, respectively. *f* represents the excitation rate, 0.01, 0.1, and $1s^{-1}$, respectively. (a) Stimulated CW-OSL curves using model of Figure 2.7 at a variety of temperatures. Here, $D = 10$ dose units and $f = 0.1s^{-1}$. (b) Stimulated CW-OSL curves as a function of excitation rate *f*, for $D = 100$ dose units. (c) Stimulated CW-OSL curves as a function of dose for $f = 0.1s^{-1}$. (From McKeever *et al.*, 1997)

2.6.1.3 Theoretical explanation of the temperature dependence of OSL

Bøtter-Jensen *et al.* (2003) summarized the possible processes that may give rise to the temperature dependence of OSL production, and they are shown in Figure 2.8.

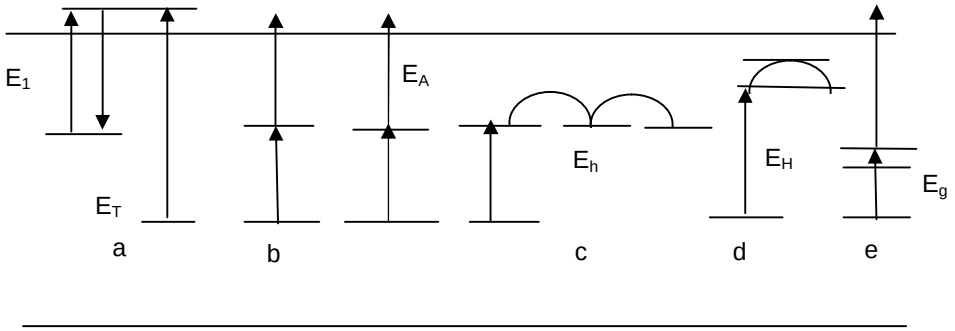

Figure 2.8 Schematic representation of the processes that my give rise to the temperature dependence of OSLs, including (a) the effect of shallow traps (McKeever *et al*., 1997; Markey *et al.,* 1996); (b) thermal assistance from an excited state (Hutt et al., 1988); (c) donor-acceptor hopping (Poolton et al., 1994); (d) band tail states hopping (Poolton *et al.*, 1995a, b; 2002a, b); and (e) ground state excitation (Spooner, 1994) (From Bøtter-Jensen *et al.,* 2003)

There are five mechanisms or models to explain temperature dependence:

(a) The effect of shallow traps (Markey *et al*., 1996). The temperature-dependence of OSL material rises due to the trapping of optically stimulated charges by shallow traps. The thermal activation energy is identified with thermal trap depth of the shallow traps, E_1.

(b) Thermal assistance from an excited state (Hutt *et al*., 1988). The optical excitation to a defect excited state is followed by thermal excitation to the de-localized band. The thermal activation energy is E_A.

(c) Donor-acceptor hopping (Poolton *et al*., 1994). The thermal activation energy is identified with E_h, the hopping energy required to hop from the first excited state of the trap (donor), and the acceptor is the recombination centre (acceptor).

(d) Band tail states hopping (Poolton *et al*., 1995a,b; 2002a,b). The activation energy E is identified with the band tail hopping energy E_H.

(e) Ground state excitation in quartz (Spooner 1994). This mode based on an array of ground states energies, from where optical excitation to the conduction band can occur. The thermal activation energy is E_g.

The temperature dependence effect of Al_2O_3:C results in thermal quenching, the variation of OSL with temperature. The luminescent efficiency decreases as the temperature increases (McKeever *et al*., 1997a; Murry and Wintle, 1998). The

luminescence from different Al_2O_3:C samples may be show different concentrations of shallow traps (Akselrod *et al.*, 1998a).

2.6.1.4 Excitation power

Due to the negligible effect of the shallow traps at high temperatures and the stable charge in the shallow traps the excitation rate of the CW-OSL is the same. However this is not the case at intermediate temperatures.

The excitation rate (in units of s^{-1}) is given by the product of the illumination intensity (photon flux) and the photoionisation cross-section of the trap.

Figure 2.7b shows the results from McKeever *et al.* (1997a) in variations of OSL curves as a function of excitation rate at an intermediate temperature and a fixed dose (100 dose units). For higher excitation rates (equal to 1), there is no initial peak observed. Along with the decreasing excitation rate (equal to 0.1) and (equal to 0.01), the peak can be observed again. Meanwhile the decay rate tends to decrease as power decreases.

2.6.1.5 Dose effect

Figure 2.7c shows the stimulated OSL curves as a function of dose that was made with a fixed excitation power at an intermediate temperature (McKeever *et al.,*1997a). The initial peak is more clearly visible at higher doses. The position shift of the peak in the curves occurs slightly earlier as the dose increases.

2.6.2 Linear modulated OSL (LM-OSL)

2.6.2.1 Mechanism and process

Linear modulated OSL (LM-OSL), as an alternative technique to CW-OSL, is based on the stimulation intensity (light power) linearly ramped from zero to a preset value during luminescence readout (Figure 2.4). In the measurement of LM-OSL, the luminescence shows a linear increase until the traps are depleted sufficiently that the signal decreases and eventually decays to zero.

Bulur *et al.* (1996) used a simplified model to represent three different orders of kinetics: first-order, second-order, and general order kinetics.

2.6.2.2 Characteristic of LM-OSL curves

An example of LM-OSL from Al_2O_3:C demonstrated by Bulur *et al.* (2001) is shown in Figure 2.9.

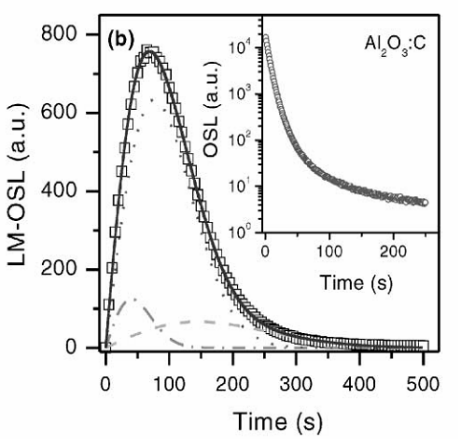

Figure 2.9 Experimental LM-OSL curves from Al_2O_3:C. The Al_2O_3:C was irradiated by 100 mGy, pre-heated by 180˚C/10 s, stimulated with blue light, and measured under 75˚C. The inset shows the CW-OSL curve obtained under the same conditions (From Bulur *et al.,* 2001).

The typical LM-OSL curves show that:

- An initial linear increase as the stimulation power rises, followed by a Gaussian decrease to zero in OSL intensity as the traps deplete.
- Each peak corresponding to the optical release of charge from different trap types.
- A LM-OSL peak whose position is dependent on the wavelength (through the wavelength dependence of photoionisation cross-section σ) and on the linear modulation ramp rate γ (Whitely and McKeever, 2001, Bøtter-Jensen *et al.*, 2003). The peak shifts occurs earlier at higher ramp rates or at a larger cross- section values. Examples of LM-OSL curves for different values of the wavelength and ramp rate are shown in Figure 2.10.
- The LM-OSL peak shifts with temperature if the photoionisation cross-section has significant temperature dependence (Bøtter-Jensen *et al.,* 2003).
- The relationship between the de-trapping rates and the stimulation light intensity was observed to be linear for Al_2O_3:C (Bulur *et al.,* 2001).

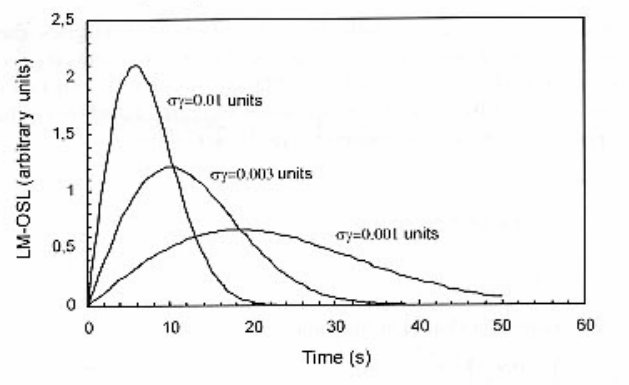

Figure 2.10 Stimulated LM-OSL curves for first-order kinetics, using three different values of the product $\sigma\gamma$. For fixed ramp rates γ, the LM-OSL peaks appear at shorter times as the photoionisation cross-section σ increases. For fixed σ, the peaks appear at shorter times as the ramp rate increases. Note: all peaks start at *t=0*. (from Bøtter-Jensen *et al.*, 2003)

2.6.2.3 Relationship between LM-OSL and CW-OSL

The only difference between CW-OSL and LM-OSL techniques is that LM-OSL uses linear increased stimulation intensity instead of the fixed intensity used in CW-OSL.

Bulur (2000) demonstrated a simple transformation to convert CW-OSL curves to LM-OSL curves from a Na-feldspar sample. The comparison between the continuous wave (CW), the transformed pseudo-IR-stimulated luminescence, and the experimental LM-OSL curves is shown in Figure 2.11. The experiment result shows good agreement between the pseudo-LM-OSL curve and the experimental CW-OSL curve.

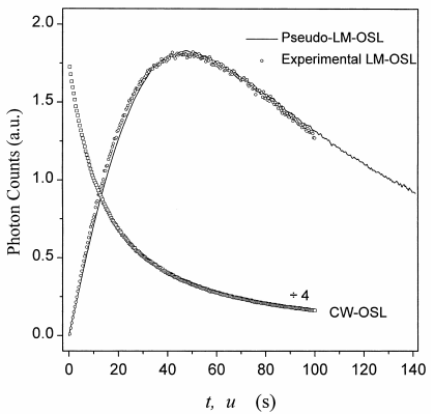

Figure 2.11 Comparison between CW-OSL, transformed Pseudo-LM-OSL and experimental LM-OSL curves from a Na-feldspar sample. CW-OSL and experimental LM-OSL curves were obtained using IR-stimulation. A ramp time *P=100* was used in transformation calculation and experiments. (From Bulur 2000)

The first-order kinetic transformation can be translated to the second-order and the general order by the expressions for calculation (Bulur 2000).

2.6.2.4 Advantage of LM-OSL technique

- Enhanced resolution in an OSL signal
- Rapid determination of OSL curve parameters: the peak maximum and the peak position
- Very useful to distinguish which luminescence originated from what trap.
- Easier to discriminate the luminescence decay processes with different physical parameters, the number of the trapped electrons and time-constant of the decay of the luminescence.
- There is a linear relation between the de-trapping rates and stimulation light intensity for Al_2O_3:C (Bulur, 1996)
- Traps with fast, slow and medium rates of de-trapping may be more easily resolved by using LM-OSL compared with CW-OSL (Bøtter-Jensen *et al.*, 2003)

2.6.3 Pulsed OSL (POSL)

2.6.3.1 Mechanism and process

Pulsed OSL (POSL) is based on a pulsed stimulation with different pulse intensity, pulse width and pulse period (lifetime). The stimulation source is pulsed at a particular modulation frequency and a pulse width chosen to appropriately match the lifetime of the luminescence.

The optical stimulation intensity is separated in two parts: the emission during the excitation pulse and the emission after the excitation pulse. The efficiency of the POSL process is represented by the ratio of the luminescence emitted after the pulse to that emitted during the pulse (McKeever *et al*, 1996). In POSL stimulation mode, only the OSL emission between the pulses rather than during the pulses is measured. POSL technique is very sensitive to the luminescence lifetime of material. POSL detects the faster decay due to the intrinsic F-centre luminescence lifetime, which is typically 35 ms at room temperature for Al_2O_3:C (Markey *et al.,* 1995) (Figure 2.12). The POSL signal is usually acquired at short times with a

strong, prompt, temperature-independent OSL component, which is stronger than the delayed signal from OSLs (Akselrod *et al*., 1998a).

In some OSL samples, a slower decay with longer lifetime is observed. This decay corresponds to the re-trapping of the released charge from deep, stable traps to shallow, unstable traps. This is called “delayed OSL (DOSL)” (Yoder and Salasky, 1997) . The OSL intensity is measured after the pulse of the stimulated light. DOSL detects a much slower decay, typically 545 ms at 25˚C. This means that DOSL is highly temperature-dependent (Figure2.12).

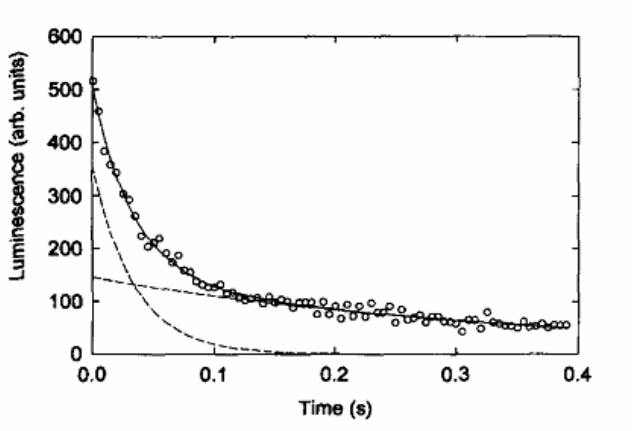

Figure 2.12 OSL decay curves acquired after a stimulation pulse from a laser at 25˚C. The decay has been fitted to two exponentials: 1) temperature-independent faster decay with lifetime 35 ms; and 2) temperature-dependent slower decay with 545 ms. (from Markey *et al*., 1995)

2.6.3.2 Characteristics of a POSL curve

Bøtter-Jensen *et al*.(2003) used a schematic way (Figure 2.13) to illustrate the relationship between stimulation pulse intensities and pulse widths while keeping the result (representing stimulation energy) of intensities and pulse width constant. From these curves it can be seen that:

- A rise to the peak in pulse width (build-up), followed by a decay of the luminescence in response to the excitation pulse. (Figure 2.13 and Figure. 2.14).
- The total integral under each of the curves is constant. This represents the total charge released from the trap.
- When the pulse width is varied, the proportionality constant of the area under

the curve after the pulse varies.

- The efficiency decreases as the pulse width increases. (Figure 2.14).

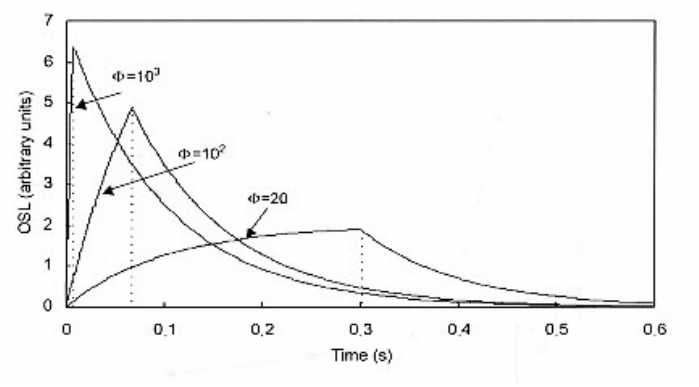

Figure 2.13 Schematic illustrating the variation in the ratio of the light emitted during a pulse to that emitted after the pulse as the pulse width changes for fixed stimulation energy per pulse. A luminescence lifetime of 100 ms was assumed. Stimulation pulse intensities are 10^3, 10^2 and 20 energy/s associated with pulse widths of 6.6, 66, and 300 ms. Note: It is assumed that the concentration of charge release per pulse is negligible compared with the total trapped charge concentration. (from Bøtter-Jensen *et al*., 2003)

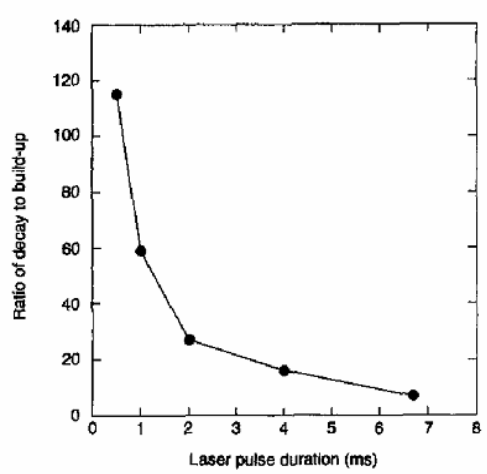

Figure 2.14 Ratio, represents the efficiency, of the luminescence emitted after the pulse to that emitted during the pulse. (from Markey *et al.,* 1996)

2.6.3.3 Relationship between POSL and CW-OSL

In the CW-OSL measurement, the luminescence is continually monitored during the optical stimulation until all the trapped charges are depleted. The stimulating light is separated from the emitted light by use of filters. In POSL measurement the

luminescence is only detected after the ending of the stimulating light pulse and discrimination between the stimulation and the emission is accomplished by using shutters.

When the separation of two pulses is small, the relaxation time is very short compared with the wider excitation pulse width, and the POSL is equal to CW-OSL.

2.6.3.4 Advantage of POSL technique

POSL provides a very effective separation of stimulation light and luminescence light which removes noise. Luminescence can be detected without using heavy filtration to remove the stimulation laser light.

Compared to DOSL, POSL has a high sensitivity and weaker temperature dependence. The integrated light output in a typical POSL measurements is approximately a factor of 7~8 greater than that of DOSL (Akselrod *et al.*, 1998a). POSL luminescence comes from the direct recombination of released charge carriers at luminescence sites. The DOSL signal comes from the capture of released charge carried by shallow traps (Akselrod *et a*l., 1998a).

2.7 Summary

In this chapter, the physical aspects of optically stimulated luminescence (OSL) was reviewed, including: luminescence theory, stimulated relaxation phenomena, energy transition of luminescence process, and photoionisation cross-section. Three main OSL modes/techniques are reviewed and compared based on their mechanism and process, curve characteristics and advantages and disadvantages. These help us to better understand OSL technique for further applications.

Chapter 3 OSL Properties of Al_2O_3:C

3.1 Introduction

Al_2O_3:C as a suitable material for thermoluminescence (TL) dosimetry was introduced by Akselrod *et al* (1990). It's unique dosimetric properties include: its high TL sensitivity (approximately 60 times greater than that of LiF:Mg, Ti); its simple glow curve (the well separated TL and TSEE (Thermally stimulated exo-electron emission) dosimetric peaks at 190^{o}C), its low background and dose threshold (0.1 μGy with nitrogen flow); its low fading during storage in the dark room (less than 5% per year); good reproducibility (<2%) and re-usability without annealing; its simple emission spectrum (with a maximum at 420 nm which corresponds to the maximum sensitivity of low noise), high sensitivity when read by a photomultiplier tube; its wide dose range from 10^{-7} to 10 Gy; and a relatively low effective atomic number (10.2).

α- Al_2O_3:C detectors were initially produced in the form of a single crystal (Akselrod *et al.* 1990). To meet the needs for skin dosimetry, dose mapping, and other dosimetry in personal and environment dosimetry, *α*- Al_2O_3:C was developed in different forms such as powders of various grain sizes, and thin layers on substrates (Akselrod *et al*. 1993).

The TL sensitivity of Al_2O_3:C is about 40-60 times higher than that of LiF TLD-100 (Akselrod *et al.*, 1990, 1993) making it suitable for low-dose, short-exposure applications (McKeever *et al*., 1995). However, the drop in sensitivity observed at higher heating rates, due to the thermal quenching, (Kitis *et al*., 1994; Kortov *et al*., 1994) makes Al_2O_3:C inconvenient for routine TL dosimetry where fast heating automatic readers are often used.

Al_2O_3:C is highly sensitive to the light in four ways:

(1) the generation of a TL signal in un-irradiated samples (Izak-Biran and Mocovitch, 1996) results from the absorption of light by oxygen-vacancy centres caused by the generation of free charge carriers (Summers, 1984);

(2) a light-induced fading of the TL signal influences the wavelength dependence and time dependence for fixed wavelengths (Moscovitch *et al*., 1993; Walker *et al*.,1996);

(3) the photo-transfer of charge from deep states to shallower states gives rise

to a photo transferred TL (PTTL) signal (Akserlrod *et al*., 1993; Oster *et al.*, 1994; Colyott *et al*., 1996) and results in the optically-induced transfer of charge from traps responsible for deep energy levels to “dosimetry traps“.

(4) and finally, the development of the phenomenological model (Bøtter-Jensen and McKeever, 1996a; McKeever *et al.*, 1996) predicts Al_2O_3:C as exceptionally high sensitivity material for OSL than for TL.

The unique dosimetric properties of Al_2O_3:C can make an OSL technique a better candidate for in vivo dosimetry in external beam radiotherapy than Thermoluminescence (TL) dosimetry (Hu *et al*., 2009).

3.2 Historical overview of Al_2O_3:C development

Table 3.1 shows the historical overview of Al_2O_3:C development as OSL material.

Table 3.1 Historical Overview of Al_2O_3:C Development

Year	Author(s)	Contribution
1990	Akselrod *et al.*	1) Introduced Al_2O_3:C as suitable material for TL dosimetry with unique dosimetric properties, especially as the sensitivity is about 40~60 times higher than that of LiF TLD-100. 2) Al_2O_3:C in form of single crystal
1993	Akselrod *et al.*	Al_2O_3:C in powdered form of various grain sizes, thin layer on substrates.
1994 1994	Kitis *et al.* Kortov *et al.*	Al_2O_3:C rapidly loses its sensitivity as the heating rate rises due to the thermal quenching
1995	Izak-Biran & Mocovitch	The generation of a TL signal in unirradiated samples
1993 1994 1996	Akselrod & Gorelova Oster et al. Colyott et al.	Study of photo transferred TL (PTTL) in Al_2O_3:C
1993	Moscovitch *et al.*	Yellow light appears to be less effective than unaltered fluorescent and incandescent light
1994	Rathbone *et al*.	Red light is less effective than light of a shorter wavelength.
1996	Walker *et al*.	1) Wavelength dependence range from 250 nm to 650 nm; 2) Time dependence for fixed wavelength
1996 1996	Bøtter-Jensen & McKeever McKeever *et al.*	Development of a phenomenological model

3.3 Crystal structure of Al_2O_3:C

The crystal structure of Al_2O_3 was clearly described by Bøtter-Jensen *et al*.(2003) (Figure 3.1 below). Each Al^{3+} ion is packed closely by six O^{2-} ions in C_2 symmetry, where each O^{2-} ions is surrounded by four Al^{3+} ions.

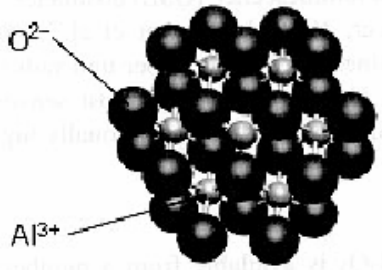

Figure 3.1 Crystal structure of Al_2O_3 shows that the Al^{3+} ions is packed closely by six O^{2-} ions in C_2 symmetry, where each O^{2-} ions is surrounded by four Al^{3+} ions. (from Bøtter-Jensen *et al*., 2003)

Al_2O_3 is an amphoteric aluminium oxide. It shows high optical, chemical and thermal stability under irradiation. However, when Al_2O_3 contains impurities it can become sensitive to radiation.

In Al_2O_3:C, the main OSL material, carbon impurities play a very important role in catalysts for the formation of oxygen vacancy centres, and can be presented in concentrations as high as 5000 parts per million (ppm) (Akselrod *et al.*, 1993). The amounts of other common impurities, including Ca, Cr, Ti, Ni, Si, Cu, Mg and Fe, vary depending on the growth conditions and fabrication (Gimadova *et al.,* 1990; Akselrod *et al.*, 1990; 1993; Springis *et al*., 1995). Some impurities should be kept to a minimum or avoided, especially Ti impurities (Molnar *et a*l., 2001) as they provide efficient recombination pathways for charge carriers.

The currently available Al_2O_3 materials for OSL dosimetry are provided by the following companies. They can be in the form of single crystals, poly-crystals, powders, and thin evaporated film:

- Harshaw Saint-Gobain (Cleveland, USA)
- Rados (Finland)
- Landauer Crystal Growth Facility (Stillwater, USA)
- Nexstep Technologies (Stillwater, USA)

- Several research laboratory sources in Russia (Urals) and Latvia (Riga)

TLD-500 from Saint-Gobain and similar materials for use in OSL dosimetry are usually in the form of discs with a 5 mm diameter and 1 mm thickness. The Al2O3 used in the Landauer Luxel^{TM} OSL dosimeters is in the form of powder.

3.4 Characteristics of Al_2O_3:C

3.4.1 Al_2O_3:C stimulation and emission characteristics

3.4.1.1 Stimulation

Obtaining the stimulation spectrum is very complex and is dependent on the radiation and readout history of each sample and the extent of a deep trap's filling. The wavelength dependences of the photoionisation cross-sections of the traps contributing to the OSL signal and the wavelength dependences of the transfer of charge from deep traps into dosimetric and other shallower traps can influence the stimulation curve.

Markey *et al.* (1995) used an Ar-ion laser as an excitation source to measure the OSL stimulation spectrum from Al_2O_3:C (TLD-500) by using a pulsed OSL mode. The power from the laser at each wavelength was adjusted to give the same number of photons per unit time per unit area incident on the sample. The most intense emission was observed at a spectrum of about 460 nm (Figure 3.2a) which then rose continuously to then form a wider plateau which peaked at about 480 nm. The samples were irradiated by a $^{90}Sr/^{90}Y$ beta-particle source given a dose of 0.04Gy and stimulated with a single laser pulse with 150 mW power and 100 ms pulse width. The decay of luminescence in response to the excitation pulse is shown in Figure 3.3a.

Walker *et al.* (1996) used a 1000 W Xe arc lamp as an illumination source, and the wavelength was selected by monochromator with a band width of 20 nm. The photoconductivity peak spectrum was approximately 450~470 nm.

Bøtter-Jensen *et al*. (1997) used a continuous scanning monochromator attached to a broad-band stimulation light source to measure the stimulation spectrum from Al_2O_3:C (Figure 3.2c). The stimulation spectrum shows a rising continuum at lower wavelengths in addition to a smooth broad stimulation resonance peaking at around 500 nm. The samples were irradiated by a $^{90}Sr/^{90}Y$ beta-particle source, given a

dose of 0.06Gy and then stimulated with a wavelength band 420-550 nm at a density of 16mW/cm^2. The decay curve is shown in Figure 3.3b.

A variation of the stimulation peak was noted by previous studies. It may be produced due to the complex stimulation spectra and measurement procedures. However, an apparent resonance in the optical stimulation curve trend is also significant. For various stimulation spectrums, Al_2O_3:C commonly shows a rising continuum at lower wavelengths, then rising to a peak over a broad wavelength range. When stimulated in these wavelength regions, the OSL signal from Al_2O_3:C exhibits a bright and rapidly decaying curve (Figure 3.3).

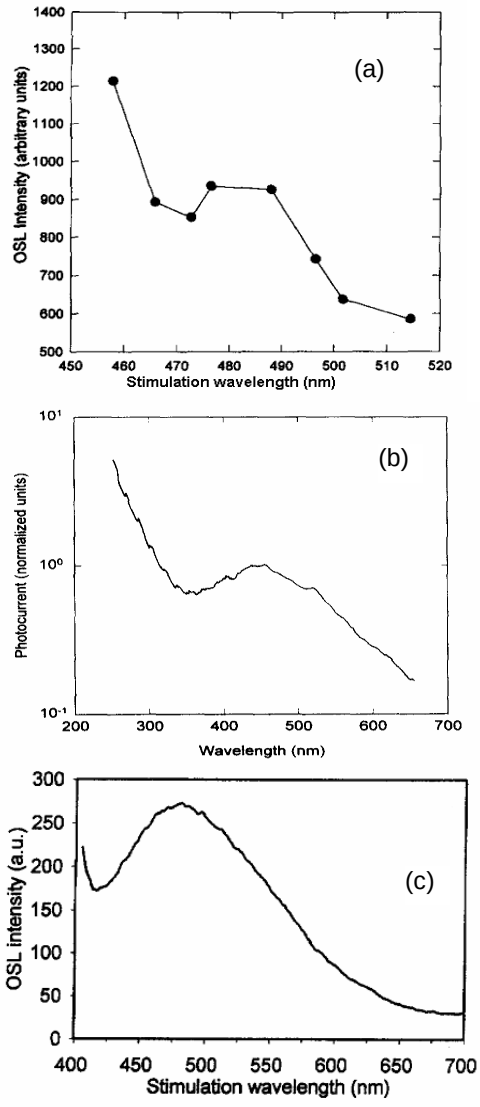

(a) OSL stimulation spectrum for Al_2O_3:C obtained using an Ar-ion laser as a stimulation light source in pulsed OSL mode. The power from the laser at each wavelength was adjusted to give the same number of photons per unit time per unit area incident on the sample. (From Markey *et al.,* 1995)

(b) OSL photoconductivity spectrum for Al_2O_3:C obtained using a Risø monochromator with band width of 20 nm. The samples were irradiated with a dose of 862 Gy and scanned with a light wavelength between 250 nm and 650 nm. (From Walker *et al.,* 1996)

(c) OSL stimulation spectrum for Al_2O_3:C obtained using the Risø visible monochromator and a broad-band hologen lamp stimulation light source. Detectrion filter: U-340. (From Bøtter-Jensen *et al.,* 1997)

Figure 3.2 Excitation spectra for OSL from Al_2O_3:C (TLD-500)

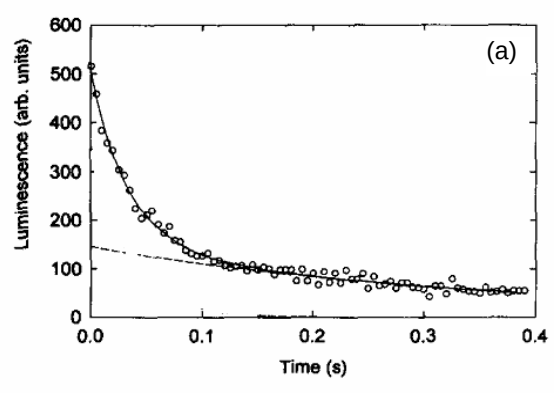

(a) Decay curve of an OSL signal at 25˚C at the end of the laser pulse. The decay has been fitted to two exponentials. The faster component is temperature independent and the lifetime (~35 ms) corresponds to the F-center lifetime. The lifetime of the slower component (~545 ms at 25˚C) is temperature dependent (from Markey *et al.,* 1995)

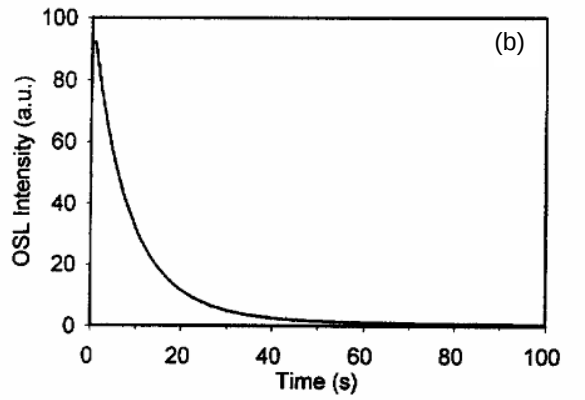

(b) Decay curve of OSL from Al_2O_3:C after irradiation by a $^{90}Sr/^{90}Y$ particle beta source with a given equivalent dose of 0.06Gy and stimulated with a wavelength band of 420-550 nm. (From Bøtter-Jensen *et al*., 1997)

Figure 3.3 Decay curve of OSL from Al_2O_3:C (TLD-500)

The stimulation wavelengths at 205, 230, 255, and 300 nm (Figure 3.4) are an intrinsic feature and not radiation induced (Bøtter-Jensen *et al.,* 2003). The stimulation peak at 205 nm is a result of electron transitions from the 1S ground state to the 1P level in F-centres and neutral oxygen vacancy centres. The stimulation wavelengths at 255 and 230 nm resulted from 1A to 1B and 2A levels in the F^+-centres, followed by 1B to 1A relaxation and emission at 326nm. The stimulation near 300 nm and emission band at near 500 nm results from A1 interstitial ions or is caused by F-centre clusters (Pogatshnik *et al.,* 1987; Tale *et al.*, 1996; Pelenyov *et al*., 2001).

3.4.1.2 Luminescence

Whitley and McKeever (2000) demonstrated an isometric plot of the luminescence emission spectrum from 360 to 580 nm from Mg-doped Al_2O_3:C irradiated over a wavelength stimulation region from 200 to 320 nm (Figure 3.4). The emission peak is at approximately 420 nm with a direct stimulation in the F-centre, peaking at 205

nm. The emission peak is at 420 nm due to relaxation from the excited 3P state to the 1S ground state (Evans and Stapelbroek, 1978; Summers, 1984). With a fixed emission wavelength of 420 nm, the stimulation spectrum widens up to 600 nm (Figure 3.5), and even up to infra-red region (Bulur *et al.*, 1998; Bailiff and Clark, 1999; Erfurt *et al.,* 2000).

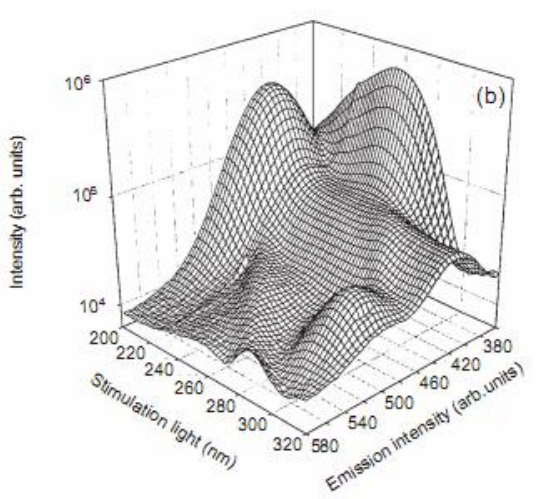

Figure 3.4 Isometric plot of the stimulation spectra (200 ~ 320 nm) emission spectra (360 ~ 580 nm) from an irradiated 0.1% Mg-doped Al_2O_3:C sample. The shoulder emission peaking is around 420 nm with stimulation peaking near 205 nm. (From McKeever *et al.,* 1999)

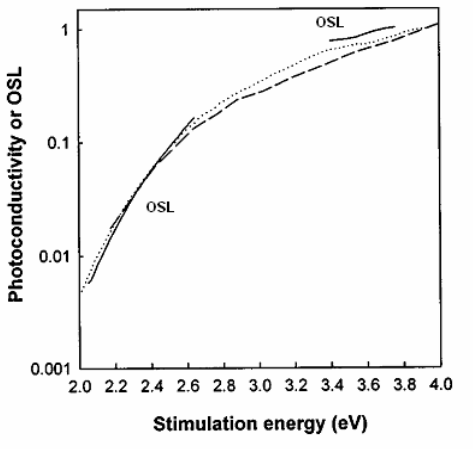

Figure 3.5 Comparison of OSL stimulation spectra (solid line) with photoconductivity after Al_2O_3:C was irradiated 300 Gy using a ^{60}Co source. The OSL spectrum was obtained using a fixed emission wavelength 420 nm. (From Whitley and McKeever, 2000)

Electron hole transitions in Al_2O_3:C OSL via de-localized bands was theoretically explained by the Markey *et al.* (1995). They measured the time-resolved OSL emission spectrum from irradiated Al_2O_3:C following pulsed stimulation with the 514 nm line from an Ar-ion laser. They found that the emission peak at around 410 – 420 nm remained fixed at this wavelength during the entire decay process. The emission spectrum at 410 – 420 nm is also the main emission band observed in photoconductivity (Walker *et al.*, 1996; Whitley and McKeever, 2000; 2001) , TL (Akselrod *et al.*, 1993; McKeever *et al*, 1999), and radioluminescence (RL) (Erfurt *et al.*, 2000; Poolton *et al.,* 2001) from this material.

The infra-red emission spectrum was observed near 700 – 790 nm for OSL (Erfurt *et al.*, 2000) and TL (McKeever *et al.*, 1995).

3.4.2 The OSL response of Al_2O_3:C to radiation exposure

Al_2O_3:C is a suitable material for TL dosimetry with its unique dosimetric properties, but it is the light-induced fading of a Al_2O_3:C signal that makes it a strong candidate for optically stimulated luminescence (OSL) (Akselrod *et al.,* 1990; 1993).

Sections 3.4.2.1 to 3.4.2.2 below discuss the main advantages of OSL over TL when they are used as dosimeters.

3.4.2.1 Good response linearity over wide dose range

Akselrod and McKeever (1999) demonstrated the pulsed OSL (POSL) dose response of Al_2O_3:C over a wide range of the radiation doses from 10^{-4} Gy to 10 Gy (Figure 3.6). The anion-deficient Al_2O_3:C samples (powders deposited between plastic layers, grown by Stillwater, supplied by Landauer Inc.) were exposed to a $^{90}Sr/^{90}Y$ source. The dose response was measured by a POSL dosimetry system and shows that there is good linearity over the whole measurement range. This feature makes OSL calibration procedures simpler and makes it easier to determine an unknown dose.

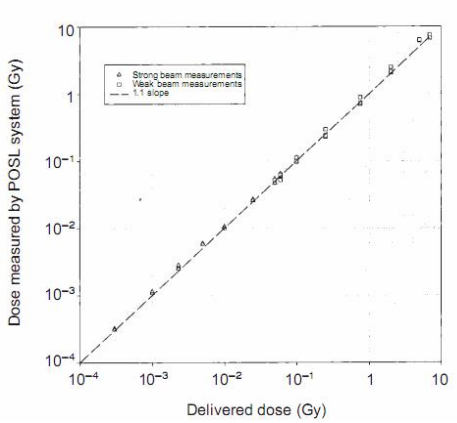

Figure 3.6 Dose response for Al_2O_3:C powder. The POSL signal was measured by using a weaker laser beam (0.01 W, data indicated by □) for high-dose levels and a stronger beam (1.2 W, data indicated by Δ) for the low-dose levels (From Akselrod and McKeever, 1999)

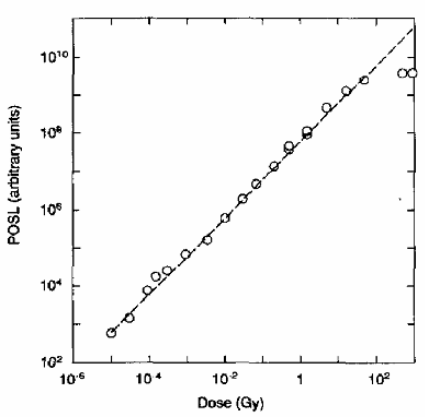

Figure 3.7 Dose responses for α-Al_2O_3:C using POSL. The POSL counts are summed over 100 laser pulses, each of 30 ms duration, with a gate time of 4 ms and a dwell time of 2 ms. (From McKeever *et al.*, 1996)

McKeever *et al.* (1996) showed there was good OSL dose response linearity from 5 μGy up to 50 Gy. Above that the dose response appeared to be saturated (Figure

3.7).

3.4.2.2 Reusability

Bøtter-Jensen *et al.* (1997) demonstrated the results of a repeated single aliquot regeneration method in OSL measurements of Al_2O_3:C exposed to 4 μGy of ^{60}Co gamma radiation and read using a Risø scanning monochromator (Figure 3.8). Measurements were repeated at multiple times by using green light bleaching with and without preheat at 100˚C/30s prior to OSL readout. The results showed that Al_2O_3:C had an excellent reusability and there was no significant measurable fading of the OSL signal when exposed to low doses. This study also shows that preheat prior to OSL readout is unnecessary.

Akselrod and McKeever (1999) also showed an illustrative example for the re-exposure and re-measurement of OSL samples by using their POSL method. The same samples were irradiated to different known doses from $3x10^{-4}$ Gy to 2 Gy (Figure 3.9). The OSL signals were monitored by a POSL dosimetry system. Each measurement consisted of 4000 laser pulses administered over 1 s. They found that the standard deviation of five re-estimated dose values were between 1.5 to 3 %. This characteristic makes OSL calibration procedures simpler.

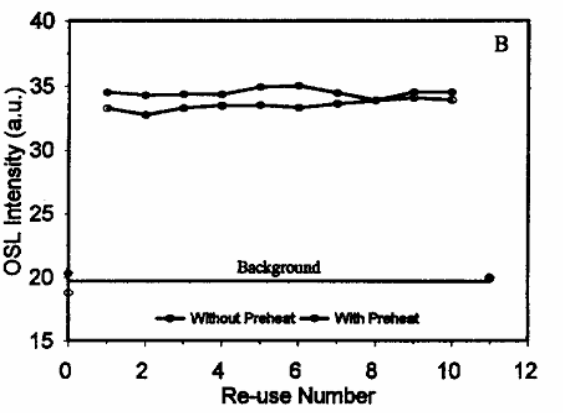

Figure 3.8 Repeated single aliquot regeneration OSL measurements of Al_2O_3:C after exposed to the same dose of 4 μGy ^{60}Co gamma radiation. The two curves represent: 1) preheat at 100˚C/30 s prior to OSL readout; 2) no preheat. Note the background readings (undosed dosimeter readings before and after the regeneration cycle. (From Bøtter-Jensen *et al.*, 1997)

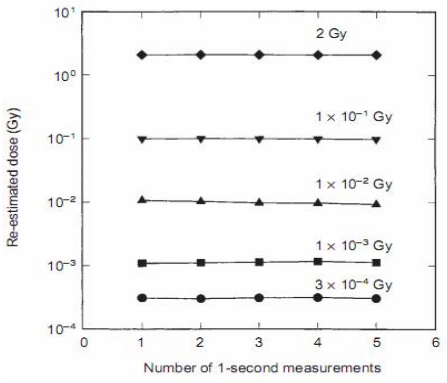

Figure 3.9 Dose reassessments for five repeated POSL measurement for the initial dose from $3x10^{-4}$ Gy to 2 Gy. (From Akselrod and McKeever, 1999)

3.4.3 Temperature dependence of Al_2O_3:C OSL

It is well known, that when used for optically stimulated luminescence, Al_2O_3:C pre-heating is not necessary. However, many researchers investigated and demonstrated the variations in the shapes of the OSL decay curve at different temperatures. McKeever *et al.* (1997) and Bøtter-Jensen *et al.* (2003) described several processes that give rise to a temperature dependence in OSL response; OSLDs show a higher dose when read at higher than when read at lower ambient temperatures. Five models to explain this effect are described in details in section 2.6.1.3. However, it should be noted that although this is a factor for some readers, others adjusts for temperature dependence by ensuring a consistent internal temperature during the reading.

Markey *et al.* (1995) observed that the POSL signal from Al_2O_3:C increased with sample temperatures as shown in Figure 3.10. They concluded that the rise of OSL signal on the decay time is dictated by two components: (1) a faster component that is temperature independent (for low temperatures) with a life time of around 35 ms which is associated with the F-centre luminescence (Summbers 1984); (2) a slower component that is temperature dependent and is due to phosphorescence from shallow states with trap depths of 0.65 eV and 0.77 eV respectively (Figure 3.11). The latter two traps from the shallow states produce a TL at temperature below that of the main TL peak in Al_2O_3:C.

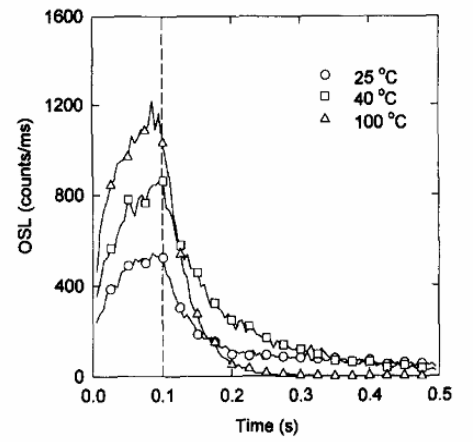

Figure 3.10 Time-resolved OSL from α- Al_2O_3:C following irradiation at room temperature with a dose of 0.04 Gy $^{90}Sr/^{90}Y$. A single laser pulse (150 mW, 100 ms wide) was used to excite the OSL. The measurement temperatures were 25˚C, 40˚C, and 100˚C, respectively. (From Markey *et al.*, 1995)

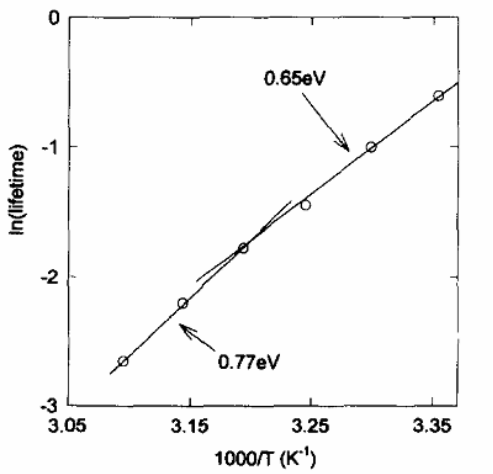

Figure 3.11 Arrhenius plot of the variation of the lifetime of the slow component as a function of temperature. Two activation energies are 0.65 eV and 0.77 eV. (From Markey *et al* 1995)

Akselrod *et al.(*1998b) demonstrate that when Al_2O_3:C was irradiated at 200 K (-73˚C), the TL glow curve consists of three peaks: peak I at 265 K (~0˚C, peak II at 310 K (~70˚C) and peak III at 450 K (~200˚C) when heated at 0.4˚C/s (Figure 3.12). The shallow and deep traps also affect the OSL properties of Al_2O_3:C due to the strong correlation between TL peak III at 450 K (~200˚C) and the OSL signals.

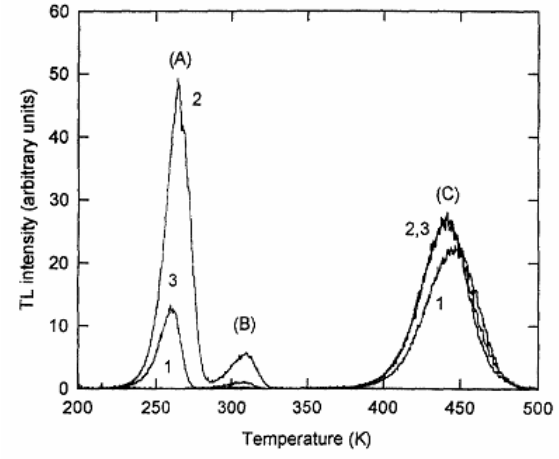

Figure 3.12 Glow curves from (1) POST-quality, (2) TLD-quality, (3) DOSL-quality Al_2O_3:C samples irradiated at 200 K and heated at 0.5 K/s. TL is observed in three temperature regions: (A) ~230K-280 K (-43˚C -7˚C); (B) ~280 K – 320 K (7˚C -47˚C); and (C) ~400 K – 480 K (127˚C -207˚C). In each case, the dose was delivered approximately 150 µGy. (From Bøtter-Jensen *et al.*, 1997)

The thermo-optical luminescence (TOL) measurements with the Al_2O_3:C samples were used to investigate the importance of shallow traps. The measured TOSL is the combination of OSL and TL. Duller and Bøtter-Jensen(1993) investigated the OSL signal from TOL measurements using feldspars. The OSL signal as a function of temperature was calculated by subtracting the TL signal from the TOL signal according to the defined procedures. The TOL curve for Al_2O_3:C is shown in Figure 3.13 (Bøtter-Jensen *et al.,* 2003). Their OSL readings were temperature dependent. The OSL signal increased up at peak to ~150˚C, then a sharp decrease occurs. The decrease is partially due to the emptying of the dosimetric traps and partially due to the strong thermal quenching of F-centre emissions (Kortov *et al.,* 1994; Akselrod *et al.,* 1998b). The TL curves in Figure 3.13 clearly show peak II and peak III.

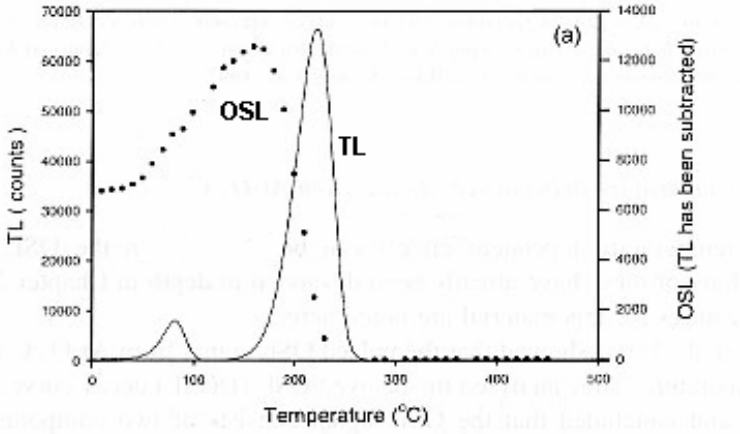

Figure 3.13 Thermo-optical luminescence (TOL) characteristics of Al_2O_3:C after 1 Gy $^{90}Sr/^{90}Y$ beta dose irradiation at room temperature and heated at 2˚C/s. The OSL (dot line) and TL (solid line) curves against temperature (From Bøtter-Jensn *et al.*, 2003).

The illumination of an irradiated Al_2O_3:C sample with visible light will remove the main dosimetric TL peak that had been described by previous studies(Moscovitch *et al.,* 1993; Walker *et al.,* 1996; Akselrod *et al.,* 1993; Colyott *et al.,*1996). However, the relationship between the TL and the OSL sensitivities are complex. McKeever *et al.* (1999) showed a general relationship between POSL and TL intensity with a considerable variation from sample to sample. Akselrod and Akselrod (2002) demonstrated the different relationships in some materials characterized by a narrow TL peak and a wide TL peak. Whitely and Mckeever (2000) described a complex distribution of optical traps depths due to photoionisation cross-section. The variation in the TL peak's shape, width and position as functions of dose may influence the variation of the distribution (Walker *et al.,* 1996).

Temperature dependence is due to the contributions from deep traps and dosimetric trap(s). Deep traps' contribution increases along with a decreasing in stimulation wavelength. The contribution directly from deep traps is only a small component of the OSL signal, 2~3%, when stimulating light in the range of the green wavelength (Bøtter-Jensen *et al.,* 2003), and 10% when stimulating light at 465 nm (Whitely and McKeever, 2000) is used. Bøtter-Jensen *et al.(*1997) indicated that the deep traps' effect is negligible in environmental dosimetry where smaller doses are measured (1 mGy).

However, it may be difficult to distinguish the temperature dependence of the OSL due to the deep traps from that due to dosimetric trap(s). Figure 3.14 shows the temperature dependence of OSL demonstrated by Bøtter-Jensn *et al.* (1999). They observed the following features of OSL: (1) in the flat plateau region (60~140˚C) where there is no OSL coming from shallow traps; (2) the steep decrease region (150~220˚C) where the TL glow peak at 200˚C may relate to the most OSL sensitive traps ; (3) and that at temperatures of up to 220~550˚C where the decay becomes slower. These results are in good agreement with the study from Markey *et al*.(1996) where Al_2O_3:C single crystals received 1.5 Gy dose. (4) Beyond 500˚C, the OSL signal of Al_2O_3:C chips which received 1 Gy falls almost down to the instrumental background. This recommends that an annealing temperature of 500˚C as this temperature is enough to zero the Al_2O_3:C dose completely. This approach fills the deep traps but empties the dosimetric traps.

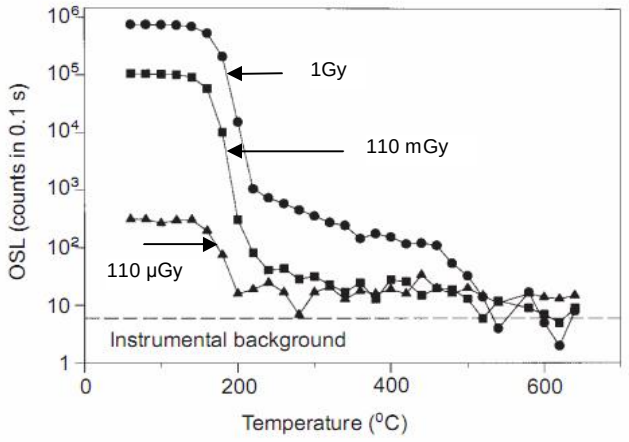

Figure 3.14 Plots of OSL signals against pre-heat temperature for Al_2O_3:C chips irradiated 1 Gy(dot), 110 mGy(square) and 100 µGy(triangle), respectively, using a $^{90}Sr/^{90}Y$ beta source and measured at room temperature (from Bøtter-Jensn et al., 1999). Note the logarithmic Y axis.

3.4.4 OSL signal zeroing from Al_2O_3:C

The contribution directly from deep traps in environmental dosimetry accounts for only a small amount of the OSL signal. This is negligible because the dose is rather small (1 mGy) and the deep traps are largely unfilled (Bøtter-Jensen *et al*.,1997). However the contribution may rise to 2~3% when stimulated with a wavelength in the green range (Bøtter-Jensen *et al.*, 2003), and 10% when stimulated with wavelength at 465 nm (Whitely and McKeever, 2000). Therefore, in a single sample calibration sequence it is necessary that the luminescence from earlier irradiations of the same sample are reduced to negligible fractions of their initial values by either thermal annealing or bleaching with stimulation light (Bøtter-Jensn *et al*.,1999).

3.4.4.1 Thermal annealing

When a smaller dose is measured (~1 mGy) in environmental dosimetry, the deep traps' effect is negligible (Bøtter-Jensen *et al.,* 1997) (Figure 3.15).

Earlier studies related to OSL characteristics from Markey *et al.*(1996) suggested that it is necessary to do pre-annealing at 900˚C to avoid the effect of the charges in deep traps on repeated measurements if irradiation doses higher than 1Gy are used.

Bøtter-Jensen *et al.*(1999) indicated that an annealing temperature of 500˚C is sufficient to zero Al_2O_3:C dose completely even if the exposed dose is as high as 1 Gy (Figure 3.15).

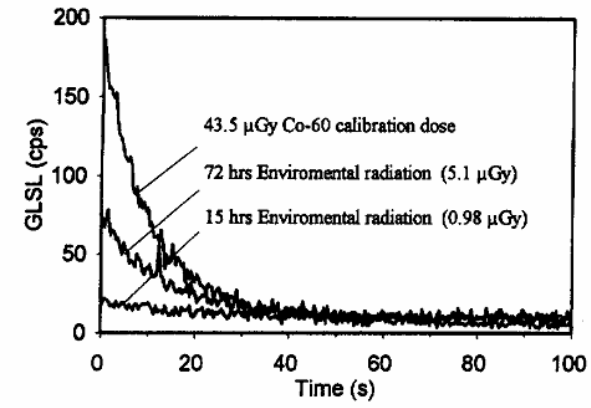

Figure 3.15 OSL decay curves from Al_2O_3:C dosimeters exposed over 15 and 72 hrs to the natural environmental radiation representing evaluated integrated doses of 0.98 and 5.10 µGy, respectively, compared to that from 43.5 µGy ^{60}Co gamma calibration dose. (From Bøtter-Jensen et al., 1997)

3.4.4.2 Bleaching with stimulation light

Bøtter-Jensen et al.(1999) pointed out that the OSL signal is generally depleted to less than 1% of the initial value over 35 s at a power density of 30 mW/cm^2 by using blue light (470 nm) stimulation (Figure 3.16). This feature allows the zeroing of OSL signals by sunlight on location in the field, which are typically used in environment dosimetry.

Bøtter-Jensen *et al*.(1999) also irradiated an Al_2O_3:C single crystal chip with 100 µGy from ^{60}Co gamma radiation and then bleached these with unfiltered sunlight for 8 hours. After bleaching, the measurement result showed a residual OSL signal dose of 0.4 µGy which is close to the background reading and is negligible.

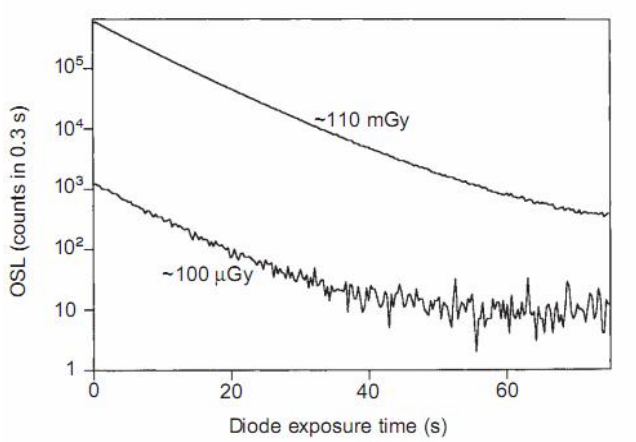

Figure 3.16 OSL decay curve from Al_2O_3:C exposed to 110 mGy and 100 µGy beta radiation at room temperature (From Bøtter-Jensen et al.,1999). Note the Y axis is logarithmic.

3.5 Summary

This chapter reviews previous publications discussing the properties of Al_2O_3:C as a material for OSL dosimetry including studies of it's crystal structure, stimulation and emission characteristics, response to radiation exposure, temperature dependence and thermal and light annealing. These properties make Al_2O_3:C a good candidate for many dosimetry fields including radiation therapy.

Chapter 4 Literature review of Al_2O_3:C based OSL Measurement Techniques in Medical Dosimetry

4.1 Introduction

The wide range of applications of OSL in radiation dosimetry such as: personal monitoring, environmental monitoring, space dosimetry, UV dosimetry, medical dosimetry, and retrospective dosimetry, have stimulated research institutes and manufacturers to develop OSL dosimetry systems. Up to now, there are at least four types of OSL dosimetry systems based on Al_2O_3:C available:

1) Personal dosimetry products from Landauer (Landauer Inc. Glenwood, IL), such as the InLight™ dosimeter with the MicroStar reader and the Luxel™ dosimeter associated with the automated Risø TL/OSL-DA-15 reader (Risø National Laboratory, Denmark), have been successfully used as they have a wide range of radiation detection capabilities, useful in personnel and environment monitoring and other areas (Yukihara *et al.* 2004; 2005; Akselrod and McKeever, 1999).
2) OSL and radioluminescence (RL) that have medical applications in remote optical fibre dosimetry: The Risø TL/OSL OSL real-time optical fibre dosimetry system has played a key role in *in-vivo* dosimetry (Anderson *et al.*. 2006, 2008; Anzar *et al*, 2004; Edmund e*t al.,* 2006).
3) Single Grain systems, similar to the one based on charge coupled device (CCD) image technique or to the one based on the single grain luminescence (SGLL) technique. These are suitable for very small OSL samples. The Risø single grain OSL attachment is designed for measurements of single OSL grains.
4) The Daybreak High Capacity OSL reader from Oak from Daybreak Nuclear Systems (Bernal and Bogard, 2004). This reader is capable of exposing up to 30 samples, Landauer Luxel™ detectors, to beta radiation (Bortolot 2000) .

It is worthy to mention that the CEM2 of Universitẽ Montpellier II from France is devoted to OSL Dose Mapping technique (Packaging dosimetry) research. This system has also demonstrated it's use for radiotherapy dosimetry for X-rays, Electrons, Proton, Gamma knife and Dental images (Dusseau *et al*, 1998; 1999; 2000; 2001; Polge *et al*. 2001; Idri *et al.,* 2004). However, as the materials used are non-Al_2O_3:C based, this system will not be discussed further.

The first two systems and their associated OSL dosimeters are potentially suitable for use in medical dosimetry. More information about the Risø TL/OSL reader is described below, the InLight™ OSL dosimeter and MicroStar reader(Landauer Inc. Glenwood, IL) will be introduced in Chapter 6.

4.2 Risø TL/OSL reader

In 2000 Risø National laboratory Demark started to develop a TL/OSL compatible reader which integrates a light detection system, a thermal stimulation system and an optical stimulation system. The reader can read the OSL sample provided by Landauer Inc., such as Luxel™ or TLD-500 samples grown at the Urals Polytechnic Institute (Russia).

The OSL dosimeters used with the Risø TL/OSL reader from Landauer Inc. are the same materials as the InLight dosimeters. They are also based on a thin layer of carbon-doped aluminium oxide powder (Al_2O_3:C) deposited onto a clear plastic film. Each dosimeter element can be cut in various sizes as required.

The Risø TL/OSL reader system consists of two separate units, the reader and the controller. The essential components of the reader are a light detection system, a luminescence stimulation system, and calibration sources (Figure 4.1).

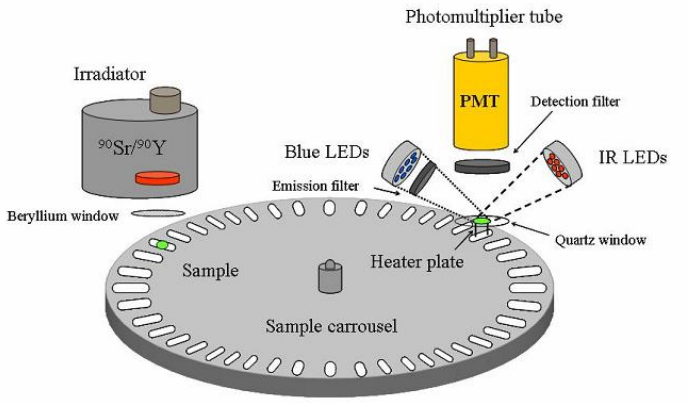

Figure 4.1 Schematic drawing of a Risø TL/OSL reader. (from Risø user manual)

The calibration source is either a beta source or an X-ray generator. The light detection system is composed of a photomultiplier tube (PMT) in combination with suitable detection filters. The PMT detects the emitted luminescence. The maximum detection efficiency is at between 200 and 400 nm. Suitable filters serve both to

shield the PMT from scattered stimulation light and to define the spectral detection window. Three filters are available for this system: a Hoya U-340 filter (7.5mm thick, Φ = 45 mm) for quartz OSL, and the combination use of a Schott BG 39 (2 mm thick, Φ = 45 mm) and Corning 7.59 (4 mm thick, Φ = 45 mm) filters for feldspar OSL.

The luminescence stimulation system (Figure 4.2) is composed of a heating element (for TL measurement) and an optical stimulation unit (for OSL measurement). The two stimulation mechanisms can be used separately or in combination which provides the added flexibility that OSLD readings can also be made by heating them to a suitable temperature, rather than only by using light. The heating element is used to heat the sample and to lift the sample into the measurement position. The sample can be heated up to 700 ˚C. A Nitrogen flow is required to cool the sample. The optical stimulation unit is located in a ring between the sample heater and the PM tube. The optical stimulation unit has two stimulation sources: infrared (IR) light emitting diodes (L.E.D's) and blue light emitting diodes (L.E.D's). Forty nine (49) L.E.D's mounted in seven clusters are used. The IR stimulation region is 800 – 900 nm. The total power of the 21 IR L.E.D's is 145 nW/cm^2 at the sample position (Bøtter-Jensen *et al*., 2003). The blue L.E.D's have a peak emission at 470 nm. Total power from the 28 blue L.E.D's is 50 nW/cm^2 at the sample position (Bøtter-Jensen *et al*., 2003). A green long pass filter is incorporated in front of each blue LED cluster to reduce the intensity of the tail of the spectrum where the detection system operates. Forty-eight (48) samples can be put into a sample carrousel simultaneously. The rotation of the carrousel is under computer control. The optical stimulation mode can be Continuous wave OSL(CW-OSL), Linear modulated OSL (LM-OSL) and Pulsed OSL (POSL).

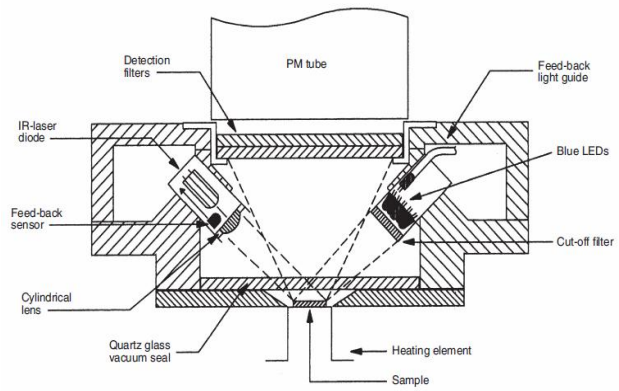

Figure 4.2 Schematic diagrams of the combined blue LED cluster and IR laser diode OSL unit. (From Bøtter-Jensen *et al.,* 2002)

4.3 OSL real-time optical fibre dosimetry technique (Standard RisøTL/OSL measurement system)

4.3.1 Introduction

The International Commission on Radiological Units and Measurement report (ICRU 24, 1976) stresses the importance of real time in-vivo dose monitoring for radiotherapy. An ideal in-vivo dosimeter system is able to measure the absorbed doses in-vivo in real-time to provide a feedback of irradiated dose.

Various studies have been done using different measuring tools such as coin-shaped ionization chambers, diamond dosimeters (Laub *et al.,* 1999), scintillators(Beddar *et al.* 1992a,1992b), thermoluminescence dosimeters (TLDs) (Loncol *et al.,* 1996; Essers and Mijnheer, 1999; Van Dan and Marinello, 2006) , P-N junction diodes (Edward, 1988; Yoker *et al.,* 2005; Van Dan and Marinello, 2006), metal oxide semiconductor field-effect transistors (MOSFETs)(Soubra *et al* 1994; , Peet and Pryor 1999), electronic portal imaging devices (EPIDs) (Essers *et al*., 1995; 1996; 1999; Hansen *et al.,* 1996; Heijmen *et al,*, 1995; Kriby *et al.,* 1995; Yin *et al.,* 1994; Zhu *et a*l., 1995; McDermott et al., 2006; 2008; Miften *et al.*, 2007; van Elmpt *et al.*, 2008; 2009) or conventional port films (Huyskens *et al.,* 1994; Fiorino et al., 1993; Van Dam *et al., 1*992; Weltens *et al.*, 1994), and optically stimulated luminescence (OSL) dosimeters (Huston *et al,* 2002; Anzar *et al.,* 2004; Andersen *et al.*, 2006). Currently, TLDs and P-N junction diodes are the most common tools for clinical trails.

Huston *et al* (2001) suggested that a remote optical fibre system may be used in in-vivo dosimeters for radiation therapy. Anzar *et al.* (2004) verified a head and neck IMRT plan by using a radioluminescence/optically stimulated luminescence (RL/OSL) optical-fibre dosimeter system with a single crystal Al_2O_3:C from Landauer (Landauer Inc., Chicago, USA). Andersen *et al*.(2006) demonstrated a 13 fields IMRT plan dose verification in a phantom by using OSL probes.

At present, Risø National Laboratory, Demark, and Oklahoma State University(OSU), USA and the other research groups are focusing on designing a real-time optical fibre in vivo dosimetry by using OSL material.

The technical development of a real-time optical fibre dosimetry system using Al_2O_3:C as an OSL dosimeter was initiated at OSU by Polf *et al.* (2002, 2004) in

USA and Ranchoux *et al* (2002) in France. Since then, the technology has continued to be further developed by Gaza *et al (2004)* and Marchmann *et a*l (2006).

4.3.2. Al_2O_3:C OSL fibres in in-vivo dosimetry

In in-vivo dosimetry it is essential that the dosimeters or probes should have the following key characteristics: 1) small size, 2) high spatial resolution for the dose measurement 3) and the ability to be read out multiple times both accurately and rapidly.

When a small crystal of aluminium oxide doped with carbon Al_2O_3:C is exposed to radiation, both RL and OSL signals can be obtained. RL is collected while the radiation beam is on, whereas OSL is measured with the laser beam switched on after the irradiation has been completed (Anzar *et al* 2004) .

Akselrod *et al* (2007) described in detail the development of Al_2O_3:C single crystal fibres using the Stepanov crystal growth process for remote OSL dosimetry. The resulting fibres can be obtained in diameters of 300, 500, 1000 and 200μm, and can be cut into pieces of different lengths, from 0.2 mm to 9mm.

Figure 4.3 shows the five stages for producing Al_2O_3:C fibre dosimeters:

(1) For pulling single crystal Al_2O_3:C fibre, designing a shaping/drawing unit which can control of the fibre diameter and the cross-sectional shape. Figure 4.9(1a) shows a smoother fibre surface for better diameter control, and Figure 4.9(1b) shows a thin-walled molybdenum tubing to control the fibre diameters less than 300μm.

(2) Cutting the Al_2O_3:C fibre to a required length .

(3) Splicing the Al_2O_3:C fibre with radiation hard optical epoxy to a silica fiberoptic guide.

(4) Attaching the fiberoptic guide to a standard FC connector.

(5) Coupling the optical fibre and Al_2O_3:C sensor to the computer controlled RL/OSL reader.

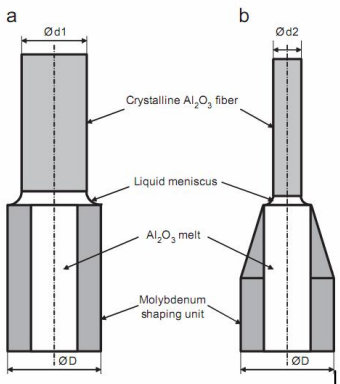

(1) Designed shaping unit to pull single crystal Al_2O_3:C fibers which determines the diameter and the cross-sectional shape.

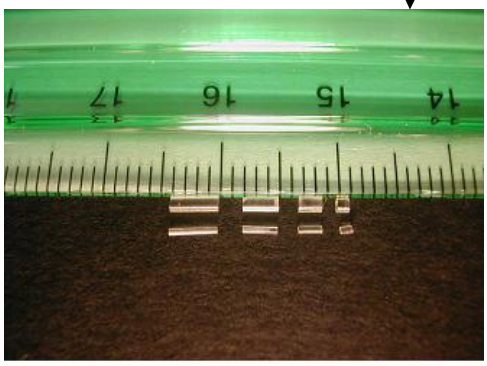

(2) Cut single crystal Al_2O_3:C fiber into different lengths

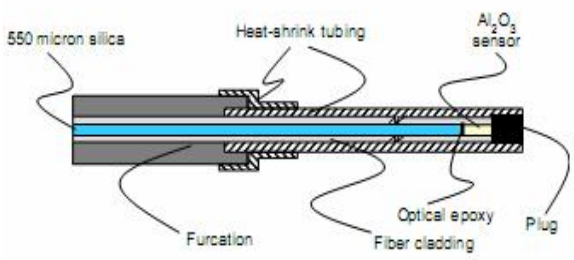

(3a) Diagram of the design of a fiberoptic probe with Al_2O_3:C sensor.

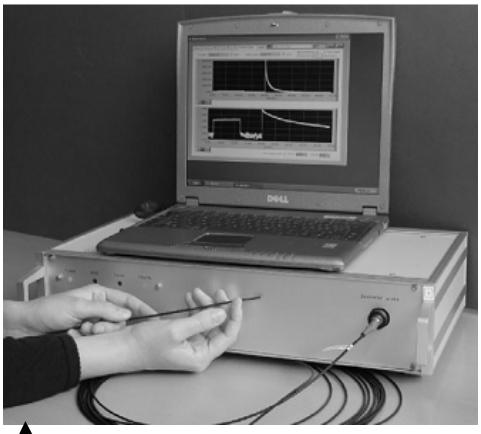

(5) A Riso RL/OSL system with optical fiber cable and Al_2O_3:C sensor (Marianne et al, 2004)

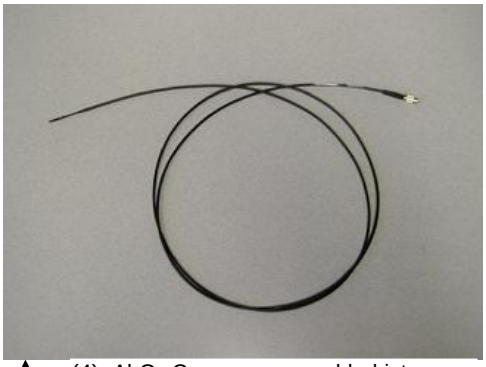

(4) Al_2O_3:C sensor assembled into a fiberoptic probe with a standard FC connector.

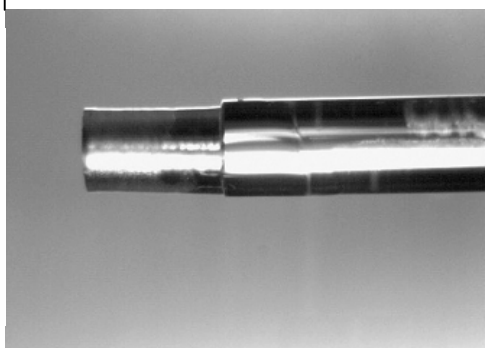

(3b) Al_2O_3:C fiber embedded in radiation hardened optical epoxy mounted to a silica fiberoptic guide

Figure 4.3 Al_2O_3:C fibers at different stages of production (Akselrod *et al,* 2007)

4.3.3 Main components of the OSL fibre reader

The typical schematic diagram of the single-fibre RL/ROSL reader is shown in Figure 4.4. It contains three parts: a sensor crystal, an optical detection system and signal-processing electronics (shown in Figure 4.3(5)).

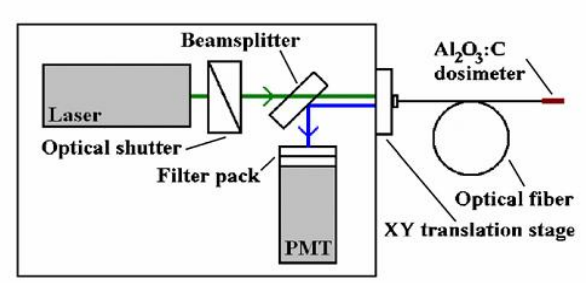

Figure 4.4 Diagram of RL/OSL reader (Gaza *et al*. 2004)

A green Nd:YAG laser light (λ = 532 nm) is connected to the optical fibre and stimulates OSL from the small size Al_2O_3:C single crystal connected at the distal end. The blue luminescence signal (~ 420 nm) is collected by the same optical fibre, reflected through 90˚ by a beam-splitter and fed to the light detector (PMT). A filter pack placed in front of the PMT separates the blue luminescence signal from the green background of scattered laser light. A TTL signal modulating the stimulation light output can be applied either directly to the laser (reader designed by Riso) or via an electro-mechanical shutter (readers designed by Oklahoma State University and Landauer). All components described above are packed into a light-tight box which is controlled by a PC computer equipped with a DAQ-card and running dedicated software. Continuous-wave (CW) lasers used have optical output powers ranging from 20 to 100mW by Oklahoma State University (OSU, USA), while 50mW power by Landauer (Landauer, Inc., Glenwood, IL). The width of the laser pulses was approximately 20 ns at an repetition frequency of 4 kHz (Gaza et *al*., 2004).

4.3.4 Measurement procedures and data processing algorithms

Gaza *et al* (2004) described two techniques for measuring the luminescence signals as well as algorithms for dose / dose-rate calculation from the raw data: (1) The radioluminescence (RL) and post-irradiation OSL associated with RL protocol algorithm from Riso (Figure 4.5a), and (2) Periodic OSL stimulation associate with dynamic depletion algorithm from Landauer and OSU (Figure 4.5b).

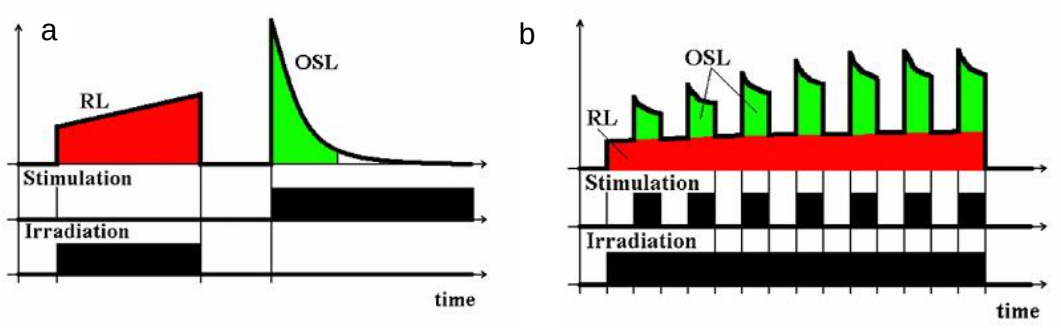

Figure 4.5 Two measurement techniques of OSL fibre readers. (a) RL and post-irradiation OSL stimulation procedure; (b)Periodic OSL stimulation procedure. (Gaza *et al.*, 2004)

4.3.4.1 RL and post-irradiation OSL measurement procedure

The radioluminescence (RL) and post-irradiation procedure require: 1) measuring the radio-luminescence signal emitted during irradiation by an initially blanched sample without laser light stimulation and 2) measuring the optically stimulated signal after the irradiation. The OSL for a given amount of stimulation is proportional to the dose absorbed in the dosimeter during irradiation.

The "RL protocol" algorithm (Akselrod *et al.,* 2007) used in this procedure is based on the assumption that the RL sensitivity (RL-signal per dose-rate unit) is only a function of the dose received by the probe since the initial RL signal (RL response at zero dose) is reproducible and is relatively independent of beam quality (Aznar *et al.*, 2004). It assumes that the sensitivity changes can be fully characterized in a single calibration experiment.

The advantage of the RL and post-irradiation measurement technique is that the post-irradiation measurement will not be affected by the 'stem effect' (the scintillation and Cerenkov signals from the light guide). So, any error induced by the Cerenkov effect during the real-time dose measurement of RL can be corrected in a subsequent treatment. The dose estimations from post-irradiation OSL followed "RL protocol" algorithm agreed with the dose readings by diodes measurement within 2% (Gaza *et al.,* 2004).

4.3.4.2 Periodic OSL stimulation

This measurement technique uses pulsed laser stimulation during irradiation. The luminescence signal is measured without laser stimulation measured and is

composed of scintillation and Cerenkov signals from the fibre optic and the RL from the Al_2O_3:C dosimeter. This luminescence signal can be defined as the background luminescence from the dosimeter. During the laser stimulation period, the OSL signal is superimposed on this background luminescence from the dosimeter. Under the laser stimulation, the OSL signal can be separated from background luminescence through the substraction of two consecutive signals with and without laser stimulation, and be integrated over an equal time intervals. Both the integrated background luminescence signal and the OSL signal are increased during irradiation; the OSL signal correction is based on estimated shape of OSL curve.

Gaza *et al*. (2004) gave the following formula to calculate the periodic OSL signal:

$$OSL'(n) = OSL(n) + \sum_{i=1}^{n-1} OSL(i) F_D(i)$$

Where $OSL'(n)$ is the nth corrected OSL signal. $OSL(n)$ is the intensity of the nth measured OSL. The F_D is the depletion factor which varies during the duration of an experiment and is estimated from the shape of the OSL curve. The OSL signal is produced as luminescence components from different traps with characteristic decay times. The F_D is dictated by the intensities of these components in the integrated OSL signal. Therefore, the two major components' intensities depend on the sample history and in particular the dose rate .

The advantage of the periodic stimulation procedure is that it limits the saturation effects in the detector. The periodic stimulation OSL correction accurately follows the abrupt changes in dose rate and keeps the system's dose response linear. (Gaza *et al.* 2004).

4.3.5 OSL fibre system dosimetry characteristics

4.3.5.1 Reproducibility

The reproducibility of OSL was found to be 0.2% when irradiated to 50kV x-rays (Anderson *et al* 2003). Anzar *et al.* (2004) reported the reproducibility of OSL measurements to be 0.1% (1standard deviation (SD)) when exposed to 18 MV photon beams and 0.5% (1SD) when exposed to 6MV phone beams.

4.3.5.2 Energy dependence

Aznar *et al*., (2004) delivered 2 Gy with 6 MV and 18MV photon beams and found the variation in output for these two energies to be 0.6% (1 SD) for OSL signals.

4.3.5.3 Dose-rate dependence

In theory, the absorbed dose estimated by OSL will be independent of dose rate. Aznar *et al* (2004) used a Varian Clinac 2300EX to generate 6 MV photon beam and dose rates from 100 to 600 MU min^{-1}. The OSL and RL signals were normalized to the average of all measurements. The OSL variation was 0.3% (1 SD). The relations of the amplitude of the RL signal vs. the dose rate showed good linearity.

4.3.5.4 Angular dependence

Anzar *et al.,* (2004) tested angular dependence with a RL/OSL optical-fibre dosimeter system. In order to minimize the effects of a potential setup error they collected the data from angles of 0^o to 179^o, and normalized to the value at 90^o. They also collected the data from 180^o to 360^o and normalized to the value at 270^o. They found that the OSL signals had a deviation of 1.3% for the 90^o normalization group and 1.7% for the 270^o normalization group.

4.3.6 OSL fibre system clinical applications and performance in radiotherapy

4.3.6.1 For measurements of depth dose and off-axis dose distributions

Aznar *et al.,(*2004) compared the central axis depth-dose distribution (PDD) and the off-axis dose profile (OAR) measured by an OSL fibre system using a p-doped Si-diode detector from Scanditronix / Wellhofer. The results showed that:

- The largest discrepancy between RL/OSL data and the diode data occurred at a shallow depth. This is due to the positioning uncertainty in the high-dose gradient region and the under-response of diodes at shallow depth (Heydarian *et al.* 1996).
- Beyond the build-up region the discrepancy between the RL/OSL data and the diode was 1% (1SD).

4.3.6.2 *In vivo* measurements for head and neck IMRT plan

Aznar *et al.(*2004) reported the use of a RL/OSL fibre dosimetry system for head and neck IMRT plan in-vivo checks.

Firstly, they calibrated the RL/OSL fibre dosimetry system in a phantom against standard treatment plans. They found that the discrepancy between the data measured by the calibrated RL/OSL fibre dosimeter and the data from the plans were within 1%. This included the uncertainty in the re-positioning of the detector in the field at the specified depth of measurement.

Secondly, they carried out the comparisons for in vivo dosimetry in virtual patients for a head and neck IMRT plan. This was simulated by using a phantom with tissue equivalent material inserts. The data measured by a calibrated RL/OSL fibre dosimeter and the data from TPS was compared. In this case, they found that the dose measured by a RL/OSL fibre dosimeter was 5% below the dose expected by the TPS.

4.4 Summary

The previous publications show that Al_2O_3:C based OSL dosimetry systems have the characteristics that make them suitable for both off-line and on-line clinical dosimetry in radiotherapy. These characteristics include: a wider dose response range, good dose linearity (Akselrod and McKeever, 1999; Yukihara *et al*., 2004) , high reproducibility (Anderson *et al.,* 2003; Aznar *et al*., 2004; Yukihara *et al*., 2005), less energy dependence (within 1% standard deviation for 6M and 18MV photon(Aznar *et al.,* 2004)), dose-rate independence (Aznar *et al.,* 2004), and angular dependence within 1.5% (Jursinic 2007, Aznar *et al.*, 2004). An on-line OSL fibre dosimetry system provides a relatively mature technique and has been used clinically for in-vivo dosimetry (Aznar *et al.,* 2004; Anderson *et al.,* 2006). However, it can only be used for point measurement. The use of two dimensional OSL film with a 2D scanner may provide a tool which can extend the OSL into an area dosimetry.

For many years in vivo dosimetry was traditionally commonly carried out using TLD and semiconductor dosimeters. If one compares OSL to TLD dosimetric characteristics and physical flexibility, the OSL dosimeter could potentially become either an alternative or replacement in-vivo dosimetry technique. OSL dosimeters can be made as thin as film and as they are more flexible can be mounted on the patient skin surface. They are less influenced by angular beam entry and offer significantly simpler handling compared to TLDs.

Chapter 5 Literature Review of the Tools and Techniques used in In-vivo Dosimetry in Radiation Therapy

5.1 Introduction

In-vivo dosimetry uses absorbed dose detection. Dosimeters are placed on the patient's skin or in natural cavities. In vivo dosimetry is the most direct method for monitoring the dose delivered to the patient receiving radiation therapy (van Dan and Marinello, 2006).

The purpose of the chapter is to review the historical development, typical characteristics of commonly used detectors, and their applications for in-vivo dosimetry. This will provide some background information and act as a reference for the use of OSL detectors for in-vivo dosimetry.

As briefly described in Chapter 4.3, the measurements of in-vivo dose were recommended by several national and international organizations (ICRU report 24, 1976; Noel *et al*., 1995). The International Commission on Radiological Units and Measurement report (ICRU 24, 1976) states that in-vivo dosimetry plays an important role in monitoring radiation therapy. In-vivo measurements provide additional safeguards against both major systemic errors and random errors (such as setup error, calculation errors) that might be missed during a pre-treatment check (Leunens *et al.,* 1990; Leunens, 1992; Essers, 1996; Essers and Mijnheer, 1999). An ideal in in-vivo dosimeter system is real-time and provides feedback during irradiation.

The main clinical applications of in-vivo dosimetry include: 1) comparison of the dose received by detectors placed on the skin and the dose calculated by a TPS and 2) to check if the target dose is correctly delivered.

Various *in-vivo* studies have been done using different measuring tools such as coin-shaped ionization chambers, diamond dosimeters, scintillators, thermoluminescence dosimeters (TLDs), P-N junction diodes, metal oxide semiconductor field-effect transistors (MOSFETs), electronic portal imaging devices (EPIDs), conventional port films and optically stimulated luminescence (OSL) dosimeters. TLDs and diodes are the most common tools for clinical use.

Diodes have been widely employed for in-vivo dosimetry since the 1980's with the advantages of easy use and relatively inexpensive and real-time point-dose readout which allows the immediate investigation and correction of errors encountered during dose delivery. Diode in-vivo dosimetry has been well documented (Edward, 1988; Yoker *et al.,* 2005; van Dam and Marinello 2006).

TLDs offer many characteristics in the form of powders, or solid dosimeters in the form of rods, chips, or pellets which make them suitable for in-vivo dosimetry purposes. Suitable characteristics include small dose rate and energy dependence and a wide dose range linear response (Essers and Mijnheer, 1999). However TLDs have a limited reproducibility and cannot provide real-time information (Loncol *et al.,* 1996).

Using diode and TLDs, with careful calibration and with sensitivity factors taken into account, in-vivo patient dose verification accuracy of about 1 ~2% can be reached (1SD) (Essers and Mijnheer, 1999).

Electronic portal imaging devices (EPID) have been used to measure 2D patient transmission dose since the 1990's and have developed rapidly since that time. Combined with cone-beam CT (CBCT) technology, EPIDs are now used for 3D dose reconstruction and 3D in vivo dose verification (Lee *et al*., 2008; McDermott *et al*., 2008; van Elmpt *et al.,* 2008; 2009; van Zijtveld *et al*., 2007a,b). On average, they can achieve a verification measurement accuracy within 3%, or 3mm, for 3D conformal or IMRT treatments (van Elmpt *et al.,* 2009).

MOSFETs offer the advantages of immediate read-out, small size and permanent storage of the dose (Soubra *et al* 1994). They also have less favourable characteristics such as angular dependence, sensitivity changes with use and a relatively short life time which restricts their clinical use (Ramani *et al* 1997, Peet and Pryor 1999).

Diamond detectors with small size and good tissue equivalence have been considered to be suitable for clinical purposes but their dose-rate dependence and the need for pre-irradiation (Laub *et al* 1999) limit their use for in-vivo dosimetry.

Although the current designs of plastic scintillators offer good tissue equivalence, the systems make it difficult to subtract the Cerenkov radiation noise (Beddar *et a*l 1992a,1992b) without compromising the size of the optical fibre bundle. This can be critical if the fibre is to be inserted in the body.

More recently some publications reported the use of OSL for in-vivo dosimetry. Huston *et al* (2002) suggested that an optical stimulated luminescence (OSL) system may be used as an in-vivo dosimeter for radiation therapy. Anzar *et al.* (2004) verified a head and neck IMRT plans by using a radioluminescence / optically stimulated luminescence (RL/OSL) optical-fibre dosimeter system with single crystal Al_2O_3:C from Landauer (Landauer Inc., Chicago, USA). They found that there was a 0.09±0.05 Gy difference between the measured dose (1.76 ±0.05 Gy) by OSL and the planed dose calculated (1.85 Gy). Andersen *et al*.(2006) demonstrated a 13 field IMRT plan dose verification in a phantom using OSL probes. Their result showed a 0.9% difference between OSL and RL measured results and there was a good agreement (within 2%) between the planned and the delivered dose. On the other hand, Meeks *et al.* (2002) used an optically stimulated luminescence dosimeter (OSLD) (Luxel™, Landauer Inc., Glenwood, IL) to investigate the extra-target dose delivered to patients during intracranial and head and neck IMRT treatments delivered with a tomotherapy treatment unit. Their result shows that the correlation of the dose accuracy of OSLD to a known dose was within 5% and that patient dose varies inversely by the distance from the centre of the target.

5.2 Definition and concept of in-vivo dosimetry

In-vivo dosimetry is defined as “the ultimate check of the actual dose delivered to an individual patient and can only be performed at the patient level” (Essers and MiInheer,1999). It is usually performed to detect dose errors in individual patients, to detect errors in core procedures, to evaluate the quality of specific treatment techniques or to evaluate the dose in situations in which the dose calculation is inaccurate or not possible (van Dan and MiInheer, 2006).

An overall QA procedure is strongly recommended during the dose delivery by radiation (Kutcher *et al.,* 1994). In-vivo dosimetry assists in monitoring dose, adjusting treatment plans and reducing dose delivery uncertainties.

The major goals of in-vivo dosimetry include:

- Identifying the setup errors for individual patients (Mijnheer, 1994; Leunens *et al,* 1994; van Bree *et al,* 1994; Van Esch *et al,* 2002; Ciocca *et al.* 2003; Higgins *et al,* 2003);

- Accounting for the dose discrepancies in the actual treatment caused by contour inaccuracies, tissue inhomogeneities, dose calculation algorithms, and so on. (Leunens *et al,* 1990;1992)
- Evaluating the quality of the specific treatments (Marinello *et al,* 1992; Dyk *et al.,* 1986; Karzmark *et al.,*1987) ;
- Evaluating the dose in situations in which the dose calculation is known to be inaccurate or impossible (Butson *et al* 1998).

In-vivo dosimetry measurement can be divided into three categories: entrance dose measurement, exit dose measurement and intra-cavity dose measurement. Entrance dose measurements are mainly used to check the output and performance of the treatment unit (or apparatus) and the accuracy of the patient's setup. Exit dose measurements can be used for the same purpose, but can also give some extra information about patient's parameters (such as shape, size, and tissue heterogeneity) that may affect the dose calculation (Loncol *et al.*, 1996). Target dose measurements are used either to check if internal structures have received the planned dose or to determine the ways of modifying the treatment technique in order to obtain the required dose distribution. Intracavitary dose measurement is another form of measuring the target dose by putting detectors into body cavities to measure the organ dose, for example the oesophageal tube, rectum, vagina and bladder.

The detailed descriptions for each of these categories for in-vivo dosimetry are given by Van Dan and Marinello (2006) and ICRU report 24(1976). It should be noted that the definition of the exit dose in ICRU report 24 is different from that by Van Dan and Marinello. Van Dan and Marinello defined the exit dose "at a distance of d_{max} from the exit surface on the beam axis". This definition implies that condition of a complete electron backscatter (because d_{max} is larger than the electron backscatter range but smaller than the photon backscatter range) must be met. In contrast ICRU report 24 describes the exit dose as "the absorbed dose delivered by a single fixed beam of radiation to the surface of the patient through which the beam emerges." The ICRU concept of exit dose is adopted by the following experiments from Chapter 9.

5.3 The requirement for clinical accuracy and consistency

Many groups have formulated a 3~4% (1SD) accuracy requirement in absorbed dose delivered by radiation for daily clinical patient treatment (Brahme, 1984;

Brahme *et al*., 1988; ICRU Report 24, 1976; Mijnheer *et al.*,1987; Lanson *et al.,* 1995). The recommendation of ICRU report 24 are that the dose delivered to the patient should vary by less than ± 5% from the prescribed dose. This requires a comprehensive QA program executed throughout the whole radiation therapy process.

There are many factors that can affect the accuracy of dose delivery to a target volume in a patient, These include tumour localization (including patient contours, patient mobilization, tissue inhomogeneities, and internal organ motion (Essers *et al.,* 1993; Kroonwijk *et al.*, 1998; Lanson *et al.,* 1995), machine calibration (including treatment unit, imaging unit and radiation measuring devices) and dose calculation (treatment planning systems) (Leunens *et al*., 1992).

Some previous researchers reported that a high accuracy of approximately 1~2% (1SD) in in-vivo dosimetry can be achieved if detectors (diodes and TLDs) are carefully calibrated and the factors of sensitivity influence taken into account (Mijnheer 2008; Yorke et al., 2005; Essers and Mijnheer 1999). Tung et al.(2004) reported that diodes can reach a -1.0%±2.7%(SD) accuracy with a maximum absolute deviation of measured doses from planned without equivalent thickness correction and 0.7%±1.8%(SD) with maximum in 4% with equivalent thickness correction . Similar as diodes, when carefully calibrated the accuracy of TLDs can be 2% (1SD) (Mijnheer et al., 2008). Tung et al.(2004) reported that TLDs can reach an accuracy of -0.1%±5.4%(SD) with a maximum 11% deviation. The mean difference between the MOSFET and TLD was -3.0%±0.2% (SD) (Bloemen-van et al., 2007)

Previous studies have discussed the sources of various errors involved in patient treatment. The overall average accuracy permitted for patient treatment has been assessed to be 3.5 % (ISD) for the dose delivery (Hamers *et al.,* 1991; Mijnheer *et al,* 1987). This means that the uncertainty from random errors is 3.2% and the uncertainty from patient set-up and beam monitoring alone is 1.8% (Mijnheer *et al*, 1987).

5.4 Diode dosimeters in *in-vivo* dosimetry

5.4.1 History of diodes for *in-vivo* dosimetry

Diodes have been widely employed in in-vivo dosimetry since the 1980's as they are easy to use. They are relatively inexpensive and provide real-time point-dose

readings that allow the immediate investigation and correction of errors encountered during dose delivery.

5.4.2 Diode detectors and electrometers

P-N junction diodes are most commonly used for in-vivo dosimetry. N-type silicon is doped with impurities of a pentavalent element (donor). In N-type silicon, the electrons are the majority and holes are the minority carriers. P-type silicon is doped with impurities of a trivalent element (acceptor). In P-type silicon, the holes are the majority and electrons are the minority carriers.

The physics behind the silicon diode use for in-vivo dosimetry is well described. This includes general information about PN junction diodes (Yoker, 2005), indirect recombination (Robert, 2002) and the interplay between material properties and the sensitivity of clinical diodes (Shi *et al.,* 2003).

Most commercially available diode detectors are capped with build-up materials of various thicknesses. Silicon diodes are read using electrometers to determine the accumulated dose received from radiation. Charge-to-pulse converters (CPC) and analogue-to-digital converters (ADC) are two basic types of electrometers connected to diodes (Yoker *et al*., 2005).

5.4.3 Characteristic of diodes used in *in-vivo* dosimetry

The advantages of diodes for in-vivo dosimetry include: good linearity over the normal dose range encountered, real-time readout and ease to use. However, the characteristics of diodes depend on the following factors:

1. Instantaneous dose-rate dependence / dose per pulse dependence.
2. Accumulated dose influence: the sensitivity of A diode may decrease with the accumulated dose.
3. Temperature influence: the sensitivity of diode may either increase or decrease with temperature.
4. Detector design which may influence the directional dependence (especially for large angles), energy dependence, field size dependence, and dose perturbation.
    a. The directional dependence is caused partly by the detector construction (including transmission through varying thickness of the build-up or cable at large angles) and partly by the back scatter from

the patient or phantom. The directional dependence could be different for photon and electron beams, especially at large angles.

b. The energy dependence is associated with suitable build-up cap materials. The energy dependence arises from the electrode attachment, protective housing and build up material. High Z materials are preferred.
c. The diode reading per MU increases with increasing field size. For large (40x40 cm^2) fields, the diode field-size dependence can differ by up to 5% from ion-chamber measurements (Alecu *et al.,* 1998; Rikner *et al.,* 1987; Greig *et al.* 1996; Eveling *et al*., 1998; Wierzbicki and Waid, 1998).
d. Diodes may perturb the radiation field and cause a dose shadow (a decrease in dose) below the diode. Dose perturbation is caused by several factors such as the effective thickness of the diode, the beam modality and energy, the field size, and the depth of interest (Alecu *et al*., 1998).

5.4.4 QA of diodes for *in-vivo* dosimetry

The above mentioned uncertainties of diodes can be minimized by using the following procedures:

1. Dose-rate dependence should be included in calibration in the dose range for patient treatment.
2. Pre-irradiation at high dose (several kGy) can reduce this influence
3. Comparing the temperature at phantom calibration to that at patient treatment to decide if the temperature corrections for in-vivo dose measurement are a concern.
4. To minimize the influence from detector construction, users can choose the energy range appropriate to photons or electrons to be used.

The American Association of Physicists in Medicine (AAPM) report 87 (Yoker *et al.,* 2005) and the European Society for Therapeutic Radiology and Oncology (ESTRO) report (Van Dan and Marinello, 2006) provides a very detailed description diodes use for clinical in-vivo dosimetry including acceptance testing, calibration, correction factors, continuing QA , etc..

With careful calibration, and by using proper correction factors, a diode accuracy and reproducibility of 1.8% (1SD) can be reached (Tung *et al.,* 2004). The spread in

the ratio of measured and calculated dose was reported to be 2.8% and 4.9% (1SD) for entrance and exit dose measurements (Essers and Mijnheer, 1999).

A quality assurance program for diode use for in-vivo dosimetry must be established. The quality assurance should be scheduled daily, weekly, monthly and annually by the clinical physicist. The accuracy tolerance for diode in-vivo dosimetry is designed to be less than 2%.

5.4.5 Clinical application of diode for in-vivo dosimetry

Diode use in in-vivo dosimetry was firstly reported in the 1980's, and have been used for entrance and exit dose dosimetry as well as total body irradiation (TBI) (Briot *et al*., 1990; Bloemen-van *et al*., 2007) and Intensity-modulated radiation therapy (IMRT) (Higgines *et al*., 2003).

5.5 Thermoluminescence detectors (TLDs) in in-vivo dosimetry

5.5.1 History of TLDs for in-vivo dosimetry

Thermoluminescence (TL) detectors have been used as a dosimetry tool for in-vivo dosimetry for several decades and is well documented in the literature (Van Dan and Marinello, 2006).

5.5.2 TL dosimeters and readout systems of TLD

The TL phenomenon belongs to the same family as stimulated relaxation phenomena (SRP). The theories for Luminescence and SRP have been described in details in section 2.1, section 2.2 of Chapter 2. Thermoluminescence (TL) is the ability of some materials, especially of crystal materials, to release the energy received from radiation by light, normally in the visible light range when heated. TL is similar to OSL in that electrons trapped in defects can be stimulated to generate luminescence emission by thermal methods, but not by laser light.

An ESTRO report (Van Dan and Marinello, 2006) gave a very clear review of TL dosimeters and its readout systems. The followings are some summarized key points.

5.5.2.1 TL dosimeters

TL detectors are composed of phosphors and impurities. The commonly used phosphors for TL detectors are lithium fluoride (LiF), lithium borate ($Li_2B_4O_7$), calcium sulphide ($CaSO_4$) and calcium fluoride (CaF_2). The impurities are also called activators which are doped with phosphors such as LiF: Mg-Ti is magnesium and titanium doped with lithium fluoride.

Most TL materials are made to be equivalent to either soft tissues or to bones. Soft tissue or lung equivalent TL materials include: LiF (Mg, Ti), LiF (Mg, Ti, Na), $Li_2B_4O_7$:Mn, and $Li_2B_4O_7$:Cu. Bone equivalent TL materials include: $CaSO_4$:Mn, $CaSO_4$:Dy, CaF_2:Mn, and CaF_2:Dy.

TL materials can either be in the form of powders or solids. The solid dosimeters can be made of single crystals, polycrystalline extrusions (extruded rods, sintered pellets or chips) or homogeneous composites of the phosphor powder and some binding material.

5.5.2.2 TL readers

Thermoluminescence is a process where imperfect crystals absorb and store the energy from ionizing radiation which can then be re-emitted, by heating, in the form of visible light. The dose is then collected by a photomultiplier (PMT) system. The amount of light emitted is correlated to the absorbed dose received by the TL material (McKeever, 1985). Heating the TL material causes the trapped electrons to return to the valence band by emitting visible light. The light output is detected and measured by a photomultiplier tube and the equivalent dose is then calculated. A typical glow curve LiF:Mg,Ti(TLD-100) is shown in figure 5.1 which shows luminescent output against temperature (Horowitz, et al., 2008). The shape of the glow curve is complex and depends upon the: 1) energy level of the traps and TL centres within the crystal and the relative densities of each trap/TL centre, 2) lifetime of the electron populations within each type of trap and 3) prior preparation of the TL crystal before exposure. The light output from TL material is not easily interpreted. When the material is heated, the electrons trapped in "shallow" traps are released, and when heating continues, the electrons in deeper traps are released. This creates a glow curve with multi peaks. Ideally, the highest peak of the curve is used to calculate the dose equivalent. However it is often difficult for the user to obtain the highest temperature peaks which may lead the user to extend the heating cycle beyond the thermal range of the reader. As a result the peak value may appear to vary. The area under the curve represents the radiation energy deposited on the

TLD.

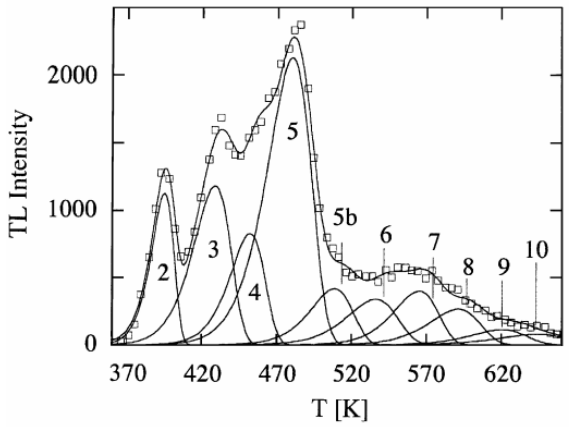

Figure 5.1 A typical glow curve of LiF:Mg,Ti(TLD-100) following 100 Gy ^{60}Co irradiation at a heating rate of 1K/s $^{-1}$. (From Horowitz et al., 2008)

After completing the readout procedure, the TL material is either entirely back to its original state with no trapped electrons remained, or it must have an annealing (special heating procedure) to restore it to its original state. After that the TLD is ready for reuse.

A typical TLD reader contains a tray or planchette, heater and a photomultiplier tube (PMT) with an electronic amplifier to record the emitted light. The tray or planchette holds the dosimeters in a readout chamber. The heater heats the TLD. Two different temperatures are used, a preheating temperature used to clear unstable peaks, and a readout temperature used to collect the information from the dosimetric peaks. The PMT measures the light output and the meter/recorder collects the data.

Detecting the TL light is variable from one reader to another because it depends on the composition of the PM photocathode and on the spectral transmission of the tube window. A good reader should have a PM with a large spectral transmission and should allow a quick interchange of the associated filter in order to be adaptable to different TL materials (Van Dan and Mearinello, 2006).The most commercially available TL readers are from Thermoelectron (USA) and FIMEL (France).

5.5.3 Characters of TLDs for *in-vivo* dosimetry

TLDs offer many advantages which make them suitable for in-vivo dosimetry: high sensitivity, a very small volume, good resolution, directional independence,

temperature and energy independence in the therapeutic dose range, very small dependence on dose rate, high dynamic dose range and the ability to store the dose received for a long period. In addition to that, there is no need for cabling and that makes TLDs much operationally convenient than diodes and MOSFETs, which require cabling and a different bias voltage setting.

However, in practice, some intrinsic characteristics of TLDs suggest that they require careful handling. Van Dan and Mearinello (2006) give very detailed instructions for using TLDs for in-vivo dosimetry, including thermal fading correction (signal stability after irradiation), individual sensitivity calibration and correction (variation in sensitivity for both solid or power TLD dosimeters), dose response range linearity (avoid using sublinear region) and energy correction factors:

- Variation in sensitivity within quoted specifications, TLDs can be matched within ±5%. But an approximately 40% variation in sensitivity among the TLD samples is exhibited by TLDs from different manufacturers (Fairbanks *et al.,* 1993).
- Very sensitive to the environmental temperature and the readout conditions and the handling procedures: a TLD may suffer a signal loss of up to 40% when using a contact planchet-type heating instrument (Kron *et al.,* 1993b). Wood et al. observed a 7% error when using different trays in an automatic TLD reader (Wood and Mayles, 1995).

5.5.4 QA of TLDs for clinical *in-vivo* dosimetry

Based on the characteristics of TL materials described above, the TL dosimeters should be calibrated before they are used clinically.

Theoretically individual TLDs should be calibrated. However, as the procedure requires extremely stable reading, annealing and manipulation conditions, that would be very hard to achieve. In practice when a large number of detectors or powders are used, they are commonly placed into two groups, one for calibration and the other for patient dose measurement. The readings from patient detectors are converted to dose by comparing their signal to that of the calibrated detectors (Van Dan and Mearinello, 2006).

The methods for TLD calibration are similar to those of diodes (section 5.4.4). The same ionization chamber can be used as a reference in the same phantom setup. The differences in distance of the ion-chamber and TLD to the source should be

considered. The time interval between the TLD calibration and use for patient dose measurement should be kept short enough to limit the fading phenomena effects down to less than 1% (Van Dan and Mearinello, 2006). In addition, clinical correction factors should be taken into account to ensure TLDs measurement accuracy.

With careful calibration an accuracy and reproducibility of 2% can be reached (1SD) (Kron 1995; Ostwald *et al.,* 1995; Van Dan and Marinello, 2006).The difference between measured and calculated doses was found to be 4.9% and 5.0% (1SD) for the entrance and exit dose measurement respectively (Essers and Mijnheer, 1999).

5.5.5 Clinical application of TLDs in *in-viv*o dosimetry

Their small size and no need external connections make TLDs suitable to measure skin dose (Kron, 1993; 1995; Noel, *et al*.,1995; Thomas and Palmer, 1989) for total skin electron irradiation (TSEI) (Ostwald *et al*., 1995, Mijnheer *et al,* 1987; Weaver *et al.,* 1995), total body irradiation (TBI) (Briot *et al*., 1990, Bloeman-van *et al*., 2007), and dose verification for conventional (Hamers *et al*., 1991; Kron *et al.,* 1993) and IMRT treatment (Ling *et al*, 1997; Van Esch , 2002; Engstrom *et al.* 2005). TLDs can also be used to measure the dose in organs at risk during the treatments allowing a prediction of the probability of radiation injury to the skin, eye, spinal cord or abdomen in the case of pregnant women.

5.6 Electronic portal imaging devices (EPIDs) for in-vivo dosimetry

EPIDs have become an essential component of a linear accelerator system. They permit the acquisition of treatment field images in a digital format for patient positioning. An EPID has a potential use for in-vivo measurements and 3D dose verification.

The first generation EPIDs were liquid-filled ionization chambers EPIDs (Li-Fi EPID) developed during the late 1980s and early 1990s at the Netherlands Cancer Institute, Amsterdam. Varian (Varian, Palo Alto, CA, USA) built the first commercially available product with the name “Portal Vision”.

A type of scintillation crystal-photodiode detector, named RT-IMAGE, was developed at the Royal Marsden Hospital in London (Morton *et al.,* 1991). It was a linear scanning array imager (Symonds-Tayler *et al*., 1997) which was used for

transit dosimetry (Hansen *et al.,* 1996) and for dose images (Mosleh-Shirazi *et al.,*1998).

Camera-based EPIDs were developed and became commercially available twenty years ago. Commercial EPID systems are available from Philips SRI-100 (Philips Medical Systems, Best, The Netherlands), Elekta iView (Elekta Oncology Systems, Crawley, UK), and TheraView NT (Cablon, Leusden, The Netherlands), Beamview (Siemens Medical Systems, Germany). A camera based EPID consists of a fluorescent phosphor-screen with a metal plate on top that converts high-energy photons into visible photons. These photons are imaged with a video camera (mostly CCD-based cameras) by means of mirrors and a lens, a large portion of the field can be imaged quickly due to the fast read-out of the camera. The camera also has a high spatial resolution.

The most common EPIDs today are based on amorphous-silicon arrays (a-Si EPID). The a-Si EPID, also called "flat panel imager" was firstly described by Antonuk *et a*l. at the University of Michigan Medical Centre, Ann Arbor, USA, commercially available since 2005, becoming popular as the major linear accelerator's makers equipped this type of EPID as a package with their accelerators such as Siemens OptiVue, Elekta iView GT and Varian a-Si Portal Vision.

Van Elmpt *et al.* (2008) gave a very detailed literature review of EPIDs for dosimetry purposes that described their physical characteristics, dosimetry properties, stability, and calibration methods. For the several reasons, such as the absence of commercially available software solutions, limited use of EPIDs for set-up verification and the lack especially for patient-specific dose verification, EPID as a routine clinical dose verification tool has not been widely used. However, several research groups reported their clinical experience of using EPID based for in-vivo IMRT plan dose verifications (Pasma *et al.,* 1999; Kroonwijk *et al.,* 1998) and a-Si based EPIDs (McDermott *et al.,* 2006; Nijsten *et al*., 2007; Piermattei *et al.,* 2006; Van Elmpt *et al*., 2009).

5.7 Metal oxide semiconductor field-effect transistors (MOSFETs) for in-vivo dosimetry

MOSFETs have been reported as an alternate dosimetry tool in in-vivo dosimetry for total body irradiation (TBI), high-dose irradiation (HDR), low-dose irradiation (LDR) (Cygler *et al*., 1995), skin dose (Ramani *et al* 1997, Scalchi *et al.,* 2005) and

entrance dose measurements (Peet and Pryor 1999).

The basic theory and techniques for using MOSFETs as radiation dosimeters is described by Gladstone and Chin (1991). MOSFETs offer the advantage of continuous monitoring during irradiation, instant read-out, small size and permanent storage of the total dose (Soubra *et al* 1994), but the other characteristics, such as angular dependence, sensitivity changes with use, and relatively short life time impair their clinical application (Ramani *et al* 1997, Peet and Pryor 1999).

Ramani *et al* (1997) reported dosimetry characteristics of MOSFETs that include: 1) an energy-dependent variation in response of up to 28%; 2) angular dependence observed between 140˚ and 220˚ gantry angles with an over-response of dose variations up to 15% for 6 MV. At gantry 180˚ dose over-response was also observed for ^{60}Co (28%), 6 MV (18%), 18 MV (13%), and 25 MV (13%) photon beams at d_{max}; 3) the variation in accumulated dose is 2% in the dose range from 0 to 180 Gy; 4) no significant temperature dependence was observed in clinical dosimetry; 5) there was no dependency on impurities or on environmental conditions.

5.8 Summary

This chapter discusses the definitions, concepts and accuracy requirements for performing in-vivo dosimetry, and summarized the existing in-vivo dosimetry techniques to provide some background information and as a reference for the use of OSL detectors for in-vivo dosimetry.

There are several alternative dose measurement tools for in-vivo dosimetry reported available today that include plastic scintillator dosimeters, diamond dosimeters, optical stimulation luminescence dosimeters and radiochromic film dosimeters. Van Dan and Mearinello (2006) provides brief summaries for each of them in terms of the theory involved as well as their characteristics, advantages and disadvantages and clinical applications. Currently the diode and TLD dosimeters are widely used for in-vivo dose measurements, but the protocols for using them correctly need to be well-established.

Chapter 6 Evaluation of Landauer's MicroStar Reader

6.1 Introduction

The OSL dosimeter or detector from Landauer has been chosen for radiation dosimetry in many areas including personnel radiation dose monitoring (Akselrod *et al.,* 2000) (Luxel+), medical environment dose measurement, radiotherapy treatment dose measurement (Meeks *et a*l., 2002; Perk *et al*., 2007; Viamonte *et al*., 2008) and in-vivo dosimetry (Anzar *et al*., 2004; Akselrod *et al*., 2007), etc.. Aznar *et al.*(2004) successfully used an Al_2O_3:C based dual-probe optical fibre dosimeter system in in-vivo dosimetry for checking head and neck IMRT treatments (Aznar *et al*. 2004). A solid phantom was also used for radiation field central axis depth-dose measurements.

The research in this paper was based on the Landauer InLight^{TM} dosimeter and MicroStar^{TM} reader. My experiments are intended to test the stability of the micrStar OSL reader and to estimate the reproducibility of this reader with OSLDs.

6.2 Instrumentation

6.2.1 InLight OSL Dosimeter (OSLD)

There are two kinds of OSL dosimeters from Landauer (landauer, Inc., Glenwood, IL), the InLight^{TM} dosimeter (quad detector,) and the InLight^{TM} Dot dosimeter (single detector).

The InLight^{TM} dosimeter contains four OSL dosimeter elements (labelled with E1, E2, E3, E4, respectively) mounted on a single slide. These dosimeters are based on a thin layer of carbon-doped aluminium oxide Al_2O_3:C powder deposited onto a clear polyester film. Each dosimeter element is a disc of 0.3 mm thick and 7 mm in diameter. Each slide is designed for storing the detector elements in a light-tight case containing metal and plastic filters to filter the detectors from radiation (Figure 6.1). The black light-tight case can protect the detector from visible light wavelengths (10^{-7}) but permits gamma or X-ray (wavelength 10^{-14}~$10^{-10)}$ transmission. The filter patterns, an open window, with aluminium, another with copper, and one with plastic, provide qualitative beam information.

As an alternative dosimeter, InLight^{TM} Dot dosimeters (Figure 4.2) have all the same

characteristics providing an alternative to the InLight™ dosimeters. For the dot dosimeter there is only one OSL dosimeter element mounted on a light-tight case without any filters, which is more suitable for point dose and patient dosimetry. To fit the MicroStar reader, the dot must be snapped into an adapter. Instead of using E1 to E4 position's readout, dots require only position E1.

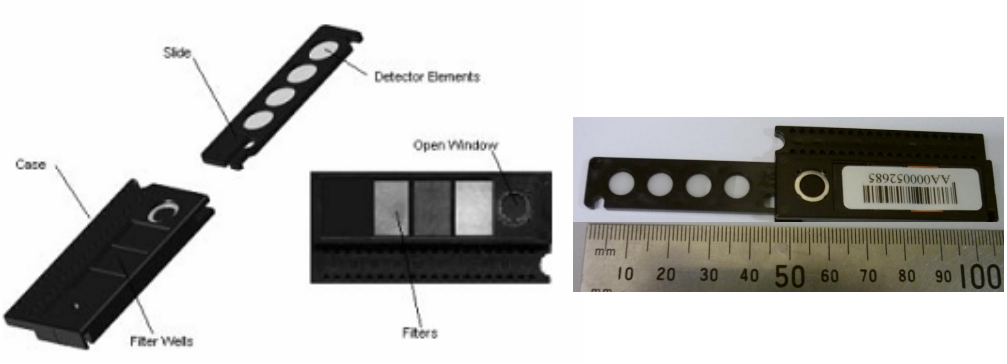

Figure 6.1 The InLight™ OSL dosimeter

Figure 6.2 The InLight™ dot dosimeter

Recommendations from the manufacturer state that for repeated readouts each reading from the dosimeter depletes the signal by less than about 0.2% per reading and that background radiation exposure will increase the dose when calibrating the dosimeters. For calibration purposes the reading can be repeated a maximum of 10 times.

In these experiments, the internal slides of InLight™ dosimeter (quad detectors,) were separated from the cases and had all their filters removed. Before and after irradiation, the slides were stored in light protected cases for re-analysis and re-use. As the InLight™ Dot dosimeter (single detector) was mounted without any filters, the whole case could be irradiated. When taking the reading, the dot dosimeter must be

snapped into an adapter. Similar to the InLight^{TM} dosimeter, the dot dosimeter was stored in a light protected case for its re-analysis and re-use.

6.2.2 InLight^{TM} manual MicroStar^{TM} reader system

The InLight MicroStar reader system (Figure 6.3) is an automated dosimetry system using optically stimulated luminescence (OSL) technology. A light emitting diode (LED) array is used in the read-out process to stimulate the dosimeters, and a photomultiplier tube (PMT) detects and measures the light emitted by the OSL material. The PMT uses a highly sensitive photon counting system. The amount of light released during optical stimulation is directly proportional to the radiation dose and the intensity of the stimulation light. The manufacturer estimates a precision of approximately 0.2% for each reading (Landauer MicroStar User manual, 2006).

The MicroStar reader system consists of a reader, an external control computer and dosimetry software. The reader contains a reader drawer, a Measuring Position Dial, and a USB port through which the reader is connected to the control software. Once the OSLD is paced inside the MicroStar reader, after rotating the knob, the case slides open and the read-out is initiated by switching on the light-emitting diode (LED). In standard operating mode the software outputs the raw photomultiplier counts. Due to its extensive use as a personal dosimetry system over many years,

Figure 6.3 Images of microStar^{TM} reader (from Landauer microStar User manual, 2006)

the sensitivity of the dosimeter and a calibration factor can be pre-loaded to convert the raw counts to mrem. In this study, one used only the raw photomultiplier counts and then convert these manually to the dose by using individually calibrated factors.

The Measuring Position Dial has three sections with eight positions: 1) Home

Position (H/P) is a blank; 2) specific reader part, with three positions (DRK, LED, CAL) allowing full calibration; and 3) a selector that allows the measurement of up to four dosimeters (E1 to E4). The process is as follows:

(a) DRK is to measure the dark count from the photomultiplier tube (PMT) with the shutter closed and the L.E.D.'s off. This allows measurement of the inherent electronic noise of the PMT.

(b) CAL is to measure the counts from the PMT exposing to a calibration source composed of a plastic scintillator in which a small amount of ^{14}C radioactive material is embedded. This provides a calibration of the sensitivity of the PMT.

(c) LED is to measure the luminescence from the dosimeters when stimulated by the L.E.D's.

6.3 Methodology

A significant advantage of OSLDs over TLDs is that an OSLD can be read multiple times. The Landauer OSLDs and MicroStar reader system is specially designed to read a single dosimeter several times during irradiation without signals loss.

The experiments in this study are intended to test the stability of the MicroStar reader; and to estimate the reproducibility of the MicroStar reader system with OSL dosimeters/dosimeters. The random fluctuations of repeated readings following an exposure/irradiation of a dosimeter are assessed. The random orientation error of a single dot dosimeter is also estimated. The sensitivity test of individual OSL dosimeters is described in Chapter 7.

6.3.1 Establishing a standard baseline for reader performance

Fluctuations in signals can arise within the reader from the following sources 1) LED brightness fluctuations 2) the photomultiplier tube (PMT) response 3) electronic noise 4) positioning of the OSL in the optical beam.

The output of the reader system at the three MicroStar dial positions was measured: DRK, CAL and LED. The DRK position is designed to measure the dark count of the photomultiplier tube (PMT) with the shutter closed and the L.E.D’s off to indicate the inherent electronic noise level of the PMT. The CAL measures the counts from the PMT with the shutter open to radiation from a small amount of ^{14}C radioactive

material embedded in a plastic scintillator. This provides a calibration of the reader response. The LED is used to measures the counts from the PMT when it is illuminated by the high intensity light source of the internal array of 36 L.E.D.'s.

With the loader of the reader emptied and closed, the Measuring Position Dial was turned counter clockwise from Home Position (H/P) to positions of DRK, CAL and LED step by step. The measured counts displayed in window were recorded manually. The procedure was repeated 100 times and all the readings taken were compared to the average value of the 100 times' readings' counts, which is the specified reader standard. The values suggested by the manufacturer are that DRK counts should be less then 30, for CAL and LED counts should be within ±10%(1σ) of the established average value for the specific reader.

6.3.2 Reader reproducibility / stability with OSL dosimeters

The initial test was performed to assess the repositioning accuracy of the holder. The reducibility/stability of the reader was evaluated by taking several readings of the dosimeters after a single exposure.

Both the InLight^{TM} Dot Dosimeter (single detector) and the InLight^{TM} Dosimeter (quad detector) used in this study were divided into two groups. The first group of dosimeters was provided by Landauer. These dosimeters were pre-irradiated by Landauer to known radiation dose levels (0, 50and 100 or 500 cGy) using 80kVp diagnostic x-rays. Another group were irradiated on site under known radiation dose levels (50, 100, 200, 300, 400, 500, 600, 700 and 800 cGy) using 6MV-X from Siemens Primus Linear Accelerator. The output in monitor units per cGy of the accelerator had been calibrated according to the absorbed dose calibration protocol of IAEA TRS-398 in water at the depth of dmax. The monitor units per cGy for a 10x10cm^2 beam size at the source-to-surface (SSD) of 100cm was 1cGy/1MU.

Each dosimeter was read 7 times, then averaged for the 1st 3 and 1st 5 and then all 7 readings, after single irradiation. For a relative readout comparison of the data, no pre-irradiation was given and no background was subtracted. The standard deviation to the mean was used for comparing all the results.

6.3.3 Random fluctuations of repeated readings

Due to the uncertainty of the readout, based on the data from section 6.3.2, the standard deviation of the mean PMT counts and the standard deviation of the mean

based on 3 raw readings, 5 readings and 7 readings were compared.

6.3.4 Random orientation error of dot dosimeter

The initial purpose of this test was to analyse the potential random errors caused by operator error during the readout procedure, for example, if the dot dosimeter was snapped into the adapter with the wrong side facing out.

Each dosimeter has a dosimeter number including sensitivity code and serial number. As mentioned in MicroStar reader's user manual, when the dot dosimeter is snapped into an adapter, the sensitivity code and serial number (SN) should face front. However, in practice, the dot dosimeter also can be put into an adapter in opposite direction with the sensitivity code and serial number facing back. There is no warning from the reader of this error.

One dot was irradiated with a known dose. A reading was repeated 10 times consecutively for both sides of the inserted disc. The different readings from both sides were compared.

6.4 Results and discussion

6.4.1 Reader performance test

The individual counts measured in each mode (mean counts and standard deviation (SD) of the 100 consecutively repeated readings) and the values suggested by the manufacturer were compared. The instrument specifications are

- DRK counts should be less then 30, the observed value was 6±2 (Mean±SD) counts, which reaches the criteria.
- CAL counts should also be within ±10% of the mean. Figure 6.1 shows the population histogram of the CAL signal. The experiment data is 1621±44 (Mean±SD). All the results of CAL lie within ±10% of the mean, which meets the criteria.
- LED counts should be within ±10% of the mean. The experiment data is 622±50(Mean±SD). However, in the LED data (Figure 6.4), 14% of LED counts are outside the suggested criteria. It is of interest that the LED data distribution shows a double peak histogram. This perhaps indicates an 8% change in intensity of the L.E.D's during exposure to the L.E.D's.

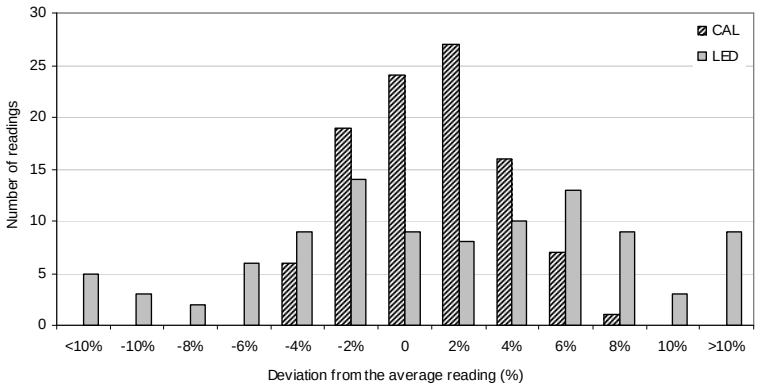

Figure 6.4 Stability of the MicroStar reader for multiple CAL and LED counts. The readings were compared with the average readings of all 100 readings using the MicroStar reader LED setting .

6.4.2 Reader reproducibility / stability with OSL dosimeters

The results of dosimeters by Landauer exposed to known doses are shown in Table 6.1 (single detector pellicles, Inlight^{TM} Dot) and Table 6.2 (Cartridges of 4 detector pellicles, Inlight^{TM}) and. The irradiation doses were 0 cGy, 50 cGy 100 cGy for the InLight^{TM} Dot Dosimeter and 0 cGy, 50 cGy, 500 cGy for the InLight^{TM} Dosimeter. The average standard deviation to the mean read dose of the InLight^{TM} Dot Dosimeter shows 1%, 1.2% and 1.8% in a maximum of 4 detector pellicles for repeated readouts 3, 5 and 7 times respectively. The average standard deviation to the mean of InLight^{TM} Dosimeters shows 1.3%, 1.6% and 2.2% in maximum for repeated readouts 3, 5 and 7 times respectively. One may notice that the lower readings (lower exposure such as background) have higher standard deviations because the PMT baseline's counts are different.

The results of the dosimeters exposed with doses of 50, 100, 200, 300, 400, 500, 600, 700 and 800 cGy using 6MV x-rays from a Siemens Primus Linear Accelerator are shown in Table 6.4 (single detector pellicles, Inlight^{TM} Dot) and Table 6.3 (Cartridges of 4 detector pellicles, Inlight^{TM}). These show the slightly higher deviations compared with the pre-irradiated dosimeters from Landauer. The averaged standard deviation to the mean dose is within 2.5% for both single and quad detectors.

The reports from Vlamonte *et al*. (2008) and Miller *et al.* (2006) showed much lower

random fluctuations compared to my results. Viamonte *et al* (2008) shows that the standard deviation in the reader's signal is about 1%(1SD) for a single exposure. The report from Miller and Murphy (2007) shows good re-read precision on five dosimeters exposed to 100 cGy. Their standard deviation of 0.5% (1SD) was based on an average of seven readings without re-exposure.

It should be noted that the uncertainty due to the reader (0.2%) is considered small compared to those of the statistical fluctuations in the signal.

Table 6.1 MicroStar Reader reproducibility test using a calibrated InLight™ Dot dosimeter from Landauer. The dosimeters were pre-irradiated 0 cGy, 50 cGy and 100 cGy respectively. The data is based on 3, 5and 7 repeated raw readings, respectively.

		Based on 7 raw readings			***Based on 5 raw readings***			***Based on 3 raw readings***		
ID #	***Dose (cGy)***	***Mean***	***SD***	***SD of Mean (%)***	***Mean***	***SD***	***SD of Mean (%)***	***Mean***	***SD***	***SD of Mean (%)***
DA09332097N	0	103.4	2.9	**1.05%**	102.8	1.64	**0.71%**	102.3	2.1	**1.17%**
DA09334296J		102.1	2.5	**0.94%**	101.8	2.17	**0.95%**	101.3	2.9	**1.64%**
DA09331309P	50	159481	7.27	**1.13%**	159372	5049	**1.42%**	157268	9.5	**2.08%**
DA09333619E		147344	4749	**1.94%**	148739	8224	**2.47%**	145635	5666	**3.95%**
DA093337788		159608	7563	**0.85%**	160965	2819	**0.78%**	160761	9955	**1.01%**
DA093312312	100	315441	3572	**1.05%**	313314	9480	**1.35%**	311327	2807	**2.31%**
DA09333708F		327606	8746	**0.22%**	326870	1808	**0.25%**	326746	12433	**0.45%**
DA09332029Q		328020	1944	**0.76%**	326697	7581	**1.04%**	324200	2535	**1.70%**
Average				**0.99%**			**1.12%**			**1.79%**

Table 6.2 MicroStar Reader reproducibility test with a calibrated InLight ™ dosimeter from Landauer. The dosimeters (four detectors labelled with E1 to E4 mounted in a single cartridge) were pre-irradiated 0 cGy, 50 cGy and 500 cGy, respectively. The data is based on 3, 5and 7 repeated raw readings, respectively.

			Based on 7 raw readings			***Based on 5 raw readings***			***Based on 3 raw readings***		
ID #	***Dose (cGy)***	***Posi.***	***Mean***	***SD***	***SD of Mean (%)***	***Mean***	***SD***	***SD of Mean (%)***	***Mean***	***SD***	***SD of Mean (%)***
CC000	0	E1	93	6	**2.32%**	93	7	**3.35%**	91	9	**5.56%**
37311E		E2	92	3	**1.22%**	92	3	**1.55%**	93	2	**1.30%**
		E3	94	4	**1.70%**	93	5	**2.38%**	92	7	**4.12%**
		E4	92	4	**1.60%**	91	4	**2.06%**	93	4	**2.58%**
CC000	0	E1	88	4	**1.74%**	89	3	**1.67%**	88	2	**1.36%**
372934		E2	90	5	**1.94%**	89	6	**2.80%**	91	3	**1.59%**
		E3	89	2	**0.85%**	89	2	**1.00%**	88	2	**1.31%**
		E4	87	5	**1.95%**	88	5	**2.79%**	89	7	**4.30%**
CC000	0	E1	86	5	**2.38%**	87	6	**3.11%**	88	5	**3.29%**
37310G		E2	89	4	**1.50%**	89	4	**2.05%**	91	4	**2.77%**
		E3	87	5	**2.22%**	86	6	**3.09%**	86	7	**4.97%**
		E4	87	1	**0.60%**	87	1	**0.43%**	87	1	**0.66%**
CC000	50	E1	48092	996	**0.78%**	47841	1069	**1.00%**	48179	604	**0.72%**
372356		E2	49647	1705	**1.30%**	49125	1774	**1.61%**	49703	2239	**2.60%**
		E3	50380	1332	**1.00%**	50083	1468	**1.31%**	49828	1933	**2.24%**
		E4	52414	607	**0.44%**	52405	606	**0.52%**	52342	847	**0.93%**
CC000	50	E1	43863	1816	**1.57%**	43498	2078	**2.14%**	44745	1331	**1.72%**
37230G		E2	44685	1846	**1.56%**	45117	996	**0.99%**	44905	578	**0.74%**
		E3	45263	2862	**2.39%**	45272	3502	**3.46%**	44524	4699	**6.09%**
		E4	46929	356	**0.29%**	47027	307	**0.29%**	46992	425	**0.52%**
CC000	50	E1	47467	1090	**0.87%**	47277	1274	**1.21%**	46479	889	**1.10%**
37233A		E2	50919	1197	**0.89%**	50874	1299	**1.14%**	50625	1711	**1.95%**
		E3	49898	1589	**1.20%**	49544	1738	**1.57%**	48759	1905	**2.26%**
		E4	51246	849	**0.63%**	51181	1020	**0.89%**	50646	977	**1.11%**
CC000	500	E1	462807	13182	**1.08%**	462503	15992	**1.55%**	459952	22038	**2.77%**
373429		E2	477491	10444	**0.83%**	473662	9923	**0.94%**	473275	6447	**0.79%**
		E3	481997	9127	**0.72%**	483201	5831	**0.54%**	482634	8080	**0.97%**
		E4	486840	2326	**0.18%**	486876	2381	**0.22%**	486078	2957	**0.35%**
CC000	500	E1	566160	15735	**1.05%**	572584	8200	**0.64%**	571298	9296	**0.94%**
373338		E2	599647	8203	**0.52%**	600998	7137	**0.53%**	601123	3995	**0.38%**
		E3	592019	17746	**1.13%**	593550	17502	**1.32%**	592669	18302	**1.78%**
		E4	603928	8675	**0.54%**	605330	9886	**0.73%**	607287	6686	**0.64%**
CC000	500	E1	495249	14859	**1.13%**	497010	17338	**1.56%**	493409	17650	**2.07%**
372281		E2	518309	10586	**0.77%**	517490	12836	**1.11%**	511925	14487	**1.63%**
		E3	505288	8107	**0.61%**	507104	6637	**0.59%**	509163	8180	**0.93%**
		E4	519482	18409	**1.34%**	517351	20804	**1.80%**	521774	21531	**2.38%**
Average		**E1**			**1.32%**			**1.61%**			**1.75%**
		E2			**1.17%**			**1.41%**			**1.53%**
		E3			**1.07%**			**1.35%**			**2.16%**
		E4			**0.84%**			**1.08%**			**1.50%**

Table 6.3 MicroStar Reader reproducibility test of a single exposure with a 6MV Linear Accelerator (Cartridges of 4 detector pellicles, Inlight™ dosimeter). The data is on the average of 5 consecutive detector raw readings.

Dose (cGy)	*Element*	*Mean PMT counts (Based on 5 raw readings)*	*Standard Deviation (SD)*	*SD of Mean (%)*
50	E1	48204	2061	**1.91%**
	E2	48030	3050	**2.84%**
	E3	49123	1890	**1.72%**
	E4	48522	3204	**2.95%**
100	E1	89546	4330	**2.16%**
	E2	94219	5596	**2.66%**
	E3	94848	2321	**1.09%**
	E4	94540	4818	**2.28%**
200	E1	160266	16380	**4.57%**
	E2	172276	5502	**1.43%**
	E3	167210	15584	**4.17%**
	E4	154142	9170	**2.66%**
300	E1	285020	17169	**2.69%**
	E2	303649	7186	**1.06%**
	E3	305918	3937	**0.58%**
	E4	307698	3101	**0.45%**
400	E1	361004	15351	**1.90%**
	E2	408552	20623	**2.26%**
	E3	397247	22907	**2.58%**
	E4	399134	22282	**2.50%**
500	E1	439920	7909	**0.80%**
	E2	469165	10447	**1.00%**
	E3	469729	24151	**2.30%**
	E4	456268	47658	**4.67%**
600	E1	512191	33159	**2.90%**
	E2	469165	25431	**2.42%**
	E3	622830	13977	**1.00%**
	E4	629895	5657	**0.40%**
700	E1	624120	28868	**2.07%**
	E2	704260	19804	**1.26%**
	E3	698703	23607	**1.51%**
	E4	687577	26346	**1.71%**
800	E1	680047	27129	**1.78%**
	E2	769386	10386	**0.60%**
	E3	723988	36128	**2.23%**
	E4	727205	31394	**1.93%**
Average				**2.31%**

Table 6.4 MicroStar Reader reproducibility test on a single exposure with a 6MV Linear Accelerator (single detector pellicles, Inlight™ Dot Dosimeter) using doses of 50, 100, 200, 300, 400, 500, 600, 700and 800 cGy, respectively. The data is on the average of 5 consecutive detector raw readings.

Dose (cGy)	*Mean PMT counts (Based on 5 raw readings)*	*Standard deviation (SD)*	*SD of Mean (%)*
50	48005	2093	**1.95%**
100	94029	2088	**1.05%**
200	190995	2381	**0.56%**
300	285240	12891	**2.02%**
400	372122	17671	**2.12%**
500	477658	23704	**2.22%**
600	592547	30241	**2.28%**
700	697947	25638	**1.64%**
800	855900	28250	**1.48%**
Average			**1.76%**

6.4.3 Random fluctuations of repeated readings

Due to the uncertainty of the readout, the Mean PMT counts based on 3 raw readings, 5 readings and 7 readings are compared. The results from section 6.4.1 show that the reading based on more sequential readouts of the detector show lower standard errors as expected; for example 7 raw readings were better than 5 raw readings.

6.4.4 Random dot dosimeter orientation evaluation

The correct orientation of the OSL dot is with the active powder layer facing the beam. Readouts were taken in the correct orientation, the adapter with sensitivity code and serial number facing out, and with the opposite orientation. The result shows in Table 6.5. The readout in the incorrect orientation is 11% lower than that in correct orientation.

Table 6.5 Error analysis due to incorrect orientation of a Dot dosimeter. The OSL dot was irradiated to a known dose.

Readout No.	SN Right origination	SD Wrong origination	Diff (%)
1	90674	84406	
2	93462	82325	
3	95393	82458	
4	93357	84625	
5	95067	85564	
6	94686	85147	
7	95643	82170	
8	94636	80819	
9	93284	86227	
10	95745	84092	
Mean ± SD	**94195±1549**	**83783±1747**	**-11.05%±2%**

6.5 Summary

In this study the performance of Landauer's MicroStar system was assessed as well as the reproducibility and stability of OSL dosimeters for radiation dose measurement in radiotherapy.

Background reader counts for DRK, CAL and LED were evaluated and showed that:

- The DRK counts are all inside the specification of less than 30 counts stated by the manufacturer.
- The CAL counts are all inside the specification of 10% over the mean recommended by manufacturer.
- The LED counts are 14 % outside the suggested criteria from the manufacturer and show a bimodal distribution.

The reader performance was accessed with two groups of OSL dosimeters:

- Group 1- dosimeters were exposed by the manufacturer to a known radiation dose levels with diagnostic x-rays.
- Group 2 –dosimeters were irradiated at known radiation dose levels with 6 MV linear accelerator x-rays.

The results are:

- Based on the average of 5 readings, Group 1 (radiation dose levels for diagnostic x-ray range) shows slightly lower standard deviations compared with that of Group 2 (radiation dose levels for radiation therapy x-ray range) for both two types of dosimeters.
- The two types of dosimeters, single detector and quad detector show only slight differences in performance. The single detector shows a slightly higher standard deviation to the quad detectors.
- The readings based on more readouts of the detector (e.g.7 raw readings rather than 5) shows lower standard deviations as expected.
- Detectors exposed to lower doses show higher standard deviations, also as expected statistically.
- Single dot dosimeter should be snapped into the adapter correctly as a wrong orientation can cause a 11% error.

6.6 Conclusion

The reproducibility testing is based on a Landauer OSL measurement technique using fixed OSL dosimeter dots in a cartridge. No normal reading distribution can be obtained from each measurement reading. In clinic practice the user would expect to repeat the readings several times and average the readings to improve the measurement result reliability. Reproducibility testing is important to evaluate the reliability of measurement results.

The experimental results show that the InLight^{TM} OSL system (reader and dot dosimeter) has dosimetric characteristics that are suitable as a clinical dosimetry tool for radiation therapy dosimetry. Careful calibration and good understanding of the performance of the reader can help to improve usage and measurement accuracy.

Chapter 7 Performance of Al_2O_3:C Optical Luminescence Dosimeters (and specifically, Landauer's InLight^{TM} Dosimeter) for Clinical Radiation Therapy Applications

The following dosimetry characteristics of OSLDs and associated readers should be optimal if OSLD is to be suitable for radiation dosimetry, including: sensitivity, reproducibility, dose response characteristic, dose response dependence on the signal, energy dependence, and angular dependence. In addition the readout technique, pre-irradiation history and accumulated dose affect accuracy.

7.1 Introduction

Millers and Murphy (2007) irradiated 5 unscreened Luxel dosimeters (Landauer, Inc., Glenwood, IL, USA) to 1 Gy and found a 7.0% sensitivity different between the 5 dosimeters.

Yukihara et al. (2005) reported the reproducibility of thin OSL dosimeters based on Al_2O_3:C powder. The dosimeters were pre-bleached before use and then were irradiated to a fixed dose. The Risø TL/OSL-DA-15 reader was used in CW-OSL mode. The reproducibility represented by the ratio of S/SR, where S is the total OSL emission from the first readout, and SR is the total OSL signal received radiation with a reference dose. They found that: 1)86% of points are within ±1% of the mean value; 2)the maximum difference (standard deviation obtained by the Gaussian fit) of the overall the mean S/SR value of the package was 0.7%.

Using OSL detectors from Landauer Inc. and a POSL dosimetry system, Akselrod and McKeever (1999) showed that the dose-response curve in the dose range of 4cGy to 10 Gy is a linear within 1.5% standard deviation.

Yukihara et al. (2004) demonstrated that, for doses up to 1000 Gy, the OSL dose-response curve showed a linear-supralinear-saturation behaviour, followed by a decrease in the response for doses higher than those required for saturation. The degree of supra-linearity and the saturation level varied from sample to sample. Depending on the variation in the samples, the saturation dose varied between 30 to 300 Gy. Above the saturation dose, the total OSL area showed a slight decrease in all samples. Landauer LuxelTM showed the same result. The qualitative behaviour

of the OSL dose response did not depend whether the sample was heated or bleached.

Yukihara et al. (2004) pointed out that the dose response varied with the choice of the signal and readout technique. To compare the dose response variation with the choice of the signal, they used the total area under the OSL decay curve (TOSL) and initial OSL intensity to demonstrate the shape of OSL decay curves. The TOSL represents the luminescence integrated over the time of a 300 seconds stimulation. The initial OSL intensity represents the luminescence averaged over the time of the first 3s of stimulation. OSL and TL readout techniques were compared for the shape of dose response. Their experimental data shows clearly that: 1) At low dose range the shape of the OSL decay curves remain constant and the TOSL and initial OSL intensity are equivalent; 2) At high dose range, the TOSL and initial OSL intensity are not equivalent; 3)On average, the TOSL and initial OSL intensity are equivalent only at a dose range of up to around 10 Gy. Beyond this the decay curves show differences. The separation point of curves varies with different samples. The Luxel^{TM} dosimeter curve shows moderate supra-linearity and a higher saturation dose compared to other samples; 4)The readout technique (TL or OSL) also changes the shape of the dose response curve; 5)The luminescence emition rate of the OSL decay curves increases with dose.

The pre-irradiation history of the OSL dosimeters will affect OSL sensitivity due to the deep dose filling during irradiation. Yukihara et al. (2004) demonstrated the sensitivity changes of OSL dosimeters by irradiating them with a pre-dose from 0.7 to 1000Gy followed by a test dose of 0.7Gy. They found that: 1)At lower dose ranges, as the pre-dose increased, the OSL sensitivity rises 1.3~1.8 times to the signal when no pre-radiation is applied; 2)After pre-irradiation doses up to 20–50 Gy, the OSL dosimeters are sensitized depending on the different samples; 3)At higher dose range, after reaching the peak values, the OSL sensitivity starts to drop; 4)The OSL sensitivity may drop below the initial sensitivity depending on different samples.

Yukihara et al. (2005) reported on using OSLD to measure percentage depth–dose (PDD) on the central axis of the radiation field in radiation therapy. The dosimeters were irradiated with 6MV photons at depths from 0.5cm~15cm with a 100cm source-to-surface-distance (SSD) setup and delivered 100 MU. The results were in good agreement with the doses expected from the standard PDD tables. The largest from their report was 1.1% at a depth of 15 cm. The overall relative standard deviation was smaller than 0.6%.

For OSL dosimeters the experiments from Anzar et al.(2004), Jursinic (2007), Viamonte et al. (2008) show that there is no noticeable energy dependence in photon dose-response curves for energies from 6MV to 18 MV. However Viamonte et al. (2008) demonstrated a 4% difference from Co60 to higher energies (6~18MV). They suggested that an energy correction factor should be applied to the OSL dosimeters if they were calibrated by using Co60 and intend to be used for higher energies.

Jursinic (2007) reported a 0.9% angular dependence for OSLD (InLight/OSL Dot dosimeters from Landauer, Inc., Glenwood, IL) by irradiating OSLDs 360 degrees to 50 cGy with of 6 MV x rays using a 10x10 cm2 field.

Jursinic (2010) reported the OSLD sensitivity decreases and the extent of supralinear increases with accumulated doses up to 60 Gy. Beyond 60 Gy of accumulated dose, the OSLD sensitivity increases and the extent of supralinearity decreases or reaches a plateau, depending on the optical annealing process.

This chapter focused on those characteristics of OSL material (AL_2O_3:C) that are particularly important for radiation dosimetry. These include high sensitivity to both electron and photon beams, a large dynamic range, good linearity and post-irradiation stability. OSL dosimeters should also be insensitive to temperature variations and capable of multiple uses after suitable optical annealing.

The dosimetric characteristics of a commercial OSL dosimetry system developed by Landauer was tested with the respect to:

- The sensitivity of individual OSL dosimeter(s)
- The linearity of the OSL readout-dose calibration curve
- The dose dynamic range of the OSL material
- Read out time dependence
- Directional / Angular dependence
- Reproducibility
- Incremental exposure dose characteristics
- The optimal annealing process with visible light
- Optical annealing
- Fading and reusability

7.2 Instrumentation

7.2.1 OSL dosimeters and reader system

The OSL dosimeters (OSLD) (Landauer, Inc., Glenwood, IL) used in this study are described in Chapter 6 and are based on a thin layer of carbon-doped aluminium oxide, Al_2O_3:C, powder deposited onto a clear polyester film. The OSLDs are either four elements mounted on a single slide, or a dot dosimeter. In these experiments, when using four OSLD elements mounted on a single slide, the internal slides were separated from their cases and removed all filtration.

The OSL reader is described in detail in chapter 6.

7.2.2 Irradiation equipment

7.2.2.1 Radiation source

In this study, the OSLDs were irradiated by 6 MV and 10 MV X-rays and 5, 7, 9, 10, 12, and14MeV electron beams from a Siemens Primus Linear Accelerator. The linear accelerator's output in monitor units per cGy had been calibrated according to the absorbed dose calibration protocol of the IAEA TRS-398 in water at the depth of d_{max}. Monitor units per cGy for a 10x10cm beam size at a source-to-surface distance (SSD) of 100cm was set to 1cGy for 1MU.

7.2.2.2 Solid slab square phantom

Standard commercial 30x30cm^2 solid water slab phantoms, with a depth that can vary based on requirements were used in most experiments as their average electron density is the same as that of water (Computerized Imaging Reference System, Norfolk, VA, USA). A special slab was made in-house to hold the OSL dosimeters, sandwiched between two solid water slabs, one of which provided an appropriate build-up thickness and another one which was 10cm thick to provide sufficient back scatter attenuation (Figure 7.1). The build-up thicknesses varied depending on the experiments performed. Wax was used to fill the cavity around the OSL dosimeters when the in-house manufactured OSL phantom was used.

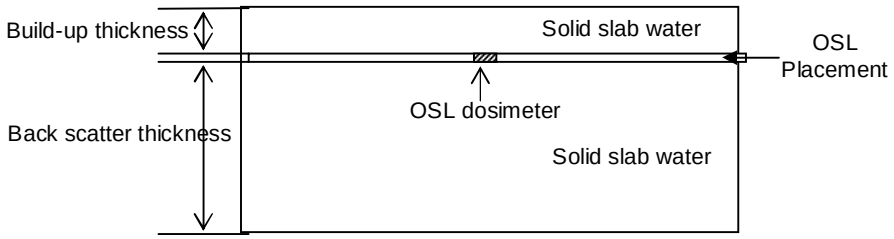

Figure 7.1 Schematic of standard 30x30 cm^2 solid water slabs (Computerized Imaging Reference System, Norfolk, VA, USA)

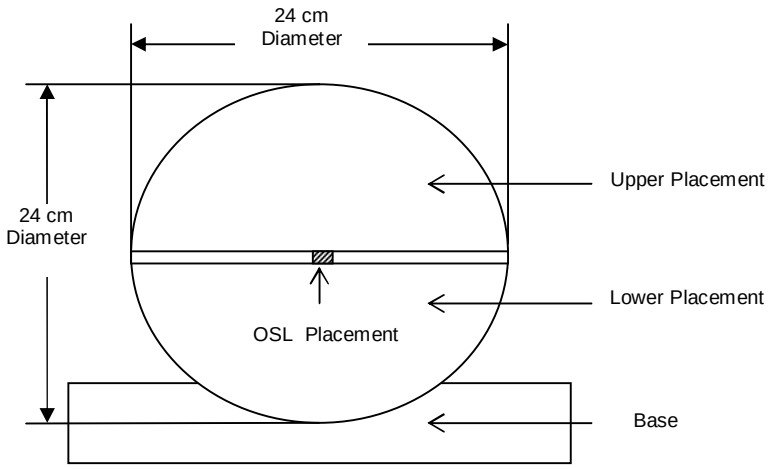

Figure 7.2 A diagram of the spherical phantom including a placement and other modifications for Dot OSL dosimeters.

.

7.2.2.3 Solid sphere phantom

The standard square slab phantom is good for routine dose calibrations but not suitable for performing the angled beam test. A solid sphere phantom (Yang 2005) constructed from perspex (Figure 7.2) was also used in my study for the directional dependence test.

The solid sphere phantom was original designed to perform measurements using film, TLD, and ion chambers (Yang, 2005). Most parts of this phantom were adopted and customized it with an in-house placement for holding OSL dosimeters. The phantom was 24 cm in diameter and consists of 4 pieces: the base, the lower and

upper half placements and an additional slab which includes two half perspex slabs and an in-house OSL placement allowing the dot OSL dosimeter to be inserted into and centred within the phantom. Wax was used to fill the cavity around the OSL dosimeters.

7.2.3 Annealing light source

In this study, two kinds of stimulating light sources, a fluorescent lamp and an incandescent (halogen) lamp were used.

The fluorescent lamp was a gas-discharge lamp using electricity to excite mercury vapour. The excited mercury atoms produce short-wave ultraviolet light, which causes a phosphor to fluoresce visible light. The Fluorescent lamps chosen were cool-white fluorescents with a correlated colour temperature (CCT) of approximately 4100 K (3827 ºC) and a colour rendering index (CRI) range from 82 to100.

The halogen lamp is a type of incandescent lamp. Inside a halogen lamp a tungsten filament is sealed into a compact transparent envelope filled with an inert gas and a small amount of halogen (such as iodine or bromine). A halogen lamp produces a continuous spectrum of light ranging from ultraviolet to infrared. The Halogen lamp one used was a cool beam source with a CCT of around 3000 K (2727 ºC) and a CRI around 100.

To avoid the temperature influence from the lamps, the fluorescent lamps were mounted on the ceiling and more than 2.5 meters away from the OSL. The halogen lamp was put on a table 1 meter away from the OSL.

7.3 Methodology

7.3.1 Irradiation setup

Figure 7.3 and Figure 7.4 show the arrangement of the phantom and irradiation beam in my experiments.

The arrangement in Figure 7.3a was used for the most measurements including OSL dosimetric calibrations and beam data collection. The setup was carried out by using a source-to-surface distance (SSD) of 100 cm. The build-up thicknesses are

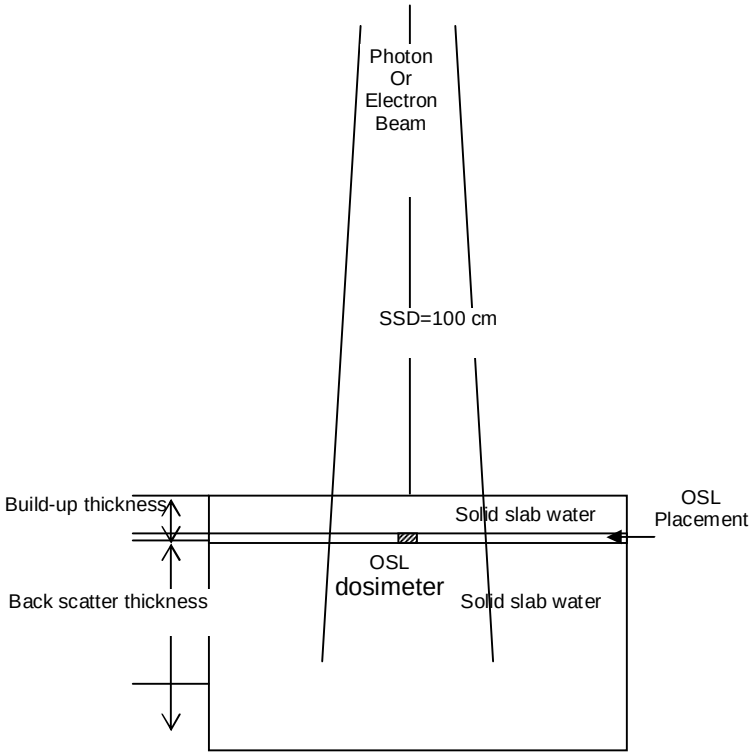

Figure 7.3a SSD irradiation setup for OSL detectors in a solid slab phantom to create two different equivalent depths: d_{max} of various beam qualities (were calculated to the depth of 2mm beyond the peak value of maximum PDDs) and 5 cm (for energy dependence experiments). The 10cm thickness below the OSL detector is for the back scatter.

the dmax depth equivalent of each energy or 5 cm for energy dependence experiments. The dmax of various beam qualities were calculated to the depth of 2mm beyond dmax of PDD in order to perform measurement in a more stable region. Figure 7.3b shows the setup arrangement with a source-to-axis distance (SAD) of 100 cm to the centre of OSLDs. The build-up and back scatter thicknesses vary depending on the requirements.

Figure 7.4 shows the arrangement used for the directional / angular dependence test. The setup for the spherical phantom was exactly the same as that used with the square one, but an SAD of 100 cm was set to the isocenter of the spherical phantom, which is also the centre of OSL dosimeter. The linear accelerator's gantry rotation radiation and mechanical isocenter was checked before the experiment. The radiation isocenter was obtained using film with the upper (Y) jaw set at 1 cm width, lower (X) jaw (MLC) at 40 cm width and collimator angle at 90 degrees. The radiation isocenter was a circle with a diameter of less than 2 mm for 6 MV X-rays. The mechanical isocenter was a circle with a diameter of less than 1.5 mm.

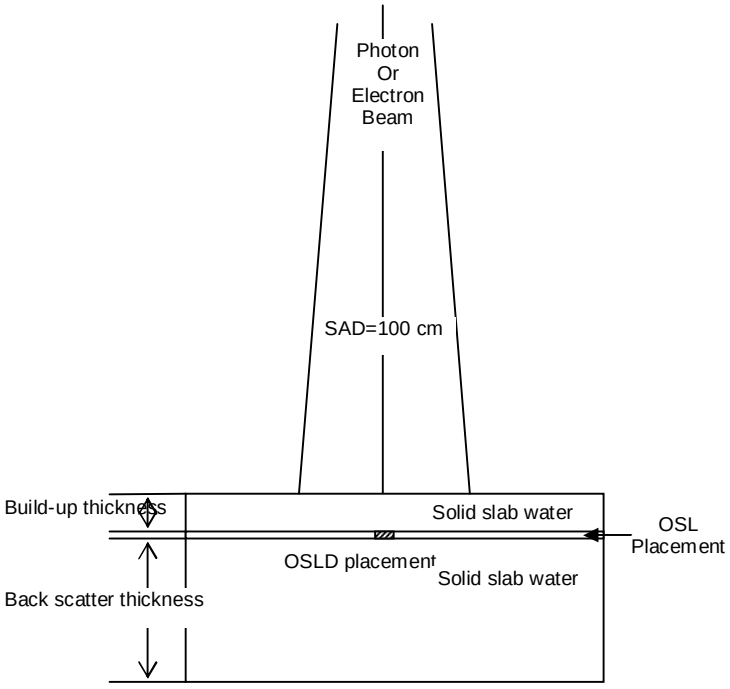

Figure 7.3b SAD irradiation setup used for the stability and reproducibility experiment in a solid slab phantom (Plastic Water®)

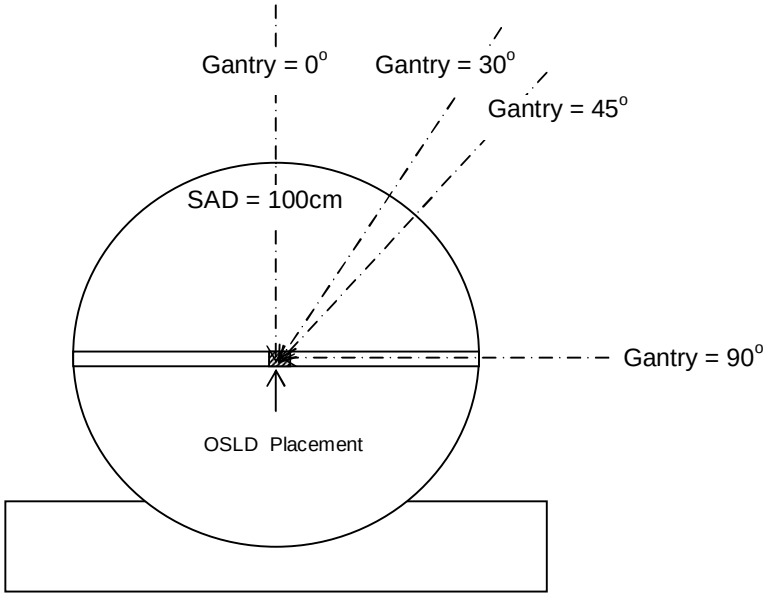

Figure 7.4a Irradiation setup for OSL dosimeters in the spherical phantom with an additional mount for OSL placement. The isocentre was set to the center of an OSLD, as well as the center of the phantom

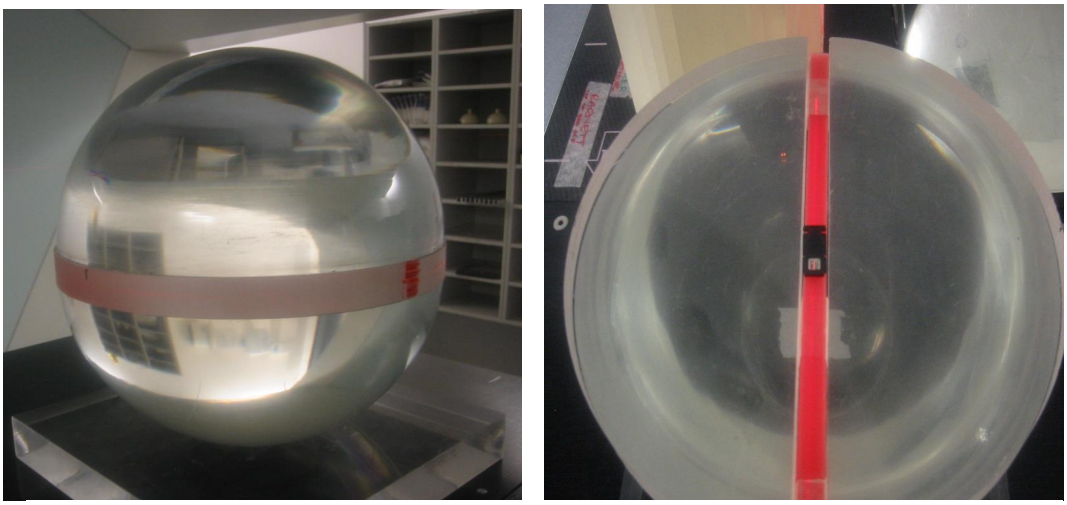

Figure 7.4b The spherical phantom with additional components and OSL dot placement.

7.3.2 Sensitivity

7.3.2.1 Variation of sensitivity

The sensitivity of OSL dosimeters depends on the radiation dose absorbed by the dosimeter and the amount of luminescence emitted by the dosimeter when it is optically stimulated. The sensitivity of each OSL may also vary due to variations in manufacturer packaging and shipping time. The sensitivity calibration of the InLight OSL Dosimeters supplied by the manufacturer is based on their originally intended use in radiation protection dosimetry where high accuracy is not required. For OSLD applications in radiotherapy more accuracy is required and a special calibration is needed.

During the read out process, the orientations of the cartridges of four detector pellicles (InLight^{TM} dosimeters) with their cases are always fixed. The single detector pellicles (InLight^{TM} Dot dosimeters) need to be mounted properly in an adapter with the marked sensitivity code and serial number facing front, as described in Chapter 6.

7.3.2.2 Sensitivity factor

The “sensitivity factor” is the ratio of an individual detector's sensitivity to the average sensitivity of all detectors used. Twenty (20) OSL dosimeters were irradiated to a dose of 100 Monitor Units (MUs) with SSD setup (Figure 7.3a) and

the build-up thickness was d_{max} (dmax was calculated from PDD) at the condition described in Figure 7.3a. The sensitivity of the dosimeter is defined here as the detector response normalized to a dose of 100cGy. These dosimeters were unscreened and were not pre-irradiated.

Another group with seven (7) screened OSL dot dosimeters (from the same delivery package) was tested as well. The OSLDs were irradiated to a dose of 100 Mus using a SAD setup (Figure 7.3b) and a 10cm build-up. The sensitivity of the dosimeter was defined here as the detector response normalized to a dose of 100 monitor units (MUs).

The sensitivity difference between the highest and lowest readings, the standard deviation from the mean were calculated.

7.3.2.3 Dose and beam energy dependence

For an ideal radiation dosimeter the sensitivity should be independent of dose (I.e. a linear response) and independent of type of radiation. Otherwise an energy correction factor would be required. Considering that the OSL coating material contains a high Z component, some types of energy dependences for high and low energies could exist. This issue could be clarified by further research.

Using the same setup as shown in Figure 7.3b, the OSL dosimeters were exposed to a series of radiation doses of 5, 10, 25, 50, 100, 200, 300, 400, 500 and 800 cGys for 6 MV and 10 MV photon beams. The sensitivity factors derived for each dose reading is the ratio of raw readings per dose compared to that of the mean.

7.3.3 Dose-response curve linearity, dynamic range and dependence on beam quality

The dose-response curve linearity and the dynamic range are dependent on the physical characteristics of the dosimeter. An ideal dosimeter or the dosimetry system for dosimetry in radiotherapy should have good dose-response linearity over a wide dose range. Otherwise non-linear correction factors or high order polynomial fits need to be applied.

The measurements of the linearity of the OSL dose response and dynamic range dependence on beam type and energy were carried out using 224 dosimeters. These were irradiated by one of the following combinations of beam type and

energy: 6MV and10MV photon beams as well as 5, 7, 9, 10, 12 and 14MeV electron beams. Each slide of 4 detectors was irradiated using 50, 100, 200, 300, 400, 500 and 800cGys. For each photon and electron beam energy, the average and standard deviation of OSL reading/cGy were calculated from four OSL dosimeters. The standard deviations derived were used in all subsequent uncertainty estimates and provided with 2SD error bars as shown in the figures.

7.3.4 Directional / angular dependence

Some detectors or dosimeters have a directional dependence. For example some diode readings are highly depend on their orientation to the incident beam direction (Alecu *et al*., 1998; Eveling *et al*., 1999; Shi *et al*., 2000). A directional response is caused by 1) the construction of the detector, such as transmission through various thicknesses of the build-up, the physical size of detector, and cabling; 2) the back scatter from the angle of incidence of secondary electrons and 3) the energy of the incident radiation. Directional dependence is important in in-vivo dosimetry. Compared to diodes, TLDs have minimal directional dependence which makes them suitable for in-vivo dosimetry in low dose and outside of the field dose measurements. As OSLDs are very similar to TLDs, they may be suitable for in-vivo dosimetry although the directional dependence of OSLs are also a parameter that must be considered.

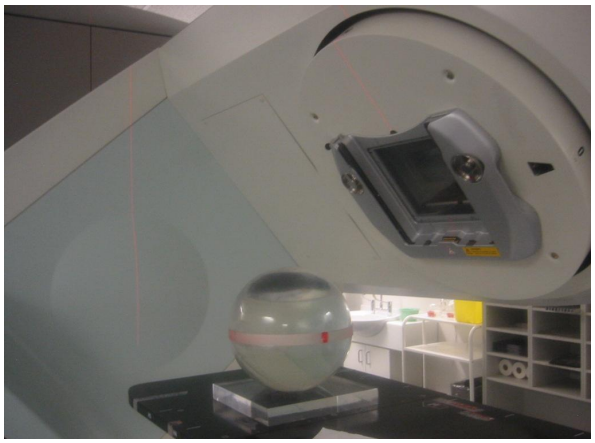

Figure 7.5 The directional depencence experiment image

The directional or angular dependence experiment (Figure 7.4a, 7.5) was carried out in a spherical phantom with single dot OSLD inserted (OSL placement) at the isocenter. The phantom with OSL placement was placed at a source-to-axis

distance (SAD) of 100 cm and field size of 10x10cm at the centre plane of the OSLD. A prescribed dose of 100 cGy by 6 MV X-rays was delivered. Four gantry angles of 0˚, 30˚, 45˚and 90˚ were used. Four (4) new Dot OSLDs were used in this study. Each dosimeter was irradiated at four different angles. The ten (10) consecutively acquired readings taken at each angle for each dosimeter were averaged. The average was then normalized to a gantry angle of 0˚.

7.3.5 Incremental exposure characteristic

For clinical planning purposes the accumulated or incremental dose response characteristics of OSL dosimeters should also be considered. The four OSL dosimeters involved in this experiment were irradiated using 6MV-Xrays and doses of 10, 25, 50, 100, 200, 300, 400, 500 and 800 cGys. After each of the 10 incremental exposures, the dosimeters were read 5 times. No annealing procedure was used between the exposures.

7.3.6 Post-irradiation readout time dependence

The dependence of OSL dosimetry on readout time was studied by consecutively and repeatedly reading out the OSL material after a single initial irradiation. Four (4) dosimeters were irradiated using a single dose of 500cGy 6MV X-rays. After irradiation the OSLDs were read after successive intervals of 30 minutes from 30 minutes after irradiation to 4.5 hours after. In consideration of potential fading, the OSLDs were only read once at each interval.

7.3.7 Reciprocity effects affecting OSL materials

As in photographic processes, reciprocity failure can occur where several short exposures to radiation may not produce the same readout as a single equivalent dose. The reciprocity of the OSL detectors was tested by giving nine stepped irradiations to the four (4) OSL dosimeters on a single slide. The OSL detectors were read 5 times consecutively after each irradiation step with no optical annealing between doses. A total of 9 exposures were given with incremental doses of 10, 20, 50, 100, 200, 300, 400, 500 and 800cGy. The difference between consecutive readouts were calculated and normalized to a 1cGy dose. The maximum, minimum and mean readings for a 1cGy reading were compared and the standard deviation from the mean was calculated.

7.3.8 Optical annealing

OSL dosimeters can be reused as their radiation memory will be wiped out by optical annealing with visible light. A simple optical annealing test was performed by continuously exposing OSL dosimeters, irradiated with 500cGy, to an optical annealing light source. The optical annealing light source was held at a fixed distance (1 meter) from the OSL dosimeter and there were no significant heating effects. The OSL signal was read every 30 minutes in the first 8 hours then every 3 hours until 28 hours after irradiation. The decay curve of the OSL readings was fitted to a trendline calculated by power law. The efficiency of the optical annealing process was compared by exposing one set of irradiated detectors for two hours to a fluorescent white light source and a second set to an incandescent halogen 20Watt source. The ratios of the readings before and after optical annealing were compared to provide a measure of the efficiency of each light source.

7.3.9 OSL signal fading and re-use potential

The test for the fading of an OSLD and the potential of multiple re-use was based on a readout cycle of irradiation: reading – annealing, that was repeated three times;. Each time the dosimeter was irradiated to 500cGy using the setup shown in Figure 7.1. The reading was taken two hours after irradiation. Annealing was able to bring OSLD dose readings very close to their initial background levels.

7.4 Results

7.4.1 Sensitivity

7.4.1.1 Sensitivity factor

Table 7.1 shows the raw measurement readings for the sensitivity test of 20 individual unscreened OSL dosimeters exposed to a dose of 100 cGy. The sensitivity of individual OSL dosimeters had a standard deviation of 7%.

These results were similar to that reported by Millers and Murphy (2007), who also found the standard deviation of 5 unscreened OSL detectors irradiated by 1Gy to be ±7.0%. It also shows a similar result when compared with the measurements of thermoluminescent dosimeters (TLDs) reported by Thomas and Palmer (1989).

Table 7.2 shows the raw measurement readings for the sensitivity test of 8 individual, screened dot OSLDs (from same delivery package of the manufacturer)

exposed to a dose of 100 cGy each with a setup SAD of 100 cm and a 10 cm build-up. The sensitivity of individual OSL dosimeters has a standard deviation within ±2%.

Table 7.1 Sensitivity of 20 unscreened OSL dosimeters. The OSLDs were irradiated with 100 MUs at a SSD of 100cm at dmax. The data is the average of 5 consecutive detector readings.

Dosimeter No. (*i*)	Raw OSL reading (R_i)	Normalized to Mean (Sensitivity Factor) (F_S)
1	88253	1.032
2	78000	0.912
3	86682	1.013
4	81840	0.957
5	88166	1.031
6	88424	1.034
7	86293	1.009
8	85095	0.995
9	76980	0.900
10	87101	1.018
11	81020	0.947
12	80778	0.944
13	76966	0.900
14	87116	1.019
15	81038	0.947
16	80772	0.944
17	89523	1.047
18	93037	1.088
19	96380	1.127
20	97107	1.135
Maximum	**97107**	**1.135**
Minimum	**76966**	**0.900**
Mean ± SD	**85529±6003**	**1.00 ± 0.07**

Table 7.2 Sensitivity of 7 screened dot OSLDs with an irradiation of 100 cGy. The OSLDs were put in a 30x30cm slab phantom at a SAD of 100cm with a 10 cm build-up. The data is the average of 5 consecutive detector readings

Dosimeter No. (*i*)	Raw OSL readings (R_i)	Normalized to Mean (Sensitivity Factor) (F_S)
1	30576	1.023
2	29965	1.002
3	30012	1.004
4	30243	1.012
5	29133	0.975
6	29004	0.970
7	30323	1.014
Maximum	**30576**	**1.023**
Minimum	**29004**	**0.970**
Mean ± STDEV	**29894±600**	**1.00 ± 0.020**

7.4.1.2 Sensitivity curve vs. dose and beam energy

The original data were derived from the measurement results from figure 7.7 and 7.8 in section 7.4.2

Figure 7.6 shows that sensitivity (signal/cGy) was not significantly different for the two photon beam energies used.

For this study:

- both sensitivity curves increase with increases in irradiated dose and exhibit a linear trend.
- uncertainties (1SD) for the two energies tested show a slight difference: 3% for 6MV and 5% for 10 MV.

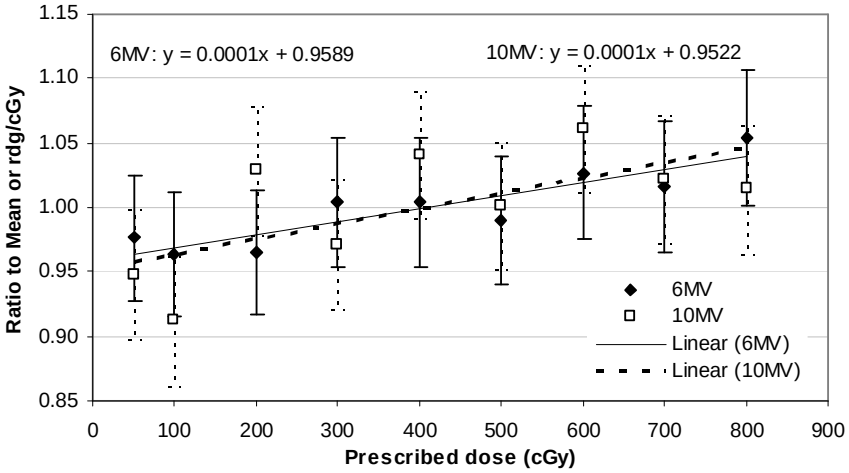

Figure 7.6 OSL response comparisons over different energies. OSL dosimeters were irradiated using doses ranging from 50cGy to 800cGy in solid water with a 5cm build-up and 10cm for back scatter. 5% error bars are shown.

7.4.2 Dose-response linearity and dynamic range

The results show that OSL dose-response curves are almost linear for both 6 MV and 10 MV photon beams (Figure 7.7 and 7.8) for dose ranging from 50cGy to 800cGy. Below 200cGy the relationship is linear; above 200cGy and below 600cGy the curve deviates from linear by at most 1.5%; for the dose range from 600cGy to 800cGy the curve deviations lie within 2.0% from the linear.

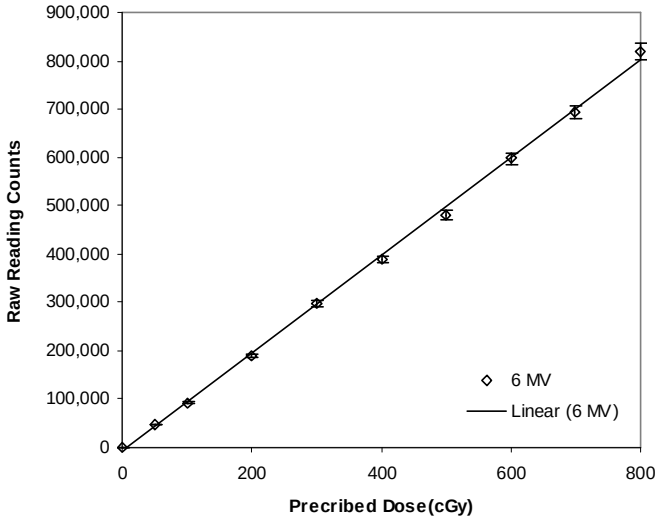

Figure 7.7a Dose-response curve for a 6MV photon beam with the dose range from 50cGy to 800cGy in solid slab phantom with a 5cm build-up and 10 cm thickness back scatter. The line is the least square fit to the data. The 2% error bars shown are separately derived for each dose from the readings of four OSL dosimeters

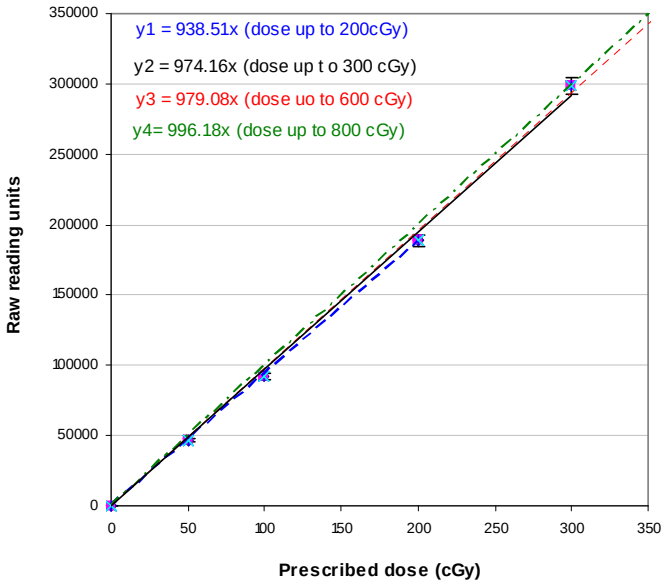

Figure 7.7b Partial dose-response curve for a 6MV photon beam with original data derived from Figure 7.7a. The 2% error bars shown are separately derived for each dose from the readings of four OSL dosimeters

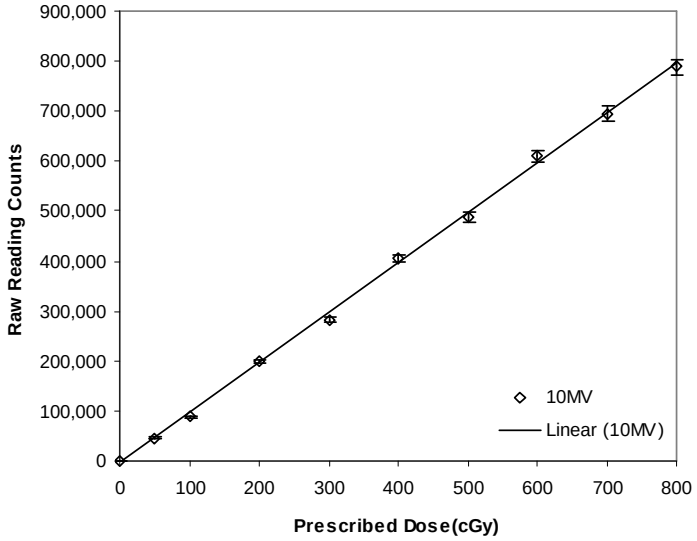

Figure 7.8 Dose-response curve for a 10MV photon beam with a dose range from 50cGy to 800cGy in solid slab phantom with a 5 cm build-up and a 10 cm thickness back scatter. The 2% error bars shown are separately derived for each dose from the readings of four OSL dosimeters .

Figure 7.7b derived original data from Figure 7.7a. It shows three linear trendlines derived from different dose ranges with intercept to 0 (x: prescribed dose(cGy))

- Line 1 (blue): linear trendline based on a dose range from 0~200 cGy, represented by: $y1 = 938.51x$
- Line 2 (black): linear trendline based on a dose range from 0~300 cGy, represented by: $y2 = 974.16x$
- Line 3 (red): trendline based on a dose range from 0~600 cGy, represented by: $y3 = 979.08x$
- Line 4 (green): trendline based on a dose range from 0~800 cGy, represented by: $y4 = 996.18x$

There is no significant difference in slope of the trendline based on dose range from 300 cGy to 600 cGy. The measured data at 200 cGy show a lower response than the overall data, which reduces the slope in line 1. This is believed to be due to errors in measurement. The slope of the trendline (line 4), which is based on a dose range from 0 to 800cGy is 2% higher than that of trendline 2 and 3.

As mentioned in section 7.4.1.1, the sensitivity of each OSL may be different if it comes from a different package from the manufacturer. This experiment was

repeated 10 times with 6MV using different packages of OSLDs. The data is shown in Table 7.3 The results are linear for all OSL dosimeters in the measured dose range. However the slopes of the trend-lines show some differences.

Table 7.3. The raw readings for beam quality dependence with different OSL dosimeter groups irradiated by 6 MV photons using doses ranging from 50cGy to 800cGy.

DOSE(cGy)	R1	R2	R3	R4	R5	R6	R7	R8	R9	R10
50	45120	47946	46376	45193	49875	42498	40571	48458	47984	46881
100	86218	93995	97454	85906	97321	84816	87097	93274	94009	92159
200	192304	186704	187714	179890	196287	163469	170862	183689	190976	188560
300	313237	300098	297678	287008	294505	264101	253388	300550	285221	298487
400	371054	387777	409825	400835	378026	368648	367305	391471	372102	389483
500	494060	471685	505653	473321	457520	435130	443905	458759	477637	480427
600	635994	599972	616802	566297	569244	543409		592499	592526	597640
700	701054	712582	697603	670285	688514	609641		678644	697926	693987
800	818018	830612	804218	812812	831347	698049		725142	855879	819381

The results of this study agrees with those reported by Viamonte *et al* (2007*),* who found a linear response for InLight OSL material up to 400 cGy, and by Miller and Murphy (2007) who investigated Luxel OSL dosimeters for the dose range from 0.1cGy to 100Gy and found the dose-response of a Luxel OSL with a supra-linear to a linear curve and then returning to a sub-linear curve over the remaining dynamic range.

7.4.3 Beam quality dependence

Dose response vs. radiation beam energy is very important as the energy spectrum is quite complex due to the fact that the backscattering photons contain a different more low energy spectrum than the original incoming photons and it is this change in energy spectrum that is likely to be responsible for dose response changes. Dose response at the low energies present in scattered radiation varies with the primary photon flux and shape of the exit side skin surface due to the variation in the thickness of the back scatter material.

The experiments measuring dependence on beam type and energy were carried out by using 224 dosimeters. The 224 dosimeters were used for 6MV, 10MV photon beams and 5, 7, 9, 10, 12 and 14 MeV electron beams. Each group was irradiated with a series of seven radiation doses of 50, 100, 200, 300, 400, 500 and 600 cGys

for each beam quality. The average and standard deviation of the OSL reading/cGy were calculated and all measured values were normalized to the mean value for the eight photon and electron beams displayed in Figure 7.9 and shown in Table 7.4 The sensitivity response to the different beam types and energies shows a possible trend with higher energy electron beams showing a 6% lower response than that of the lower energy electron and photon beams. Consequently, when OSLDs are used with varying beam qualities, separate calibrations are recommended.

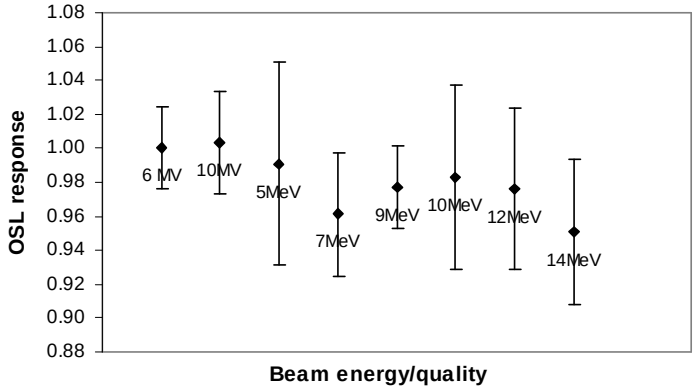

Figure 7.9 Energy dependence of OSL detectors for photon beams of 6 MV and 10 MV and electron beams with energies from 5MeV to 14 MeV. The OSL responses are normalized to 6 MV. Twenty-eight dosimeters were used for each energy. The error bars respect 2σ for the mean values of all the energies

Table 7.4 Beam quality dependence for 6MV and 10MV photon and 5,7,9,10,12 and 15 electron beams with irradiated dose range from 50cGy to 600cGy. The OSL response are normalized to the mean value of all the energies

Dose (cGy)	6 MV	10MV	5MeV	7MeV	9MeV	10MeV	12MeV	14MeV	SD (1σ)
50	1.03	1.02	0.97	1.03	1.02	0.98	1.01	0.94	±0.031
100	0.99	0.96	0.91	0.99	0.94	1.08	1.10	1.03	±0.062
200	1.00	1.06	1.14	1.00	0.98	0.89	0.98	0.95	±0.069
300	1.08	1.02	0.93	0.96	0.99	1.11	0.95	0.96	±0.060
400	1.04	1.08	1.02	0.90	1.02	1.00	1.03	0.90	±0.034
500	0.98	1.00	1.05	0.95	0.99	0.98	0.99	1.06	±0.034
600	1.01	1.03	1.05	1.03	1.03	0.98	0.90	0.95	±0.047

The dose response data shown in Table 7.5and 7.6 The dose-response for the 6 and 10 MV photon beams are similar to each other although there are some differences(Table 7.5. However the dose response relationships for the 6 electron beam's energies show a bigger deviation of up to 4.9% below the photon beam (Table 7.6. Any possible relationship between this deviation and the beam energy is masked by noise in the measurements.

Table 7.5 Beam quality dependence for 6MV and 10MV photon beams with an irradiated dose range from 50cGy to 800cGy. The OSL responses are normalized to the mean value of all the energies.

Dose (cGy)	6 MV	10MV	SD(1σ)
50	1.008	0.992	±0.008
100	1.019	0.981	±0.019
200	0.970	1.030	±0.030
300	1.026	0.974	±0.026
400	0.981	1.019	±0.019
500	0.993	1.007	±0.007
600	0.990	1.010	±0.010
700	0.999	1.001	±0.001
800	1.019	0.981	±0.019

Table 7.6 Beam quality dependence for 5,7,9,10,12 and 14 electron beams with an irradiated dose range from 50cGy to 600cGy. The OSL response is normalized to the mean value of all the energies.

Dose (cGy)	5MeV	7MeV	9MeV	10MeV	12MeV	14MeV	SD(1σ)
50	0.978	1.039	1.025	0.993	1.017	0.948	±0.030
100	0.905	0.979	0.929	1.068	1.093	1.025	±0.069
200	1.154	1.008	0.994	0.897	0.991	0.956	±0.078
300	0.946	0.978	1.007	1.126	0.970	0.973	±0.059
400	1.038	0.918	1.044	1.022	1.055	0.922	±0.057
500	1.047	0.949	0.989	0.978	0.983	1.053	±0.037
600	1.061	1.041	1.041	0.986	0.911	0.960	±0.053

The standard deviation of the normalized response for both photon and electron beams is on average ±0.052 (Table 7.4. The average difference between the normalized response difference of 6 and 10 MV photons is on average ±0.015 (Table 7.5. Among 6 electron beams the standard deviation in normalized response is on average ± 0.054 (Table 7.6).

The previous investigations from Aznar *et al.* (2004), Jursinic (2007) and Viamonte *et al.* (2008) show there is no noticeable energy dependence in the photon dose-response curves for the energy range from 6 to 18 MV, which is in good agreement with my results. Viamonte *et al* demonstrated a 4% difference from ^{60}Co to higher energies and they recommended that an energy correction factor should be applied to the dosimeters when they are calibrated for use with ^{60}Co and are when being used for dosimetry at higher energies (6-18 MV). My result is also in good agreement with Schembri and Hijmen (2007), who reported a difference between the photon and electron beam energies of 3.7%, and also with those reported by Jursinic (2007).

7.4.4 Directional /Angular dependence

Four OSLDs were irradiated with 6 MV photons using the same dose at different beam gantry angles: 0, 30, 45 and 90 degrees as shown in Figure 7.5. Table 7.6 shows the raw measurement readings and the dose response for four selected gantry angles normalized to the mean of the readings for those angles. The $Mean_1$ in table 7.6 shows the average of four gantry angles for the same OSLD, where the SD_1 shows their standard deviation. The $Mean_2$ in the table shows the average of four OSLDs irradiated at the same gantry angle, where SD2 shows their standard deviation.

Table 7.7 shows the dose response of four OSLDs using a gantry at 30, 45, and 90 degrees. After being normalized to a 0 degree gantry angle, the variations in normalized response are within ±0.7% at 30, 45 and 90 degrees. These results are close to those reported by Idri *et al.* (2004), which notes that a directional dependence is less than 0.8%.

Table 7.7 Raw measurement readings of the directional dependence of OSLD

OSLD #	Gantry angle				$Mean_1 \pm SD_1$
	0	30	45	90	
DA07807455N	18149±212	17944±304	18392±309	18504±311	18247±217
DA07807371V	17790±428	18636±198	18773±289	18352±211	18388±377
DA07807421Y	19427±113	19038±270	18805±301	18661±151	18982±289
DA0780738U	19246±302	19487±85	18976±302	18662±224	19083±322
Mean2±SD2	18653±806	18776±655	18736±158	18535±126	
Normalized to Gantry=0	0.0%±4.3%	+0.7%±3.5%	+0.5%±0.8%	-0.6%±0.7%	

7.4.5 Incremental exposures / Accumulated dose

Figure 7.10 shows the response for four (4) OSLDs irradiated by 6MV photons with dose increments ranging from 10cGy to 800cGy in the solid water slab phantom. The uncertainties are based on 5 consecutively repeated readings of each OSL dosimeter for each exposure. The data points represent the response (reading per cGy) associated with each dose increment.

The solid line in Figure 7.10 shows a good linear response to the dose for all of the measurement points with an intercept close to zero dose. The standard deviation for

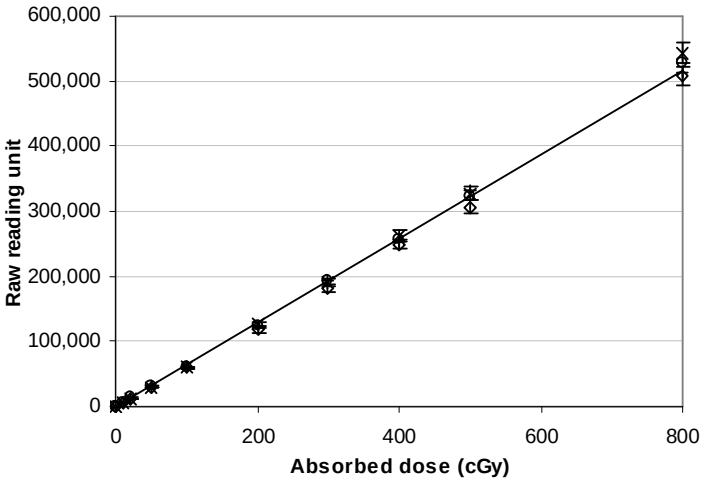

Figure 7.10 Response of OSL dosimeters under an incremental dose in cGy for 6MV Linear Accelerator irradiation. Four dosimeters were used through all dose values to 800 cGy. The solid line shows a good linear fit through all the measurement points, with an intercept close to zero). The error bars add to represect ±3% (2SD) uncertainty.

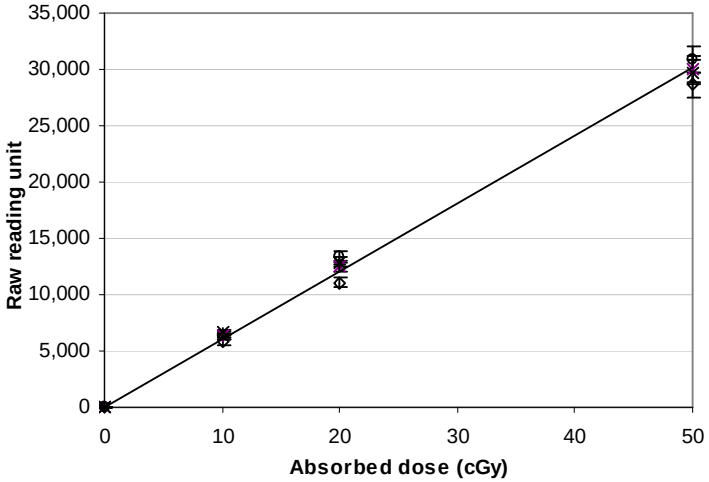

Figure 7.11 Response of OSL dosimeters under an incremental dose (in cGy) for 6MV Linear Accelerator irradiation. Four dosimeters were used for all dose values up to 400 cGy. The solid line shows a good linear fit through all measurement points, with an intercept close to zero. The error bars were added to represent ±3.7% (2SD) uncertainty.

the measured points is ±3% for the dose range of 50 cGy to 800 cGy. Based on the same data set, for comparison another two straight line fits are calculated for the dose range from 0 to 50cGy and 0cGy to 400cGy. For the dose range of 10cGy to 50cGy (Figure 7.11), the mean deviation from the line fit is ±3.7%. For the dose range of 50cGy to 400cGy (Figure 7.12) the mean deviation from the line is ±2.5%.

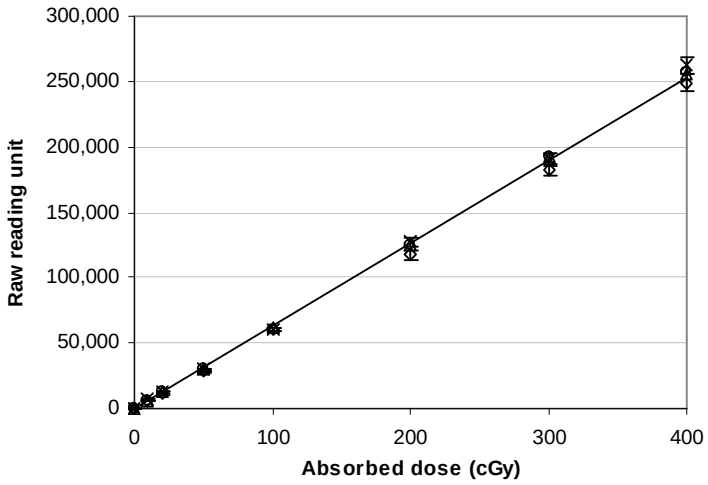

Figure 7.12 Response of OSL dosimeters under an incremental dose (in cGy) for 6MV Linear Accelerator irradiation. Four dosimeters were used through all dose values up to 400 cGy. The solid line shows a good linear fit through all the measurement points, with an intercept close to zero. The error bars were added to represent ±2.5% (2SD) uncertainty

The accumulated dose response of my results is in good agreement with that reported by Viamonte (2008), whose experiments were also performed using three Landauer dosimeters, who found dose to be linear at the dose range from 50cGy to 400cGy for ^{60}Co irradiation. Similar results were also demonstrated by Schembri and Heijmen (2007). The results demonstrate that a single calibration factor is applicable throughout this range for accumulated doses.

As OSL maintains a good linear trend under incremental exposure condition which makes it suitable for radiation dosimetry used to 3D conformal and IMRT treatment plan checks.

7.4.6 Post-irradiation readout time dependence

Table 7.8 shows the raw readings of post-irradiation readouts for 4 OSLDs irradiated with 6MV x-rays to 500cGy. The OSL dosimeters were read after an interval of between 30 minutes and 4.5 hours after irradiation. The plot in Figure 7.13 shows the results compared to the readout after 2 hours. The result shows that there is a significant decrease in signal over the first 4 measurements (0.5 hour to 1.5 hours). After the first two hours, the reading stabilizes within measurement uncertainties of within 0.5%. The stored signal therefore shows some decay within the first two hours but seems to stabilize thereafter.

The previous investigations from Viamonte *et al* (2008) and Schembri and Heijmen (2007) showed slight differences to my results. Viamonte *et al* performed measurements over a period of 1 hour to 21 days after irradiation. They found no noticeable change of OSL signal in the first 6 hours after irradiation followed by about 2% reduction to the signal in the first 5 days which then became stable till to 21 days. Schembri and Heijmen continued the measurements to 17 days following irradiation and found the reduction in OSL signal was less than 2% over 38 days.

In my study, one focused on the first few hours rather than days to evaluate readout time dependence. If OSL response signal reduction is based on irradiation or measurement times instead of the measurement period, my results are consistent with the findings of Viamonte *et al* (2008) and Schembri and Heijmen (2007) with the response signal of the OSLD slightly reduced for the first 5 or 6 readings and then becoming more stable thereafter.

Table 7.8 Post-Irradiation reading time dependence. OSLDs were irradiated 500cGy using a 6MV X-ray. Post-irradiation readings were taken an interval of 30minutes between 0.5 to 4.5 hours. $Mean_1 \pm SD_1$ represents the average and standard deviation from 4 OSLDs. $Mean_2 \pm SD_2$ represents the average and standard deviation from 9 interval readings from each OSLD.

No	Post-irradiation Reading time (hrs)	OSLD 1	OSLD 2	OSLD 3	OSLD 4	$Mean_1 \pm SD_1$
1	0.5	405008	448738	445463	441856	435266±17638
2	1.0	399659	436257	420277	429201	421349±13743
3	1.5	388070	416655	408047	427921	410173±14578
4	2.0	389430	419993	402284	430155	407965±12933
5	2.5	384341	411172	401152	417283	403487±12464
6	3.0	386588	408823	395319	422483	403303±13614
7	3.5	388463	420403	407077	428530	408618±14214
8	4.0	389164	406665	400190	429787	406452±14854
9	4.5	383939	416717	397464	431680	407450±18203
	$Mean_2 \pm SD_2$	**390518±6697**	**420603±13260**	**408586±14774**	**428766±6800**	**411563±9762**

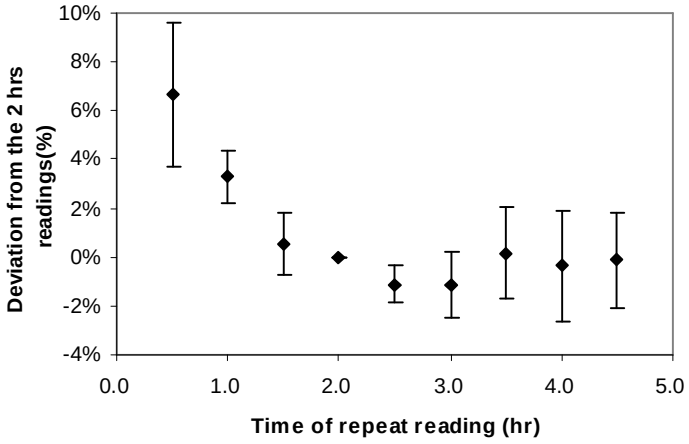

Figure 7.13 Readout time dependencies with measurement reading differences after this group of OSL dosimeters was irradiated with a 500cGy calibrated dose. The readings were acquired from 30 minutes to 4.5 hours increments of each 30 minutes after exposure. The figure shows the deviation from reading at 2 hours. The 1SD from 4 OSLDs was add as error bar on the average for each interval readout time(diamond marker).

7.4.7 Reciprocity

Table 7.9 and Figure 7.14 together shows the response for 4 OSL dosimeters irradiated incrementally from 10 cGy to 800 cGy in the solid water slab.

Table 7.9 Comparison of 4 OSLDs irradiated incrementally from 10cGy to 800cGy in slab water phantom with a 5 cm build-up and a 10cm back scatter. The readings were taken 5 times for each OSLs of each exposure. The difference between consecutive readouts were calculated and normalized to 1cGy dose.

Dose(cGy)	Step	OSLD1	OSLD2	OSLD3	OSLD4
10	1	589	654	642	639
20	2	579	645	633	654
50	3	592	631	616	640
100	4	599	627	620	623
200	5	595	636	623	639
300	6	608	635	642	643
400	7	622	656	638	641
500	8	615	653	646	644
800	9	620	654	640	652
	MAX	622	654	646	654
	MIN	579	627	616	623
	Mean±1σ	**602±4.72**	**642±3.31**	**633±3.48**	**642±2.75**

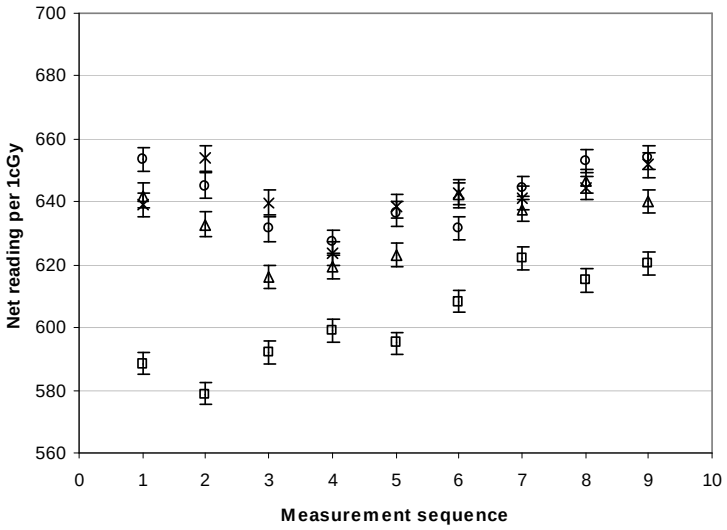

Figure 7.14 Reproducibility comparisons of 4 OSL dosimeters irradiated incrementally from 10cGy to 800cGy in a water with a 5cm build-up and 10cm back scatter. The readings were taken consecutively 5 times for each OSLD for every exposure. Each net reading deducts previous background radiation. The standard deviation to the mean value was added.

The uncertainties are based on 5 repeated readings for each OSL and exposure. The data points represent the response (reading per cGy) associated with each dose increment. If the OSL dosimeter follows the reproducibility rule, then these plots should be horizontal. It is noticeable that three OSL dosimeters show similar variations of sensitivity with each dose increment, while the fourth one varies dramatically from the other three. The standard deviation to the mean value is about 0.6%. These results are in very good agreement with the report from Yukihara *et al.* (2005) using Al_2O_3:C powder and a Risø TL/OSL-DA-15 reader. Their data showed standard deviation to the mean value is 0.7% and 86% of points are within ±1% of the mean value.

7.4.8 Optical Annealing

The rate of optical annealing is shown in Figure 7.15. In the first 30 minutes of optical annealing, the readout signal was reduced by approximately 98%. The reduction rate of the background signal follows a power law after 2 hours that is given by:

$$\text{Background signal} = 3632\ t^{-1.3}$$

In this study, the OSL dosimeters were read during optical annealing every 30

minutes up to 6 hours and then every 2.5 hours to 28 hours. The final readings, after 28 hours of the optical annealing process, showed a reduction to approximate 4.4% of the initial signal level. This reading level is close to the original background reading levels of unexposed OSLs. The result has good agreement with the results from Yukihara *et al.*(2004), Edmund *et al.(*2006) and Juristic(2007).

In order to determine if OSL dosimeters can be considered re-useable for clinical dosimetry, a new OSL cartridge with 4 dosimeters was cycled through successive

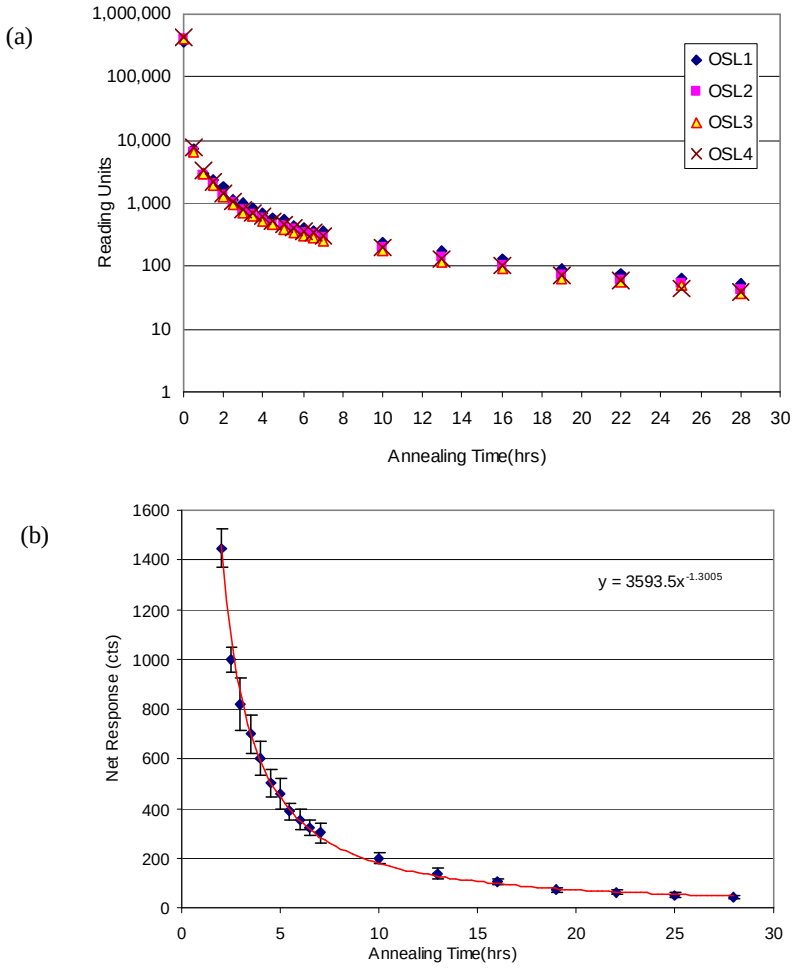

Figure 7.15 Annealing Efficiency analysis with six OSLs irradiated to 500cGy with the annealed measurement readings acquired after the annealing process.(a) The annealing process is set every 30 approximately 98.2% in the first 30 minutes. (b) The power equation line is added to evaluate the annealing minutes in the first 8 hours, then every 3 hours until to 28 hours. The readout signal was reduced by trend from 2 hours to 28hours based on the average of 4 OSLDs. The error bar is the standard deviation of OSLDs

irradiation – readout - optical annealing cycles. Figure 7.16 shows the results from this experiment. These suggest that after three cycles the readout increases for all 4 dosimeters by up to 10% of the signal. This is possibly due to incomplete optical annealing after each readout or to radiation damage to the OSL dosimeter with the result that it cannot be annealed. Charge could remain in the deep traps which may alter OSL dose sensitivity.

A simple comparison of annealing efficiency for two different light sources, fluorescent (white) and Incandescent (12Volt Halogen, 20Watt cool beam source, yellow), showed that the Incandescent light source was more effective for OSL annealing (Table 7.10). The ratio of OSL readout before and after the dosimeters were annealed show that the Incandescent light reduced the average readout signal to 9.5% of its original intensity, but the fluorescent light achieved a reduction to 53% of the original intensity.

Table 7.10 Annealing efficiency comparing the ratio of measurement reading changes between two different light sources, fluorescent (white) and Incandescent (yellow), after 2 hours annealing. The ratio indicated a significant difference. Average readings were based on 8 OSL dosimeters of each group.

	Fluorescent (White)	**Incandescent (Yellow)**
Average reading before annealing	107	105
Average reading after annealing	57	10
Percentage of original reading	**53%**	**9.5%**

7.4.9 Fading and reuse ability

Table 7.11 and Figure 7.16 together show the comparison of 3 cycles of: irradiation – reading – annealing. Each OSLD was irradiated by 500cGy of 6MV x-rays. The data indicates that OSL response increases through three readout cycles for all four dosimeters. The average increase in response over two cycles is about 6% and for three cycles is about 8% of the initial (first time) response after annealing.

Table 7.11 Fading and reusability

Original reading					
Used No.	**E1**	**E2**	**E3**	**E4**	
1st	405008	448738	437253	441856	
2nd	417284	472764	471073	474599	
3rd	442443	480982	473572	477744	
Percentage Difference (%)					
Used No.	**E1**	**E2**	**E3**	**E4**	**Average**
1st	0.0%	0.0%	0.0%	0.0%	0.0%
2nd	3.0%	5.3%	7.7%	7.4%	5.9%
3rd	9.2%	7.2%	8.3%	8.1%	8.2%

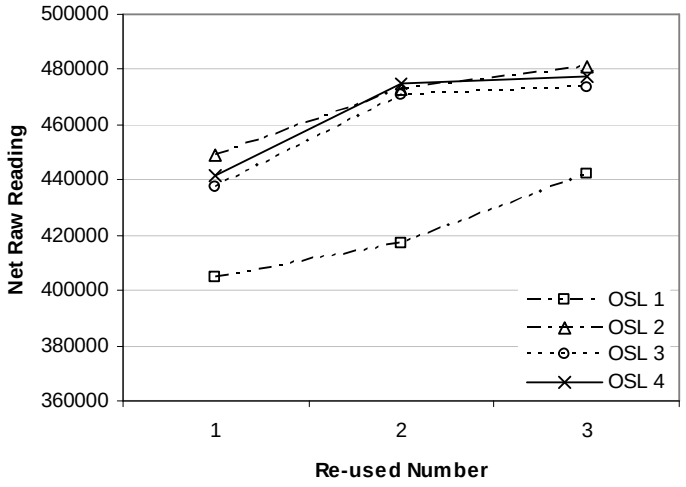

Figure 7.16 OSL re-use ability analysis. Three (3) repeated process circles: irradiation reading annealing in one new OSLD. 500cGy was delivered with 6MV x-rays. Readings were taken two hours after irradiation. Annealing brings the OSLD almost to the initial background level.

7.5 Summary

The purpose of this research focused on testing specifically the Al_2O_3:C based OSL system in terms of evaluating it's dosimetric characteristics and performance with megavoltage beams and to assess it's suitability for use in radiotherapy.

This evaluation included assessing the sensitivity of individual OSLDs at various

beam qualities, their dose-response curve linearity, dose dynamic range, beam quality dependence, directional/angular dependence, incremental exposure dose characteristics, reproducibility, as well as assessing the optimum annealing process, optimal optical source, their fading and re-using ability.

The experimental results show that:

- Sensitivity of different OSLDs vary about 7.0% for unscreened OSLDs and 2.0% for screened OSLDs
- OSL dosimeters can be repeatedly read to provide statistically useful results for one irradiation. The standard deviation calculated from multiple readouts is 2.4% on average. This result suggests that the current OSL dosimetry techniques can provide more reliable measurement results compared with those of TLDs for external beam radiotherapy dosimetry.
- In radiotherapy energy range, OSL dosimetry provides a wide dose response range, good dose linearity and reproducibility for doses up to 800cGy, with the maximum deviations of 2.0% from linearity. For the doses below 600 cGy deviations are less than 1.5%.
- There is no significant (less than 0.5%) variation in dose in the dose range of up to 600 cGy or at 200 cGy, which is generally the most clinically relevant dose per fraction range for radiotherapy.
- There is an almost energy independent linear dose-response shown for both electron and photon beams. The energy dependence standard deviation for 6 and 10 MV photon beams is 2.0%, while there is 5.0% deviation among electron beam energies from 6 to 14MeV.
- The directional/angular variation is ±0.7% between gantry angles at 0, 30, 45, and 90 degrees.
- Incremental exposure / accumulated dose dose-response curves show a slightly higher variation (3.0%) than that of a single exposure (2.0%) up to 800 cGy. This makes it possible for OSLDs to be used repeatedly for multiple dose measurements without using an intermediate optical annealing process. This may however increase the noise level.
- Simple optical annealing procedures can be used with either a fluorescent light source or an incandescent light source, with the later one being more effective. However, the optical annealing procedure is not able to erase the previous measurement readings completely. Over 3 cycles of: irradiation – reading – optical annealing, there is almost a 10% increase in dose response, making the accurate measurement of the residual signal after

optical annealing vital before reusing the OSL dosimeter.

In addition, the most important factor is that the reliability of the dose measurement can be reduced by each optical annealing process as measurement reading noise may increase significantly.

7.6 Conclusion

The experimental results demonstrated that OSLD shows the following characteristics: of providing a wide dose-response range with good linearity shown by maximum deviation of 2.0% in the dose range from 600cGy--800cGy and with a deviation of 1.5% for the doses below 600cGy; of having good reproducibility of 0.6% for the 4 OSLDs irradiated incrementally from 10cGy to 800cGy; of having small enough discrepancies that results can adequately represent dose changes for clinical point dose measurement. Lower beam energy dependency can practically simplify the calibration procedure. OSLDs have little fading effect and good reusability and have good dose-response consistency among OSL dosimeters.

Therefore OSL, as a new clinical dosimetry tool, may suitable for real time dosimetry and for treatment plan quality assurance (QA) checks. Unlike TLDs, OSL dosimeters in the form of a flexible film can be tailored to suit to the different shapes or sizes of radiation beams, and to various patient applications. Compared with TLD, the OSL measurement process is much simpler and OSL readouts can be taken repeatedly for a single radiation exposure which leads to a lower uncertainty among the repeated readings. The material can be reused by overlaying subsequent doses over previous measurements without the need of annealing.

Combined with other dosimetry techniques OSL dosimetry can be used in radiotherapy as an alternative tool for treatment plan dose verification, for monitoring the doses received by sensitive tissues or organs at risk and for the radiation beam data acquisition, for example dose distribution maps and beam profiles with the use of two-dimensional OSL sheets.

The conclusion of this study is that OSL dosimetry can provide an alternative dosimetry technique for use in 3D and IMRT plan verification if a proper measurement protocol is established. As mentioned above, over several repeated cycles of "irradiation-readout-annealing" OSL sensitivity variations may reach an unacceptable level.

Chapter 8 Preliminary Study of OSL use for Patient Dose Verification in Intensity-Modulated Radiation Therapy (IMRT)

8.1 Introduction

Intensity-Modulated Radiation Therapy (IMRT) is a treatment delivery technique using intensity-modulated beams which usually results in advantageous dose distributions compared to those of three-dimensional conformal radiotherapy (3DCRT). Two aspects distinguish IMRT from conventional 3DCRT: the optimization process in the planning phase and the use of customized non-uniform fluence distributions in treatment delivery (Boyer, 2001). An IMRT plan can generate very conformal dose distributions with steep dose gradients which maximize the dose to the target (tumour) and minimize the dose to the surrounding critical organs and structures. Consequently IMRT requires good target specification and better target localization and immobilization.

The clinical objectives of IMRT are to make sharper dose fall-offs at the target volume boundary in order to: enable a reduction in clinical treating margins, reduce toxicity to nearby critical structures, to improve the efficiency of treatment and to enable dose escalation. Two aspects distinguish IMRT from conventional 3DCRT: the optimization process in the planning phase and the use of customized non-uniform fluence distributions in treatment delivery (Boyer, 2001). An IMRT plan can generate very conformal dose distributions with steep dose gradients which maximize the dose to the target (tumour) and minimize the dose to the surrounding critical organs and structures. Consequently IMRT requires good target specification, and better localization and immobilization of target.

The basic requirements of executing IMRT are: 1) a TPS with inverse planning software and optimization algorithm capabilities; 2) treatment units equipped with multi-leaf collimators (MLC's) which can do ‘step & shot’ static (sMLC) or dynamic MLC (dMLC) IMRT or are equipped with proprietary pneumatic dynamic multi-leaf collimators (MIMiC; NOMOS Corp, Sewickley, PA) which can do fan beam rotational IMRT.

As IMRT is a complex technique a comprehensive QA program is essential to guarantee correct delivery. Therefore a complete IMRT QA program normally covers

an accuracy check of the delivery systems including verification of the mechanics, electronics and the software of the treatment unit and MLCs; the accuracy check of the treatment-planning systems including verification of the dose calculation algorithm and checks of the patient positioning devices.

The QA(QC) procedures for checking MLC-based Linear accelerator delivery systems (including sMLC, dMLC, and MIMiC based) are well established and described by many authors (Boyer *et al.* 2001; LoSasso *et al.,* 1998; 2001; Saw *et al.*, 2001a; 2001b; Low *et al.,* 1998a; 1998b; 1999), and have also been well documented (Klein *et al.*, 2009).

Anatomy based planning using Computer Tomography (CT) or Magnetic Resonance Imaging (MRI) images fused with functional imaging, such as Positron Emission Tomography (PET) or Magnetic Resonance Spectrospcopy (MRS), achieves good target specification. The goal of TPS IMRT plan calculations are not only to optimize the beam intensity fluence maps according to the user defined target, critical structure and other tissue dose constraints, but also to work out the economic delivery of the MLC patterns and positions as well as the optimal monitor units (mu's). Currently, apart from the commissioning of a TPS for planning, an IMRT plan should follow the conventional TPS QA procedure recommended in the AAPM task group 53 (Fraass *et al*., 1998). The most important QA procedure for the commissioning of a TPS for IMRT planning is verifying the calculated dose distributions. This can normally be done by comparing the dose distributions and the individual beam intensity fluence calculated out in TPS in homogenous geometric or Anthropomorphic phantom with the dose distributions and the beam intensity fluence measured in the same phantom(Low, 2002). A single beam plan is usually used to check the beam depth dose, beam profile (including beam penumbra), and beam MUs. The beam intensity fluence and dose distributions tests are very simular to checking patient-specific IMRT plans. Patient-specific IMRT plan checks are essentially needed for every patient's IMRT plan to ensure its accuracy.

The check of a patient's treatment plan requires verification of correct patient positioning and the delivered dose. There are many factors which may influence the patient's treatment positions and dose, but the most important ones are patient motion during delivering (intrafraction motion) and the repeatability of the patient's treatment positions (interfraction motion). The patient's intrafraction motion caused by respiratory, skeletal muscular, cardiac, and gastrointestinal systems can be significant (Yu et al., 1998; Keall et al., 2006). Many clinics currently use either daily

or weekly images for pre-treatment patient positioning verification. Pre-treatment localization with Electronic Portal Imaging Devices (EPIDs), cone-beam CT (CBCT), static kilovoltage (kV) imaging, ultrasound, orthogonal radiographs, optical systems and real time image guidance during delivery with respiratory gating systems provide better localisation and immobilization of target during treatment delivery. AAPM task group 75 (Murphy et al., 2007) refers to managing imaging dose during IGRT treatment.

The comparison between the doses calculated by planning systems and the doses measured in a phantom is the critical component of IMRT acceptance testing and commissioning and for patient IMRT QA. Two factors determine the accuracy of the measurements: the type of detectors and the special location of the detector detecting the dose. The high dose-gradient and time-dependent dose characteristics of IMRT delivery set the constraints in choosing the proper dosimeters and techniques (IMRTCWG, 2001).

The ionization chamber is still a commonly used dosimeter for IMRT plan point dose check measurements even though the entire fluence distribution must be delivered for each measurement. With a smaller diameter of cylindrical chamber, the accuracy can reach 1% (Low *et al.* 1998b)

Thermoluminescent dosimeters (TLDs) can also be used for IMRT point dose measurements (Tsai *et al.*1998; Low *et al.* 1999b), and with careful calibration TLD chips can achieve a 3% accuracy.

Radiographic films can provide 2D dose distribution checks and this characteristic would make them more suitable than ionization chambers and TLDs for relative dosimetric measurements, but this is not the case as the quality of the results is to variable depending on the processing technology and image processing technique including film processor, film scanner linearity, and so on. Film dosimetry is commonly used only for visual dose distribution checks and is not reliable or consistent enough when used for measuring absolute dose.

Meeks *et al*. (2002) used the optically stimulated luminescence dosimeter (OSLD) (Luxel™, Landauer Inc., Glenwood, IL) to investigate the extra-cranial dose received by patients with intracranial IMRT head and neck treatments using a serial tomotherapy treatment unit (NOMOS' multivane intensity modulating collimator(MIMiC)). Anzar *et al.* (2004) studied head and neck IMRT treatments using radioluminescence/ optically stimulated luminescence (RL/OSL) optical-fibre

dosimeter system with single crystal of Al_2O_3:C from Landauer (Landauer Inc., Chicago, USA). Andersen *et al.*(2006) also demonstrated 13-fields IMRT plan dose verification in a phantom by using OSL probes.

The objective of this experiment focused on exploring the possibilities of using OSL dosimeters (OSLD) with MicroStar readers to verify point and dose distributions of an IMRT plan.

My procedure for IMRT plan OSL dose verification is as follows: The OSL detector was calibrated at reference point(s) in the phantom to the dose calculated by a TPS at the same point(s). A simplified OSL reading technique with high accuracy and reproducibility, when compared to the radiation dose given, was used to determine the OSL detector readings. The IMRT plans used simulated the treatment of nasopharynx, prostate and lung cancers, and were delivered to an in-house made spherical phantom with Al_2O_3:C OSL detectors placed at pre-selected measurement points.

Three clinical IMRT plans; nasopharynx, prostate and lung were chosen for this experiment. Conventional CT scans of phantoms and patients were exported to a commercial CMS XIO TPS (CMS Inc., St. Louis, MO). IMRT acceptance testing and commissioning had been completed for the XIO TPS and it was ready for clinical use. To measure the dose and the dose distributions obtained from the TPS for the patient's IMRT plans of nasopharynx, prostate and lung, the patient's plans were first hybrided into a water-equivalent spherical phantom and corresponding hybridized IMRT plans were made. The calibrated OSLD's were inserted into the same water-equivalent spherical phantom before taking the verification measurements. The doses calculated by the TPS and the ones measured by OSLDs were compared.

To achieve above mentioned goals, the experiments were divided into three steps:

- OSLD calibration
- Point dose verification in a small region for the selected three clinical IMRT plans
- Dose distribution curve comparison with that of a TPS in a larger region for three selected clinical IMRT plans

8.2 Instrumentation

8.2.1 OSL dosimeters and reader systems

The 4 dots OSLDs and the microStar reader used in this study have been introduced in Chapter 6. The internal slides were separated from the cases and all filtration removed.

The sensitivity of the OSLDs and the calibration factor from the manufacture can be set into the reader system and converted to counts per millirem by using the manufacturer's calibration factor. However, as mentioned in previous chapter, this is not suitable for radiotherapy. In this study only raw reader counts were used that were converted manually to dose using experimentally derived calibration factors.

It should be noted that the sensitivity of the detector varies with each package of OSL's. My previous experimental results showed a 2% variation of OSLD sensitivity when they came from the same package (Table 7.2) and up to 7% variation when they came from different package (Table 7.1). OSL dosimeters were chosen from the same package to avoid this uncertainty.

8.2.2 The spherical phantom used in OSL calibration and IMRT plan dose verification planning

A regular geometric phantom can be used to verify IMRT dose distribution even though it is dissimilar to patient shape. The advantage of this type of phantom is that it is designed and fabricated easily with tight spacial tolerances and various detectors can be inserted. Alignment of dosimeter location to marks on the phantom can easily be achieved.

A solid sphere phantom (Figure 8.1, described in section 7.2.2.3) (Yang, 2006) made of perspex was used in this study. This phantom is 24 cm in diameter and consists of 4 separate pieces, the base, lower half, upper half and an OSL placement (OSLDs surrounded by wax filler). The filler ensures a minimal air gap around OSL detectors. The OSL detectors were placed in the centre of the sphere. The relative location of the dosimeters and external alignment marks are carefully marked on the phantom.

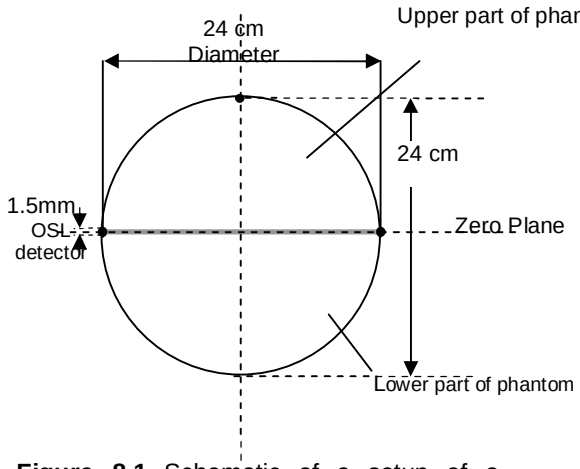

Figure 8.1 Schematic of a setup of a spherical phantom. Three dots(anterior,lateral) indicate the fiducial markers

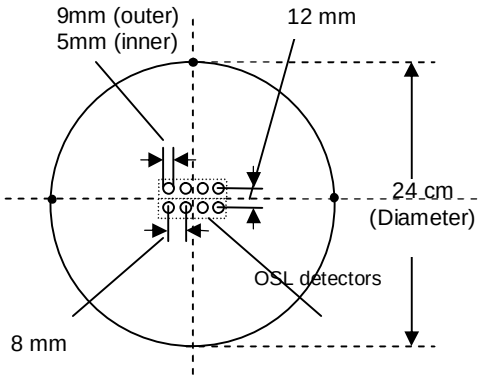

Figure 8.2 Schematic of OSL detectors in a spherical phantom. Three dots (anterior, lateral) indicate the fiducial markers.

8.2.3 Irradiation source

In this study, the OSL dosimeters were irradiated with 6 and 10 MV X-rays using a Siemens Primus Linear Accelerator equipped with a 58 leaf collimator. The linear accelerator's output in monitor units per cGy had been calibrated according to the absorbed dose calibration protocol of IAEA TRS-398 in water at a depth of d_{max}. The monitor units (MUs) per cGy for a 10x10cm^2 beam size at the source-to-surface distance (SSD) of 100cm was set to 1cGy/1MU.

8.2.4 CT scanner and TPS system

The Computer Tomography (CT) scanner used for planning and to produce DRR's was a GE LightSpeed Radiotherapy Computer Tomography (CT) scanner (GE Medical Systems, Milwaukee WI, USA). The scanner has a large bore (80cm) and performs 4-slice helical scanning. The Spherical Phantom was scanned using the same scan protocol chosen for patients to ensure consistency.

CT scanned images were sent to a CMS Focal / XiO (CMS Inc. St Louis, MO, USA) treatment planning system (CMS Focal 4.34 and XiO 4.34).

8.3 Methodology

8.3.1 Calibration of OSL dosimeters

From my previous study (chapter 7), the sensitivity variation of the OSL dosimeters from the same package is within 2%. No individual OSLD calibration is necessary, however an individual calibration of each OSLD was performed for this experiment. The calibration was carried out using the spherical phantom centred at 100cm SAD using a 10x10cm^2 fixed field size. The delivered dose to the OSLD measurement point was prescribed to 1Gy and calculated by TPS (CMS XiO). The OSLD was calibrated against an ion chamber.

8.3.2 Patient's IMRT cases

The process of inverse IMRT planning includes:

- The user provides the TPS with clinical goals including specific dose prescriptions for the target and specific tolerance doses for normal tissues.
- The user provides the TPS with delivery method constraints including selecting the beam orientation (angle) and energies.
- The TPS performs optimization using the entered plan parameters
- The user evaluates the resulting dose pattern and modifies the beam orientations or energies and dose prescriptions or tolerances as needed.
- Plan QA
- Implementation

IMRT is well-suited for instances in which the target volume is highly irregular in shape, and in close proximity to radiosensitive critical structures. IMRT performs better in higher doses regions as long as dose-volume constraints are correctly placed. IMRT does not perform as well at lower doses.

Three clinical patient's IMRT cases were chosen including nasopharynx, prostate, and lung, respectively. A Nasopharynx case was chosen because there are multiple critical organs at risk (OAR) around the target. A prostate case was chosen due to occurrence of a sharper fall-off of isodose at the target-volume boundary. A lung case was used for testing OSLD response with higher beam energies (10MV).

High energy photons (usually greater than 10 MV) are commonly used in 3D conformal radiotherapy due to their dosimetric advantages: greater penetration

depth and skin-sparing potential. However, high energy photons may show more disadvantages when used for IMRT:

- Modulation in TPS. For small fields, electron equilibrium losses greater laterally and brings results in a widen penumbra (Wang et al., 2002). This causes dose reduction near the beam edge and along the central axis in high gradient regions (White et al., 1996)
- Neutron contamination. High energy IMRT treatment need to increase monitor units for higher neutron fluence and higher dose equivalent (Howell et al., 2005).

Figures 8.5a, 8.6a, 8.7a show the original plan for patients. All treatment plans for the selected tumours consisted of multiple IMRT segments delivered at five (5) gantry angles using 6 or 10 MV x-rays.

8.3.3 IMRT plan dose verification procedure

Treatment planning system are able to apply the designed fluence distribution from a patient's IMRT treatment plan to the hybridized plan in phantom without fluence re-optimization (IMRTCWG, 2001). This allows us to: 1) to shift a patient's intensity distribution to a measurement phantom, 2) to compare and analyse the measured and calculated dose distributions in the same phantom, and 3) to re-locate the plan to a predefined position where the dosimeters can be located.

The hybridized treatment plan dosimetric verification was performed using the same spherical phantom with OSLs inserts at the same locations as those that were used in the OSL calibration.

The spherical phantom with OSLDs inserted was placed on the CT table with the OSL placement plane vertically aligned with the CT scan axis and centred with the aid of three fiducial markers on the phantom. (Figure 8.3). The two fiducial markers on both sides of the phantom determined the central plane horizontally and the one on the top of the phantom determined the central plane vertically. The origin of the phantom was aligned to the CT scanner and linear accelerator by matching the positioning lasers to the three fiducial markers. Each group of OSL detector placements was set to the centre (origin) of the phantom. The scanned CT images were sent to a CMS XiO TPS.

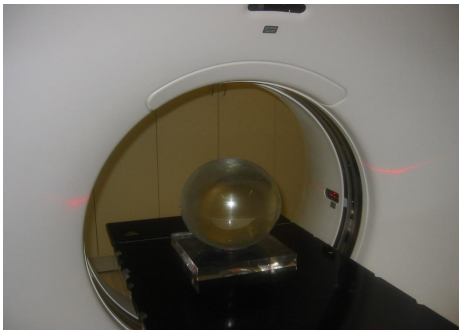

Figure 8.3 The setup on CT table of spherical phantom with OSL inserts

Then three selected plans were hybridized to the spherical phantom with unchanged fluence distributions. The isocenters were set to a SAD of 100 cm, which is also the centre of the OSL placement. The dose distributions in the plane of the OSL detectors in the spherical phantom are shown in Figure 8.5b-d, 8.6b-d, 8.7b-d. Eight (8) points were pre-assigned in the spherical phantom for each dose measurement. The plans were delivered by 6 or 10 MV X rays. The delivered dose was 1Gy to the isocentre.

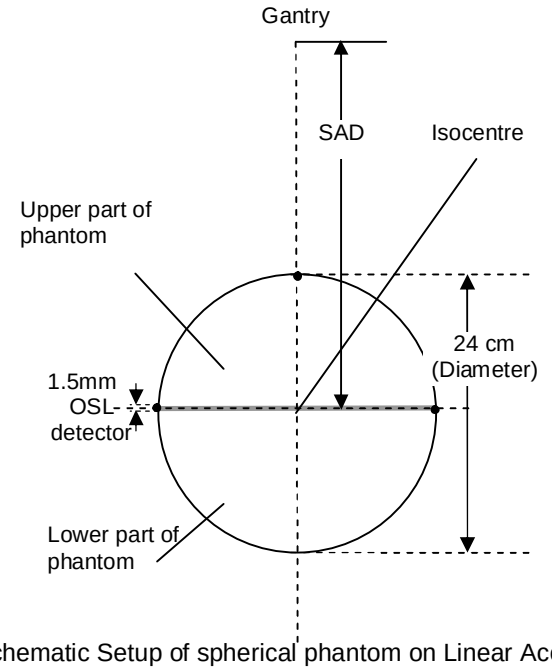

Figure 8.4 Schematic Setup of spherical phantom on Linear Accelerator for IMRT dose verification using OSLDs. The three dots (anterior, lateral) indicate the three fiducial markers.

By using the positioning lasers in treatment room of the linear accelerator, the origin of the phantom is set to the isocentre with the aid of the three fiducial markers on the phantom to ensure the same setup as during the CT scans (Figure 8.4).

8.3.4 OSL measurement data analysis

The OSLDs were read prior to radiation exposure and the average was taken of ten (10) consecutive readings and these were used as the zero-point for subsequent readings. The irradiated OSLDs were read using a MicroStar reader at 2 hours after irradiation for both OSLDs calibration and OSLDs IMRT plan measurement. The raw counts were averaged from ten consecutively readings, and then subtracted from the unexposed average reading. The raw counts from the IMRT cases were converted to absolute dose, and then the dose verification analyses were performed according the following formula:

The average measurement dose (D_{OSL}) is subsequently given in a shorthand form as:

$$\begin{aligned} \overline{D}_{OSL} &= \frac{\overline{R}}{R_c} \\ D_{OSL} &= \overline{D} \pm SD(n) \end{aligned} \tag{8.1}$$

The dose differences of the measured to the calculated (Δ*D*) from TPS is

$$\Delta D = (D_{OSL} - D_{TPS}) \pm SD \pm \sigma \tag{8.2}$$

The percentage of the dose differences (*Diff(%)*) is

$$Diff\,(\%) = (\frac{\Delta D}{D_{TPS}})/100 \tag{8.3}$$

Where: R is the average readout counts of 10 readings for each OSL detector, R_c is the calibrated OSL detector readouts. σ is the setup uncertainty of 2mm isocenter shift in three directions (lateral, longitudinal, vertical) from section 8.3.5. D is the converted dose. D_{TPS} is the planed dose.

Naspharyx IMRT plan

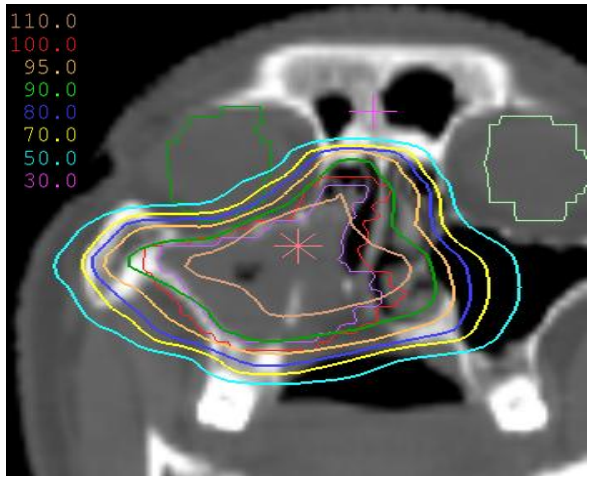

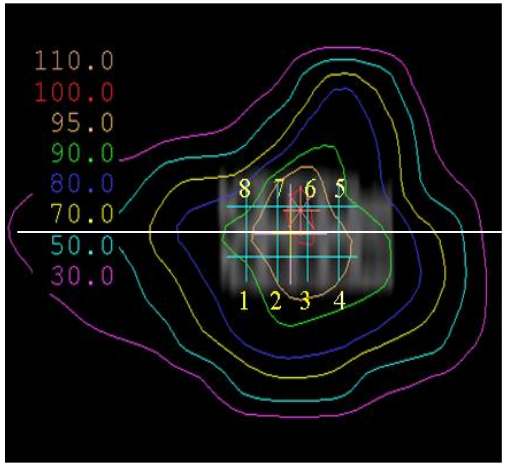

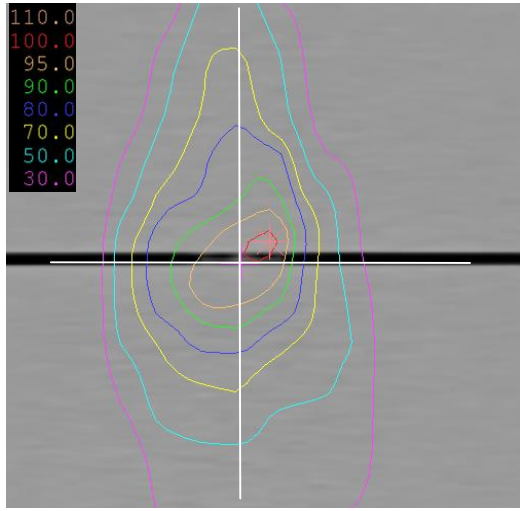

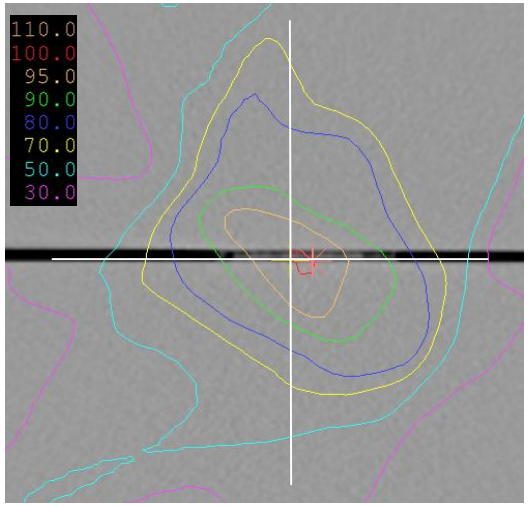

Figure 8.5 Nasopharynx IMRT treatment plan dose distribution. IMRT plan was delivered using 6 MV-X rays. Prescription dose was normalized to the setup isocentre for both patient and phantom. The color labels show the percentage dose lines.

(a) Coronal cross-section for the slice at the isocentre of the patient's plan. Multiple measurement points are located in highest dose gradient region.

(b) Coronal cross-section at iso-centre slice of phantom's plan. White line corresponds to the position of the transverse and sagital cross-section, respectively.

(c) Sagital cross-section of phantom's plan. White line corresponds to the position of the transverse and coronal cross-section, respectively.

(d) Transverse cross-section at iso-centre slice of phantom's plan. White line corresponds to the position of the coronal and sagital cross-section, respectively.

Prostate IMRT case

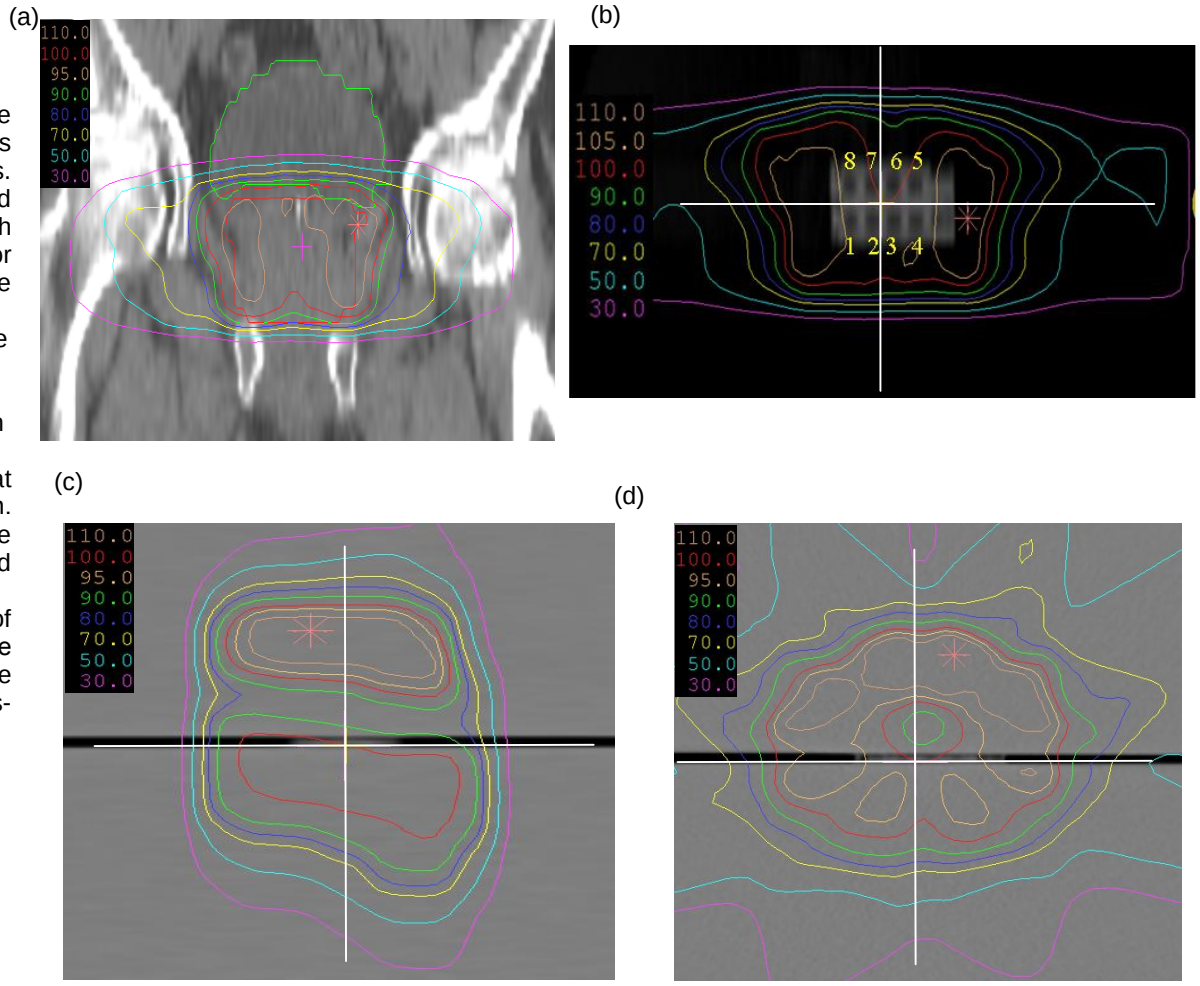

Figure 8.6 Prostate IMRT treatment plan dose distribution. IMRT plan was delivered using 6 MV-X rays. Prescription dose was normalized to the setup isocentre for both patient and phantom. The color labels show the percentage dose lines.

(a) Coronal cross-section for the slice at the isocentre of the patient's plan. Multiple measurement points are located in highest dose gradient region.

(b) Coronal cross-section at isocentre slice of a phantom's plan. White line corresponds to the position of the transverse and sagital cross-section, respectively.

(c) Sagital cross-section of phantom's plan. White line corresponds to the position of the transverse and coronal cross-section, respectively.

(d) Transverse cross-section at isocentre slice of phantom's plan. White line corresponds to the position of the coronal and sagital cross-section, respectively.

Lung IMRT case

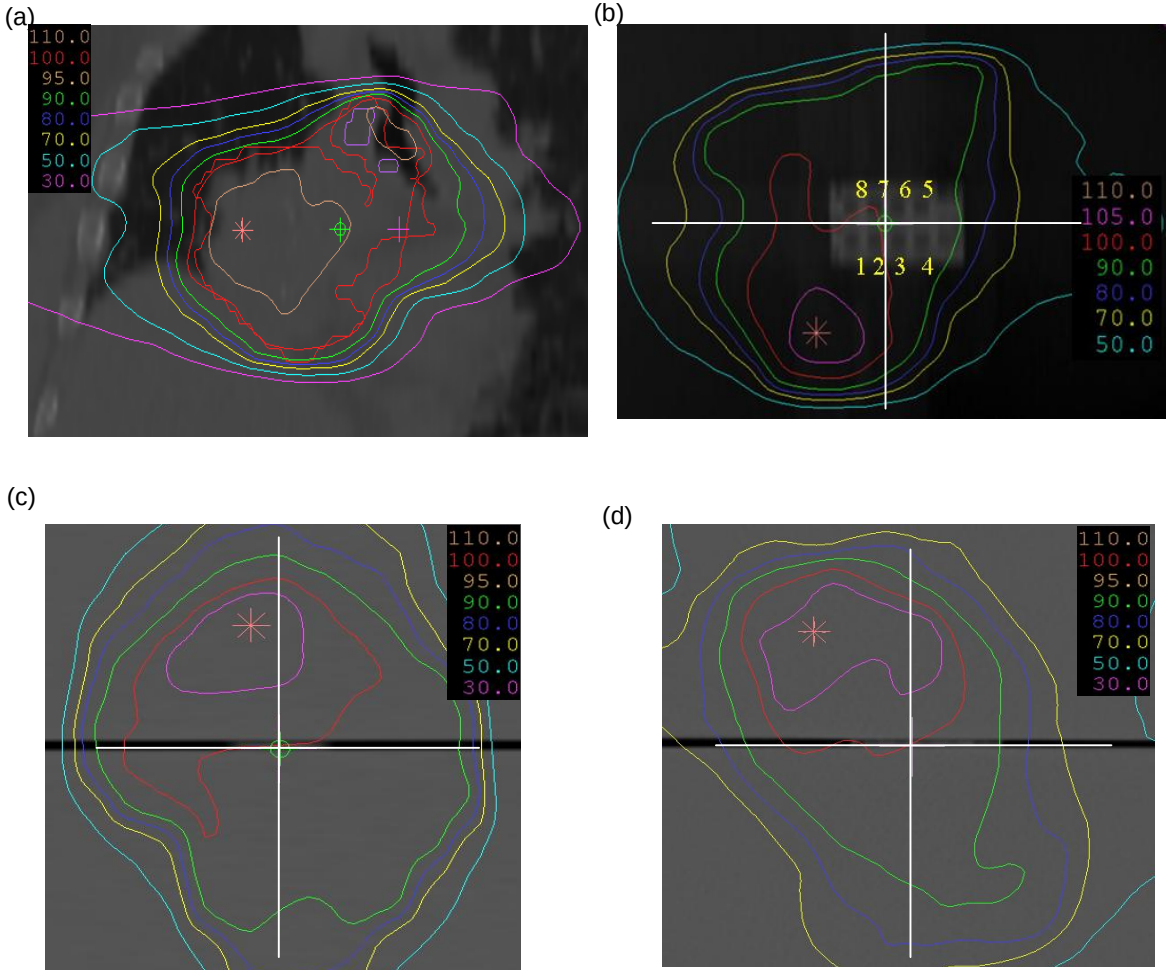

Figure 8.7 Lung IMRT treatment plan dose distribution. IMRT plan was delivered using 10 MV-X rays. Prescription dose was normalized to the setup isocentre for both patient and phantom. The color labels show the percentage dose lines.

(a) Coronal cross-section for the slice at the isocentre of the patient's plan. Most measurement points are located in flat dose gradient region.

(b) Coronal cross-section at isocentre slice of phantom's plan. White line corresponds to the position of the transverse and sagital cross-section, respectively.

(c) Sagital cross-section of phantom's plan. White line corresponds to the position of the transverse and coronal cross-section, respectively.

(d) Transverse cross-section at isocentre slice of phantom's plan. White line corresponds to the position of the coronal and sagital cross-section, respectively.

83.5 Setup uncertainty evaluation from TPS

Of the three clinical IMRT cases (nasopharynx, prostate, and right lung) chosen for dose verification, two have relatively steep dose gradients (nasopharynx and prostate), one a slightly lower dose gradients (lung), and one a concave-shaped dose gradient (prostate), as shown in Figures 8.5, Figure 8.6, and Figure 8.7. Therefore, for point dose comparisons, the setup errors should be taken into account when using fiducial markers for set-up positioning.

To simulate the influence of the set-up error on the dose results measured, for the three clinical cases, isocentre shifts of ±2.0mm and ±1.0 mm away from the real isocentre point in three directions (X: lateral, Y: longitudinal, Z: vertical) individually were applied, and for each shift a dose distribution calculation using the XiO TPS was performed again. The same dose verification and comparison as mentioned above was executed. The results show that there was little difference in dose distribution due to the isocentre shifts of ±2.0mm and ±1.0 mm in three directions.

8.4 OSL measurement results

8.4.1 Nasopharynx IMRT plan dose verification

For the nasopharynx plan, the doses measured by OSL dosimeters at the selected measurement points in the phantom were compared with those calculated by TPS (Figure 8.5b) as shown in Table 8.2.

The plan calculated doses for these 8 selected points range from 0.88Gy to 1.01Gy. The measurement doses for the same 8 points range from 0.86Gy to 1.01Gy, with a maximum dose difference of 0.04 ± 0.03(SD) and with maximum dose percentage difference of 3.3% ± 3.2%. The setup uncertainty (2mm) contributes about ±0.05Gy (±5.2%) to the maximum dose difference.

The dose measured at point 6 (1.01 ± 0.02Gy) showed the highest dose difference (0.04 ± 0.02 Gy) compared to the one calculated in the plan (0.97Gy) , followed by point 5 with 0.88 ± 0.02Gy versus the planed dose (0.91Gy) and at point 8 0.93 ± 0.01Gy versus the planed dose (0.96Gy). Point 2, 3 and 4 showed the lowest dose difference between that measured and calculated.

Meeks *et al*. (2002) used an optically stimulated luminescence dosimeters (OSLD) (Luxel™, Landauer Inc., Glenwood, IL) to investigate the extra-cranial dose received

by patients during intracranial and head and neck IMRT treatments by using a tomotherapy treatment unit. The OSLDs were put at the surface of the sternum and abdomen for patient dose measurement. Their results showed that OSLD dose accuracy to the known dose was within 5% and that patient dose varies inversely to the distance from the centre of the target.

Anzar *et al*. (2004) verified head and neck IMRT plans by using a radioluminescence/ optically stimulated luminescence (RL/OSL) optical-fibre dosimeter system with single crystal of Al_2O_3:C from Landauer (Landauer Inc., Chicago, USA). A catheter with two RL/OSL optical fibres inserted was put into the patient's oesophagus through the nose. They found a 0.09±0.05 Gy dose difference between measured dose (1.76 ±0.05 Gy) and the planed dose (1.85 Gy).

Andersen *et al*.(2006) demonstrated the use of OSL probes with a 13 field IMRT plan dose verification in a phantom . They focused on using radioluminescence (RL) from optical fibre Al_2O_3:C dosimeters rather than using optically stimulated luminescence (OSL). Their results showed a 0.9% difference between OSL and RL measured results, and with 2% a good agreement between the planned and the measured dose.

My result has a good agreement with that reports from Meeks *et al*.(2002), Anzar *et al*. (2004)and Anderson *et al*.(2006).

Table 8.2 OSL Point measurement verification results for the Nasopharynx IMRT case. SD represents the standard deviation of the averages of 5 readouts. ΔD represents the difference of OSLD measured dose to TPS calculated dose. σ represents setup uncertainty(2mm). Diff(%) represents the percentage difference between OSLD measured to TPS calculated dose**.**

Measurement points	TPS Calibrated (Gy)	OSL Measured (Gy) (Mean±SD)	ΔD ±SD ± σ (Gy)	*Diff(%)* (ΔD /TPS ± SD ±σ)
Point 1	0.88	0.86 ± 0.01	-0.02 ± 0.01 ± 0.04	-2.3% ± 1.1% ± 4.5%
Point 2	0.99	0.98 ± 0.02	0.01 ± 0.02 ± 0.02	1.0% ± 2.0% ± 2.0%
Point 3	1.01	1.00 ± 0.02	-0.01 ± 0.02 ± 0.02	-1.0% ± 2.0% ± 2.0%
Point 4	0.94	0.93 ± 0.03	-0.01 ± 0.03 ± 0.02	-1.1% ± 3.2% ± 2.1%
Point 5	0.91	0.88 ± 0.02	0.03 ± 0.02 ± 0.03	-3.3% ± 2.2% ± 3.3%
Point 6	0.97	1.01 ± 0.02	0.04 ± 0.02 ± 0.01	4.1% ± 2.1% ± 1.0%
Point 7	0.99	1.01 ± 0.01	0.02 ± 0.01 ± 0.02	2.0% ± 1.0% ±2.0%
Point 8	0.96	0.93 ± 0.01	-0.03 ± 0.01 ± 0.05	3.1% ± 1.0% ± 5.2%
Overall diff			**± 0.04 ± 0.03 ± 0.05**	**± 3.3% ± 3.2% ± 5.2%**

8.4.2 Prostate IMRT plan dose verification

For prostate plans the doses measured by OSL dosimeters at the selected measurement points were compared with those calculated for the prostate plan in a TPS (Figure 8.6b) as shown in Table 8.3.

The plan calculated doses for these 8 selected points are in a range from 0.92Gy to 1.04Gy. The measurement doses for the same 8 points are in range from 0.92Gy to 1.06Gy with a maximum dose difference of 0.05 ±0.03(SD) and with a maximum dose percentage difference of 4.8%±3.1%. The setup uncertainty of (2mm) contributes about ±0.06Gy (±6.5%) to the maximum dose difference.

The dose measured at point 4 (0.99 ± 0.01Gy) shows the highest dose difference (0.05 ± 0.01 Gy) compared to the plan calculated dose of 1.04Gyfollowed by point 3 (0.97 ± 0.02Gy) versus a plan dose of 1.0Gy and point 8 (1.06 ± 0.01Gy) versus a plan dose of 1.03Gy. Point 6, 1, 5 and 7 show a lower dose difference between the one measured and the one calculated

Table 8.3 OSL Point measurement verification result for the Prostate IMRT case. SD represents the standard deviation of the averages of 5 readouts. ΔD represents the difference of OSLD measured dose to TPS calculated dose. σ represents setup uncertainty(2mm). Diff(%) represents the percentage difference between OSLD measured to TPS calculated dose.

Measurement points	TPS Calibrated (Gy)	OSL Measured (Gy) (Mean±SD)	ΔD ±SD ± σ (Gy)	*Diff(%)* (ΔD /TPS ± SD ±σ)
Point 1	1.04	1.05 ± 0.02	0.01 ± 0.02 ± 0.01	1.0% ± 1.9% ± 1.0%
Point 2	1.00	0.97 ± 0.02	-0.03 ± 0.02 ± 0.03	-3.0% ± 2.0% ± 3.0%
Point 3	0.97	0.95 ± 0.02	-0.02 ± 0.02 ± 0.04	-2.1% ± 2.1% ± 4.1%
Point 4	1.04	0.99 ± 0.01	-0.05 ± 0.01 ± 0.02	-4.8% ± 1.0% ± 1.9%
Point 5	0.97	0.96 ± 0.01	-0.01 ± 0.01 ± 0.04	-1.0% ± 1.0% ± 4.1%
Point 6	0.92	0.92 ± 0.01	-0.00 ± 0.01 ± 0.06	0.0% ± 1.1% ± 6.5%
Point 7	0.98	0.97 ± 0.03	-0.01 ± 0.03 ± 0.03	1.0% ± 3.1% ± 3.1%
Point 8	1.03	1.06 ± 0.01	0.03 ± 0.01 ± 0.01	2.9% ± 1.0% ± 1.0%
Overall diff			**± 0.05 ± 0.03 ± 0.06**	**± 4.8% ± 3.1% ± 6.5%**

8.4.3 Lung IMRT plan dose verification

The doses measured by OSL dosimeters at the selected measurement points were compared with those calculated by a TPS (Figure 8.7b) for a lung plan as shown in Table 8.4.

The dose calculated for these 8 selected points are in range of 0.98Gy to 1.02Gy. And the measurement doses for the same 8 points are in range of 0.97Gy to 1.01Gy

with a maximum dose difference of 0.02±0.02(SD) and a maximum dose percentage difference of 2.0%±2.0%. The setup uncertainty (2mm) contributes about ±0.02Gy (±2.0%) to the maximum dose difference.

Table 8.4 OSL Point measurement verification results for the Lung IMRT case. SD represents the standard deviation of the averages of 5 readouts. ΔD represents the difference of OSLD measured dose to TPS calculated dose. σ represents setup uncertainty(2mm). Diff(%) represents the percentage difference between OSLD measured to TPS calculated dose.

Measurement points	TPS Calibrated (Gy)	OSL Measured (Gy) (Mean±SD)	ΔD ±SD ± σ (Gy)	*Diff(%)* (ΔD /TPS ± SD ±σ)
Point 1	1.02	1.01 ± 0.02	0.01 ± 0.01 ± 0.01	1.0% ± 1.0% ± 1.0%
Point 2	1.01	1.01 ± 0.02	0.00 ± 0.01 ± 0.01	-0.0% ± 1.0% ± 1.0%
Point 3	1.00	0.98 ± 0.02	-0.02 ± 0.01 ± 0.01	-2.0% ± 1.0% ± 1.0%
Point 4	0.98	0.98 ± 0.01	-0.00 ± 0.01 ± 0.02	0.0% ± 1.0% ± 2.0%
Point 5	0.98	0.97 ± 0.01	-0.01 ± 0.01 ± 0.01	-1.0% ± 1.0% ± 1.0%
Point 6	0.99	1.00 ± 0.01	0.01 ± 0.02 ± 0.01	1.0% ± 2.0% ± 1.0%
Point 7	1.00	1.01 ± 0.03	-0.01 ± 0.02 ± 0.01	1.0% ± 2.0% ± 1.0%
Point 8	0.99	0.99 ± 0.01	0.00 ± 0.02 ± 0.01	0.0% ± 2.0% ± 1.0%
Overall diff			**± 0.02 ± 0.02 ± 0.02**	**± 2.0% ± 2.0% ± 2.0%**

8.4.4 Setup uncertainty evaluation

In order to evaluate the reliability of OSL dosimetry and analyse the degree to which measurement results can be influenced by position setup accuracy, the measurement readings were compared with those made by shifting the treatment isocentre along two opposing directions within a ±1mm range.

8.4.4.1 Nasopharynx IMRT case (Figure 8.8)

- The maximum dose variations at 8 points are within 0.05Gy, in the six points the dose variations are within 0.02Gy.
- For Points of 3,4,6,7 located in the lower dose gradient region, the dose variations at these point are within 0.01Gy when the isocentre is shifted 1mm in three directions, but they increase to 0.02Gy when the isocentre was shifted 2mm in three directions.
- However for point 1 and 8 located in the higher dose gradient region, the dose variations increased up to 0.03Gy for a 1mm isocenter shift and 0.05Gy for a 2mm isocenter shift.
- When the isocentre is moved in the negative longitudinal IEC direction, it

causes the most significant dose variation, but it would cause a much less dose variation when the isocenter is shifted in the negative lateral IEC direction.

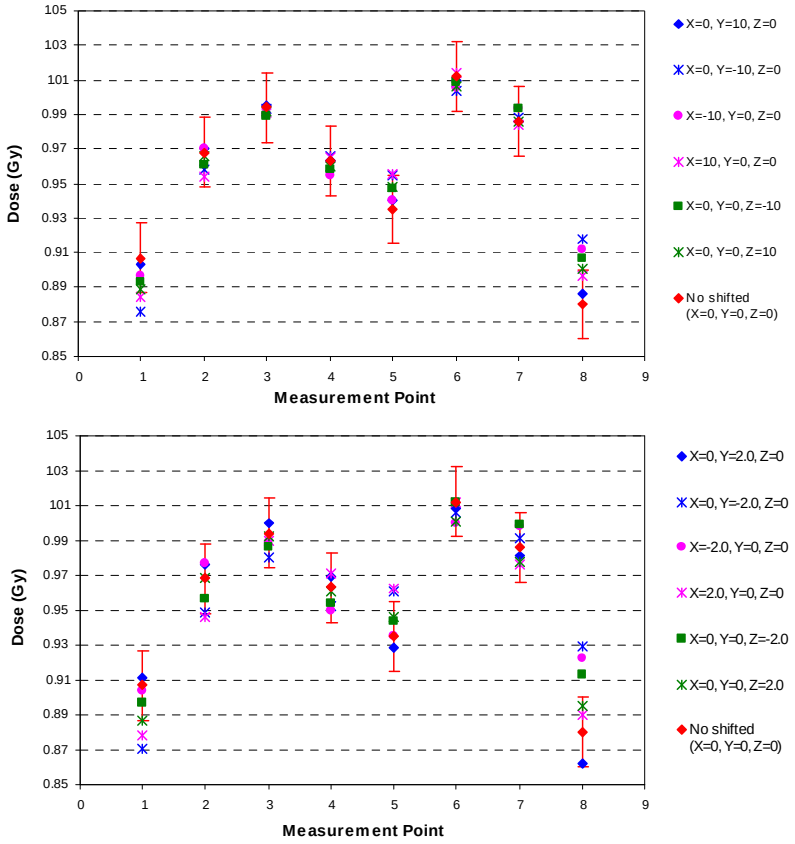

Figure 8.8 Nasopharynx IMRT case: TPS calculated doses for 8 measurement points when the isocentre is shifted ±2.0mm and ±1.0mm in three directions shown in cross-sections (X: lateral, Y: longitudinal, Z: vertical). The doses at the original positions (no shift) for each point are shown in red with a ±0.02Gy (red) error bar added.

8.4.4.2 Prostate IMRT case (Figure 8.9):

- The maximum dose variations for the 8 measurement points are within 0.06Gy; for two of these points dose variations are within 0.02Gy.
- For Points of 1 and 8 located in the lower dose gradient region, the dose variations at these point are within 0.01Gy no matter whether the isocentre shifted 1mm or 2mm in three directions.
- For point 4 located in the relatively lower dose gradient region, the dose variations are within 0.02Gy for both 1mm and 2mm isocenter shifts.

- At point 6 dose variations are the most sensitive to the isocentre shifts, especially in vertical direction. The dose variations are up to 0.04Gy for a 1mm shift and 0.06Gy for a 2mm shift. This is followed by point 3 with dose variations of 0.03Gy for a 1mm shift and 0.04Gy for a 2mm shift in the vertical direction.
- Isocentre movement along the vertical direction will cause the most dose variation.

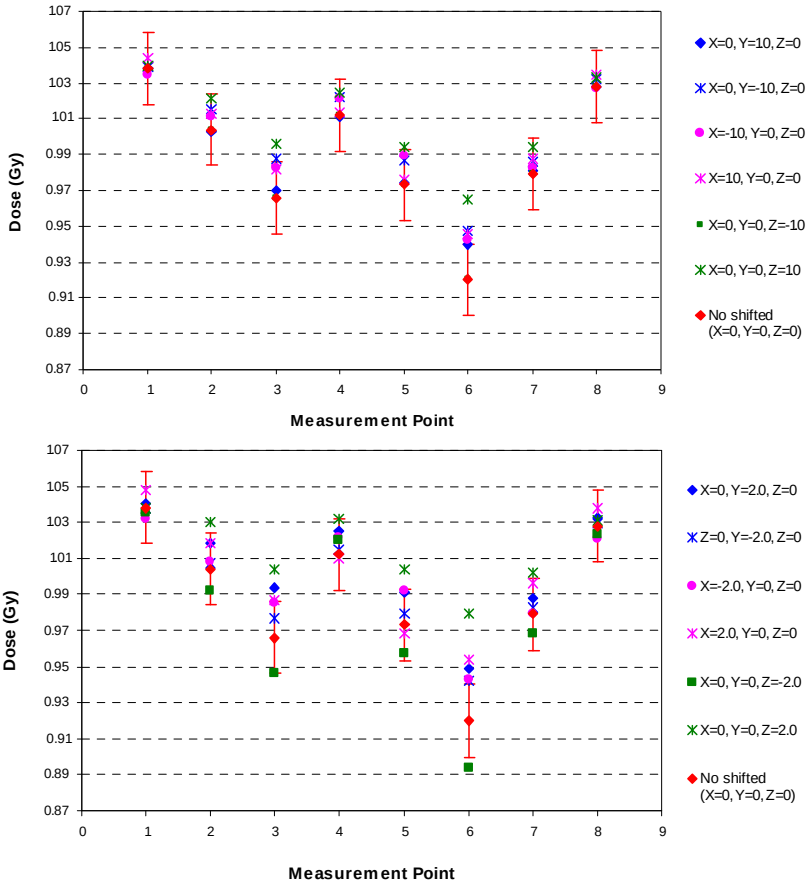

Figure 8.9 Prostate IMRT case: TPS calculated doses for 8 measurement points when the isocentre is shifted ±2.0mm and ±1.0mm in three directions shown in cross-sections (X: lateral, Y: longitudinal, Z: vertical). The doses at the original positions (no shift) for each point are shown in red with a ±0.02Gy (red) error bar added.

8.4.4.3 Lung IMRT case (Figure 8.10):

- The dose variations in all 7 points of 8 points are within 0.01Gy, but the dose variation is up to 0.02Gy at point 4 in the positive lateral direction.

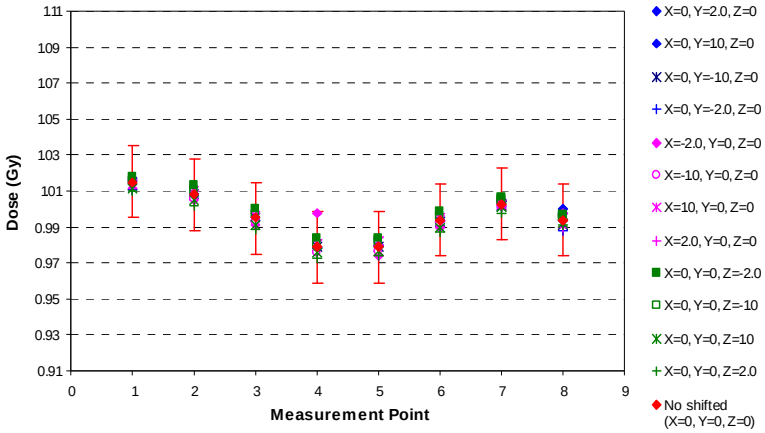

Figure 8.10 Lung IMRT case: TPS calculated doses for 8 measurement points when the isocentre is shifted ±2.0mm and ±1.0mm in three directions shown in cross-sections(X: lateral, Y: longitudinal, Z: vertical). The doses at the original positions (no shift) for each point are shown in red with a ±0.02Gy (red) error bar added.

8.5 Summary and discussion

This study aims to evaluate the potential use of Optically Stimulated Luminescence (OSL) detectors and readers for clinical radiotherapy dosimetry and what factors affect OSL measurements.

Setup error in the three selected clinical cases contributed to dose variations of up to 0.06Gy compared to the planed dose and as high as 1Gy in the high dose gradient region. This proves that OSLD measurement sensitivity is capable to verify dose changes in IMRT plan point dose measurements when performing a dose distribution check. This result also indicates that careful setup becomes a more important consideration for the IMRT point dose measurement.

Three factors need to be considered together when using a OSL detector for IMRT plan point dose measurement. They are: 1) the sensitivity of OSL dosimeters, 2) the accuracy of the OSL reader, and 3) setup uncertainty, especially in a high gradient dose distribution region.

In general, the doses measured by the OSL detectors can accurately reflect the doses calculated by a TPS if the comparison results are consistent between the measured and the calculated doses. My experimental results have shown that with careful calibration and careful setup, the dose difference between the planned and delivered dose can be within 0.04±0.03 Gy for nasopharynx cases, 0.05±0.03Gy for

prostate cases and 0.02±0.02Gy for lung cases when 1Gy is prescribed at isocenter. The biggest dose differences were 4.1%±2.1% at point 6 in the nasopharynx case, 3.3%±2.2% at point 5 in the prostate case, and 2.0%±1.0% at point 4 in the lung case.

Two kinds of systematic errors need to be taken into account. Firstly errors from the OSL material and reader. This can be avoided by careful selection of and calibration for all OSL detectors and by using averages of multiple readouts. Secondly errors from measurement. The effective measurement region of each 5mm diameter OSL micro-dot detector is an area of approximately 18.63mm^2. Therefore the dose distribution over each micro-dot will have significant differences when it located in a steep dose gradient region compared to when it is placed in a flat dose distribution region. As a consequence of the relatively large surface area of each OSL detector the error due to the patient setup precision becomes more important when doing clinical measurements.

My experimental results show that uncertainties were mostly caused by setup errors. From the transverse, sagital and coronal views of the three clinical IMRT plans the dose distribution along the longitudinal direction in nasopharynx case and the dose distribution along the vertical direction in prostate case showed the largest variations due to positional changes. The OSL measurements in the steep dose gradient region showed a bigger dose difference between the planned (TPS) and the measured (OSL) doses.

8.6 Conclusion

In conclusion, the OSL system tested can be used in radiotherapy dosimetry for both point dose monitoring and isodose verification of 3DCRT and IMRT plans if they are carefully calibrated and carefully positioned. The results of this study show that in a high dose region the overall discrepancy of OSL measurements is within 5% compared to the TPS data for the three clinical cases. When OSLD measured dose in high dose gradient regions a higher discrepancy to TPS data can be expected. However, as this accuracy is competitive to TLDs, and due to OSL's low cost, simple handling and fast processing, OSL can become a viable alternate dosimetric technique for radiotherapy quality assurance (QA) and quality control (QC).

Chapter 9 Preliminary Study of OSL Used for Patient Skin Exit Dosimetry in Megavoltage X-ray beams

9.1 Introduction

Patient exit dose measurements and estimates play a very important role in evaluating the dose actually delivered to patients receiving radiation treatments.

When a human body or a phantom receives radiation the radiation dose or dose-rate in the human body or phantom will change along with the depth. The following factors may contribute to these changes: radiation beam energy, tissue thickness or depth, field size, distance away from the source such as SSD, and the beam collimating (or collimator) system, patient skin dose (entrance or exit dose), etc.

The exit dose measurement is more complicated and involves the concept of a build-down. The build-down region at the exit side of the patient is caused by a lack of backscatter radiation from the air behind the patient (van Dan and Marinello, 2006). This lack of backscatter concerns secondary electrons and photons. The lack of electron backscatter causes a build-down of the dose only in the latter few millimetres in front of the exit surface of the patient. The lack of photon backscatter influences a much deeper region and increases as a function of field size. The Markus ion chamber is mostly influenced by a lack of photon back scatter. However, OSLs, which are similar to a TLDs, may be influenced by the lack of secondary back scatter (Kron and Ostwald, 1995).

Various studies of exit dose measurement have been reviewed in chapter 5. In this Chapter the use of OSLs as a dosimetric tool for measuring skin exit dose in megavoltage x-ray beams is investigated, particularly, for detecting the density inserts in a phantom (e.g. tumour or tissues in the human body) through exit dose measurements. The characteristics of whether a phantom containing a range of inserts with different densities and dimensions can be used for exit dose measurements were initially studied using a Markus ion-chamber before comparison was made with OSL dosimeters, although the backscatter effects from the rear wall of such an ionization chamber could not be removed (it is part of the chamber's construction).

For normal measurements a further back scatter thickness material is usually needed to add to the patient's skin. That presents no problem for an isocenter dose

check, but it is not practical for exit dose measurements as the thickness of the added back scatter material beyond the patient's skin is more than 2cm. The purpose of this study is to analyse dose response differences when varying amounts of back scatter material are added to the patient's skin.

There are several parameters which were likely to influence the response of an exit dosimeter. Calculation of expected doses at the patient surface can be very difficult due to the dose build-up conditions, the scattered radiation from shielding, and the non-uniformity in patient's contour.

The objective of this study focused on further the exploring the possible of using OSL dosimeters (OSLDs) with a MicroStar reader as a dosimetry tool for patient skin exit dose measurement (exit dosimetry). As this is a relatively new technology, it is important to compare the results with those of existing standards for radiotherapy exit dose measurement, such as the ion chamber.

For these experiments an in-house manufactured phantom was developed. This phantom contains inserts with different densities and sizes to simulate different tissue heterogeneity (to assess relative electron density), a placement for holding the Markus chamber and a placement for holding the OSLDs.

This study will investigate the following:

- Calculating the relative electron density of the phantom and tissue equivalent inserts from the exit dose
- Calculating the equivalent depth of the phantom and tissue materials and determining the exit dose
- Correction for the heterogeneity of the tissue material inserts in the phantom
- calibration of the OSL dosimeter used for the measurements of exit dose
- A comparison between exit doses measured by OSLs and those measured by the Markus ion-chamber

The steps used in this experiment to assess OSL use for exit dose measurement are: 1) Markus ion-chamber measurement to investigate the factors that may affect the skin exit dose measurement; 2) OSLD exit dose measurement following similar experimental procedures as those of the Markus ion-chamber in "1"; and 3) a comparison of measurement results from OSLDs and from the Markus ion chamber.

9.2 Instrumentation

9.2.1 Standard electron density phantom

A CIRS M062 (Computerized Imaging Reference Systems, Inc. Norfolk, VA,USA) Electron Density Phantom(Figure 9.1) was used to calibrate the density of the in-house made phantom. This CIRS M062 phantom is designed to determine the precise relationship of Computed Tomography (CT) numbers, in Hounsfield units (HU), to physical density and electron density with various known substitute tissue equivalent materials, which are made of proprietary epoxy resin. For my experiments, eight (8) different tissue inserts and a syringe plug were used that include: Lung (Inhale), Lung (Exhale), Adipose, Breast (50/50), Muscle, Liver, Trabecular Bone, Dense Bone (800mg/cc), and Syringe H_20. Their physical density and the relative electronic density (RED) values were given by the manufacturer.

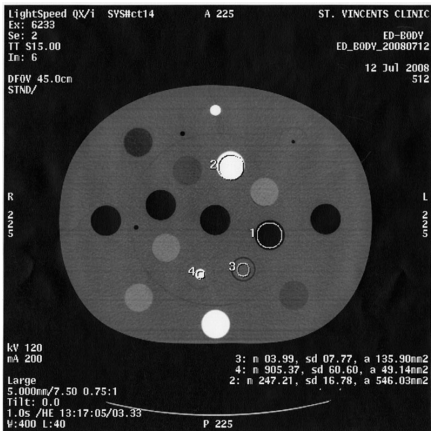

Figure 9.1 CT image of the CIRS Phantom

9.2.2 In-house phantom

An in-house manufactured phantom was used for the subsequent experiments to investigate the effect of inserts of different sizes and different densities inserted into the phantom. The phantom consists of three parts: main body, two special placements (one for the Markus ion-chamber and one for the dot OSLD) , and various density or size inserts. The main body of this phantom is made of water equivalent material (Perspex) with dimensions of 20cm (width) x 20 cm (height) x 18 cm (depth) sliced in different thicknesses. More slices of various thicknesses can be

added as required. Two special placements were made of the same material an d served to house the PTW Markus Ion-chamber and OSLD. The inserts had various densities to simulate various tissues or tumours. The dimensions of the tissue equivalent material inserts are 5cm (width) x 5cm (height) x 6cm (depth) or 5cm (width) x 7.5 cm (height) x 6 cm (depth). Figure 9.2 gives a schematic view of the phantom with an ion-chamber placement. The densities of these materials were calculated by using CT software. It should be noted that a 0.3cm thick dental modelling wax was used to fit the 6cm depth of sample 1.

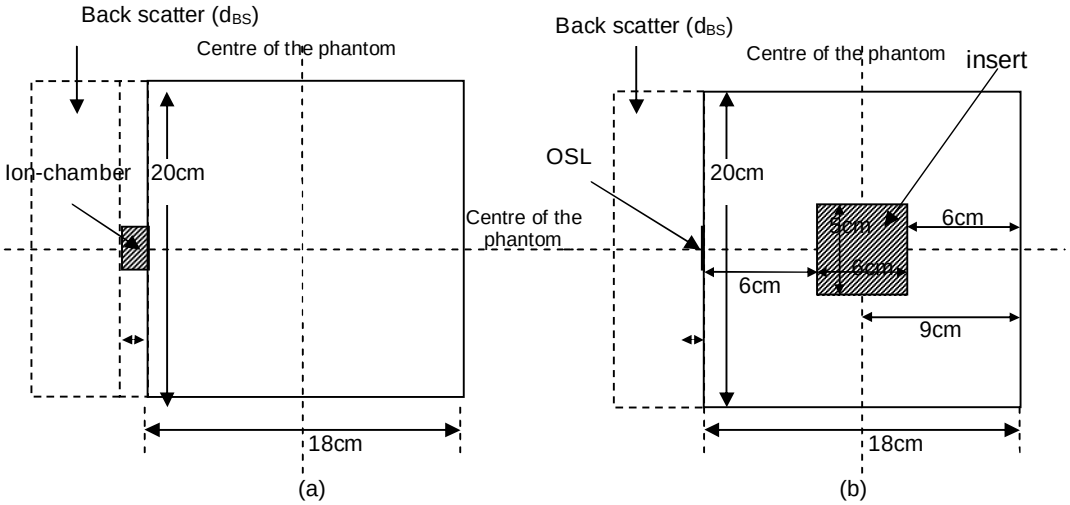

Figure 9.2 Coronal view of the in-house phantom (a) without insert and PTW Markus ion-chamber placement; (b) with inserts and OSL placement.

9.2.3 Computer Tomography (CT) Scanner

The phantoms used in this study were scanned with a GE LightSpeed CT scanner (GE Medical Systems, Milwaukee WI, USA). The GE LightSpeed CT has a 80cm diameter bore and can perform 4-slice helical scanning by using a fast rotation speed. The CT generates cross-sectional two-dimensional images of the body showing the various tissue densities. Images are acquired by rapid rotation of the X-ray tube 360º around the body. Using various setup positions the phantoms were scanned using identical scan protocols to ensure consistency (120kV, 200mA).

9.2.4 Radiation source

In this study OSL dosimeters were irradiated with 6 MV and 10 MV X-rays using a Siemens Primus Linear Accelerator equipped with a 58 multi-leaf collimator. The

linear accelerator's output in monitor unit per cGy and had been calibrated according to the absorbed dose calibration protocol, taken from IAEA TRS-398, in water a depth of d_{max}. The monitor units per cGy for a 10x10cm beam size at a source-to-surface distance (SSD) of 100cm was set to 1cGy/1MU.

9.2.5 PTW-Freiburg Advanced Markus Ion-Chamber and Fluke Advanced Therapy Dosimeter Electrometer

A PTW Markus parallel plate ion-chamber, Model 34045 (PTW-FREIBURG, Germany) associated with a Fluke Model 35040 Advanced Therapy Dosimeter Electrometer (Fluke Biomedical, NY, USA) were used as the primary dosimeters throughout the experiment.

The Markus chamber (Figure 9.3) is a vented plane-parallel electron ion chamber with a wide guard ring. It contains a chamber body and a water protection cap. The protective cap contains 0.87 mm of PMMA, 0,.40 mm of air, and a 0.03 mm polyethylene membrane (PE). The real (physical) effective measurement point is 1.06mm below the protective cap. The chamber sensitive volume is 0.02cm^3. Energy response is flat within the nominal energy range from 2 MeV to 45 MeV.

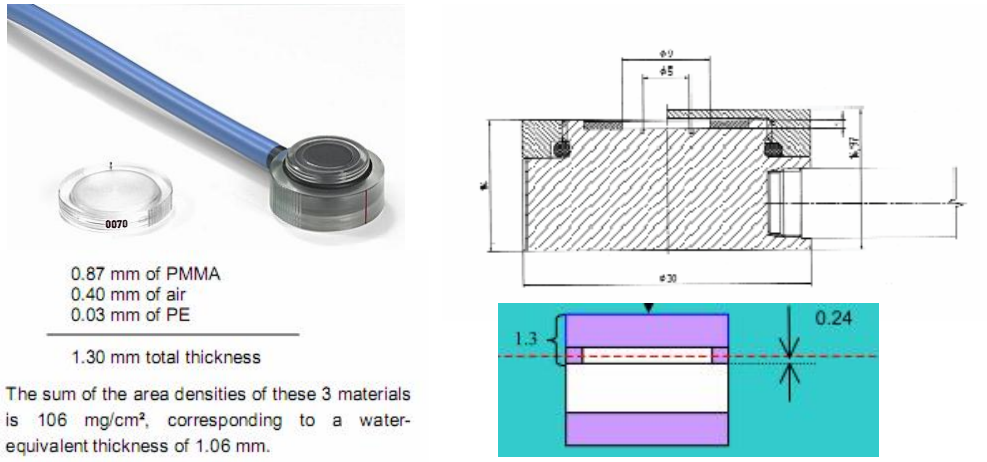

Figure 9.3 PTW Advanced Markus ion-chamber (From PTW website)

The Fluke Model 35040 Advanced Therapy Dosimeter electrometer is designed for calibration dosimetry of therapeutic radiation treatment machines and features good long-term stability (error of approximately 0.1% over five years), uncorrected

leakage of less than 10 fA over a wide temperature range, and a maximum non-linear variation from a straight line of 0.1% for all charge and current ranges.

Output readings of the Markus chamber were taken repeatedly three (3) times using the Fluke Electrometer for the selected five square fields (3x3, 5x5, 10x10, 15x15, and 20x20cm^2). Temperature and pressure were accounted for with an air density correction.

9.2.6 Optical Stimulated Luminescence (OSL) Dosimetry system

The InLight^{TM} Dot dosimeter (Figure 6.2) used in this study is comprised of one optically stimulated luminescence detector (OSLD) element. The detector is based on a thin layer of carbon-doped aluminium oxide, Al_2O_3:C powder deposited onto a clear polyester film as described in Chapter 4. Each detector element is a 7 mm diameter disc which is 0.3 mm thick. The OSLDs were read using a InLight^{TM} MicroStar reader (Figure 6.3) (Landauer, Inc., USA) which was described in detail in and chapter 6.

The sensitivity of the OSLDs and the calibration factor can be pre-loaded and can be converted to counts per mrem. However in this study one only use the raw reader counts that were then converted manually to the dose by using calibration factors derived experimentally.

As described before, the sensitivity of the detector varies with each package from the manufacturer. OSLDs were chosen from the same package to avoid this uncertainty. The previous experimental results demonstrated that there is an approximately 2% variation of OSLD sensitivity when they come from the same package (Table 7.2).

9.3 Experiment preparation: Converting CT number to density

To achieve the objective of using OSL dosimeters (OSLDs) with a MicroStar reader as a dosimetry tool for skin exit dose measurement (exit dosimetry) an in-house manufactured phantom was developed. This phantom contains inserts of different densities and sizes (to simulate tissue heterogeneity), a placement for holding a Markus chamber and an OSLD.

The goal of this experiment is to calculate the relative electron density of the in-house phantom and it's tissue equivalent inserts for further use in effective

pathlength (EPL) correction.

CT slices contain direct information that can be converted to tissue density (Munzenrider *et al*., 1977; Parker *et al.,* 1979; Geise and McCullough 1977; Henson and Fox, 1984; Seco and Evans 2006).

The density (ρ) of a material is defined as its mass per unit volume, also called mass density or physical density. The electron density (ρ_e) of a material, in quantum-mechanical effects, is defined as the probability of an electron in a unit volume.

The ability of specific tissue to attenuate radiation can be calculated from the CT numbers (in Hounsfield units) . A detector array located on the CT rotating gantry measures the radiation intensity transmitted through a body or a tissue. Each CT slice consists of a matrix of picture elements (pixels) which corresponds to a matrix of volume elements (voxels) in the body or tissue. For known tissue physical density and known scanning radiation (KV & mA), one can calibrate the pixel's value in CT numbers and then from that one can establish the relationship between the tissue's density and the CT number. In this study the physical density and relative electronic density (RED) derived from my experiments was used to calculate the equivalent thickness of the tissue inserts in the two phantoms used. RED is defined as the electron density relative to water (H_2O).

Hounsfield units (HUs) are a scale of arbitrary units used to compare CT number to the linear attenuation value. The CT number of any pixel is based on the average of all the average linear attenuation within the corresponding voxel. The HU of Water is assigned to be HU_{Water} *=0*, of air HU_{air} *= -1000*, and HU for bone depends on kVp. The range of CT numbers of various typical tissues or materials showed in Table 9.1.

Table 9.1 CT numbers of various typical tissues or materials

Tissue	CT Number (HU)
Bone	+ 400 ~ +1000
Soft tissue	+40 ~ +80
Water	0
Fat	-60 ~ -100
Lung	-400~ -60
Air	-1000

9.3.1 Methodology

To convert the CT number to electron density, the standard CIRS M062 Electron Density Phantom with tissue inserts was scanned on GE CT. The physical density and relative electronic density values for the tissue inserts taken from the manufacturer's data sheets were plotted against the relevant CT numbers taken from the CT software.

The in-house phantom (made of polyethylene) with three tissue equivalent inserts was scanned using the same protocol. Based on standard CT calibration curves the CT numbers of the slab phantom and inserts were converted to the mass densities and electron densities through interpolation.

9.3.2 Results

Figure 9.4 shows the standard CT calibration curve of the physical density and relative electron density vs. CT numbers that were obtained from the standard CIRS M062 phantom with known tissue equivalent material inserts. Both curves were normalized to the density of water. The corresponding data is shown in table 9.3.

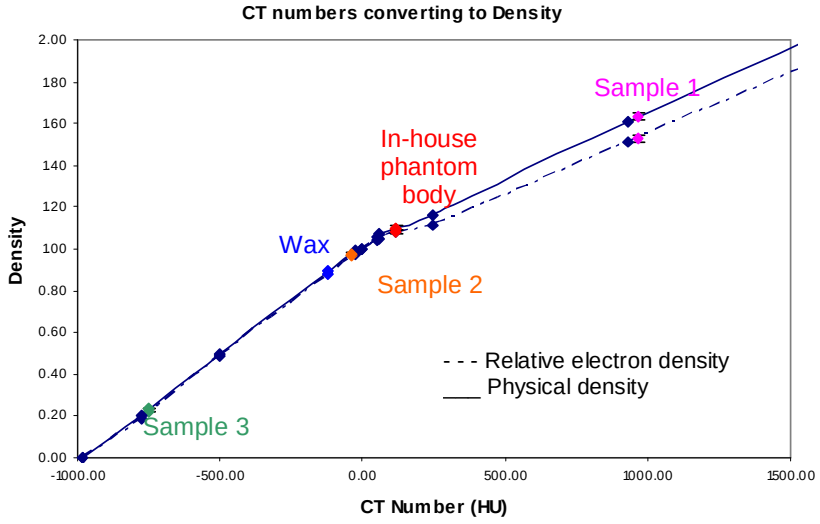

Figure 9.4 CT-to-mass density physical density curve and CT-to-electron density curve of a standard CIRS M062 phantom with associated tissue equivalent inserts (dark blue) and an in-house phantom (red) associated with three samples (in different colors) through interpolation, with added ±1% error bars. Both curves are normalized to the mass density physical density and electron density of water, respectively.

Derived through interpolation the mass densities and electron densities of the in-house phantom and its inserts are shown in the Figure 9.4. The data is shown in Table 9.2.

Table 9.2: CT HU value (120kV, 200mA) vs. Physical density and Electron Density

Tissue	CT Number	Physical Density	Relative Electron Density
Air	-982.00	0	0.013
Lung (Inhale)	-773.00	0.20	0.190
Lung (Exhale)	-502.00	0.50	0.489
Breast(50/50)	-28.00	0.99	0.976
Syringe H_20	0.00	1.00	1.000
Muscle	49.00	1.06	1.043
Liver	56.00	1.07	1.052
Polystyrene	**118.00**	**1.10**	**1.080**
Trabecular Bone	249.00	1.16	1.117
Dense Bone (800mg/cc)	930.00	1.61	1.512
	10000.00	7.240	6.800
Sample 1	**966.00**	**1.635**	**1.530**
Sample 2	**-37.00**	**0.980**	**0.970**
Sample 3	**-750.00**	**0.235**	**0.220**
Dental Modelling Wax	-120.00	**0.895**	**0.880**

9.4 Effective path-length (EPL) correction

The following experiments in my study used RED to do the heterogeneity density correction by using equivalent primary beam effective path-length (EPL) (Ahnesjö and Aspradakis, 1999). The study from Seco and Evans (2006) suggested that the electron density rather than physical density should be taken into account in photon dose calculations. They compared the EPL, based on mass-density value (ρ), to the EPL based on electron-density value (ρ_e), and found that the mass-density scaling method gave an overestimate of the primary photon fluencies for various tissues in the human body and in water equivalent materials, especially for bone and air, having differences of 6~7% and 10%, respectively. But when pair-production was considered, the extended electron-scaling method provided estimates of the primary photon fluence with differences of 1~2%.

The EPL heterogeneity correction method is originally from the O'Connor theorem (O' Connor, 1957). The O'Connor theorem states that "*the ratio of the secondary*

scattered photon fluence to that of primary photon fluence is constant in two media provided all geometric distances are scaled inversely with mass density".

Table 9.3 Calculated equivalent thicknesses of phantom and tissue equivalent inserts

Material	Electron Density Relative to H_2O *(RED)*	Geometric Thickness T_g (cm)	Equivalent Thickness T_e (cm)	Total Equivalent Measurement Depth(cm)
Phantom material (build-up)	1.08	1.3	1.40	1.50
	1.08	5.0	5.40	5.50
	1.08	2.3	2.48	2.58
	1.08	6.0	6.48	6.58
Phantom material (back scatter)	1.08	5.5	5.94	
	1.08	4.5	4.86	
	1.08	3.5	3.78	
	1.08	2.5	2.70	
	1.08	1.5	1.62	
	1.08	0.5	0.54	
Sample 1	0.22	5.7	1.32	
Sample 2	0.97	6.0	5.82	
Sample 3	1.53	6.0	9.18	
Dental Modelling Wax	0.895	0.3	0.269	
Phantom 2 combination (with sample 1)	6cm(Perspex)+5.7cm(Sample)+0.3cm(wax)+6cm(Perspex)			
		18	14.48	14.58
Phantom 3 combination (with sample 2)	6cmerspex)+6cm(Sample)+6cm(Perspex)			
		18	18.78	18.88
Phantom 1 combination	Markus: 18cm(Perspex) +0.106cm OSL: 18cm(Perspex)+0.10cm			
		18	19.44	19.54
Phantom 4 combination (with sample 3)	Markus: 6(Perspex)+6(Sample)+6(Perspex)+0.106cm OSL: 6(Perspex)+6(Sample)+6(Perspex)+0.10cm			
		18	22.14	22.24

Table 9.3 shows the calculated equivalent thickness of the phantom with different tissue equivalent inserts. The following four named phantom combinations for subsequent experiments were used:

- Phantom 1: in-house manufactured homogeneous phantom with RED=1.08 with an equivalent thickness of 19.54cm.
- Phantom 2: in-house manufactured phantom with 5cm (width) x 5cm (height) x 6cm (depth) tissue equivalent material with RED=0.22 with an equivalent thickness of 14.58cm.

- Phantom 3: in-house manufactured phantom with 5cm (width) x 5cm (height) x 6cm (depth) tissue equivalent material with RED=0.97 with an equivalent thickness of 18.88cm.
- Phantom 4: in-house manufactured phantom with 5cm (width) x 5cm (height) x 6cm (depth) tissue equivalent material with RED=1.53 with an equivalent thickness of 22.24cm.

PTW Markus effective measurement depth is 1.06mm which is equivalent to an OSL effective measurement depth of 1.0mm. Consequently both were assumed to have a 1.0mm effective measurement depth.

9.5 Verification in-house phantom using PTW Markus Ion-Chamber

The goal of this experiment was to use Markus ion-chamber measurements to confirm the calculation of the relative electron density of the in-house phantom and inserts, and to permit the calculation of equivalent depth using the EPL correction method. Using the ion chamber provides base-line data by an accepted standard which can later be compared to the results from the OSLDs.

9.5.1 PDD, TPR and TMR

Percentage depth dose (PDD) is defined as the ratio percentage of absorbed dose rate at a point to the absorbed dose rate at the maximum build-up depth on the central axis. The PDD data used in this experiment were measured in water by using a CC04 Ionization Chamber connected to a CU500E Electrometer and OmniPro™-Accept system (version 6.5) associated with a Blue phantom (Scanditronix-Wellhofer, IBA Advanced Radiotherapy, Germany). The source-to-surface distance (SSD) is100cm. As PDD varies with distance from the radiation source it is inconvenient to use PDD for direct reconstruction of dose distributions.

As an alterative, Tissue-Phantom Ratio (TPR) can be used as it is independent of SSD. The TPR is defined as the ratio percentage of the absorbed dose-rate on the central axis at a depth to that at a reference depth on the central axis the same distance away from the source, but with the water surface of the phantom moving up and down so that the ionization chamber is at the specified reference depth (Larzmark et al., 1965). When the reference depth for defining TPR is taken to the maximum build-up depth, the TPR becomes Tissue-Maximum Ratio (TMR). The

TPR data used in this test were converted from PDD data by using OmniPro^{TM}-Accept system (version 6.5) software.

In subsequent experiments the depth dose data was mostly taken from clinical TMR data derived from Linear Accelerator commissioning PDD data.

A tissue heterogeneity correction factor (THCF) describes the dose or dose rate ratio measured for heterogeneous compared to homogenous geometry. The EPL method (Ahnesjö and Aspradakis, 1999) combined with relative electron density (Seco and Evans, 2006) was used to calculate the heterogeneity correction factor.

9.5.2 Methodology

Figure 9.5 shows the calibration setup for a PTW Markus ion-chamber with a vented sensitive volume of 0.02 cm^3. Using SAD technique, the Markus Ion-chamber was inserted in the placement and the effective measurement point was set to the isocentre 100cm from the source. Build-up material with a thickness of d_{UP} was added to the effective measurement points, which yielded an equivalent thickness of 1.5 cm to match the d_{max} of the 6 MV photon beam. In addition a 5cm thickness slab (equivalent thickness 5.5cm) was added downstream along the beam's central axis for the measurement. A total back scatter (d_{BS}) thickness of 5cm from the effective measurement point where the chamber located was added to avoid backscatter influence to the chamber.

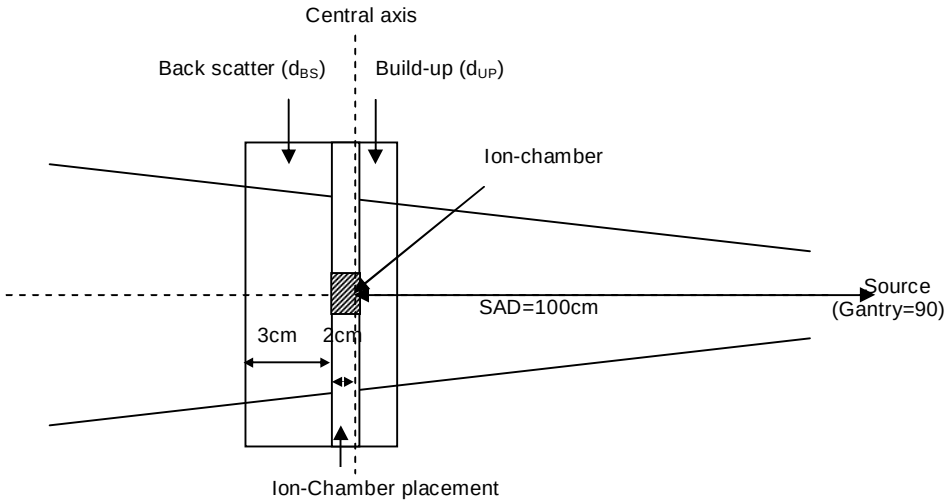

Figure 9.5 Schematic of PTW Markus Ion-chamber calibrations

All measurements were taken by delivering 100MU. The output readings from the ionization chamber were taken 3 times, using a Fluke Electrometer, for each of the five square fields (3x3, 5x5, 10x10, 15x15, and 20x20cm^2). The measured ratio (Ratio) between build-up d_{max} and d_5 was calculated. The ratio was compared to the clinical depth dose (TMR) data taken from the linear accelerator commissioning data, which had been measured in a water phantom using a CC04 cylindrical ionisation chamber under full backscatter conditions. The differences between measurements and depth dose values were calculated.

9.5.3 Results

Table 9.4 shows the excellent accuracy that the PTW Markus Ion-chamber and Fluke Electrometer achieved. As the percentage differences between the TMR values and the measurements for five(5) fields are all less than ±0.2%, the equivalent thickness of the phantom can be used for this study.

Table 9.4 Measurement data for the Verification and Calibration of a PTW Markus Ion-Chamber. The Equivalent thickness calculations of the phantom were made using the EPL method with an electron density of 1.08 for this phantom. The TMR values were taken from commissioning data of a Siemens 6MV ARTISTE. The monitor units are nC/100MU. The differences between the OSL and a TMR values are compared.

6MV-X	Square Field Size				
	3x3	**5x5**	**10x10**	**15x15**	**20x20**
Meas. (d_{max})	0.6941	0.7213	0.7619	0.7778	0.7915
Meas. (d_5)	0.6060	0.6433	0.6951	0.7172	0.7366
Cal. Ratio (d_5 / d_{max})	0.8731	0.8919	0.9123	0.9221	0.9306
Depth dose (d_5)	0.8734	0.8902	0.9120	0.9227	0.9288
% Diff (Measurement vs. TMR)	**-0.034%**	**0.190%**	**0.038%**	**-0.066%**	**0.190%**

10MV-X	Square Field Size				
	3x3	**5x5**	**10x10**	**15x15**	**20x20**
Meas. (d_{max})	0.6934	0.7315	0.7756	0.7972	0.8106
Meas. (d_5)	0.6469	0.6920	0.7390	0.7614	0.7760
Cal. Ratio (d_5 / d_{max})	0.9330	0.9459	0.9528	0.9551	0.9573
TMR (d_5)	0.9349	0.9457	0.9526	0.9536	0.9555
% Diff (Measurement vs. TMR)	**-0.201%**	**0.023%**	**0.025%**	**0.154%**	**0.193%**

9.6 Verification an OSL dosimetry system in in-house phantom

The previous experiments confirmed the calculation of the relative electron density of the in-house phantom and inserts with the EPL correction method using a Markus ion-chamber. The goal of this experiment was to verify OSL system (OSLD and reader) performance using the in-house phantom .

9.6.1 Methodology

Figure 9.6 shows the calibration setup for an OSL dosimeter that is similar to the setup for the calibration of an ionization chamber described above. The OSL was inserted into the OSL placement (2mm thickness) which was put at the effective measurement point, with the centre of the OSL disc set to the isocentre 100cm away from the source. The build-up material, with a thickness of $d_{UP,}$ was added to the effective measurement points, which yielded an equivalent thickness of 1.5 cm (EPL approximation based on ρ_e) to match the d_{max} of a 6 MV photon beam. In addition a slab of 5cm thickness (equivalent thickness 5.5cm) was added . The total back scatter (d_{BS}) thickness of 5cm from the effective measurement point where the OSL located was added to avoid the influence of backscatter to the OSL.

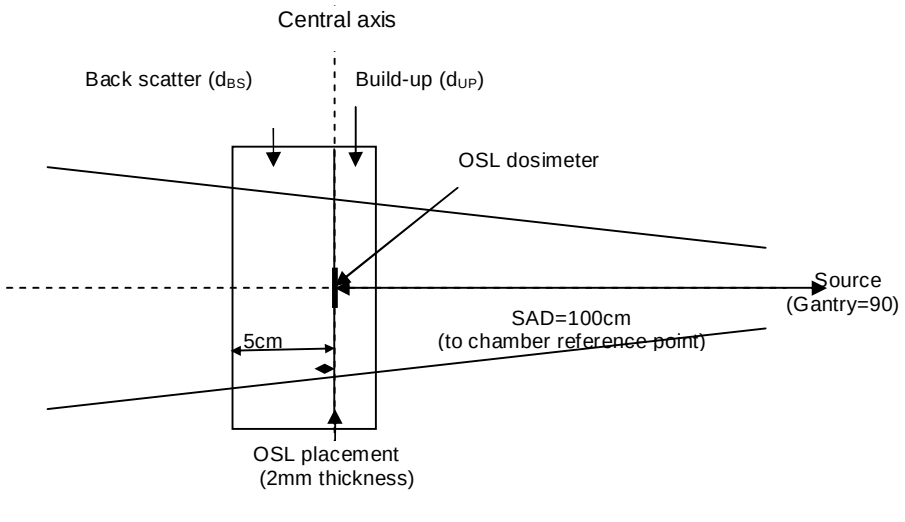

Figure 9.6 Schematic of OSL dosimeter calibration

All measurements were taken by delivering 100MU with 6MV x-rays for the selected square fields of 3x3 cm^2, 5x5 cm^2, 10x10 cm^2 and 15x15 cm^2. A total of thirty (30)

OSLDs were used in this experiment. Each OSLD was irradiated at d_{max} and d_5. The output readings were taken 10 times using a MicroStar reader. The measured ratio (*Ratio*) between build-up d_5 and d_{max} was calculated and compared to the TMR values from the Linear Accelerator commissioning data.

9.6.2 Results

Table 9.5 to table 9.8 show the raw OSL measurement data for the selected fields of 3x3cm^2, 5x 5cm^2, 10x10cm^2 and 15x15cm^2. Table 9.9 summarizes the results. OSL results compared to Linear Accelerator commissioning data were as follows:

- OSLDs show higher response in d_5/d_{max} than that of TMR values for all four field sizes.
- OSLs show a 1% higher value than the reference value for the field sizes 3x3cm^2, 5x5cm^2, and 10x10cm^2. There is an approximate 2% difference between the readings of the eight (8) individual OSLDs.
- OSL result for the 15x15cm^2 field size shows a value that is 2% higher than the TMR. There is approximately a 1% difference between the readings of the six (6) individual OSLDs.
- Compared with the results measured by a PTW Markus Ion-chamber from table 9.5, OSLs show results that are slightly higher than those of the chamber. However the results using OSLs are still suitable for clinical use with a 3% of maximum variation from the ion chamber.
- OSL result for the 15x15cm2 field size shows a value that is 2% higher than the TMR. There is approximately a 1% difference between the readings of the six (6) individual OSLDs.
- Compared with the results measured by a PTW Markus Ion-chamber from table 9.5, OSLs show results that are slightly higher than those of the chamber. However the results using OSLs are still suitable for clinical use with a 3% of maximum variation from the ion chamber.

Table 9.5 Measurement data for the Verification and Calibration of OSL dosimeters (1). 100MU was delivered to a 3x3 cm^2 field at isocentre. The calibration depth was set to an equivalent thickness of 5.5 cm (d_5). The TMR values were taken from a standard TMR table of a 6MV Siemens ARTISTE. 100MU was delivered. The SD_1 is the standard deviation of readings of each OSLD repeated 10 times. The SD_2 is the standard deviation of 8 OSL dosimeters.

	(1)	(2)	(3)	(4)	(5)	(6)
OSLD No.	Raw data at dmax d_{max} (Mean±SD_1)	Raw data at d_5 (Mean±SD_1)	Normalized to dmax d_5 / d_{max} (1)/(2)	TMR	Diff (3) – (4)	%Diff $\frac{(5)}{100}$
1	30995±334	27757±225	0.8955	0.8697	0.026	2.58%
2	32304±281	27941±183	0.8649	0.8697	-0.005	-0.48%
3	31728±200	28486±266	0.8978	0.8697	0.028	2.81%
4	30890±146	26571±164	0.8602	0.8697	-0.010	-0.95%
5	30444±337	27200±241	0.8935	0.8697	0.024	2.38%
6	31203±266	26950±229	0.8637	0.8697	-0.006	-0.60%
7	31835±158	27651±334	0.8686	0.8697	-0.001	-0.11%
8	29952±163	25562±164	0.8534	0.8697	-0.016	-1.63%
Mean±SD_2	**31169±664**	**27265±807**	**0.8747±0.198**	**0.8697**	**0.005**	**0.50%**
Minimum					**-0.016**	**-1.63%**
Maximum					**0.028**	**2.81%**

Table 9.6 Measurement data for the Verification and Calibration of OSL dosimeters (2). 100MU delivered to a 5x5 cm^2 field at isocentre. The calibration depth is set to an equivalent thickness of 5.5 cm (d_5) . The TMR values were taken from a standard TMR table of a 6MV Siemens ARTISTE. 100MU was delivered. The SD_1 is the standard deviation of readings of each OSLD repeated 10 times. The SD_2 is the standard deviation of 8 OSL dosimeters.

	(1)	(2)	(3)	(4)	(5)	(6)
OSLD No.	Raw data at dmax d_{max} (Mean±SD_1)	Raw data at d_5 (Mean±SD_1)	Normalized to dmax d_5 / d_{max} (1)/(2)	TMR value	Diff (3) – (4)	%Diff $\frac{(5)}{100}$
1	32603±149	29597±204	0.9078	0.8873	0.020	2.05%
2	32682±223	29671±273	0.9079	0.8873	0.021	2.06%
3	33507±151	29553±268	0.8820	0.8873	-0.005	-0.53%
4	31310±173	28122±234	0.8982	0.8873	0.011	1.09%
5	32020±283	29089±353	0.9085	0.8873	0.021	2.12%
6	32194±325	28049±325	0.8713	0.8873	-0.016	-1.60%
7	32116±156	28558±156	0.8892	0.8873	0.002	0.19%
8	32275±335	29223±335	0.9054	0.8873	0.018	1.81%
Mean±SD_2	**32338±631**	**28983±659**	**0.8963±0.0141**	**0.8873**	**0.009**	**0.90%**
Minimum					**- 0.016**	**-1.60%**
Maximum					**0.021**	**2.12%**

Table 9.7 Measurement data for Verification and Calibration of OSL dosimeters (2). 100MU was delivered to a 10 x10 cm^2 field at isocentre. The calibration depths were set to a equivalent thickness of 5.5 cm (d_5). The TMR values were taken from a standard TMR table of a 6MV Siemens ARTISTE. 100MU was delivered. The SD_1 is the standard deviation of readings of each OSLD repeated 10 times . The SD_2 is the standard deviation of 8 OSL dosimeters.

	(1)	(2)	(3)	(4)	(5)	(6)
OSLD No.	Raw data at dmax d_{max} (Mean±SD_1)	Raw data at d_5 (Mean±SD_1)	Normalized to dmax d_5 / d_{max} (1)/(2)	TMR value	Diff (3) – (4)	%Diff $\frac{(5)}{100}$
1	34021±133	30959±166	0.9100	0.9086	0.001	0.14%
2	33510±157	30706±151	0.9163	0.9086	0.008	0.77%
3	34260±152	31259±296	0.9124	0.9086	0.004	0.38%
4	33539±168	30549±175	0.9108	0.9086	0.002	0.22%
5	33058±114	30336±187	0.9177	0.9086	0.009	0.91%
6	32363±145	30034±187	0.9281	0.9086	0.019	1.95%
7	33486±246	30423±173	0.9085	0.9086	0.000	-0.01%
8	33296±204	30606±178	0.9192	0.9086	0.011	1.06%
Mean±SD_2	**33442±369**	**30609±310**	**0.9154±0.0098**	**0.9086**	**0.0068**	**0.75%**
Minimum					**-0.000**	**-0.01%**
Maximum					**0.019**	**1.95%**

Table 9.8 Measurement data for Verification and Calibration of OSL dosimeters (4). 100MU was delivered to a 15x15 cm^2 field at isocentre. The calibration depths were set to a equivalent thickness of 5.5 cm (d_5). The TMR values were taken from a standard TMR table of a 6MV Siemens ARTISTE. 100MU was delivered. The SD_1 is the standard deviation of readings of each OSLD repeated 10 times. The SD_2 is the standard deviation of 8 OSL dosimeters.

	(1)	(2)	(3)	(4)	(5)	(6)
OSLD No.	Raw data at dmax d_{max} (Mean±SD_1)	Raw data at d_5 (Mean±SD_1)	Normalized to dmax d_5 / d_{max} (1)/(2)	TMR value	Diff (3) – (4)	%Diff $\frac{(5)}{100}$
1	36383±376	34329±239	0.9435	0.9199	0.024	2.36%
2	35392±203	33197±297	0.9380	0.9199	0.018	1.81%
3	35887±371	33819±383	0.9424	0.9199	0.022	2.25%
4	35724±213	33339±204	0.9332	0.9199	0.013	1.33%
5	36883±263	34704±372	0.9409	0.9199	0.021	2.10%
6	36128±220	33805±159	0.9357	0.9199	0.016	1.58%
Mean±SD_2	**36066±496**	**33866±567**	**0.9390±0.0040**	**0.9199**	**0.019**	**2.07%**
Minimum					**0.013**	**1.33%**
Maximum					**0.024**	**2.36%**

Table 9.9 Summary of the Verification and Calibration of OSLDs. The data is average data from each field size from table 9.6 to table 9.9.

	Square Field Size (cm^2)			
	3x3	**5x5**	**10x10**	**15x15**
Meas. (d_{max})	31169±664	32338±631	33442±369	36066±496
Meas. (d_5)	27265±807	28983±659	30609±310	33866±567
Cal. Ratio (d_5/d_{max})	0.8747±0.0198	0.8963±0.0141	0.9154±0.0098	0.9357±0.0040
TMR value (d_5)	0.8697	0.8873	0.9086	0.9199
% Diff (Meas vs. TMR)	**0.50%±2.06%**	**0.90%±1.58%**	**0.75%±0.71%**	**2.07%±0.44%**

9.7 Summary of experiment

In this chapter one initially acquired the relative electron density of the in-house manufactured phantom by using a standard CIRS M062 CT calibration phantom. Secondly, we used the electron density and EPL method to calculate the equivalent thicknesses of the in-house made phantom. Thirdly, the PTW Markus ion-chamber was used to test the accuracy of the electron density calculation and to evaluate if OSL dosimeters could be used for my further experiments. Both measurement results using an ion-chamber and by using OSL dosimeters were compared with the clinical TMR data which was collected during the linear accelerator's commissioning. Finally it was found that the differences between reference TMR and that measured by an Ion-chamber for 5 field sizes at d_5 are all less then ±0.2%, while OSL dosimeters showed 1% higher for smaller field sizes of 3x3, 5x5, and 10x10cm^2, and up to 2% higher for a larger field size of 15x15cm^2.

Although the inaccuracy from using OSLs is slightly higher than that of an ion chamber, the results by using OSLs are still acceptable for clinical use, for example, for the verification of planning dose in physical treatment delivery and also to help to check the positioning accuracy of patient setup for treatment.

9.8 Exit dose dosimetry using Markus ion-chamber

Ion chambers are the current standard for absorbed dose measurements in radiotherapy. Consequently it is important to compare their results with those of OSLDs. In this experiment the Markus chamber was used: 1) to investigate the factors that may affect the skin exit dose measurement; 2) to measure exit dose data in identical or similar conditions to those measured with OSLDs.

In following sections (section 9.9~section 9.13)an ionisation chamber (Markus) was

used to investigate the factors that may affect the exit dose measurements.

In the experiments one studied the reduction rates for exit dose measurements in an inhomogeneous phantom with or without back scatter materials placed behind the ion chamber. Dose variations due to field size and beam energy were taken into account. The phantom size, density and the accuracy with which it is positioned may also cause the exit dose variations.

To investigate above-mentioned factors, the experiments were divided into three steps:

- Step one: Investigating the backscatter effects, of different back scatter thicknesses using a homogeneous phantom with heterogeneous inclusions, on the measurements of the exit dose. Two experiments were performed with the effective measurement point set at the isocentre or on the exit surface phantom while the isocentre is the centre of the phantom
- Step two: Determine the relationship between field sizes (ranging from $3x3cm^2$ to $20x20cm^2$) and energy (6MV and 10MV x-rays) for exit dose measurements. These experiments were only taken for putting the effective measurement point on the exit surface of the phantom.
- Step three: Comprehensive comparisons between the Markus measured and the data quoted from the standard depth dose data (Tissue-Maximum Ratio (TMR) in this case) acquired during linear accelerator commissioning.

In following section this ionisation chamber is used to investigate the factors that may affect the exit dose measurements.

These experiments studied the reduction rates for the exit dose measurements in inhomogeneous phantom with or without back scatter materials which was put behind the ion chamber. Field size and beam energy on the variations were also taken into account. The phantom size, density and its positioning accuracy may also cause the exit dose variations, etc..

To investigate above-mentioned factors, the experiments were divided into three steps:

- Step one: focuses on investigating the backscatter effect of different back scatter thickness coupled with a homogeneous phantom and heterogeneous inclusions on the measurements of the exit dose. Two experiments were

undertaken for the effective measurement position setting at the isocentre and on the exit phantom surface.

- Step two: develop a variation pattern vs. the field sizes (ranges from 3x3cm^2 to 20x20cm^2) and the energy (6MV and 10MV x-rays) for exit dose measurements. One experiment was only taken for putting the effective measurement position on the exit phantom surface.
- Step three: a comprehensive comparisons between the data measured and the data quoted from reference standard depth dose data (Tissue-Maximum Ratio (TMR) in this case) acquired during the machine commissioning.

9.9 Effect of back scatter thickness on the dose variations

This study focuses on investigating the backscatter effect of different back scatter thickness coupled with a homogeneous phantom and heterogeneous inserts. Experiments were performed to set the effective measurement point at the isocentre or on the exit surface of the phantom.

9.9.1 Markus Experiment 1: Measurement performed at isocentre in in-house homogenous phantom

The purpose of this study was to determine the influence of different back scatter thicknesses in a homogeneous phantom on the dose at the isocenter using Markus ion-chamber. The experiment was performed using a homogeneous solid water slab phantom.

9.9.1.1 Methodology

Figure 9.7 shows the setup of this experiment with the effective measurement point set at the isocentre. Using a source-axis-distance (SAD) technique, the Markus Ion-chamber was inserted in the placement with the thin window facing towards the target. The effective measurement point (1.06 mm away from the protective cap surface) was set to the isocentre 100cm from the source. The source-to-chamber effective measurement point distance (SCD) is 100cm. The 5.0cm thick fixed build-up material (d_{UP}) was added to the surface of the Markus chamber with a protective cap. The thickness of back scatter (d_{BS}) material varies from 5.5cm to 0cm for the chamber only. The Markus ion-chamber is in the special placement. It has no added build-down thickness but is surrounded by solid water. The thickness of the back

scatter (d_{BS}) material is 0, in other words the Markus ion-chamber is mounted to the surface of the phantom without being surrounded by solid water. The equivalent thickness of the back scatter material was calculated in section 9.4 and was shown in Table 9.3.

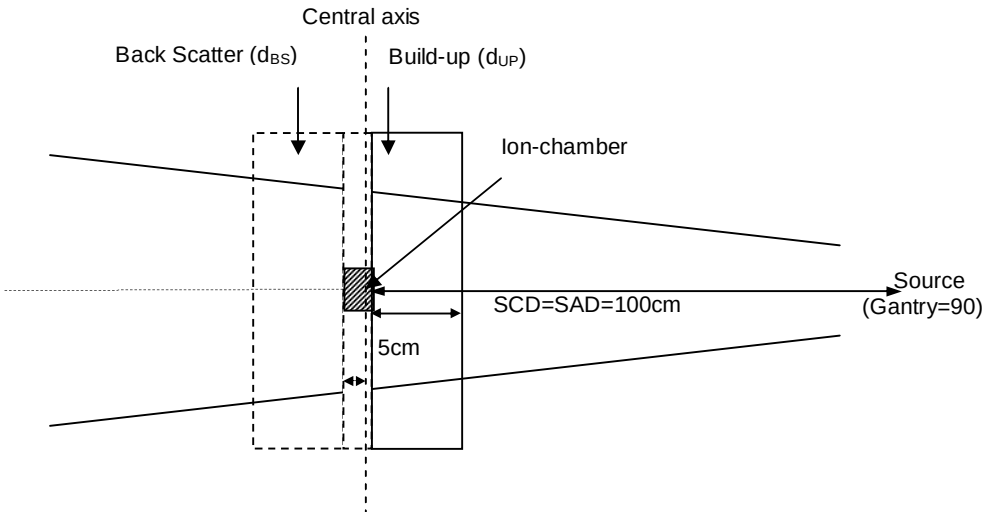

Figure 9.7 Schematic setup of Markus for back scatter thickness measurements with an effective measurement point at isocentre

All measurements were taken by delivering 100MU with 6MV and 10MV x-rays using a Siemens ARTISTE Linear Accelerator. The output readings were taken three (3) times using a Fluke Electrometer for the five selected square fields (3x3, 5x5, 10x10, 15x15, and 20x20cm^2). The output data from a 5.5cm back scatter thickness was set as the reference value to which the other readings were compared. The measured ratio (Reduction Ratio) is defined as the ratio of the readings of various back scatter thicknesses compared to the reading from the reference values with 5.5cm of backscatter. Temperature and pressure effects were accounted for.

9.9.1.2 Results

Figure 9.8 shows the raw measurement readings (nC/100MU) from the PTW Markus Ion-chamber. The mean raw readings for each field size with a back scatter thickness of 5.5cm (the effective back scatter thickness is 5.94cm) are used as the reference reading to which readings for other build down thickness are normalized. The percentage difference deviations are shown in Figure 9.9.

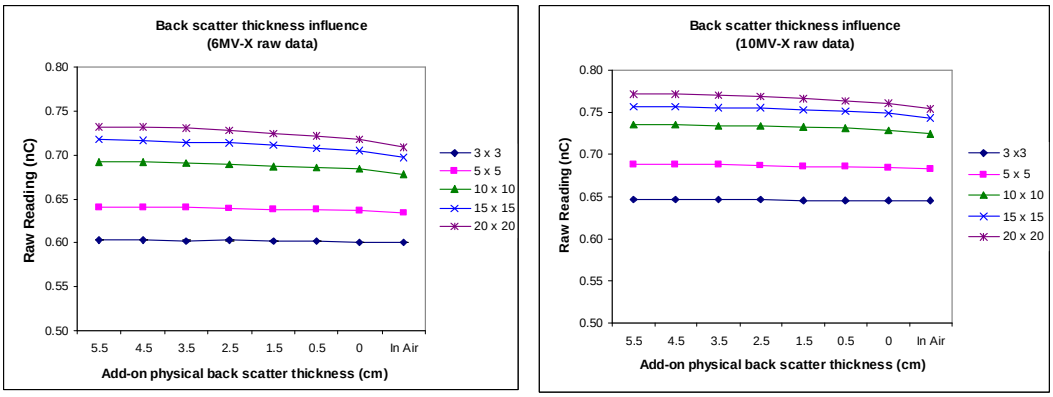

Figure 9.8 Markus Experiment 1 results (1): raw reading (nC) of a measurement point at isocentre in a homogeneous slab phantom using a PTW Markus Ion-chamber with various back scatter thicknesses. 'In Air" represents ion chamber only. 100 MU was delivered. The standard deviation is ignored as it is less than 0.5%.

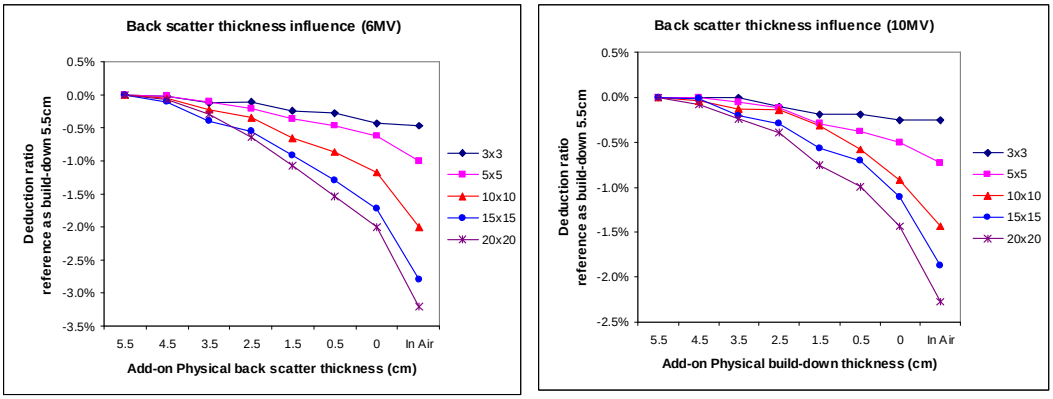

Figure 9.9 Markus Experiment 1 results (2): Percentage difference from a back scatter thickness of 5.5 to various build down thicknesses. 'In Air" represents ion chamber only. 100 MU was delivered. The standard deviation is ignored as it is less than 0.5%.

From the results it was found that:

- The readings decrease slightly with a decrease in back scatter thicknesses.
- The percentage difference goes from zero at a 5.5 cm back scatter thickness down to a negative value as the back scatter thickness reduced. The Ion-chamber only measurements show the maximum reduction.

- The percentage difference decreases from that of the 3x3cm^2 field and becomes more negative with increases in field size. For small fields, such as 3x3cm^2 and 5x5cm^2, the reduction is less than 1%, but this increases to 2% for a field of 10x10cm^2 for 6MV and to 1.5% for 10MV. For the bigger fields of 15x15 cm^2 and 20x20cm^2, the reduction is up to 3.2% for 6 MV and 2.3% for 10 MV.
- The magnitude of the percentage difference, from the 5.5 cm back scatter thickness down to zero backscatter (chamber only), decreases with the photon energy. The measurements at 6MV show a higher reduction than those at 10MV.

9.9.2 Markus Experiment 2: Measurement point set on the exit surface in a homogeneous phantom

The purpose of this study was to find the influence of different back scatter thicknesses using an in-house made phantom on the exit dose when the effective measurement point is set on the exit surface on the central axis of the beam. This experiment was performed in a solid water slab homogeneous phantom with various tissue inserts. The various phantom combinations are defined in section 9.4.

9.9.2.1 Methodology

Figure 9.10 shows the schematic setup of the back scatter material with the effective measurement point set on the exit surface of the beam axis. Figure 9.11 shows the phantom setup used to test the effect of different thicknesses of back scatter material on the exit dose with the effective measurement point set on the exit surface on the beam axis. The dimensions of the phantom are: 20cm (length) x 20cm (width) x 18cm (depth). Perpendicular to the beam axis, the phantom dimensions are 20cm x 20cm and along the beam axis the depth is 18cm. The tissue equivalent material insert with dimensions 5cm (width) x 5cm (height) x 6cm (depth) was set at the centre of the phantom. By using the source-to-axis distance (SAD) technique, the centre of the phantom (18cm x 20cm) was set to the isocentre which is 100cm away from the source; the SSD in this case is 91cm. The Markus Ion-chamber was inserted in a special placement and the effective measurement point was set at the exit surface on the beam axis where the SCD is 109.106cm (including the 0.106cm effective measurement point of the PTW Markus Ion-chamber). The back scatter material thickness (d_{BS}) varied from 5.5cm to 0.5cm in 1.0cm steps, then from 0.5 cm down to 0 cm (the Markus ion-chamber is in the special placement, has no add-on build down thickness, but is surrounded by solid

water) for the chamber only (for the back scatter material thickness (d_{BS}) is set to 0 when the Markus Ion-chamber is exposed to air).

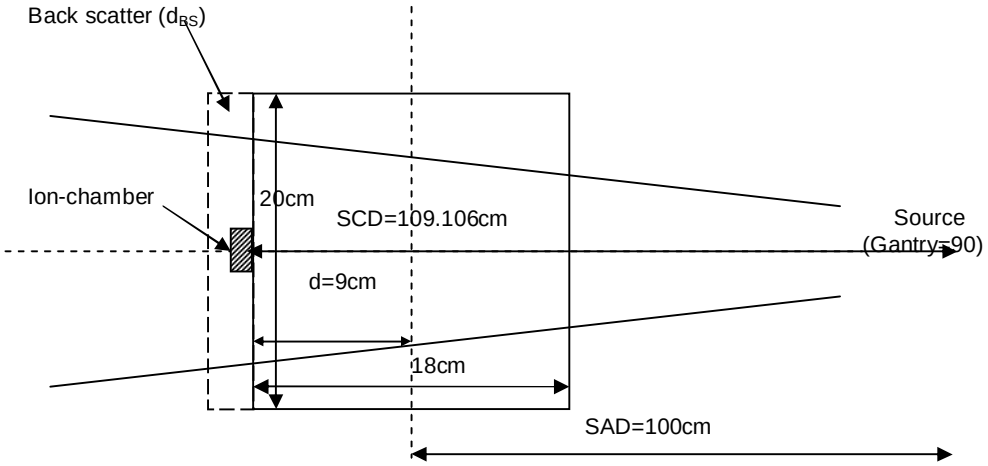

Figure 9.10 Schematic of the setup for back scatter thickness influence measurements in a Homogeneous phantom 1 for Markus Experiment 2

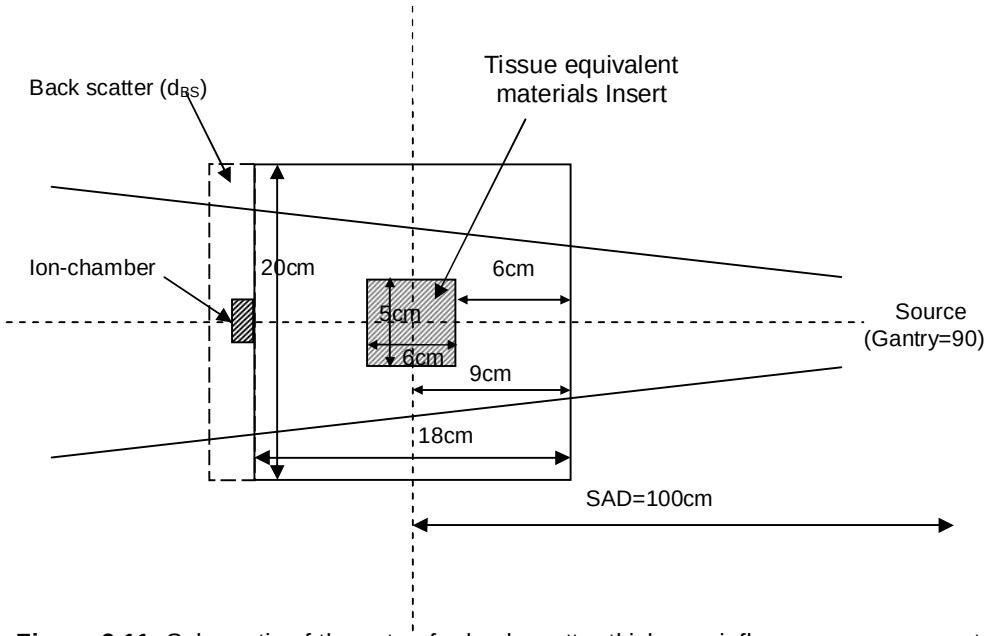

Figure 9.11 Schematic of the setup for back scatter thickness influence measurements for a phantom with tissue equivalent material inserted, phantom 2 to phantom 4 of the Markus Experiment 2.

All measurements were taken by delivering 100MU for the selected five square field sizes (3x3, 5x5, 10x10, 15x15, and 20x20cm^2) to the isocentre. The field sizes at the measurement point were calculated using inverse square law according to the SCD. The output readings were taken three (3) times with a Fluke Electrometer. The output readings of the 5.5cm back scatter thickness was set as a reference, and the other readings compared with the reference. The measured ratio (reduction ratio) is defined as the readings of various back scatter thicknesses compared to the reference values. The temperature and pressure effects were accounted for.

9.9.2.2 Results

Figure 9.12A to Figure 9.15A shows the raw readings (nC/100MU) of this experiment by using a PTW Markus Ion-chamber exposed to 6MV X-rays. For comparison, the mean raw readings were taken at each field size with an add-on back scatter thickness of 5.5cm as the reference. The percentage difference of the readings with other back scatter thicknesses to that from 5.5cm are shown in Figure 9.12B to Figure 9.15B.

Identical readings were done using 10 MV X-rays. The raw measurement readings (nC/100MU) are shown in Figure 9.16A to Figure 9.19A. The percentage difference of the reading with other back scatter thicknesses compared to that of 5.5cm are shown in Figure 9.16B to Figure 9.19B.

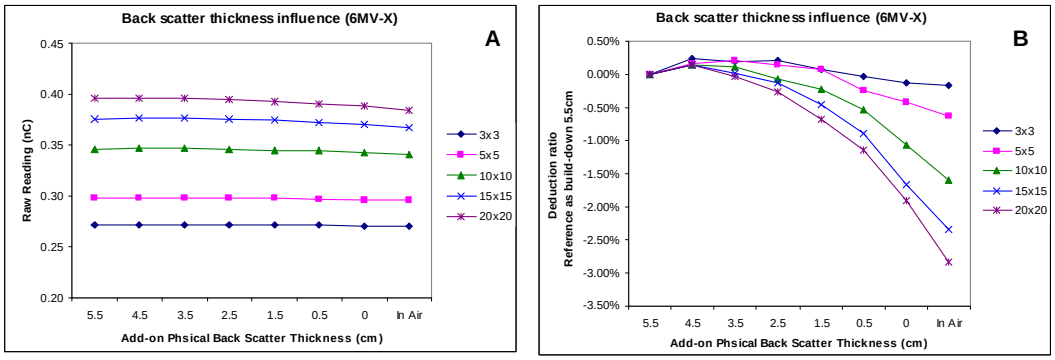

Figure 9.12 Markus Experiment 2 results (1): A:raw reading (nC) of a measurement point at exit surface in homogeneous phantom 1 with RED of 1.08 using a Markus Ion-chamber through various back scatter thicknesses. 'In Air" represents ion chamber only. B: Percentage difference from a back scatter thickness of 5.5 to various build down thicknesses. 100 MU delivered under 6 MV x-ray. The standard deviation is ignored due to less than 0.5%.

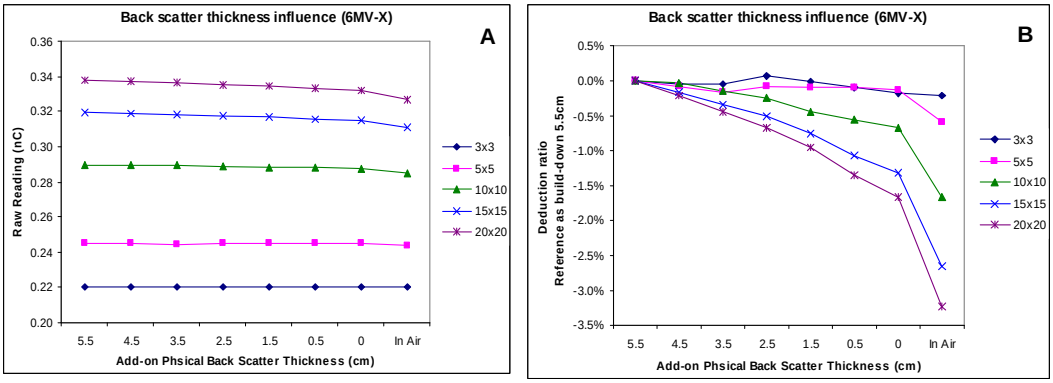

Figure 9.13 Markus Experiment 2 results (2): A:raw reading (nC) of a measurement point at exit surface in phantom 4 with RED 1.53 inserted using a Markus Ion-chamber through various back scatter thicknesses. 'In Air" represents ion chamber only. B: Percentage difference from a back scatter thickness of 5.5 to various build down thicknesses. 100 MU delivered under 6 MV x-ray. The standard deviation is ignored due to less than 0.5%.

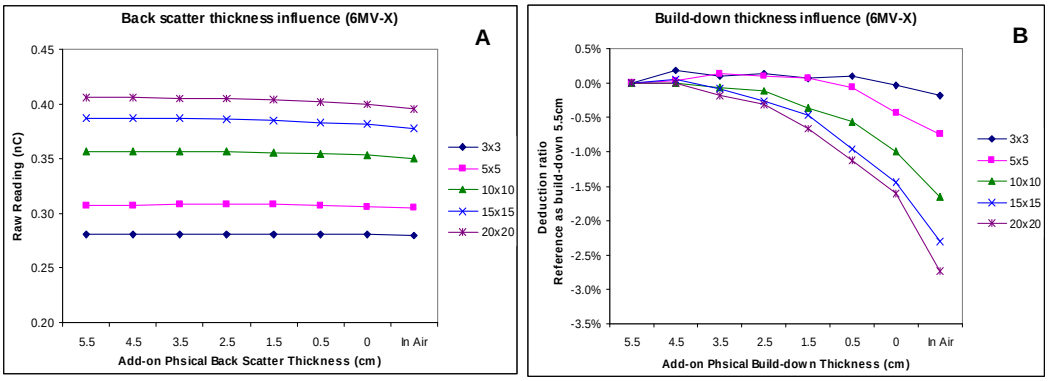

Figure 9.14 Markus Experiment 2 results (3): A:raw reading (nC) of a measurement point at exit surface in phantom 3 with RED 0.97 inserted using a Markus Ion-chamber through various back scatter thicknesses. 'In Air" represents ion chamber only. B: Percentage difference from a back scatter thickness of 5.5 to various build down thicknesses. 100 MU delivered under 6 MV x-ray. The standard deviation is ignored due to less than 0.5%.

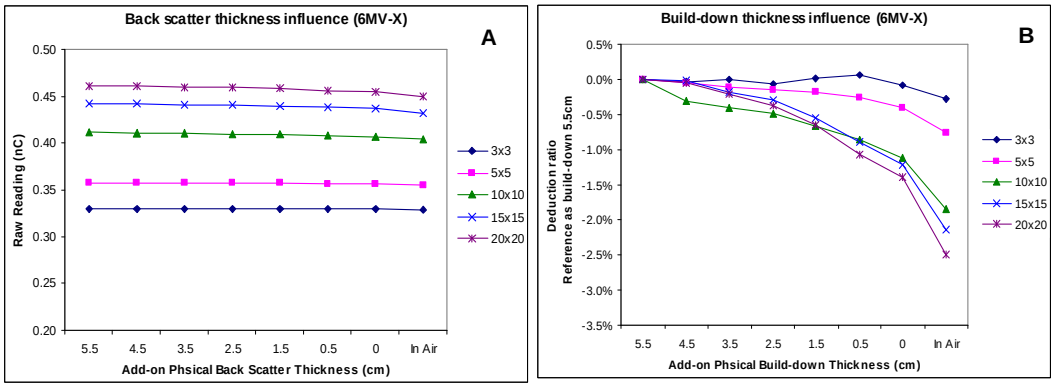

Figure 9.15 Markus Experiment 2 results (4): A:raw reading (nC) of a measurement point at exit surface in phantom 2 with RED 0.22 inserted using a Markus Ion-chamber through various back scatter thicknesses. 'In Air" represents ion chamber only. B: Percentage difference from a back scatter thickness of 5.5 to various build down thicknesses. 100 MU delivered under 6 MV x-ray. The standard deviation is ignored due to less than 0.5%.

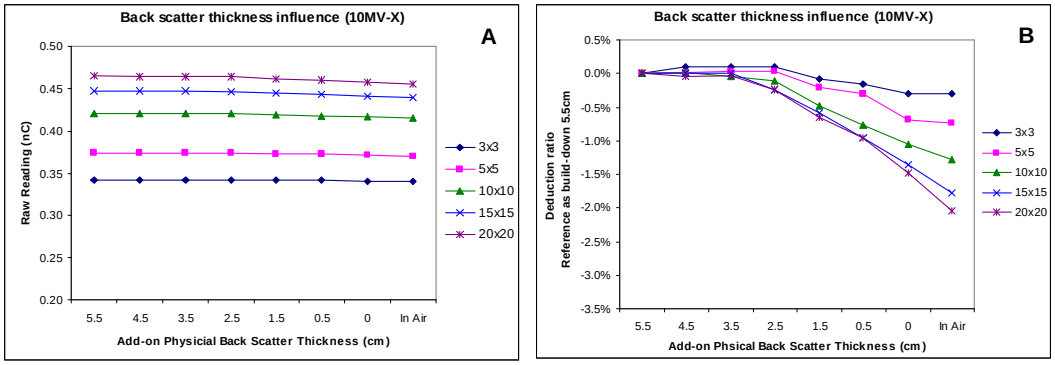

Figure 9.16 Markus Experiment 2 results (5): A:raw reading (nC) of a measurement point at exit surface in homogeneous phantom 1 with RED of 1.08 using a Markus Ion-chamber through various back scatter thicknesses. 'In Air" represents ion chamber only. B: Percentage difference from a back scatter thickness of 5.5 to various build down thicknesses. 100 MU delivered under 10 MV x-ray. The standard deviation is ignored due to less than 0.5%.

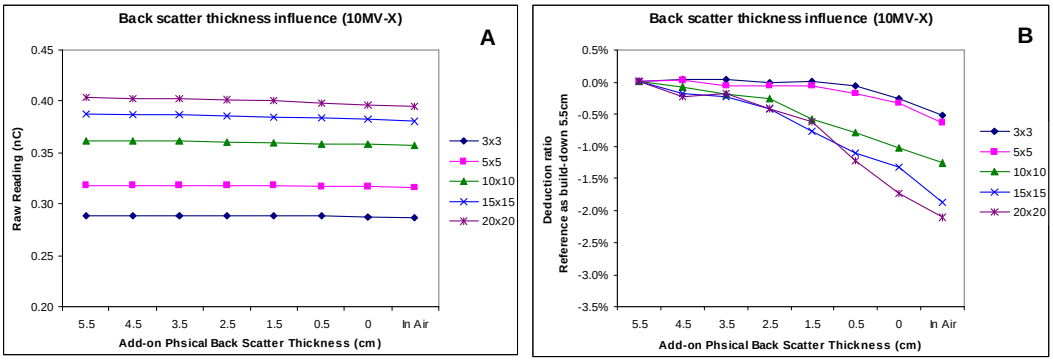

Figure 9.17 Markus Experiment 2 results (6): A:raw reading (nC) of a measurement point at exit surface in phantom 4 with RED 1.53 inserted using a Markus Ion-chamber through various back scatter thicknesses. 'In Air" represents ion chamber only. B: Percentage difference from a back scatter thickness of 5.5 to various build down thicknesses. 100 MU delivered under 10 MV x-ray. The standard deviation is ignored due to less than 0.5%.

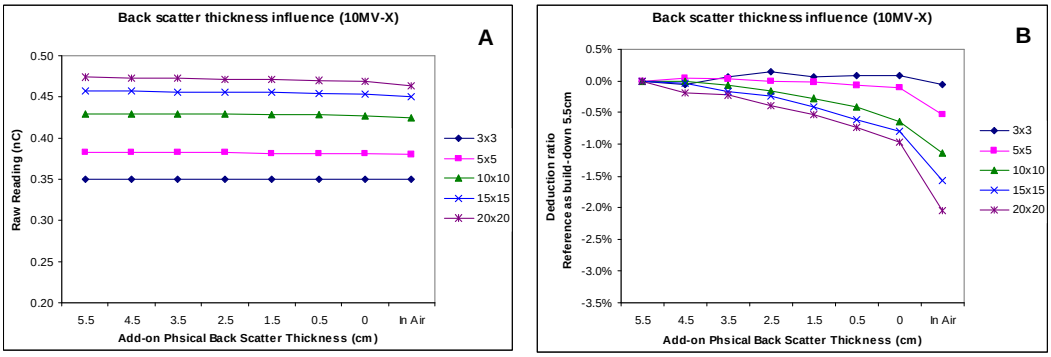

Figure 9.18 Markus Experiment 2 results (7): A:raw reading (nC) of a measurement point at exit surface in phantom 3 with RED 0.97 inserted using a Markus Ion-chamber through various back scatter thicknesses. 'In Air" represents ion chamber only. B: Percentage difference from a back scatter thickness of 5.5 to various build down thicknesses. 100 MU delivered under 10 MV x-ray. The standard deviation is ignored due to less than 0.5%.

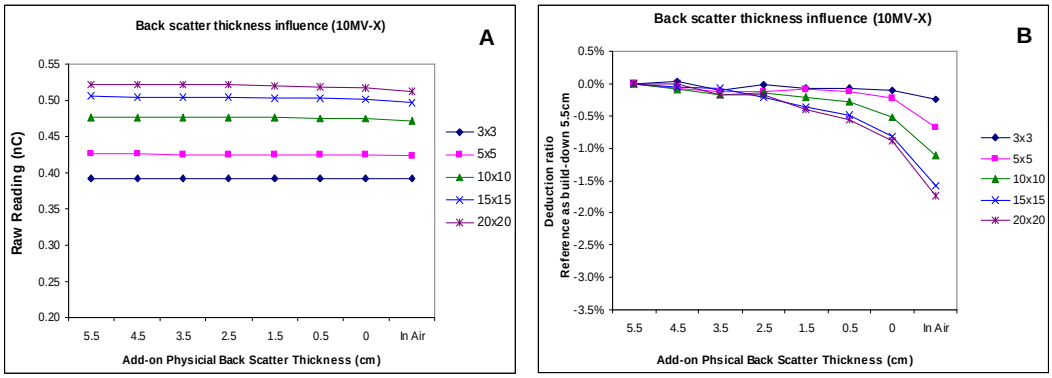

Figure 9.19 Markus Experiment 2 results (8): A:raw reading (nC) of a measurement point at exit surface in phantom 2 with RED 0.22 inserted using a Markus Ion-chamber through various back scatter thicknesses. 'In Air" represents ion chamber only. B: Percentage difference from a back scatter thickness of 5.5 to various build down thicknesses. 100 MU delivered under 10 MV x-ray. The standard deviation is ignored due to less than 0.5%.

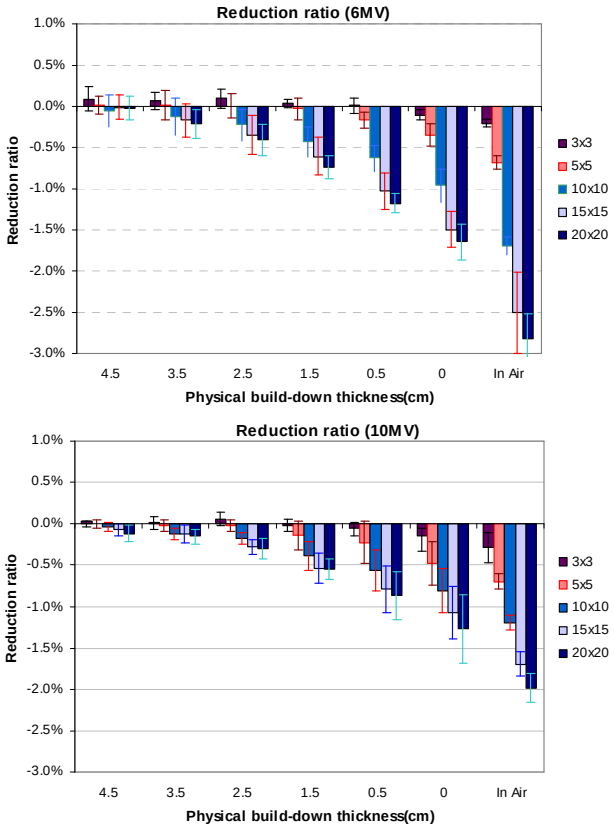

Figure 9.20 Markus Experiment 2 results (9): average back scatter thickness reduction ratio in a heterogeneous phantom 1 for exit dose measurements (using a PTW Markus ion-chamber) of 5 selected square field sizes. The data is an average based on various tissue equivalent inserts. The standard deviations of various inserts were added.

Figure 9.20 shows the summary of the average back scatter thickness exit dose reduction ratio with the four phantom combinations and 5 selected field sizes. Data was based on the average of the phantom (RED =1.08) with various tissue equivalent inserts (RED=1.53, 0.97, and 0.22, respectively) inserted. The standard deviations of the value of repeated reading is ignored due to less than 0.5%. It should be noted that the noise readings of PTW Markus chamber and Fluke Electrometer shows that the overall error (standard deviation) is less than 0.0005nC/100MU (0.05%) which can be considered to be negligible.

The results are similar in several respects to those from the previous experiment:

- Exit dose readings decrease slightly with decreases in back scatter thicknesses.
- The percentage change from the reference 5.5 cm back scatter condition, becomes more negative as back scatter thickness is reduced.
- The percentage difference becomes more negative with both increases in field size increases and reductions in build-down thickness from 5.5 cm to zero.
- Relative to the raw readings at back scatter thickness of 5.5cm, the reduction ratios increased when the back scatter thickness reduced. The 'ion-chamber only' readings show a maximum reduction ratio.
- For the homogeneous phantom 1, the reduction ratios increased with field size increases. For small fields, such as 3x3cm^2 and 5x5cm^2, the reduction ratio is less than 1%, increasing to 1.6% for a 10x10 cm^2 field for 6 MV and 1.2% for 10MV, and up to 2.8% for 6 MV and 2.0% for 10 MV for the bigger field sizes of 15x15 and 20x20cm^2.
- For heterogeneous phantom 2 to phantom 4, the reduction ratios became increasingly more negative along with an increase in field size. For small fields, such as 3x3cm^2 and 5x5cm^2, the reduction ratio is less than 1%, 1.6% for a field of 10x10 cm^2. For the bigger fields of 15x15 cm^2 and 20x20cm^2.it is an average of 3% for 6 MV and to 2% for 10 MV.
- The results for various tissue inserts show that there is not much significant difference among various RED materials. The overall standard deviation of the readings for various materials is less then 0.5% for all the field sizes.
- The magnitude of the percentage difference decreased with photon energy. The 6MV measurements show a higher reduction than those of 10MV.

9.10 Markus Experiment 3: Exit dose vs. Field Size

As described previously, the influence of the field size and shape on the exit dose may be due to secondary scattered photons.

9.10.1 Methodology

It has been shown from previous experiments that a Markus Ion-chamber can be used for exit dose measurement as the back scatter thickness will not affect the measurement results significantly. However, for more accurate measurements the back scatter factor should be considered. Due to the physical limitations of the PTW Markus Ion-chamber a minimum back scatter thickness of 1.4cm is used for this study.

This experiment investigates how much the field size affects the exit dose variations when the back scatter thickness changes. Phantoms 2, 3,and 4 described in section 9.4 were used.

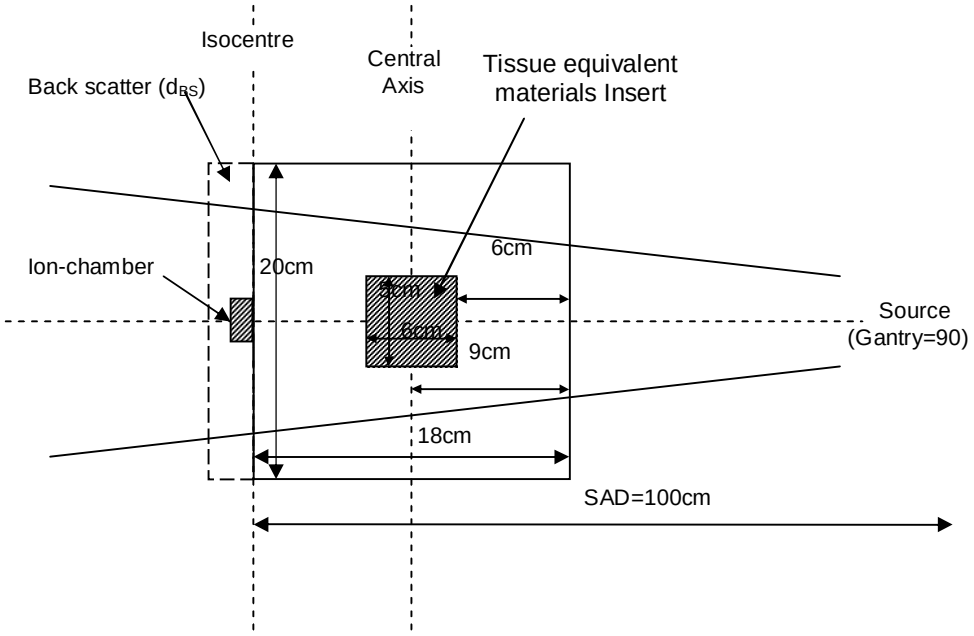

Figure 9.21 Schematic of setup for back scatter thickness influence measurements for a phantom with tissue equivalent material inserted for Markus Experiment 3

Figure 9.21 shows the schematic setup of a homogeneous phantom with tissue

equivalent material inserts to test the influence of field size on measurements with an effective measurement point at the exit surface on the beam axis for the back scatter thickness of 5.5 cm, 0.5cm, and Markus ion chamber only.

Please refer to section 9.9.2.1 for the detailed description of the process used.

9.10.2 Results

The raw readings (Figure 9.22) and the reduction ratio (Figure 9.23) for the three tissue equivalent material inserts were acquired and compared. Data with back scatter thicknesses of 5.5cm, 0.5cm, and Ion-chamber only are shown in blue, green, and red respectively. Phantom 2 with tissue equivalents inserts with a RED of 0.22 are shown as solid lines with solid markers. Phantom 3 with a tissue equivalent insert with a RED of 0.97 are shown as solid lines with hollow markers. Phantom 4 with tissue equivalents inserts with a RED of 1.53 are shown as dashed lines with hollow markers.

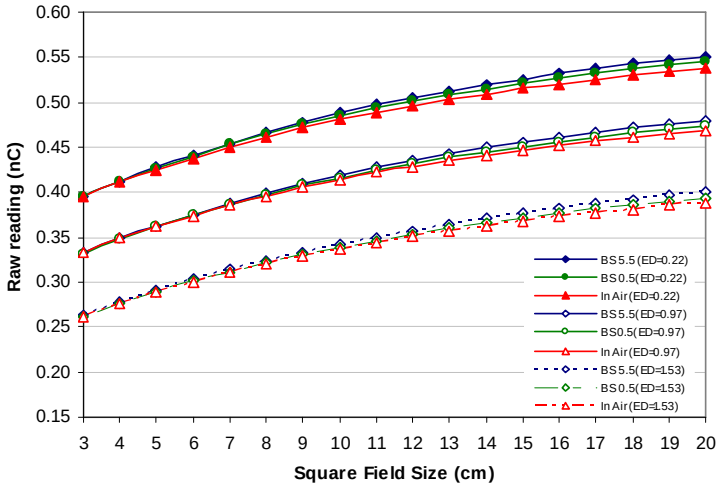

Figure 9.22 Markus Experiment 3 results (1): Raw readings against the various field sizes for exit dose measurement with various tissue inserts. Data with back scatter thickness 5.5cm, 0.5cm and Ion-chamber in the air are shown blue, green and red, respectively. The tissue equivalent inserts with a mass density of 0.22, 0.97 and 1.53 are shown in the solid lines with solid markers, solid lines with hollow markers and dash lines with hollow markers, respectively.

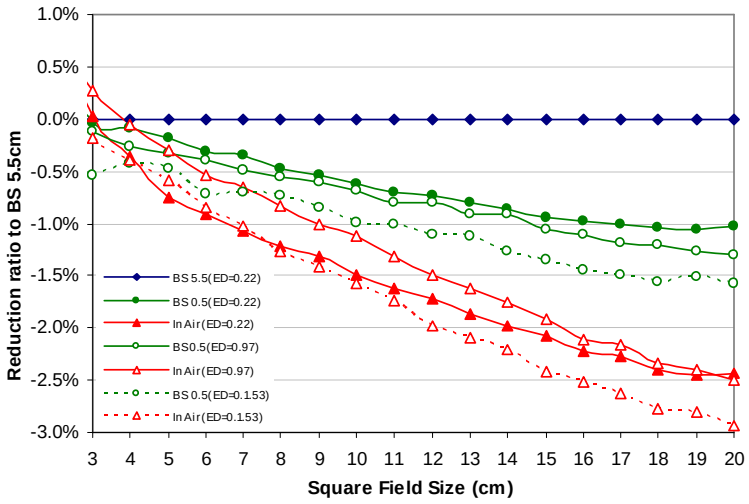

Figure 9.23 Markus Experiment 3 results (2): Reduction ratio (%) against the various field sizes for exit dose measurement with various tissue equivalents inserts. Data with backscatter thicknesses of 5.5cm, 0.5cm and Ion-chamber in the air are shown blue, green and red, respectively. The tissue equivalent inserts with a RED of 0.22, 0.97 and 1.53 are shown in the solid lines with solid markers, solid lines with hollow markers and dash lines with hollow markers, respectively.

From the results it was found that:

- As the field size increases, the difference increases, for the three back scatter thickness, from approximately 0.0% at 3x3cm^2 to -3.0% at 20x20cm^2. Please refer to table 10-13 for details
- The tissues inserts with various densities show a slight influence on the reduction ratio. As RED increases the difference for the three back scatter thicknesses increase from approximately -1.06% and -2.45% for a RED of 0.22 to -1.29% and -2.50% for a RED of 0.97, then to -1.57% and 2.93% for a RED of 1.53 at a field size of 20x20cm^2.

9.11 Markus Experiment 4: Exit dose vs. Energy

9.11.1 Methodology

Using the same setup (Figure 9.21) and experimental method as described in Markus Experiment 3, the test was repeated using a 10MV x-ray to deliver 100MU. Only the tissue equivalent material insert with an ED of 0.22 was tested. The data

was compared with that from previous results by using 6MV x-ray in Markus Experiment 3 (section 9.10).

9.11.2 Results

To compare 6MV and 10MV, raw readings (Figure 9.24) and reduction ratios (Figure 9.25) when using the tissue insert with a RED of 0.22 were acquired. Data with back scatter thicknesses of 5.5cm, 0.5cm, and zero (Ion-chamber in air) are shown in blue, green, and red respectively. Data from 6MV x-ray shows in solid lines with hollow markers, and that from 10MV x-ray shows in dashed lines with hollow markers.

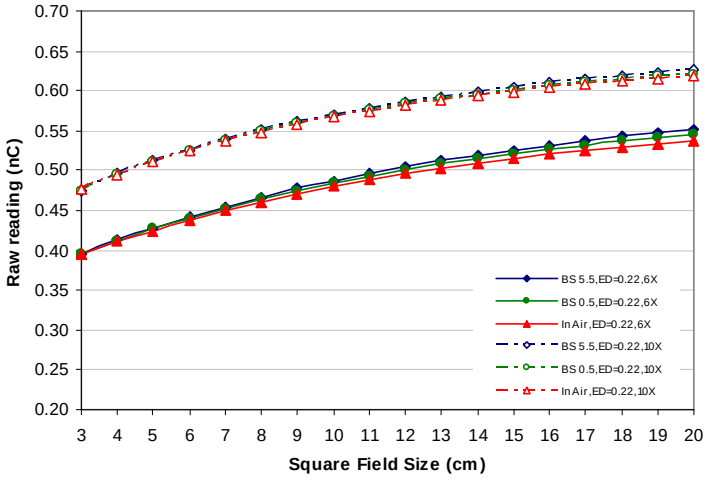

Figure 9.24 Markus Experiment 4 results (1): Raw readings for various field sizes for exit dose measurements with tissue insert RED=0.22. Data with back scatter thicknesses of 5.5cm, 0.5cm and Ion-chamber in air are shown blue, green and red, respectively. Data from 6MV x-rays show as solid lines with hollow markers and that of 10MV x-rays show as dashed lines with hollow markers.

From the results it was found that:

- With a back scatter thickness of 0.5cm, there is no significant difference between 6MV and 10MV data. The overall reduction ratio for both energies is within -1.0%.
- When the ion-chamber exposed in air, the reduction ratio for 10MV shows much less decrease than that of 6MV.
- For 10MV, the overall reduction ratios to that at full backscatter (back scatter 5.5cm) for the test field size range ($3x3cm^2$ ~ $20x20cm^2$) are less than -1.5%, while for field size smaller than 15cmx15cm they are within -1%.

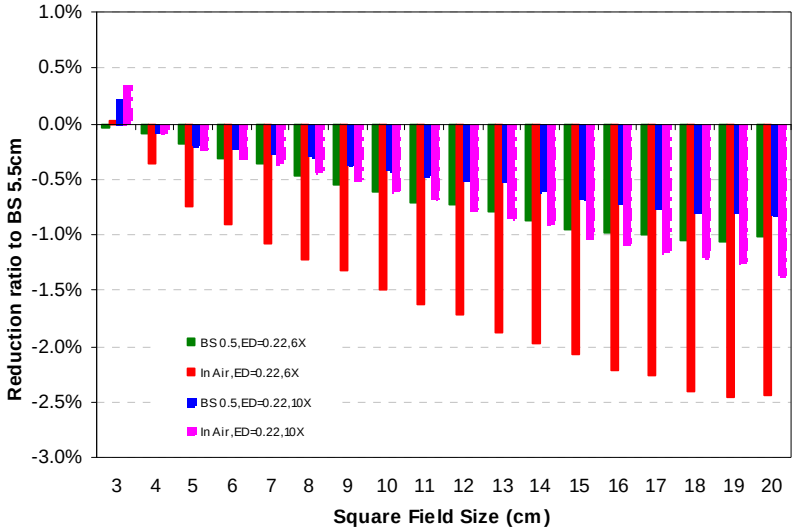

Figure 9.25 Markus Experiment 4 results (2): Reduction ratio (%) against the various field sizes for exit dose measurements with a tissue insert ED=0.22. Data with back scatter thickness 5.5cm, 0.5cm and Ion-chamber in air are shown blue, green and red, respectively. Data from 6MV x-rays shows as solid lines with hollow markers and that of 10MV x-rays show as dashed lines with hollow markers.

- For 6MV and field sizes between 3x3cm^2 and 10x10cm^2, the reduction ratio is up to 1.5% at full backscatter condition. For field sizes up to 15x15cm^2, the reduction ratio changes to 2.0%. And for field size larger then 15x15cm^2, the reduction ration is up to 2.5%.

9.12 Markus Experiment 5: Verification Markus ion-chamber measurement data

The purpose of this experiment is to compare the exit dose data measured by a PTW Markus with and without back scatter conditions to that quoted from the standard TMR data collected during the commissioning.

9.12.1 Methodology

Using the setup shown in Figure 9.5, the PTW Markus ion-chamber was calibrated at d_{max} =1.5 cm for a 6MV x-ray (from a Siemens ARTISIE 6MV Linear Accelerator) for field sizes (FSZ) from 3x3cm^2 to 20x20cm^2. A build-up (d_{UP}) of 1.5 cm was added

to the effective measurement points (EPL approximation based on equivalent thickness plus the PTW specified Markus effective measurement depth of 1.03mm) to match the d_{max} of the 6 MV photon beam. In addition, a 5.5cm equivalent build-up was added.

The Data from Experiment Exit Dose Markus Three (section 9.10) were normalized to that at d_{max} for each field size, then were compared with the depth dose (TMR) data calculated from the commissioned PDD data that were described in section 10.2. The correction factors (CF) were used for the heterogeneity correction and calculated using the EPL method.

9.12.2 Results

The compared results in phantom 2 with RED=0.22, phantom 3 with RED=0.97, and phantom 4 with RED=1.53 are shown from Figure 10.21 to Figure 10.23. No additional back scatter material was added to the PTW Markus ion-chamber.

Figure 9.26 compares the results between the measured data and the TMR data. The data measured after CF correction are shown in solid markers. The TMR data is shown as a solid line.

Figure 9.27 shows the difference between the measured data and the TMR data. The measured data was corrected using a heterogeneous correction factor.

From the results it was found that:

- With full backscatter (5.5cm back scatter) the results for the tissue equivalent inserts with RED 0.22 and 0.97 show a similar reduction ratio of within -1.0% to the TMR data for that field size range. The results for the tissue equivalent insert with RED=1.53 shows a higher reduction ratio in the range of -2.3%~-3.6% different from the reference TMR data,
- With no additional backscatter materials added (Markus chamber in air), The results for the tissue equivalent inserts with RED 0.97 show a minimum reduction ratio of within -1.5%. to the reference TMR data for the used field size range. The results for the tissue equivalent inserts with RED 0.22 show a reduction ratio of within -2.0%. to the reference TMR data for the used field size range. The results for the tissue equivalent inserts with RED 1.53 show a maximum reduction ratio of in range -3.0 % to -4.8% to the reference TMR data for the used field size range.

- Compared to the data with the full backscatter condition, the data with no additional backscatter materials added show a greater reduction ratio of within -1.0% for the used field sizes up to 10x10cm^2 , and of within -2.0% for the used field size up to 20x20cm^2 (Figure 9.28).
- For the tissue electron density closer to the density of water, the exit dose measurement shows a lower reduction ratio to the reference TMR data.
- If using the primary beam EPL method to perform the heterogeneity correction (Ahnesjö and Aspradakis, 1999) based on relative electron density scaling, an accuracy within 1% for both RED 0.22 and 0.97 inclusions can be achieved. For the higher RED 1.53, which has a density closer to bone, using the estimated EPL method can result in a difference of approximately 4%. These results have a good agreement with those reported by Seco and Evans (2006).

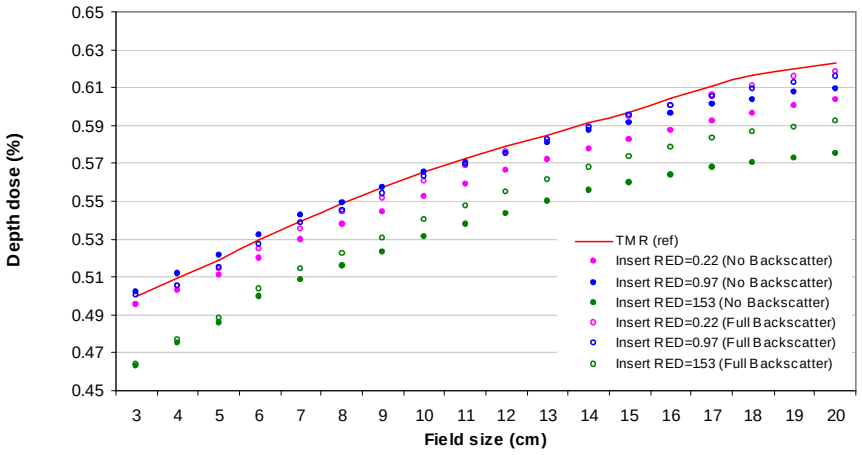

Figure 9.26 Markus Experiment 5 results (1): Comparison between measurement data and reference TMR data. The measurement data after tissue CF corrections are shown in solid markers. The TMR data are shown in solid lines. Measurement data with no additional back scatter (no backscatter) are shown in solid dots and data with 5.5cm back scatter (full backscatter) are shown in hollow dots. All the measured data were acquired using 6MV x-rays and 100MU.

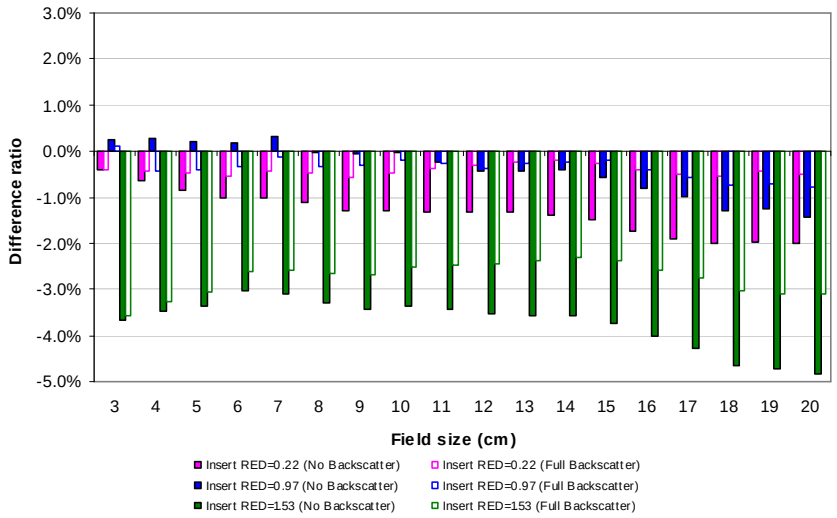

Figure 9.27 Markus Experiment 5 results (2): Percentage difference between measurement data and TMR data. The measurement data is shown after a heterogeneous CF correction. The data with no additional back scatter (no backscatter) is shown in solid columns and the data with 5.5cm back scatter (full backscatter) is shown in hollow columns.

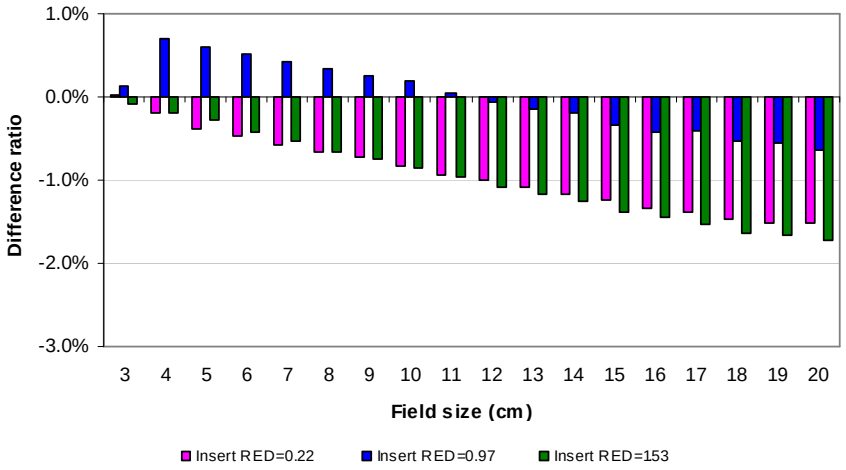

Figure 9.28 Markus Experiment 5 results (3): Reduction ratio difference between full backscatter (5.5cm) and no additional backscatter (chamber only).

9.13 Markus Experiment 6: Exit Dose variation vs. the size of tissue equivalent materials inserts

In this study the effect of tissue or tumour size on the exit dose was assessed.

9.13.1 Methodology

Based on the same setup in Figure 9.11 this experiment is an extension of Markus Experiment 2 with the same insert material with a different size. The insert material is the one with a RED of 0.22. The plane of the phantom perpendicular to the beam axis is 20 x 20cm^2 and the depth along the beam axis is 18cm. Instead of using the tissue equivalent material insert with dimension 5cm (width) x 5cm (height) x 6cm (depth), another two inserts with dimension 5cm (width) x 7.5cm (height) x 6cm (depth) and dimension 5cm (width) x 3cm (height) x 6cm (depth) were used for this experiment. The inserts either perpendicular or parallel to the beam axis are 7.5 x 5cm^2 and 3 x 5 cm^2 in size respectively. By using the source-to-axis distance (SAD) technique, the centre of the phantom (18cm x 20cm) was set to the isocentre, 100cm from the source, at an SSD of 91cm. The Markus Ion-chamber was inserted in the template and the effective measurement point was set to the exit surface on the beam axis. The SCD was 109.106cm (including 0.106cm effective measurement point of PTW Markus Ion-chamber). The initial backscatter (d_{BS}) thickness was 5.5cm, decreasing in 1.0cm steps to 0.5cm, then finally the Markus Ion-chamber was exposed to air. The Markus measurement point was set on the exit surface on the beam axis.

The phantoms, with various sizes of inserts, were named as follows:

- Phantom 2: in-house made phantom with a 5cm (width) x 5cm (height) x 6cm (depth) tissue equivalent material insert of RED=0.22. Its equivalent thickness is 14.58cm, as defined in section 9.4.
- Phantom 2B: in-house made phantom with a 5cm (width) x 7.5cm (height) x 6cm (depth) tissue equivalent material insert of RED=0.22. Its equivalent thickness is 14.58cm.
- Phantom 2S: in-house made phantom with a 5cm (width) x 3cm (height) x 6cm (depth) tissue equivalent material with RED=0.22. Its equivalent thickness is 14.58cm.

All measurements were taken by delivering 100MU under 6MV and 10MV X-rays for the selected five square field sizes (3x3, 5x5, 10x10, 15x15, and 20x20cm^2) at isocentre. The output readings were taken using a Fluke Electrometer and repeated 3 times for each measurement and averages taken. The standard deviation of the readings from the Markus chamber and Fluke Electrometer can be ignored as it is less than 0.0005nC/100MU (0.05%).

Using the output data measured for phantom 2B and 2S was compared to the data for phantom 2 in Markus Experiment 2. The averages and standard deviations for various thicknesses of inserts and for various field sizes were calculated.

9.13.2 Results

Figure 9.29 and Figure 9.20 show the raw readings measured for phantom 2B and phantom 2S with various back scatter thicknesses using 6MV and 10MV x-ray respectively. Figure 9.31 summaries the percentage difference in the average of various back scatter thicknesses between phantoms 2B and 2S to that of phantom 2.

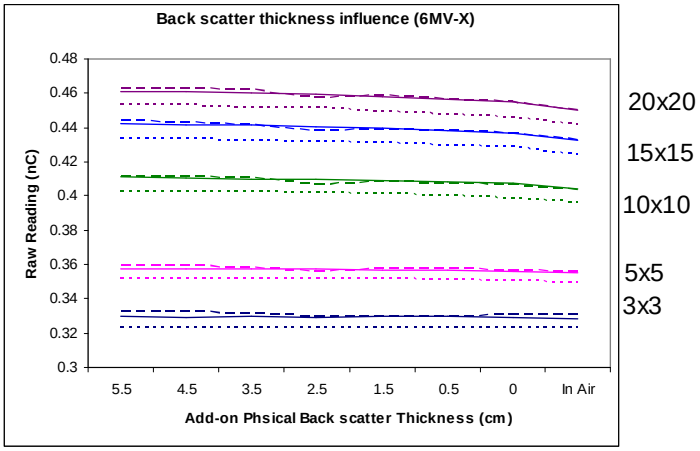

Figure 9.29 Markus Experiment 6 results (1): Comparison of raw readings of phantom 2, 2B, and 2S under 6MV x-ray irradiation. Measurement points were at exit surface and isocentre was at target centre of the phantom. The add-on physical back scatter thickness changes from 5.5cm to 0cm, then the Markus Ion-chamber exposed in air. 100MU was delivered. The solid lines represent phantom 2, long dash lines represent phantom 2B, and short dash lines represent phantom 2S.

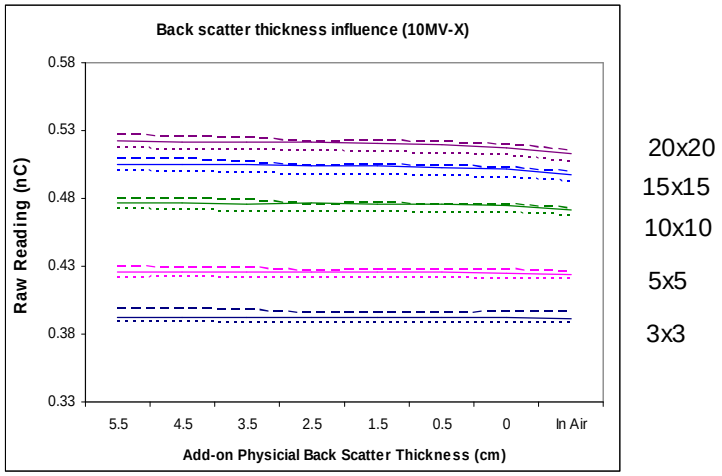

Figure 9.30 Markus Experiment 6 results (2): Comparison of raw readings of phantom 2, 2B, and 2S under 10MV x-ray irradiation. Measurement points were at the exit surface and the isocentre was at the target centre of the phantom. The add-on physical back scatter thickness changes from 5.5cm to 0.5 cm, then the Markus Ion-chamber was exposed in air. 100MU was delivered. The solid lines represent phantom 2, long dash lines represent phantom 2B, and short dash lines represent phantom 2S.

From the results it was found that:

- The readings decreased with a decrease in the insert size.
- Compared to the raw measurement readings for the 5x5cm^2 insert in phantom 2, perpendicular to the beam axis, the overall differences between the largest and smallest insert sizes were found to be within 2% in this experiment.
- Compared to the raw measurement readings for the 5x5cm^2 insert, perpendicular to the beam axis, in phantom 2, the larger insert size of 7.5x5cm^2 (phantom 2B) shows a slightly higher response. For 6MV, the responses are within 0.5% higher for the all field sizes. 10MV, for the 3x3cm^2 field size shows the highest response of 1.2% of the average for the various thicknesses of inserts, but for the other field sizes, it shows a higher response of within 1% of the average of various insert thicknesses.
- Compared to the raw measurement readings for the 5x5cm^2 insert, perpendicular to the beam axis, in phantom 2, the smaller insert size of 3x5cm^2 (phantom 2S), shows a lower response. For 6MV the responses are up to 2% lower for the all field sizes. For 10MV, the responses are around 1% lower for the all field sizes.

- The outputs from individual phantoms with various back scatter thicknesses show slight differences, but all are within 0.5%.

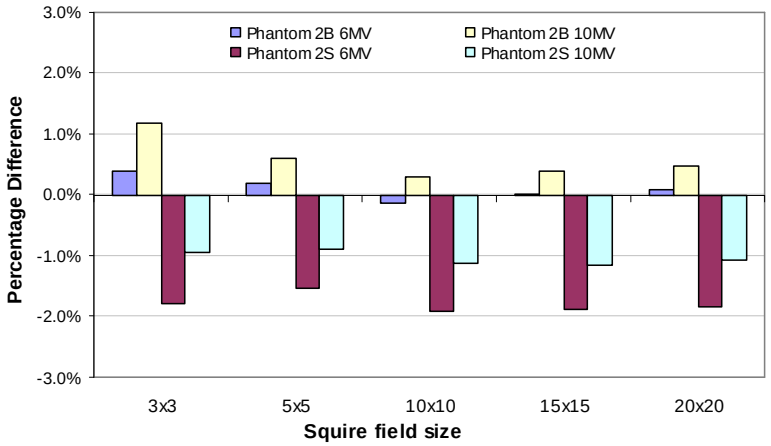

Figure 9.31 Markus Experiment 6 results (3): The effect of variations in tissue or tumor size. Comparison is between measurement data in phantom 2B and phantom 2S to that of phantom 2.

9.14 Summary of exit dose dosimetry using the Markus ion-chamber

The total dose to a point in human body or phantom is a sum of the contribution from both the primary and secondary scattered photons. A primary photon's contribution to the exit dose can be measured directly using the Markus ion-chamber, with or without added back scatter.

The influences from the primary photons on the exit dose are not changed with field size changes. This means that the changes in exit dose must be a result of the contributions of the secondary scattered photons. My exit dose measurements show that as back scatter material's thickness decreases the chamber response decreases in a way that can be expressed by reduction ratios. In other words, the measured exit dose readings (through reduction ratio) have a dependence on the field size; the reduction ratios become increasingly more negative as the field size increases (namely scattered photons increase). The fact of that without additional back scatter material placed behind the chamber there are less variations in chamber readings even for the larger field size which demonstrates again that the major contributions to the exit dose are mostly from the secondary scattered

photons.

With 10MV x-rays the readings show a lower reduction ratio compared to 6 MV. This is due to the lower back scatter from the higher energy than from low energy x-rays.

Variations in tissue or tumour sizes may affect exit dose output, however, the experiment's results have shown that there is no significant difference for the various back scatter thicknesses and field sizes.

By using the primary beam EPL method to do a heterogeneity correction (Ahnesjö and Aspradakis, 1999) based on relative electron density scaling, an accuracy of within 1% could be achieved for the RED 0.22 and 0.97 inserts. For a higher RED of 1.53, which is closed to the density of bone, using EPL estimation achieves an approximate accuracy of 4%.

The PTW Markus Ion-chamber can be used for exit dose measurement as the back scatter thickness does not affect the measurement results significantly. The Markus can also be used in air alone. Due to physical limitations of the PTW Markus Ion-chamber, the minimum back scatter thickness needed for this study was 1.4cm which could not be avoided. However, for more accurate dosimetry, back scatter factors should be considered.

9.15 Exit dosimetry using OSLD

My previous experiments show that Landauer's InLight^{TM} OSL system is suitable for radiotherapy dosimetry due to its wide dose-response range, good dose linearity and reproducibility, directional independence and lower energy dependence. Based on these characteristics, OSL detectors can be suitable for in-vivo dosimetry in radiotherapy exit dosimetry.

From this section onwards, based on the results from the ion-chamber measurements, OSL dot dosimeters (OSLDs) are used for similar experiments in place of the ion-chamber as described in the experiment summary below. To assess the use of an OSL Dosimeter for exit dose dosimetry, the studies will focus on the following topics:

- Comparisons will be carried out in a homogeneous slab phantom with heterogeneous inserts and different back scatter thicknesses materials added.

- The influence of tissue density on exit dose.
- The reduction ratios for the exit dose measured with or without back scatter materials added behind the OSL dosimeters used with an inhomogeneous phantom.
- Comparison of the exit doses quoted from clinical depth dose (TMR) values and measured by ion-chamber measurements to the dose measured by OSL.

To achieve above-mentioned goals, the experiments were divided into five steps:

- Step one: uses the methodology in chapter 9 to build a OSLD calibration baseline.
- Step two: focuses on investigating the backscatter effect of different back scatter thicknesses coupled with a homogeneous phantom and heterogeneous inserts. Two experiments were performed with the effective measurement position at the isocentre on the exit surface.
- Step three: simulates the patient treatment. One experiment was performed with the effective measurement position on the exit surface.
- Step four: makes comprehensive comparisons between measurement data, reference standard depth dose data (Tissue-Maximum Ratio (TMR) in this case) and Markus data from previous experiments.
- Step five: focuses on investigating the field size influence for exit dosimetry using OSLD. One experiment was performed with the effective measurement position at isocentre on the exit surface.

The following experiments use relative electron density (RED), given in chapter 9, to provide the equivalent thicknesses of various phantoms. The previous experimental work shows that the radiation history of the OSLD may affect OSLD sensitivity and calibration. Therefore all the OSLDs used in these experiments were ‘virgin’ and exposed a maximum of three times in a single experiment. Temperature and pressure effects were not accounted for in this study.

9.16 Calibration of OSLDs

From my previous study (chapter 7), the sensitivity variation of the OSL dosimeters from the same package is within 2%. Four (4) OSLDs from one new package were

used as calibration dosimeters for the following experiments.

The methodology was the same as described in section 9.6. With equivalent thicknesses of 5.5cm (5.0cm geometrical thickness when calculated using the EPL method shown in Table 9.3) as back scatter, the OSLDs were set to isocentre with effective measurement points of 1.5cm, 5.5cm and 10.9 cm(10.0cm geometrical thickness when calculated using the EPL method shown in table 9.3). Each OSLD was irradiated three times at three depths with 100MU using 6MV x-rays and a field size of 10x10cm^2 at isocentre. The data collected is shown in Table 9.10.

Table 9.10 Dose calibration of OSL dosimeters for exit dose measurement. 100MU delivered with 6MV to a field size of 10 x10 cm^2 at isocentre. The calibration depths were set to equivalent thicknesses 1.5cm (d_{msx}), 5.5 cm (d_5) and 10.9cm (d_{10}). The 6MV TMR values from a clinically commissioned Siemens ARTISTE were used. The SD_1 is the standard deviation of 10 repeated readings of each OSLD. The SD_2 is the standard deviation of 4 OSL dosimeters.

(a) d_5 / d_{max}

OSLD No.	(1) Raw data at dmax d_{max} (Mean±SD$_1$)	(2) Raw data d_5 (Mean±SD$_1$)	(3) Normalized to dmax d_5 / d_{max} (1)/(2)	(4) TMR d_5 / d_{max}	(5) Diff (3) – (4)	(6) %Diff $\frac{(5)}{(4)} x \frac{1}{100}$
1	31659±203	28982±307	0.9155	0.9086	0.0069	0.76%
2	31903±249	28731±185	0.9006	0.9086	-0.0080	-0.88%
3	32253±115	29549±129	0.9162	0.9086	0.0076	0.83%
Mean±SD$_2$	**31938±299**	**29087±419**	**0.9107±0.0088**	**0.9086**	**0.0021**	**0.24%**

(b) d_{10} / d_{max}

OSLD No.	(1) Raw data at dmax d_{max} (Mean±SD$_1$)	(2) Raw data d_{10} (Mean±SD$_1$)	(3) Normalized to dmax d_{10} / d_{max} (1)/(2)	(4) TMR d_{10} / d_{max}	(5) Diff (3) – (4)	(6) %Diff $\frac{(5)}{(4)} x \frac{1}{100}$
1	31659±203	24503±146	0.7740	0.7532	0.0208	2.76%
2	31903±249	24796±157	0.7773	0.7532	0.0241	3.19%
3	32253±115	25144±100	0.7796	0.7532	0.0264	3.50%
Mean±SD$_2$	**31938±299**	**24814±321**	**0.7770±0.0028**	**0.7532**	**0.0237**	**3.15%**

9.17 OSL Experiment 1: Measurement performed at isocentre in homogeneous phantom

9.17.1 Methodology

The purpose of this study is to determine backscattered dose on OSL detectors with different back scatter thicknesses using the homogeneous phantom. Simplified, the effective measurement point is on the exit surface of the beam's central axis. This experiment was performed with an in-house manufactured homogeneous solid water slab phantom without tissue equivalent material inserts (phantom "1" - see section 9.4).

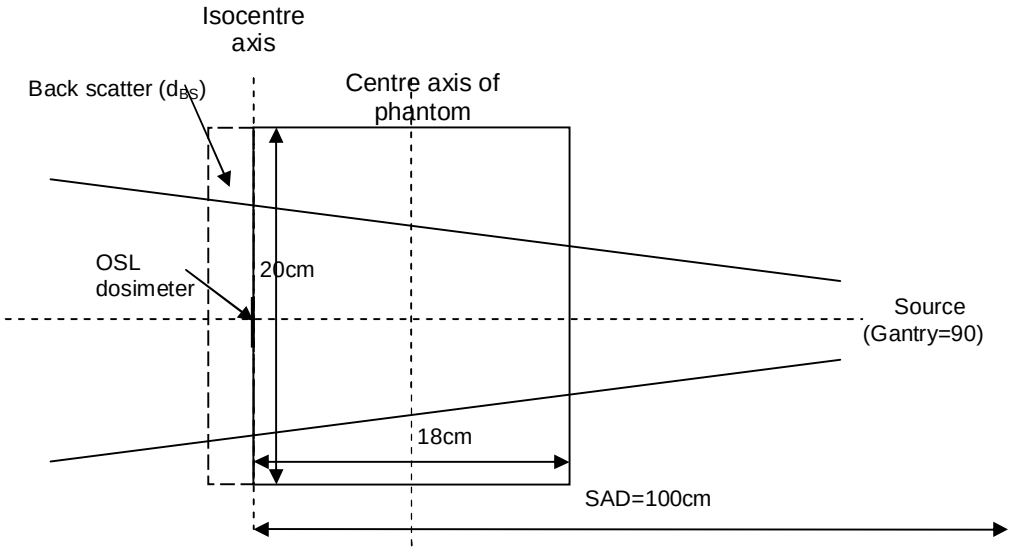

Figure 9.32 Schematic of OSL setup to assess the influence of back scatter thickness with the effective measurement point at isocentre in the homogeneous phantom used in OSL Experiment 1.

Figure 9.32 shows the schematic setup for exit dose measurements using OSLDs with back scatter material added with the effective measurement point on the exit surface of the phantom on the beam axis. The experiment was intended to follow the similar procedures to the Ionization measurement using Markus chamber discussed earlier. To simplify the experiment, the effective measurement point was set to isocentre, but equivalent to the position for setting Markus ion-chamber effective measurement point previously used, which is the source-to-axis distance (SAD), 100cm from the source. The OSLD with its case was either inserted in a specially

designed OSL placement slot (with back scatter) or mounted at the exit surface of the phantom (no additional back scatter). The dimensions of the phantom are 20cm (length) x 20cm (width) x 18cm (depth). The plane of the phantom perpendicular to the beam axis are 20cm x 20cm with a depth along the beam axis of 18cm. The source-to-chamber distance (SCD) is 100cm and the source-to-surface distance (SSD) is around 82.1cm (including 0.1cm thickness from the OSLD dot case). 100 MU was delivered with 6MV x-rays for the field size of 10 x 10cm^2 at isocentre. The equivalent depth (d_{UP}) thicknesses were added on the exit surface along the beam central axis. A total of seven back scatter (d_{BS}) thicknesses were selected and vary from 5.0cm , 4.0cm, 3.0cm, 2.0cm, 1.0cm, 0.5cm to Zero (no additional back scatter behind the OSLD). The equivalent thickness of the back scatter was calculated by using the EPL method.

All of the OSL discs were oriented in a way that the same sensitive face was used during the irradiation and readout procedure. A total of seven (7) OSLDs were used for seven back scatter thicknesses. Considering the useable life-span of OSLDs, the experiment was repeated three times. Each OSL dosimeter was irradiated 3 times with same back scatter thickness added. All OSLDs were read prior to irradiation, the readings set as background and the difference between the post-irradiation and pre-irradiation signal of PMT were taken. 10 repeated readings of each measurement were taken and the average and standard deviation were calculated. No annealing procedure was used during this experiment. The back scatter thickness of 5.0cm was defined as the full backscatter condition. The measurement data of other back scatter thicknesses were compared to the data of the full backscatter condition.

9.17.2 Results

Table 9.11 and Figure 9.33 show the raw readings of OSL measurement in the homogeneous phantom.

Table 9.12 and Figure 9.34 show the comparison (reduction) ratio of the data for various back scatter thicknesses to that at the full backscatter condition in each measurement. Each raw reading is based on 10 repeated readings. A back scatter of 5.0cm is considered as the full backscatter condition and set as reference. Thereafter, SD_1 (10), the standard deviations of 10 repeated readings were added. The average (3) and standard deviation (SD_2 (3)) are based one three irradiations.

Table 9.11: OSL Experiment 1 result (1): Raw readings for OSL measurement in phantom 1. Measurement points are at the exit surface and isocentre along the central beam axis. 100 MU was delivered with a 10x10 field size at 6MV x-rays. Each irradiation of an OSLD was read 10 times and its average and standard deviation taken.

Additional backscatter Thickness (cm)	Irradiation times (Mean±SD_1(10))				
	1	2	3	Average(3)	SD_2 (3)
5	17189±52	17219±148	17200±91	17203	15
4	17082±113	17087±137	17144±111	17104	34
3	16992±71	17027±61	16993±51	17004	20
2	16950±152	16969±168	16946± 46	16955	12
1	16904±63	16955±170	16910±80	16923	28
0.5	16854±37	16735±87	16905±72	16831	87
Zero	16330±33	16238±153	16023±124	16197	158

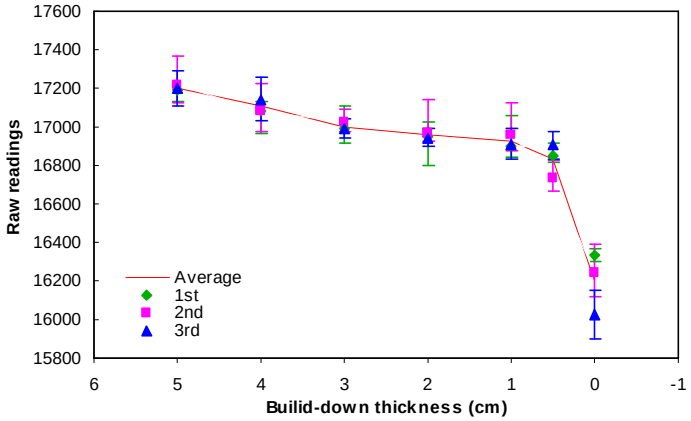

Figure 9.33 OSL Experiment 1 results (1): Raw readings of OSLDs in phantom 1. The measurement data is shown in various colors with a standard deviation from 10 repeated readings added. The averages of three measurements are shown with red solid lines.

Table 9.12 OSL Experiment 1 result (2): Reduction ratio between various back scatter thicknesses to the full backscatter condition (5.0cm) in phantom 1. Measurement points are at exit surface and isocentre along the central beam axis. 100 MU was delivered at a field size of 10x10cm^2 using 6MV x-rays. Each irradiation of an OSLD was read 10 times and the average and standard deviation were taken.

Additional back scatter Physical Thickness (cm)	Irradiation times (Mean±SD_1(10))				
	1	2	3	Average(3)	SD_2(3)
5 (as reference)	0.00%±0.30%	0.00%±0.86%	0.00%±0.53%	0.00%	0.09%
4	-0.63%±0.66%	-0.76%±0.80%	-0.33%±0.65%	-0.57%	0.20%
3	-1.15%±0.42%	-1.11%±0.36%	-1.20%±0.30%	-1.16%	0.12%
2	-1.39%±0.89%	-1.45%±0.98%	-1.48%±0.27%	-1.44%	0.07%
1	-1.66%±0.37%	-1.53%±0.99%	-1.68%±0.47%	-1.63%	0.16%
0.5	-1.95%±0.22%	-2.81%±0.51%	-1.72%±0.42%	-2.16%	0.52%
None	-5.00%±0.19%	-5.69%±0.89%	-6.84%±0.73%	-5.85%	0.97%

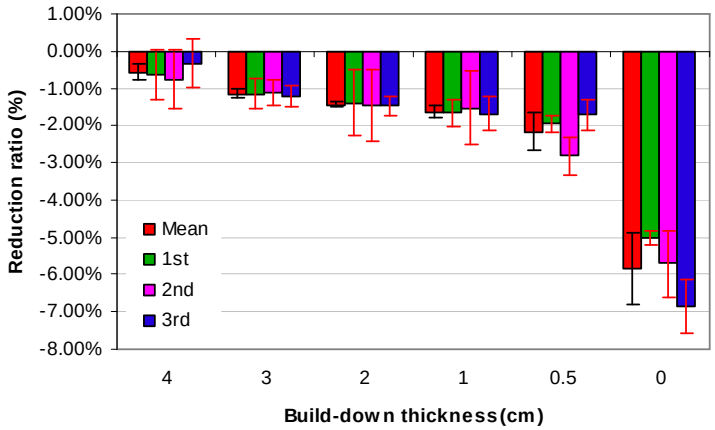

Figure 9.34 OSL Experiment 1 result(2):Reduction ratios of various back scatters to full backscatter (5.0cm). The standard deviations ($SD_1(10)$) of 10 repeated readings were added and are shown in red error bars. The standard deviations of three irradiations ($SD_2(3)$) were added on the Mean value and shown in black error bars.

9.18 OSL Experiment 2: Measurement performed at isocentre in a heterogeneous phantom

9.18.1 Methodology

This study is an extension of OSL Experiment 1. The purpose of this study is to determine the dose on OSL detectors with different back scatter thicknesses in a heterogeneous phantom (a homogeneous phantom with various tissue equivalent materials inserted). The experiment was performed using in-house phantom 2, 3 and 4 mentioned in section 9.4.

Figure 9.35 shows the schematic setup of the back scatter thickness measurements with an effective measurement point set on the exit surface of the beam axis. The dimension of the phantom is 20cm (length) x 20cm (width) x 18cm (depth). The phantom plane perpendicular to the beam axis is $20x20cm^2$ with a depth along the beam axis of 18cm. The tissue equivalent material inserts with dimensions of 5cm (width) x 5cm (height) x 6cm (depth) are located at centre of the phantom. The effective measurement point of OSLD is on the exit surface on the beam's central axis. By using SAD technique, the centre of the OSLD was set to the isocentre, which is 100cm away from the source; the SSD in this case is 82cm. The OSLD was either inserted in the placement or mounted on the exit surface of the phantom (named as zero, no additional back scatter).

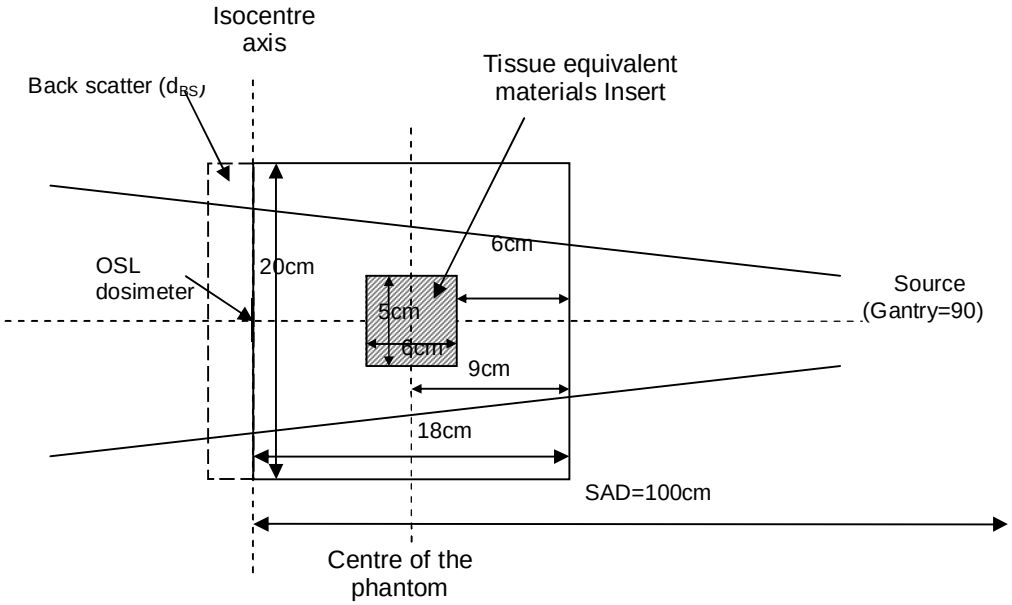

Figure 9.35 Schematic of OSL setup to assess the influence of back scatter thickness with the effective measurement point at isocentre in a homogeneous phantom for OSL Experiment 2.

Three additional back scatter (d_{BS}) thicknesses of 5cm, 1cm and zero (no additional back scatter added) were chosen. The equivalent thicknesses of the back scatter thicknesses were calculated using the EPL method shown in chapter 9.

The experimental method and data management are the same as those described in OSL Experiment 1. All of the OSL discs were oriented so that only the sensitive face was used during irradiation and readout. 15 Dot OSLDs were divided in three groups of 5 OSLDs for phantom 2, 3 and 4. Considering the OSLD's useable life-span, each OSLD was irradiated three times at the three back scatter conditions. The experiment with each identical phantom was repeated five(5) times using 5 OSLDs respectively. All OSLDs were read prior to irradiation, the readings were set as background and the difference between the post-irradiation and pre-irradiation signal of photomultiplier tube of the reader were taken. No intermediate annealing procedure was used between irradiations. The data for phantom 1 were taken from experiment Exit Dose OSL One.

All measurements were taken by delivering 100MU with 6MV x-rays to a 10x10cm^2 field size at isocentre. The output readings were taken with a MicroStar reader and repeated 10 times, with the average was taken for each irradiation. The back scatter

thickness of 5.0cm was defined as the full backscatter condition. The reading data at the other back scatter thicknesses conditions were compared to the data at the full backscatter condition.

The data measured using OSLDs were compared with the results from a Markus ion chamber from Markus Experiment 3 with the same setup. As the Markus has a 1.4cm default back scatter only two sets of Markus data were used for comparison.

9.18.2 Results

Table 9.13 shows the raw readings and the reduction ratios to the full backscatter condition (5.0cm) taken by OSLDs in the experimental phantoms. Figure 9.36 shows the raw readings and Figure 9.37 shows the comparison (reduction) ratio of the data with various back scatter thicknesses to the data at the full backscatter in each measurement. Each raw reading is based on 10 repeated readings. A back scatter of 5.0cm is considered as the full backscatter condition and these readings were set as the reference values. The SD_1 (10), standard deviations of 10 repeated readings, was added. The $Mean_2$ (5) and standard deviation (SD_2 (5)) are based on five irradiations of five OSLDs with the same back scatter condition.

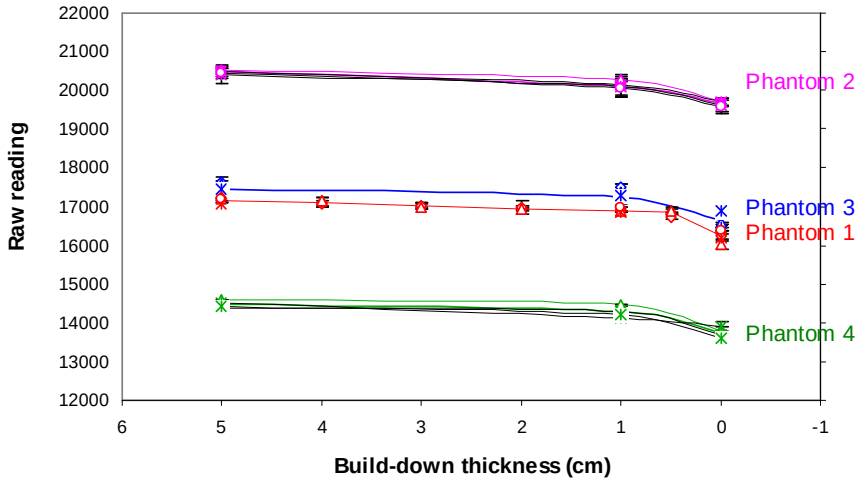

Figure 9.36 OSL Experiment 2 results (1): Raw readings of OSLDs. The averages of multiple irradiations are shown in solid lines with error bars of the standard deviations of 10 repeated readings added. Multiple exposures of each measurement were shown with various symbols.

Table 9.13: OSL Experiment 2 results: (1) Raw readings and (2) Reduction ratio for an OSLD measurement with various thicknesses to full backscatter. The phantoms were defined in chapter 9. Measurement points are at the exit surface and isocentre along the central beam axis. 100 MU was delivered at a field size of 10cm x 10cm using 6MV x-rays. Each irradiation of an OSLD was read 10 times and the average and standard deviation were taken. $Mean_1$ and SD_1 are the average and standard deviation of 10 repeated readings of each OSLD under each irradiation. $Mean_2$ and SD_2 are the average and standard deviation of 5 OSLDs of their response builddown thickness in the phantoms.

	(1) Raw readings $Mean_1 \pm SD_1(10)$			**(2) Reduction ratio (%) $Mean_1 \pm SD_1(10)$**		
	Additional back scatter Physical Thickness (cm)					
	5.0	**1.0**	**None**	**5.0**	**1.0**	**None**
OSLD #	**Phantom 1 Equivalent thickness: 19.54cm (Data from Experiment Exit Dose OSL One)**					
1	17189±52	16904±63	16330±33	0.00%±0.30%	-1.66%±0.37%	-5.00%±0.19%
2	17219±148	16955±170	16238±153	0.00%±0.86%	-1.53%±0.99%	-5.69%±0.89%
3	17200±91	16910±80	16023±124	0.00%±0.53%	-1.68%±0.47%	-6.84%±0.73%
4	17048±113	16833±63	16210±36	0.00%±0.66%	-1.26%±0.37%	-4.92%±0.22%
5	17192±88	16960±137	16374±85	0.00%±0.65%	-1.68%±0.47%	-4.76%±0.52%
$Mean_2$ (5) ± SD_2(5)	17170±69	16912±51	16235±136	0.00%±0.40%	-1.50%±0.30%	-5.40%±0.84%
Group 1 OSLD #	**Phantom 2 Equivalent thickness: 14.58cm**					
1	20103±110	20690±33	20289±109	0.00%±0.55%	0.74%±0.54%	-2.12%±0.16%
2	20475±109	20549±250	20319±97	0.00%±0.53%	0.36%±0.48%	-0.76%±1.21%
3	20455±162	20686±229	20382±179	0.00%±0.79%	-1.13%±0.88%	-0.36%±1.11%
4	20499±132	19718±50	19477±14	0.00%±0.65%	-3.81%±0.26%	-4.99%±0.07%
5	20057±191	29415±253	19928±187	0.00%±0.95%	1.79%±1.24%	-0.64%±0.94%
$Mean_2$ (5) ± SD_2(5)	20405±44	20412±80	20042±146	0.00%±0.21%	0.04%±0.39%	-1.77%±0.73%
Group 2 OSLD #	**Phantom 3 Equivalent thickness: 18.88cm**					
1	17625±151	17479±137	16453±96	0.00%±0.85%	-0.83%±0.78%	-6.35%±0.73%
2	17938±52	17998±121	17110±98	0.00%±0.29%	0.33%±0.67%	-4.62%±0.57%
3	17735±184	17818±239	17446±135	0.00%±1.04%	0.47%±1.34%	-1.63%±0.77%
4	18018±206	17926±134	17448±154	0.00%±1.14%	-0.51±0.75%	-3.16%±0.88%
5	17817±196	17907±202	17398±175	0.00%±1.10%	0.51%±1.13%	-2.35%±1.01%
$Mean_2$ (5) ± SD_2(5)	17826±125	17826±74	17171±162	0.00%±0.71%	0.00%±0.42%	-3.68%±0.94%
Group 3 OSLD #	**Phantom 4 Equivalent thickness: 22.24cm**					
1	14388±111	14313±57	13634±79	0.00%±0.77%	-0.52%±0.40%	-5.24%±0.58%
2	14728±24	14606±25	13656±109	0.00%±0.16%	-0.83%±0.17%	-7.28%±0.80%
3	14398±59	14282±58	13690±95	0.00%±0.41%	-0.81%±0.41%	-4.92%±0.69%
4	14412±67	14229±87	13603±58	0.00%±0.46%	-1.27%±0.61%	-5.61%±0.43%
5	14678±76	14279±72	14027±141	0.00%±.052%	-2.71%±0.51%	-4.43%±1.01%
$Mean_2$ (5) ± SD_2(5)	14521±167	14342±150	13722±173	0.00%±1.15%	-1.23%±1.05%	-5.50%±1.26%

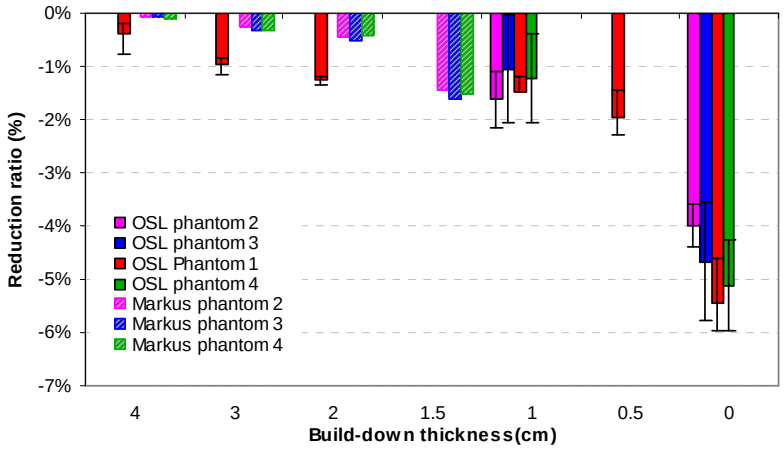

Figure 9.37 OSL Experiment 2 results (2): Reduction ratios of a variation in back scatter thicknesses to full backscatter (5.0cm). Average reductions ratios of multiple irradiations are shown with the error bars of standard deviations of irradiations (SD_2) were added. The data is compared with Markus Experiment 3 results.

The data was compared with that of Markus ion chamber measurement using the same setup as described in section 9.10. Due to the physical structure of the PTW Markus Ion-chamber, the final back scatter thicknesses were based on Markus default back scatter (1.4cm) plus additional back scatter. Only the data of the Markus with 0.5cm back scatter and Markus in the air was used for comparison (Figure 9.37). The reduction ratios of the Markus ion chamber in this comparison are normalized to an additional 5.5cm back scatter condition as there was no data with an additional 3.5cm back scatter. The difference between additional 3.5cm and 5.5cm back scatter are -0.14%, which can be ignored.

9.19 Summary of section 9.17~9.18

In comparing OSL Experiment 2 to the measurement results of the Markus chamber from Markus Experiment 3 in section 9.10, the following similarities in exit dose measurements were found using OSLDs and an ionisation chamber:

- Both OSLD and Markus Chamber readings decrease slightly with decreases in back scatter thicknesses.
- Beginning with a 5.0cm thickness back scatter, the percentage difference becomes more negative as the back scatter thickness is reduced. The OSLD measurements show a maximum reduction with no additional back scatter.

- The reduction ratios show a dramatic drop when no additional back scatter is added, showing up to 2%~6% lower than the full backscatter (5.0cm) condition. With 0.5cm back scatter added the reduction ratio increases to within 2% lower than that at full backscatter. There is no significant change when back scatter thicknesses vary from 0.5cm to 5 cm.
- As the equivalent thickness increases the reduction ratio increases.
- When the phantom contains a lower density tissue equivalent material (RED=0.22), which is the shortest equivalent thickness (14.58 cm) in this study, the OSLD response with no additional back scatter shows a maximum 2% reduction than that at the full backscatter for the three exposures, the average being 1%.
- When the phantom contains a higher density tissue material (RED=1.53), which is the deepest equivalent thickness (22.24cm) in this study, the OSLD response with no additional back scatter shows a maximum 7% reduction than that of the full backscatter condition for three exposures, the average being 6%.
- The data measured by the OSLs show slightly higher responses (the reduction ratio is lower) than those measured by the Markus ion chamber.
- The standard deviation between OSLDs is about 1%.
- Therefore it is suggested to use a minimum of 0.5 cm back scatter thickness for OSLs in exit dose dosimetry. This will reduce the OSL value only 2% compared to that at the full scatter condition.

9.20 OSL Experiment 3: Verification and comparison of OSL measurement data

9.20.1 Methodology

In this study, the data measured by OSL in OSL Experiment 1 (Measurement performed at isocentre in homogenous phantom) was compared with that of OSL Experiment 2 (Measurement performed at isocentre in heterogenous phantom) with and without backscatter to the clinical TMR data, and to that measured by PTW Markus ion chamber from Markus Experiment 3.

OSL calibration is critical for the absolute dose measurement. The data from OSLs, from the same package, calibrated at dmax (the mean of three readings) as shown

in section 9.16 were used. The data from OSL Experiment 1 and OSL Experiment 2 were chosen for comparison as there is no need to perform an inverse square calculation. The data was firstly normalized to the OSL calibration value at dmax for each field size, and then compared to the depth dose(TMR) data described in section 10.2, and then to the data of the Markus measurement from experiment Exit Dose Markus Three in section 9.10. Three back scatter conditions were compared for both the Markus chamber and the OSLDs: 1) the data from the Markus chamber with a 5.5cm back scatter was compared to that of the OSL with a 5.0cm back scatter; 2) the data of the Markus ion chamber only (with no additional back scatter and no surrounding solid water) was compared to that of the OSL with no additional back scatter; 3) the data from the Markus ion-chamber with 0.5cm additional back scatter are compared to that by OSL with 1cm additional back scatter.

9.20.2 Results

Table 9.14 compares the measurements of the OSLs to that of the depth dose (TMR) values and to the data measured by the Markus chamber from Markus Experiment 3 in section 9.10.

Table 9.14a shows the results at the full backscatter condition, Table 9.14b shows the results at the 1cm backscatter condition. Table 9.14c shows the result with no additional back scatter. The raw data is (1) used from OSL Experiments 1 and 2. The raw data at the d_{max} of 6MV (2) is quoted from section 9.17 and section 9.18. The correction factors (4) were calculated using EPL method based on tissue inserts relative RED calculated in section 9.3. TMR data (6) at the phantom's geometrical depth of 18cm of the phantom at the measurement point of chamber were set as reference. Data was normalized to dmax of 6MV x-rays (3), corrected with the CF correction method for the heterogeneity correction using EPL the method (4). The difference to both the depth dose (TMR) (7) and Markus data (8) were calculated by the equations described in the tables.

Figure 9.38 shows the comparison of results from the OSLs to those of the TMR value. The TMR are shown in a solid line with ±5% error bars added. The OSL data with their tissue inserts EPL correction are show using various colour markers.

Figure 9.39 shows the differences of the OSL data to those of the TMR value and the Markus chamber.

Table 9.14a: OSL Experiment 3 results (1): OSL Verification measurement data of a phantom with tissue equivalent inclusions. Full backscatter material (5.0cm) was added to the OSLDs. All data was acquired using 100mu 6MV x-rays. Columns 1-5 refer to OSLD measurements. Columns 6 and 8 refer to the TMR and Markus chamber data for comparison. Correction factors (4) were calculated using the effective SSD method based on relative RED to water calculated. $Diff_1$ is the difference between the OSL measurements and the reference TMR. $Diff_2$ is the difference between OSL measurements and the Markus data with an additional 5.5cm back scatter from Markus Experiment 3 in section 9.10. Other values were calculated based on the equations described in the table.

(1)	(2)	(3)	(4)	(5)	(6)	(7)	(8)	(9)
Raw data	**Raw data at dmax**	**Data Normalized to dmax** (1)/(2)	**Correction Factor (CF)**	**Data with CF Correction** (1)/(2)	**Ref TMR (d=18)**	**$Diff_1$ (%)** $\frac{(5)-(6)}{100}$	**Markus data**	**$Diff_2$ (%)** $\frac{(5)-(8)}{100}$
Phantom 2 includes insert with RED=0.22, Equivalent thickness=14.58cm								
20499	31983	0.5511	0.9686	0.5689	0.5652	-0.76%	0.5605	-0.29%
20539	31983	0.5496	0.9686	0.5675	0.5652	-0.65%	0.5605	-0.18%
20475	31983	0.5434	0.9686	0.5610	0.5652	-0.83%	0.5605	-0.36%
20378	31983	0.5365	0.9686	0.5539	0.5652	-1.09%	0.5605	-0.62%
20455	31983	0.5459	0.9686	0.5636	0.5652	-0.88%	0.5605	-0.41%
				Average		**-0.84%**		**-0.37%**
				Minimum		**-1.09%**		**-0.62%**
				Maximum		**-0.65%**		**-0.18%**
Phantom 3 includes insert with RED=0.97, Equivalent thickness=18.88cm								
17625	31983	0.4499	0.837	0.5375	0.5652	0.37%	0.5715	-0.26%
17579	31983	0.4559	0.837	0.5447	0.5652	0.23%	0.5715	-0.40%
17380	31983	0.4502	0.837	0.5378	0.5652	-0.42%	0.5715	-1.05%
17160	31983	0.4506	0.837	0.5384	0.5652	-1.13%	0.5715	-1.76%
17460	31983	0.4542	0.837	0.5427	0.5652	-0.16%	0.5715	-0.79%
				Average		**-0.22%**		**-0.85%**
				Minimum		**-1.13%**		**-1.76%**
				Maximum		**0.37%**		**-0.26%**
Phantom 4 includes insert with RED =1.53, Equivalent thickness=22.24cm								
14388	31983	0.4499	0.837	0.5375	0.5652	-2.77%	0.5401	-0.26%
14581	31983	0.4559	0.837	0.5447	0.5652	-2.05%	0.5401	0.46%
14398	31983	0.4502	0.837	0.5378	0.5652	-2.74%	0.5401	-0.23%
14412	31983	0.4506	0.837	0.5384	0.5652	-2.68%	0.5401	-0.17%
14528	31983	0.4542	0.837	0.5427	0.5652	-2.25%	0.5401	0.26%
				Average		**-2.50%**		**0.01%**
				Minimum		**-2.77%**		**-0.26%**
				Maximum		**-2.05%**		**0.46%**
Phantom 1 with RED=1.08, Equivalent thickness=19.44cm								
17189	31983	0.5375	0.9461	0.5681	0.5652	0.29%		
17219	31983	0.5384	0.9461	0.5690	0.5652	0.38%		
17200	31983	0.5378	0.9461	0.5684	0.5652	0.32%		
17048	31983	0.5330	0.9461	0.5634	0.5652	-0.18%		
17192	31983	0.5375	0.9461	0.5682	0.5652	0.30%		
				Average		**0.33%**		
				Minimum		**0.29%**		
				Maximum		**0.38%**		

Table 9.14b: OSL Experiment 3 result (2): OSL Verification measurement data of a phantom with tissue equivalent inclusions. Partial backscatter material (1.0cm) was added to the OSLDs. All data was acquired using 100mu 6MV x-rays. Columns 1-5 refer to OSLD measurements. Columns 6 and 8 refer to the TMR and Markus chamber data for comparison. Correction factors (4) were calculated using the effective SSD method based on relative RED to water calculated in Chapter 9. $Diff_1$ is the difference between the OSL measurements and the reference TMR. $Diff_2$ is the difference between the OSL measurements and the Markus data with an additional 0.5cm back scatter from the Markus Experiment in section 9.10. Other values were calculated based on the equations described in the table.

(1)	(2)	(3)	(4)	(5)	(6)	(7)	(8)	(9)
Raw data	**Raw data at dmax**	**Data Normalized to dmax** (1)/(2)	**Correction Factor (CF)**	**Data with CF Correction** (1)/(2)	**Ref TMR (d=18)**	**$Diff_1$ (%)** $\frac{(5)-(6)}{100}$	**Markus data**	**$Diff_2$ (%)** $\frac{(5)-(8)}{100}$
Phantom 2 includes insert with RED=0.22, Equivalent thickness=14.58cm								
20112	31983	0.6288	1.1495	0.5470	0.5652	-1.82%	0.5605	-1.35%
20277	31983	0.6340	1.1495	0.5515	0.5652	-1.37%	0.5605	-0.90%
20138	31983	0.6297	1.1495	0.5478	0.5652	-1.74%	0.5605	-1.27%
20088	31983	0.6281	1.1495	0.5464	0.5652	-1.88%	0.5605	-1.41%
20066	31983	0.6274	1.1495	0.5458	0.5652	-1.94%	0.5605	-1.47%
				Average		**-1.75%**		**-1.28%**
				Minimum		**-1.94%**		**-1.47%**
				Maximum		**-1.37%**		**-0.90%**
Phantom 3 includes insert with RED=0.97, Equivalent thickness=18.88cm								
17479	31983	0.5465	0.9686	0.5642	0.5652	-0.10%	0.5715	-0.33%
17368	31983	0.5430	0.9686	0.5606	0.5652	-0.46%	0.5715	-0.69%
17194	31983	0.5376	0.9686	0.5550	0.5652	-1.02%	0.5715	-1.25%
16959	31983	0.5303	0.9686	0.5474	0.5652	-1.78%	0.5715	-2.01%
17281	31983	0.5403	0.9686	0.5578	0.5652	-0.74%	0.5715	-0.97%
				Average		**-0.82%**		**-1.05%**
				Minimum		**-1.78%**		**-2.01%**
				Maximum		**-0.10%**		**-0.33%**
Phantom 4 includes insert with RED =1.53, Equivalent thickness=22.24cm								
14313	31983	0.4475	0.837	0.5347	0.5652	-3.05%	0.5401	-2.23%
14459	31983	0.4521	0.837	0.5401	0.5652	-2.51%	0.5401	-1.69%
14282	31983	0.4465	0.837	0.5335	0.5652	-3.17%	0.5401	-2.35%
14229	31983	0.4449	0.837	0.5315	0.5652	-3.37%	0.5401	-2.55%
14133	31983	0.4419	0.837	0.5280	0.5652	-3.72%	0.5401	-2.90%
				Average		**-3.16%**		**-2.34%**
				Minimum		**-3.72%**		**-2.90%**
				Maximum		**-2.51%**		**-1.69%**
Phantom 1 with RED=1.08, Equivalent thickness=19.44cm								
16904	31983	0.5285	0.9461	0.5586	0.5652	-0.66%		
16955	31983	0.5301	0.9461	0.5603	0.5652	-0.49%		
16910	31983	0.5287	0.9461	0.5588	0.5652	-0.64%		
16833	31983	0.5263	0.9461	0.5563	0.5652	-0.89%		
16960	31983	0.5303	0.9461	0.5605	0.5652	-0.47%		
				Average		**-0.63%**		
				Minimum		**-0.89%**		
				Maximum		**-0.47%**		

Table 9.14c: OSL Experiment 3 result (3): OSL Verification measurement data of a phantom with tissue equivalent inclusions. No additional backscatter material was added to the OSLDs. All data was acquired using 100mu 6MV x-rays. Columns 1-5 refer to OSLD measurements. Columns 6 and 8 refer to the TMR and Markus chamber data for comparison. Correction factors (4) were calculated using the effective SSD method based on the relative RED to water calculated in Chapter 9. $Diff_1$ is the difference between the OSL measurements and the reference TMR. $Diff_2$ is the difference between OSL measurements and Markus data with the chamber only (no additional builddown and no solid water surrounded) data from Markus Experiment in section 9.10. Other values were calculated based on the equations described in the table.

(1)	(2)	(3)	(4)	(5)	(6)	(7)	(8)	(9)
Raw data	**Raw data at dmax**	**Data Normalized to dmax** (1)/(2)	**Correction Factor (CF)**	**Data with CF Correction** (1)/(2)	**Ref TMR (d=18)**	**$Diff_1$ (%)** $\frac{(5)-(6)}{100}$	**Markus data**	**$Diff_2$ (%)** $\frac{(5)-(8)}{100}$
Phantom 2 includes insert with RED=0.22, Equivalent thickness=14.58cm								
19672	31983	0.6151	1.1495	0.5351	0.5652	-3.01%	0.5605	-1.70%
19700	31983	0.6160	1.1495	0.5358	0.5652	-2.94%	0.5605	-1.63%
19710	31983	0.6163	1.1495	0.5361	0.5652	-2.91%	0.5605	-1.60%
19610	31983	0.6131	1.1495	0.5334	0.5652	-3.18%	0.5605	-1.87%
19566	31983	0.6118	1.1495	0.5322	0.5652	-3.30%	0.5605	-1.99%
				Average		**-3.07%**		**-1.76%**
				Minimum		**-3.30%**		**-1.99%**
				Maximum		**-2.91%**		**-1.60%**
Phantom 3 includes insert with RED=0.97, Equivalent thickness=18.88cm								
16453	31983	0.5144	0.9686	0.5311	0.5652	-3.41%	0.5715	-3.40%
16597	31983	0.5189	0.9686	0.5357	0.5652	-2.95%	0.5715	-2.94%
16748	31983	0.5237	0.9686	0.5406	0.5652	-2.46%	0.5715	-2.45%
16451	31983	0.5144	0.9686	0.5310	0.5652	-3.42%	0.5715	-3.41%
16876	31983	0.5276	0.9686	0.5447	0.5652	-2.05%	0.5715	-2.04%
				Average		**-2.85%**		**-2.84%**
				Minimum		**-3.42%**		**-3.41%**
				Maximum		**-2.05%**		**-2.04%**
Phantom 4 includes insert with RED =1.53, Equivalent thickness=22.24cm								
13634	31983	0.4263	0.837	0.5093	0.5652	-5.59%	0.5401	-2.22%
13793	31983	0.4313	0.837	0.5152	0.5652	-5.00%	0.5401	-1.63%
13690	31983	0.4280	0.837	0.5114	0.5652	-5.38%	0.5401	-2.01%
13603	31983	0.4253	0.837	0.5081	0.5652	-5.71%	0.5401	-2.34%
13884	31983	0.4341	0.837	0.5186	0.5652	-4.66%	0.5401	-1.29%
				Average		**-5.27%**		**-1.90%**
				Minimum		**-5.71%**		**-2.34%**
				Maximum		**-4.66%**		**-1.29%**
Phantom 1 with RED=1.08, Equivalent thickness=19.44cm								
16330	31983	0.5106	0.9461	0.5397	0.5652	-2.55%		
16238	31983	0.5077	0.9461	0.5366	0.5652	-2.86%		
16023	31983	0.5010	0.9461	0.5295	0.5652	-3.57%		
16372	31983	0.5068	0.9461	0.5357	0.5652	-2.95%		
16880	31983	0.5120	0.9461	0.5411	0.5652	-2.41%		
				Average		**-2.87%**		
				Minimum		**-2.87%**		
				Maximum		**-3.57%**		

(a)

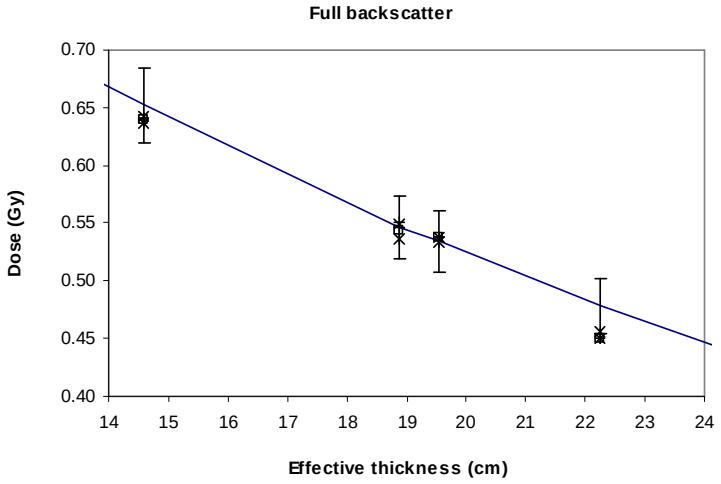

(b)

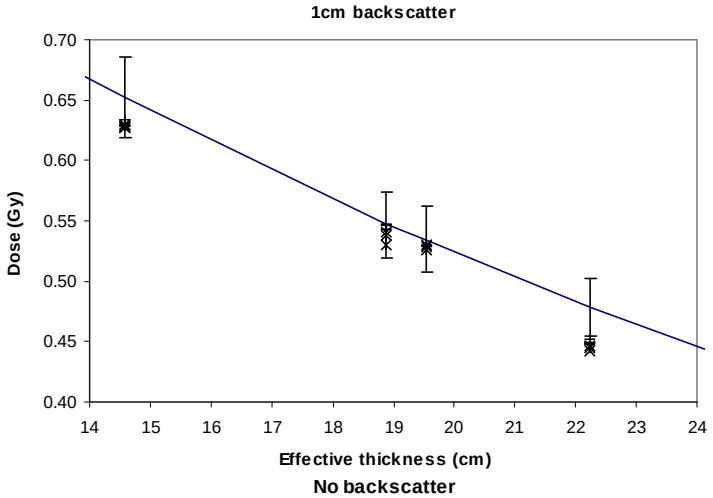

(c)

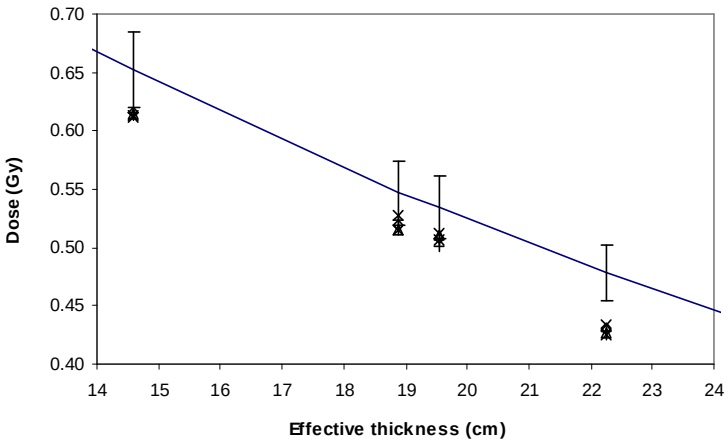

Figure 9.38 OSL Experiment 3, verification and comparison of OSL measurement results (1): Normalized OSL measurement vs. reference TMR data. The reference TMR data shows as a solid line with a ±5% error bar added. The OSL measurement data normalized to dmax are show as various color markers as given in Table 9.14. (a) 5.0cm solid water used as back scatter behind the OSLD; (b) 1.0cm solid water used as back scatter behind the OSLD; (c) no additional back scatter added.

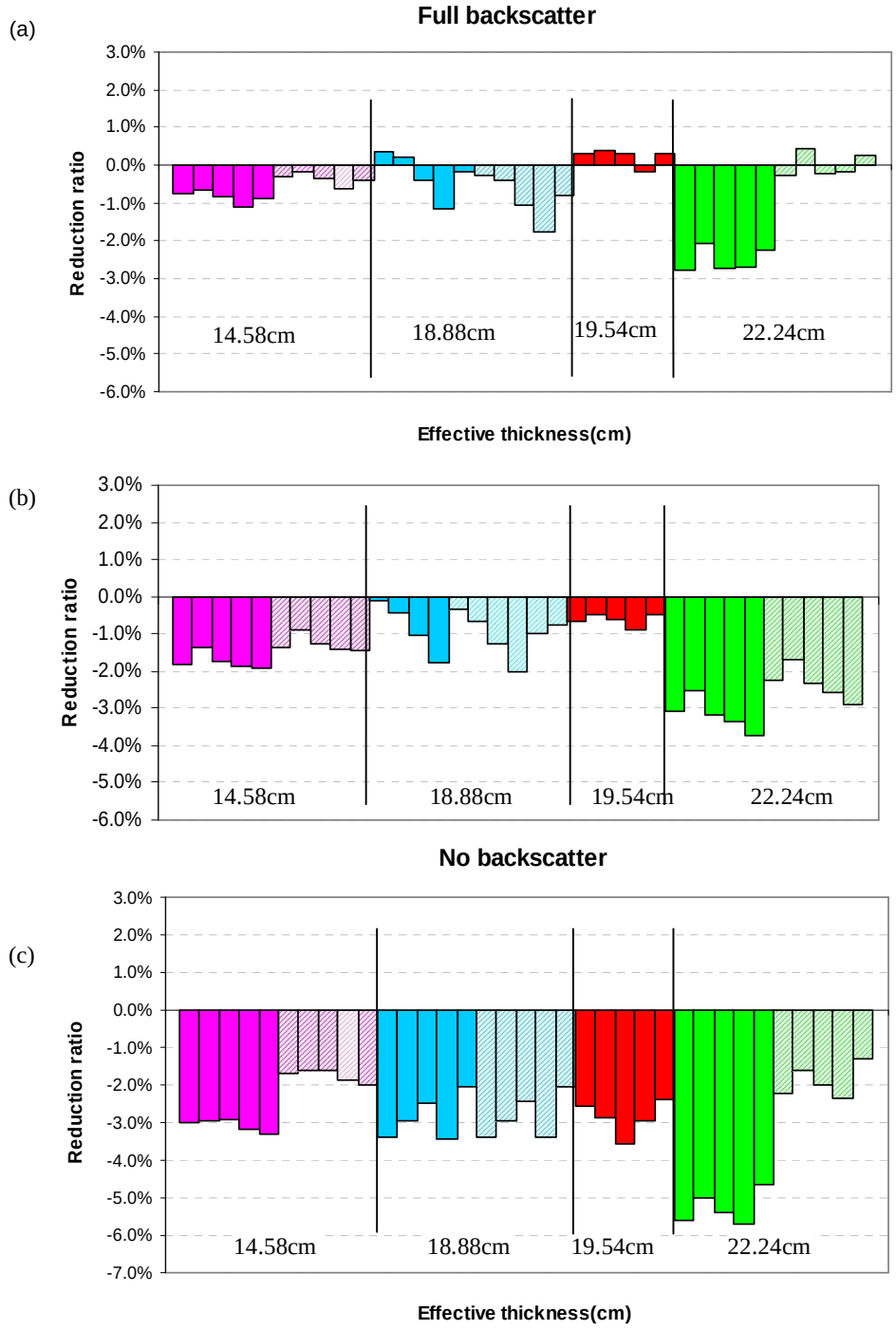

Figure 9.39 OSL Experiment 3, verification of OSL measurement result (2): Ratio difference between OSL data to reference TMR data (solid column) and Markus data (diagonal column) in (a) full backscatter and (b) 1cm backscatter and (c) no backscatter. The phantoms have various equivalent thicknesses.

From the results it was found:

(1) Compared to the depth dose (TMR) data:

   a. At the full backscatter (Figure 9.38a) condition, phantom 1 to phantom 3 show an approximately ±1% difference to the depth dose data, while for phantom 4 with longer equivalent thicknesses the data shows a maximum 2.8% (2.5% on average) reduction. The data for phantom 1 and phantom 3 with a RED much closer to the water show the lowest difference to the depth dose data.

   b. The OSL data at the 1cm backscatter condition (Figure 9.39b) show slightly lower responses (a reduction of 1%) than those at the full backscatter condition. The overall reduction difference to the depth dose data is within 2% for phantom 2, which has an equivalent thickness of 14.58cm. Similar to the data at the full backscatter condition, the data in phantom 1 and phantom 3, with a RED much closer to the water, show the lowest differences (within 1% on average) to the depth dose values. The data for phantom 4 with a greater equivalent thickness shows up to a maximum of 3.7% (3.2% on average) reduction when compared to the data from depth dose values.

   c. In the no backscatter condition (Figure 9.39c), the OSL data shows much lower responses (reduced 2%) compared to the depth dose data. The overall reduction difference to depth dose is up to 3% on average for phantom 1 to phantom 3. The data for phantom 4 with longer equivalent thickness shows up to maximum 5.7% (5.3% on average) reduction compared to the data from the depth dose values.

(2) Compared to the data from the Markus chamber measurements in Markus Experiment 2 in section 9.9:

   a. At the full backscatter condition (Figure 9.39a), the OSL data show a slightly lower response than the Markus chamber, but within 1% on average for phantom 2 and phantom 3. There is a slightly higher response compared to the Markus chamber, but within 1% on average for phantom 4 with a longer equivalent thickness.

   b. The data from the Markus chamber with 0.5cm added back scatter were compared to the OSL data with a 1cm back scatter (Figure 9.39b) (due to a consideration of the Markus design 1.4cm build-in

back scatter behind the effective measurement point). The OSL data shows a 1.5% reduction on average to those of the Markus chamber for phantom 2 and phantom 3, while showing a 2.5% reduction on average for phantom 4.

c. In the no backscatter condition (Figure 9.39c), OSL data shows a reduction of up to 2%, 3% and 2% on average for phantom 2, phantom 3 and phantom 4, respectively.

d. It should be noted that the OSL data with no additional builddown for phantom 4 shows a slightly lower reduction ratio to the OSL data with 1cm backscatter compared to the Markus chamber data.

Figure 9.40 shows a comparison of OSL data at isocentre to depth dose data. The OSL data is combined with the data from section 9.16 and section 9.17. OSL data with a 5.0cm back scatter added is shown in red; with a 1.0cm back scatter added in blue and with no additional back scatter added in green.

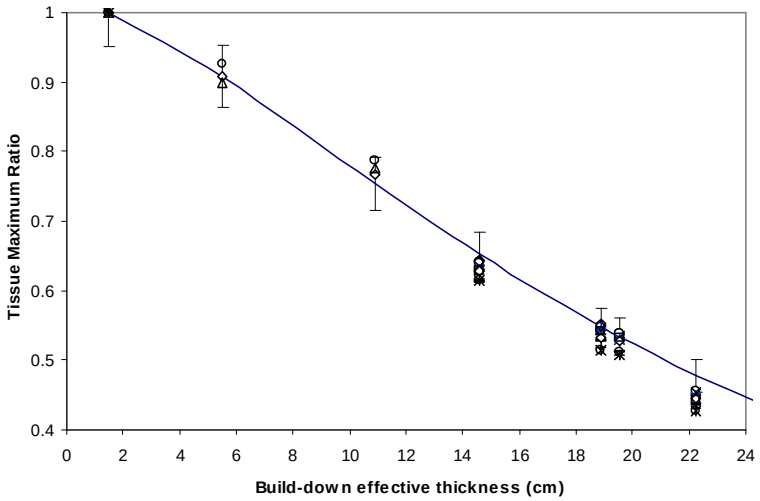

Figure 9.40 OSL Experiment 3 results (3): summarised comparison of OSL isocentre measurement data compared to TMR data. TMR data is shown with a blue solid line with a ±5% error bar added. The OSL data normalized to d_{max} is shown with red, blue and green markers for an additional back scatter of 5.0cm, 1.0cm and no additional back scatter added, respectively.

9.21 OSL Experiment 4: Measurement point set on the exit surface on the beam axis in heterogeneous phantom

9.21.1 Methodology

In this study a real patient treatment was simulated and the exit doses measured using OSLDs . The irradiation isocentre was set at the phantom centre and the effective measurement point was set on the exit surface along the beam axis. The experiment was performed using a homogeneous phantom with tissue equivalent material inserts.

Figure 9.41 shows a schematic of the setup used for this experiment. The combination of the phantom and inserts are the same as described in the previous section. However, this time the isocentre was set at the phantom centre (the insert's centre as well). The centre of the OSLD was set to the exit surface on the beam axis, 109cm away from the source at a 91cm SSD. The OSLD was either inserted in the placement or mounted on the exit surface of the phantom (no additional back scatter).

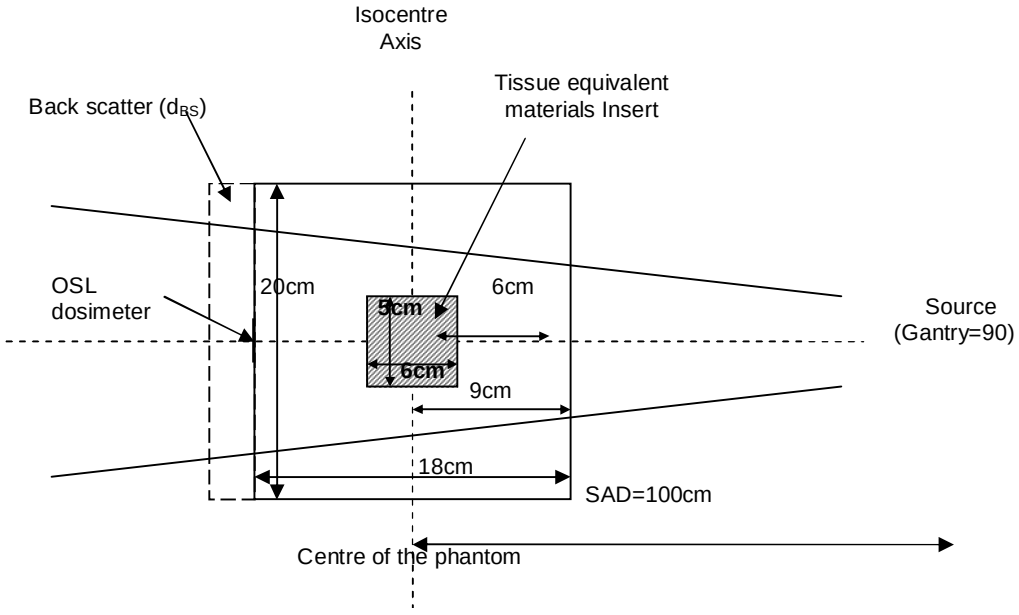

Figure 9.41 Schematic of a setup to assess how back scatter thickness influence measurements with an effective measurement point at the exit surface on in a homogeneous phantom using the same tissue equivalent materials inserts as in OSL Experiment 4.

For comparison, three additional back scatter (d_{BS}) thicknesses were chosen, 5cm,

1cm and none (OSLD in air). The equivalent back scatter thicknesses were calculated using the EPL method and are shown in section 9.4.

The experimental method and data management is the same as those described in OSL Experiment 1 (Measurement performed at isocentre in homogeneous phantom). All of the OSL discs were oriented so that the same sensitive face was used during irradiation and readout. 9 Dot OSLDs were divided into three groups of 3 OSLDs for phantom 2, 3 and 4. Considering the useable life-span of OSLD's, each OSLD was irradiated three times using the three back scatter conditions. With each identical phantom the experiment repeated three(3) times using 3 OSLDs. All OSLDs were read prior to irradiation and the readings set as background. The difference between the post-irradiation and pre-irradiation signal of photomultiplier tube of OSL reader were taken. No intermediate annealing procedure was used between exposures.

All measurements were taken by with 100MU 6MV x-rays with a 10x10cm^2 field size at isocentre. The output readings from a MicroStar reader were repeated 10 times and the average was taken for each irradiation. A back scatter thickness 5.0cm was defined as the full backscatter condition. The data at the other back scatter thickness conditions was compared to the data at full backscatter.

The data measured with OSLDs were compared to that of the Markus ion chamber from Markus Experiment 2 in section 9.9.2 which used the same setup. Considering the physical structure of a PTW Markus Ion-chamber, the final back scatter thicknesses for chamber were based on the Markus default back scatter thickness (1.4cm) plus additional back scatter thickness. The data from a Markus chamber with a 3.5cm back scatter and that of a Markus chamber in air are comparable. The data was re-normalized to the 3.5cm additional back scatter, making the final back scatter thickness equivalent to 5.0cm.

9.21.2 Results

Table 9.15 shows the raw OSL readings and the reduction ratio (comparing the raw readings at full backscatter (5.0cm) condition) measured in a homogeneous phantom with tissue equivalent material inserts. Figure 9.42 shows the raw readings only. Figure 9.43 shows the comparison (reduction) ratio of the data with various back scatter thicknesses to the data at the full backscatter condition in each measurement. Each raw reading is based on 10 repeated readings. A back scatter

of 5.0cm is considered the full backscatter condition and this data set was used as the reference. SD1 (10) present the standard deviations of 10 repeated readings, were added. The $Mean_2$ (3) and standard deviation (SD_2 (3)) are based on three irradiations of three OSLDs with the same back scatter condition. It should be noted that one OSLD used in phantom 3 with an equivalent thickness of 22.24cm seemed to have a very high response compared to that from another two OSLDs in the same builddown condition. However, there is not a large difference in the standard deviation for this OSLD among the three back scatter conditions.

The OSL results were compared with that of the Markus chamber measurements by using the same setup as in Markus Experiment 2 (Measurement performed at isocentre in heterogenous phantom) shown in section 9.9.2. Due to the physical structure of the PTW Markus Ion-chamber, the final back scatter thicknesses were based on Markus default back scatter (1.4cm) plus additional back scatter. The data from the Markus chamber only and with 0.5cm and a 5.5cm back scatter material added are comparable.

The results from OSL Experiments 4 were found to be very similar to those of the Markus Ion Chamber from Markus Experiment 2:

- The OSLD readings decrease slightly with a decrease in back scatter thickness.
- The difference compared to that at the 5.0cm back scatter condition becomes more negative as back scatter thickness reduces. The OSLD measurements with no additional back scatter show a maximum reduction.
- The overall reduction ratios show a dramatic drop when no additional back scatter material is added and are up to 6% lower than that of the full backscatter condition (5.0cm). With 1cm back scatter added the reduction ratio increases to maximum of 2% lower than that of the full backscatter condition. There is no significant change when the back scatter thicknesses vary from 1cm to 5 cm.
- As equivalent thickness increases, there is no significant difference in reduction ratios among the three phantom combinations (phantom 2, 3, and 4).
- OSL data shows a slightly higher response (lower reduction ratio) than that of the Markus chamber.

- The overall standard deviation among OSLDs are around 1.5%. Only one OSLD shows a higher difference of around 2.3%.

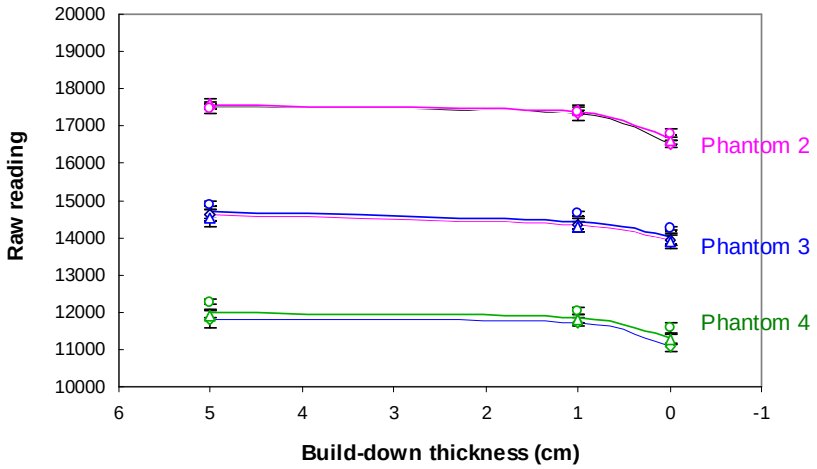

Figure 9.42 OSL Experiment 4 results (1): raw readings. The data from each measurement is shown in a certain colour with error bars added for the standard deviations of 10 readings. The averages of three OSLDs are shown with solid lines.

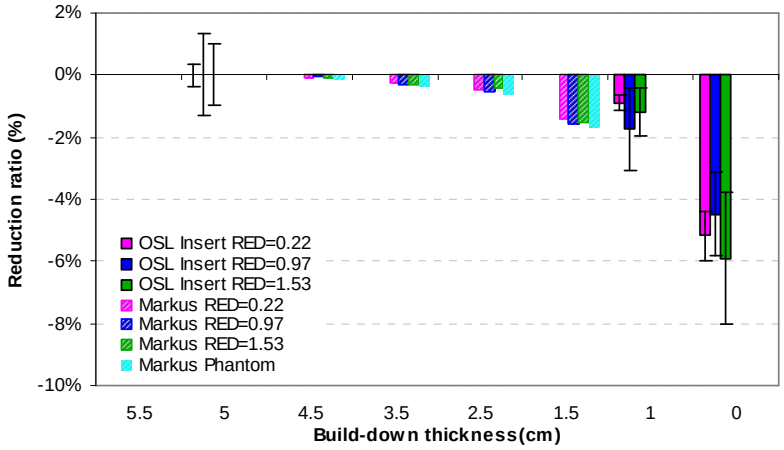

Figure 9.43 OSL Experiment 4 results (2): Reduction ratios due to variations in back scatters up to full backscatter (5.0cm). Average reduction ratios of multiple irradiations are shown with the error bars of standard deviations of the OLSDs (SD_2) added. The data is compared with the Markus results from Markus Experiment 2.

Table 9.15: OSL Experiment 4 results: (1) Raw readings and (2) Reduction ratios for OSLDs measurements with various thicknesses up to full backscatter in phantom 2, 3 and 4 (as named in chapter 9). Measurement points are at the exit surface and at the isocentre along the centre beam axis. 100 MU of 6MV and a 10x10cm^2 field size was used. Each irradiation of an OSLD was read 10 times and the average and standard deviations determined. $Mean_1$ and SD_1 are the average and standard deviation of 10 repeated readings of each OSLD under each irradiation. $Mean_2$ and SD_2 are the average and standard deviation of 3 OSLDs of their response builddown thickness in the phantoms, respectively.

	(1) Raw readings $Mean_1 \pm SD_1(10)$			**(2) Reduction ratio (%) $Mean_1 \pm SD_1(10)$**		
	Additional back scatter Physical Thickness(cm)					
	5.0	**1.0**	**None**	**5.0**	**1.0**	**None**
Group 1 OSLD #	**Homogeneous phantom (RED=1.08) includes insert with RED=0.22 Equivalent thickness=14.58cm**					
1	17533±78	17348±184	16521±107	0.00%±0.45%	-1.06%±1.06%	-5.77%±0.65%
2	17609±132	17429±106	16600±80	0.00%±0.75%	-1.03%±0.61%	-5.73%±0.48%
3	17481±153	17363±40	16778±161	0.00%±0.88%	-0.65%±0.23%	-4.02%±0.96%
$Mean_2$ (3)± SD_2(3)	17541±65	17381±42	16633±132	0.00%±0.37%	-0.91%±0.24%	-5.17%±0.79%
Group 2 OSLD #	**Homogeneous phantom (RED=1.08) includes insert with RED=0.97 Equivalent thickness=18.88cm**					
1	14635±107	14360±183	13937±128	0.00%±0.73%	-1.88%±1.27%	-4.77%±0.92%
2	14532±239	14287±131	13912±191	0.00%±1.65%	-1.69%±0.92%	-4.27%±1.37%
3	14908±66	14648±70	14256±57	0.00%±0.44%	1.74%±0.47%	-4.38%±0..40%
$Mean_2$ (3) ± SD_2(3)	14692±194	14432±191	14035±192	0.00%±1.32%	-1.77%±1.32%	-4.47%±1.37%
Group 3 OSLD #	**Homogeneous phantom (RED=1.08) includes insert with RED =1.53 Equivalent thickness=22.24cm**					
1	11830±225	11739±118	11066±113	0.00%±1.90%	-0.77%±1.01%	-6.46%±1.02%
2	11919±148	11808±118	11246±144	0.00%±1.24%	-0.94%±1.00%	-5.65%±1.28%
3	12272±73	12049±84	11586±130	0.00%±1.02%	-1.81%±0.07%	-5.59%±1.12%
$Mean_2$ (3) ± SD_2(3)	12007±233	11866±162	11299±263	0.00%±1.95%	-1.17%±1.36%	-5.90%±2.33%

9.22 OSL Experiment 5: Comparison of OSL measurement data to clinical TMR data and Markus ion chamber data

9.22.1 Methodology

Using the same methodology described in section 9.20 (OSL Experiment 3), the data measured using OSL in OSL Experiment 4 were compared to depth dose (TMR) data and to that measured using the PTW Markus ion chamber from Markus Experiment 2 in section 9.9.2. Linear accelerator commissioning data was considered as the theoretical data. It should be noted that there is no Tissue heterogeneity correction factor (CF) CF correction for the heterogeneity correction

applied in this experiment.

9.22.2 Results

Table 9.16 shows the results of the OSL measurements compared to depth dose (TMR) values and to those of the Markus chamber. Table 9.16a shows the result at the full backscatter condition. Table 9.16ab shows the result with 1cm backscatter added. Table 9.16c shows the result with no additional back scatter. The raw data (1) was also measured. Using the raw data at d_{max} of 6MV (2) from section 11.2, the averages of the four OSLDs at dmax are taken. The theoretical data (4) was obtained from a standard TMR table with relative equivalent depths. The Markus data is obtained form the Markus ion-chamber in Experiment 2 in section 9.9.2. Normalized vs. OSL data (3) is compared to the theoretical data (4) and to the Markus data (6) and the difference to reference data calculated using the equations described in the tables at the end of this section.

Figure 9.44 shows a comparison between OSL and depth dose values. The depth dose data are shown as a solid line with ±5% error bars added. The OSL data with their relative effective thicknesses corrected using EPL method show in various colour markers.

Figure 9.45 shows the differences between OSL and depth dose values and OSL and Markus ion chamber values.

The following results were found:

(1) Compared to the TMR data:

- At the full backscatter condition (Figure 9.45a), the OSL data for phantom 1 to phantom 2 show an overall difference within ±1% to the depth dose data. For phantom 4, with longer equivalent thickness, there is up to a maximum of a 3.2% (3.0% on average) reduction compared to depth dose data.
- At the 1cm backscatter condition (Figure 9.45b) OSLs show slightly lower responses (reduce 0.5%~1.0%) compared to those at the full backscatter condition. Dose response reduce up to 1% for phantom 2 and 1.5% for phantom 3. For phantom 4, with a greater equivalent thickness there is a maximum of a 3.5% (3.1% on average) reduction in depth dose.

- At the no backscatter condition (Figure 9.45c) OSLs show much lower responses than the theoretical data. The overall reduction difference to TMR is up to 3% for phantom 2 and phantom 3. For phantom 4, with a greater equivalent thickness, there is a maximum of a 5.6% (4.9% on average) reduction in depth dose.
- Compared to the OSL data acquired in OSL Experiment 3, which had a different measurement setup, the OSL data in this experiment show an approximately 0.5% lower response (higher reduction ratio).

(2) Compared to the data from the Markus measurements:

- At the full backscatter condition (Figure 9.45a), the OSL data shows a slightly higher response than that of the Markus data for phantom 2, but is within 1%. For phantom 3 and phantom 4, OSL data shows a slightly lower response than that of the Markus data, around 1% on average.
- The data of the Markus with a 0.5cm back scatter added is compared to OSL data with a 1cm back scatter due to consideration of the Markus design (1.4cm build-in back scatter behind the effective measurement point). The OSL data is 1% higher for phantom 2 and 1% lower for phantom 3 and 4 compared to the Markus chamber.
- At the no backscatter condition (Figure 9.45c), OSL data shows a reduction up to 1.8%, 2.8% and 2.3% on average for phantom 2, 3 and 4, respectively.
- It should be noted that the OSL data with no additional back scatter for phantom 4 shows a slightly higher reduction ratio than that of the 1cm backscatter and full backscatter condition. There is no significant difference between the data at full backscatter and the data at the 1cm backscatter condition.

Table 9.16a: OSL Experiment 5 results (1): Verification and comparison of OSL measurement data to clinical TMR data and Markus ion-chamber measurement data of a phantom with tissue equivalent inclusions. 5.0cm back scatter (full backscatter) was added to the OSLDs. All measured data was acquired using 100MU 6MV x-rays. OSL Raw data (1) at the 6MV dmax was measured. Doses were calculated from clinical TMR data and set as reference. $Diff_1$ is the difference between OSL measurement and theoretical dose. $Diff_2$ is the difference between OSL measurement and Markus data with an additional 5.5cm back scatter. Other values were calculated based on the equations described in the table**.**

(1)	(2)	(3)	(4)	(5)	(6)	(7)
Raw data	**Raw data at dmax**	**Data Normalized to dmax**	**Depth dose**	**$Diff_1$ (%)**	**Markus Normalized dose**	**$Diff_2$ (%)**
		(1)/(2)		$\frac{(4)-(5)}{100}$		$\frac{(4)-(6)}{100}$
Phantom 2 includes insert with RED=0.22, Equivalent thickness=14.58cm						
17533	31983	0.5482	0.5494	-0.12%	0.5418	0.64%
17609	31983	0.5506	0.5494	0.11%	0.5418	0.88%
17481	31983	0.5466	0.5494	-0.29%	0.5418	0.48%
			Average	**-0.10%**		**0.67%**
			Minimum	**-0.29%**		**0.48%**
			Maximum	**0.11%**		**0.88%**
Phantom 3 includes insert with RED=0.97, Equivalent thickness=18.88cm						
14635	31983	0.4576	0.4615	-0.39%	0.4712	-1.36%
14532	31983	0.4544	0.4615	-0.71%	0.4712	-1.68%
14908	31983	0.4661	0.4615	0.46%	0.4712	-0.51%
			Average	**-0.21%**		**-1.18%**
			Minimum	**-0.71%**		**-1.68%**
			Maximum	**1.13%**		**-0.51%**
Phantom 4 includes insert with RED =1.53, Equivalent thickness=22.24cm						
11830	31983	0.3460	0.3699	-3.23%	0.3828	-1.29%
11919	31983	0.3516	0.3727	-2.95%	0.3828	-1.01%
12272	31983	0.3622	0.3837	-1.84%	0.3828	0.09%
			Average	**-2.67%**		**-0.74%**
			Minimum	**-3.23%**		**-1.29%**
			Maximum	**-1.84%**		**0.09%**

Table 9.16b: Experiment Exit Dose OSL Five results (2): Verification and comparison of OSL measurement data to clinical TMR data and Markus ion-chamber measurement data of a phantom with tissue equivalent inclusions. 1.0cm back scatter (partial backscatter) was added to the OSLDs. All measurements were acquired using 100mu 6MV x-rays. OSL Raw data (1) at the 6MV dmax was measured. Doses were calculated from clinical TMR data and set as reference. $Diff_1$ is the difference between OSL measurement and theoretical dose. $Diff_2$ is the difference between OSL measurement and Markus data with an additional 0.5cm back scatter. Other values were calculated based on the equations described in the table.

(1)	**(2)**	**(3)**	**(4)**	**(5)**	**(6)**	**(7)**
Raw data	**Raw data at dmax**	**Data Normalized to dmax**	**Depth Dose**	**$Diff_1$ (%)**	**Markus Normalized dose**	**$Diff_2$ (%)**
		(1)/(2)		$\frac{(4)-(5)}{100}$		$\frac{(4)-(6)}{100}$
Phantom 2 includes insert with RED=0.22, Equivalent thickness=14.58cm						
17348	31983	0.5424	0.5494	-0.71%	0.5338	0.86%
17429	31983	0.5449	0.5494	-0.45%	0.5338	1.11%
17366	31983	0.5430	0.5494	-0.65%	0.5338	0.92%
			Average	**-0.60%**		**0.96%**
			Minimum	**-0.71%**		**0.86%**
			Maximum	**-0.45%**		**1.11%**
Phantom 3 includes insert with RED=0.97, Equivalent thickness=18.88cm						
14360	31983	0.4490	0.4615	-1.25%	0.4634	-1.44%
14287	31983	0.4467	0.4615	-1.48%	0.4634	-1.67%
14648	31983	0.4580	0.4615	-0.35%	0.4634	-0.54%
			Average	**-1.03%**		**-0.93%**
			Minimum	**-1.48%**		**-1.67%**
			Maximum	**-0.35%**		**-0.54%**
Phantom 4 includes insert with RED =1.53, Equivalent thickness=22.24cm						
11739	31983	0.3671	0.4022	-3.51%	0.3803	-1.32%
11808	31983	0.3692	0.4022	-3.30%	0.3803	-1.11%
12049	31983	0.3767	0.4022	-2.54%	0.3803	-0.35%
			Average	**-3.12%**		**-0.93%**
			Minimum	**-3.51%**		**-1.32%**
			Maximum	**-2.54%**		**-0.35%**

Table 9.16c: OSL Experiment 5 results (3): Verification and comparison of OSL measurement data to clinical TMR data and Markus ion-chamber measurement data of a phantom with tissue equivalent inclusions. No additional back scatter (no backscatter) was added to the OSLDs. Data was acquired using 100MU 6MV x-rays. OSL Raw data (1) at the 6MV dmax was measured. Doses were calculated from clinical TMR data and set as reference. $Diff_1$ is the difference between the OSL measurement and theoretical dose. $Diff_2$ is the difference between OSL measurement and Markus data with no additional back scatter. Other values were calculated based on the equations described in the table.

(1)	(2)	(3)	(4)	(5)	(6)	(7)
Raw data	**Raw data at dmax**	**Data Normalized to dmax**	**Depth dose**	**$Diff_1$ (%)**	**Markus Normalized dose**	**$Diff_2$ (%)**
		(1)/(2)		$\frac{(4)-(5)}{100}$		$\frac{(4)-(6)}{100}$
Phantom 2 includes insert with RED=0.22, Equivalent thickness=14.58cm						
16521	31983	0.5166	0.5494	-3.29%	0.5378	-2.12%
16600	31983	0.5190	0.5494	-3.04%	0.5378	-1.88%
16778	31983	0.5246	0.5494	-2.48%	0.5378	-1.32%
			Average	**-2.94%**		**-1.77%**
			Minimum	**-3.29%**		**-2.12%**
			Maximum	**-2.48%**		**-1.32%**
Phantom 3 includes insert with RED=0.97, Equivalent thickness=18.88cm						
13937	31983	0.4357	0.4615	-2.57%	0.4664	-3.07%
13912	31983	0.4350	0.4615	-2.65%	0.4664	-3.15%
14256	31983	0.4457	0.4615	-1.58%	0.4664	-2.07%
			Average	**-2.27%**		**-2.76%**
			Minimum	**-2.65%**		**-3.15%**
			Maximum	**-1.58%**		**-2.07%**
Phantom 4 includes insert with RED =1.53, Equivalent thickness=22.24cm						
11066	31983	0.3460	0.4022	-5.61%	0.3828	-3.04%
11246	31983	0.3516	0.4022	-5.05%	0.3828	-2.48%
11586	31983	0.3622	0.4022	-3.99%	0.3828	-1.42%
			Average	**-4.89%**		**-2.32%**
			Minimum	**-5.61%**		**-3.04%**
			Maximum	**-3.99%**		**-1.42%**

(a)

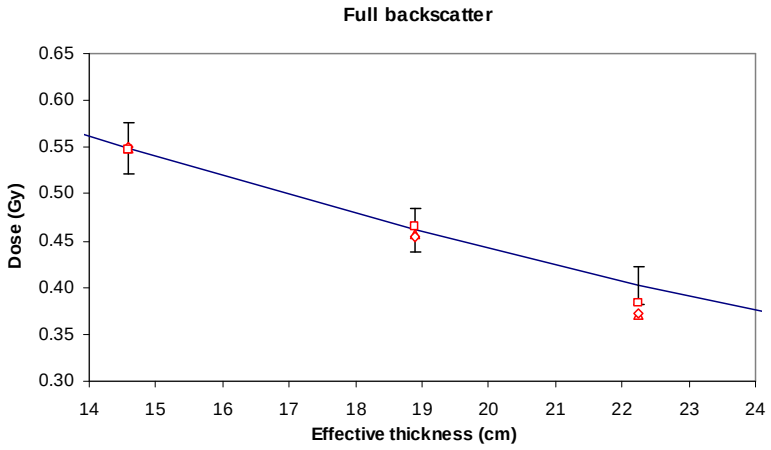

(b)

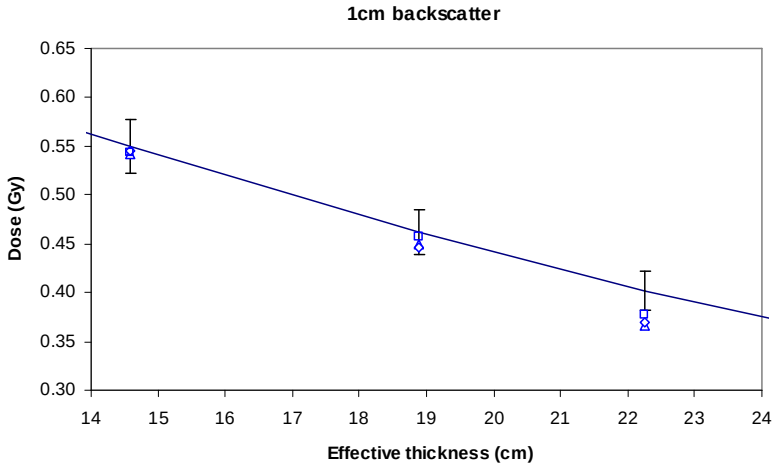

(c)

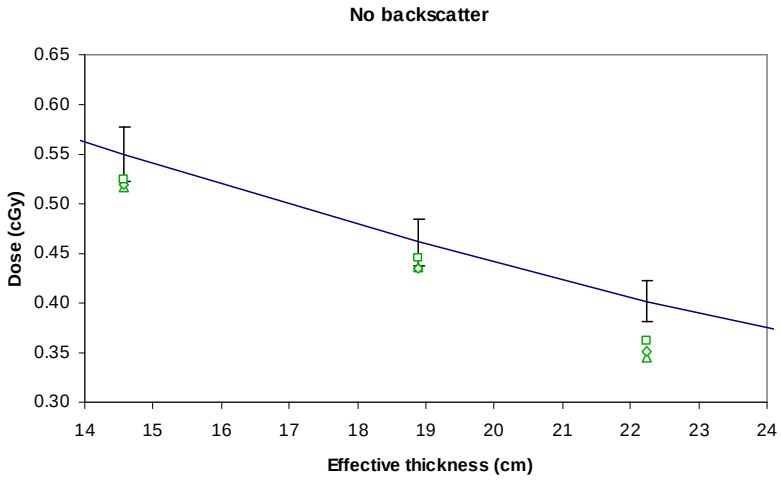

Figure 9.44 OSL Experiment 5 results: verification and comparison of OSL measurement vs. TMR values (1):TMR doses were obtained from the commissioning data of the linear accelerator used and are shown in a solid blue line with ±5% error bars added. Normalized OSL measurement doses were shown using various markers**.** (a) 5.0cm solid water as back scatter behind OSLD; (b) 1.0cm solid water as back scatter behind OSLD; (c) no additional back scatter added.

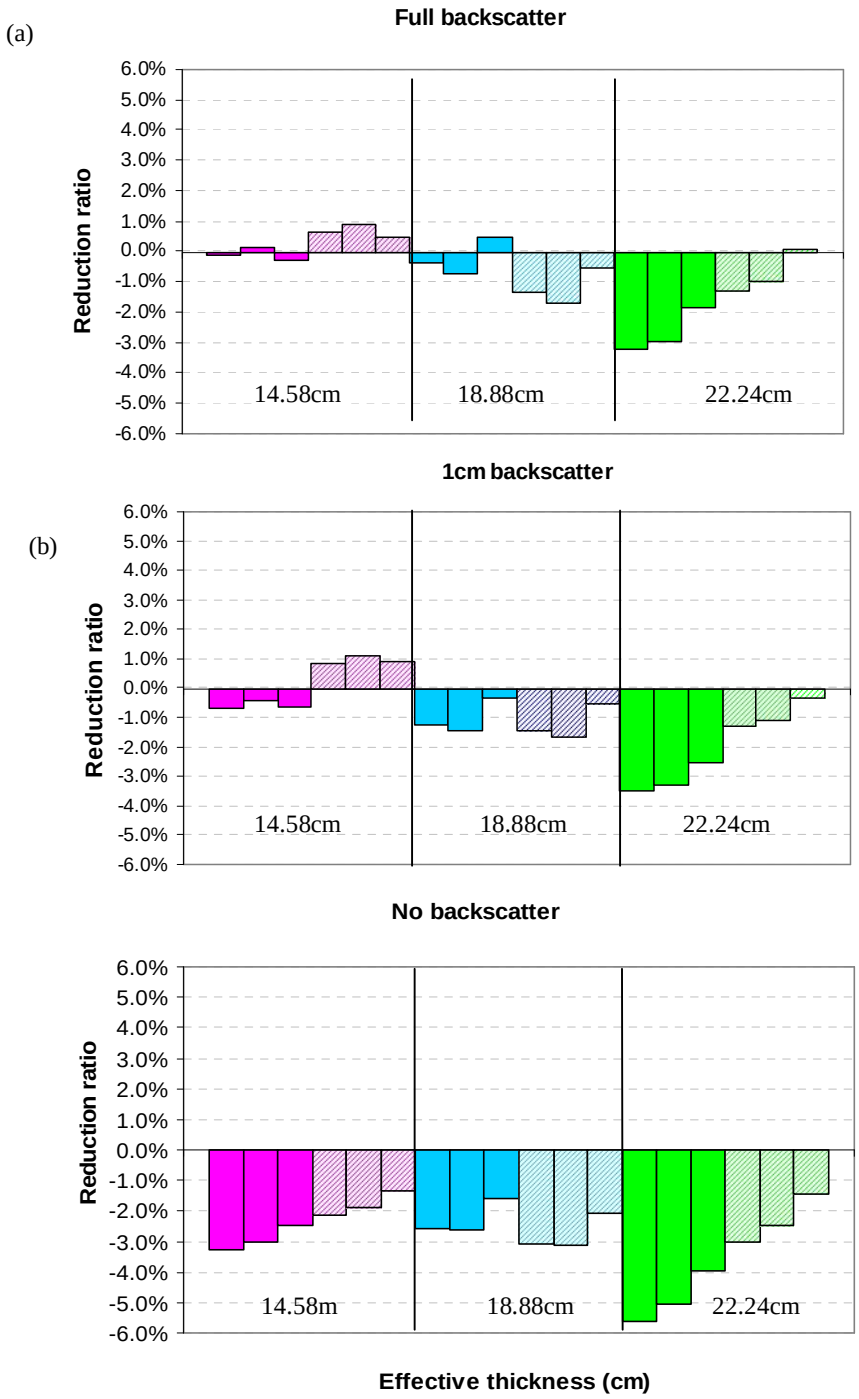

Figure 9.45 OSL Experiment 5 results: verification of OSL measurement results (2): Ratio difference between OSL data to depth dose data (solid column) and Markus data (diagonal column) in (a) full backscatter and (b) 1cm backscatter and (c) no backscatter. The phantoms have various effective thicknesses.

9.23 OSL Experiment 6: Exit dose vs. Field Size

Exit dose measurement is complicated due to the influence by lack of photon backscatter. For the Markus ion chamber, it is more pronounced by lack of photon back scatter. But for OSLs, which have similar characteristics to TLDs, exit dose measurement may be influenced by lack of secondary back scattered electrons (Kron and Ostwald, 1995). To test this OSLDs were used to measure the exit doses of different field sizes to find the discrepancy between various field sizes.

9.23.1 Methodology

Using the setup shown in Figure 9.41, the phantom and inserts combination was the same as described in the previous section. The centre of the OSLD was set to the exit surface on the beam axis, 109cm away from the source; SSD is 91cm. The OSLD was either inserted in the placement with a total backscatter thickness of 5.0cm or mounted on the exit surface of the phantom (no backscatter).

The experimental method and data analysis are the same as those described in OSL Experiment 1. All of the OSL discs were oriented in a way that the sensitive face was used during irradiation and readout. 12 Dot OSLDs were divided into four groups of 3 OSLDs for phantom 1, 2 and 3. Considering the OSLD's useable life-span, each OSLD was irradiated four times in an phantom with 5.0cm back scatter condition and four times with no backscatter added. The experiment was repeated three(3) times in each identical phantom by using 3 OSLDs respectively. All OSLDs were read prior to irradiation, and the readings were set as background. The difference between the post-irradiation and pre-irradiation signal of photomultiplier tube of OSL reader were taken. No intermediate annealing procedure was used between irradiations. No OSLD calibration was performed in this study and as a result all the raw data is relative.

All measurements were taken by delivering 100MU using 6MV x-rays to 4 selected field sizes (3x3, 5x5, 10x10, and 15x15 cm^2) at isocentre. The output readings were taken by a MicroStar reader and repeated 10 times. The average was taken for each irradiation. The back scatter thickness 5.0cm was defined as the full backscatter condition. The readings at the other back scatter thickness conditions were compared to the data at the full backscatter condition.

9.23.3 Results

Table 9.17 shows a comparison of the results from the OSL measurements to that of the depth dose (TMR) and Markus from Markus ion-chamber results from Experiment 3 in section 9.10.

Table 9.17 OSL Experiment 6 results: Verification measurement data in phantom 2 with an equivalent thickness of 14.58cm and in phantom 3 with an equivalent thickness of 19.8cm and in phantom 4 with equivalent thickness of 22.2cm. No backscatter was added for the OSLDs. Data was acquired using 100MU of 6MV x-rays. Physical/equivalent (using a EPL based on relative RED to water calculated in this chapter) separation (1), field size at isocenter; (3) clinical TMR (d=18cm) data; (4)Correction factors (CF) were calculated using a EPL method; (5) OSLD measurement dose normalized to dmax. (6) Markus ion-chamber measurement dose normalized to dmax; (7) percentage difference between OSLD and TMR; (8) percentage difference between OSLD and Markus ion-chamber were measured

(1)	(2)	(3)	(4)	(5)	(6)	(7)	(8)
Physical/ Equivalent Separation (d/d_{eff}) (cm)	**Field Size @ Isocentre (cm^2)**	**TMR**	**After CF correction**	**OSLD**	**Markus**	**OSLD vs TMR Diff (%)**	**Markus vs TMR Diff (%)**
	3x3	0.5778	0.4863	0.4701	0.4592	-3.3%	-5.6%
18 / 14.6	5x5	0.6041	0.5085	0.4844	0.4769	-4.7%	-6.2%
	10x10	0.6518	0.5486	0.5217	0.5146	-4.9%	-6.2%
	20x20	0.6835	0.5753	0.5470	0.5367	-4.9%	-6.7%
Mean±SD						**-4.5%±0.7%**	**-6.2%±0.5%**
	3x3	0.5020	38.99	38.24	37.77	-5.3%	-6.5%
18 / 19.5	5x5	0.5241	40.76	40.03	39.68	-4.8%	-5.6%
	10x10	0.5716	44.83	43.44	43.38	-5.8%	-5.9%
	20x20	0.6065	47.75	45.66	45.51	-6.7%	-7.0%
Mean±SD						**-5.6%±0.7%**	**-6.7%±0.6%**
	3x3	39.84	33.54	31.27	30.72	-6.8%	-8.4%
18 / 22.2	5x5	41.76	35.15	32.79	32.70	-6.7%	-7.0%
	10x10	46.24	38.92		38.29		-1.6%
	20x20	49.52	41.68		38.50		-7.6%
Mean±SD						**-6.7%±0.0%**	**-6.2%±3.1%**

It was found that:

- As field size increases the difference between TMR and Markus ion-chamber measurement data increase. From a field size of 3x3cm^2 to one of 15x15cm^2 ,the difference increases up to 1.6% for the three phantoms.
- The tissues inserts with various densities show only a slight influence on the reduction ratio.

- Compared to TMR, as the RED increases, the difference changes in a range from approximately -4.5%±0.7%(1SD), -5.6%±0.7%(1SD), and -6.7±0.0% for phantom 2 (with RED of 0.22 insert), phantom 3 (with RED of 0.97 insert), and phantom 4 (with RED of 1.53 insert), respectively.
- Compared to Markus ion-chamber data as the RED increases the difference changes in a range from approximately -6.2%±0.5%(1SD), -6.7%±0.6%(1SD), and -6.2±3.1% for phantom 2 (with RED of 0.22 insert), phantom 3 (with RED of 0.97 insert), and phantom 4 (with RED of 1.53 insert), respectively.

9.24 Discussion of the factors influencing the exit dose measurements

From the Markus ion chamber and OSL experiments the following factors were found which may affect the exit dose measurement including: backscatter (back scatter thickness), field size, energy, tissue size, tissue density / equivalent thickness / primary beam path-length, and calibration/control dose.

For OSL measurements the characteristics of an OSL dosimeter and its reader become more important, affected by factors such as sensitivity, life-span, beam quality dependence, dose response linearity and dynamic range (saturation), the optical annealing procedure involved, and the reproducibility / stability of the reader.

It is suggested to calibrate the OSLD under the full backscatter condition for exit dose measurements. This makes it easy to compare the measurement results either under the full or no backscatter conditions. It is important to use correction factors to convert measured dose back to reference conditions dose

Conformal three-dimension (3D) radiotherapy treatment planning systems using superposition/convolution algorithms do consider missing backscatter, so the measurement results from OSLs should be close to those calculated by the TPS at the exit dose surface along the beam axis. However, this should be confirmed by further research.

9.25 Conclusion

Based on the experimental data of the Markus ion chamber OSLDs were used for the exit dose measurements in a phantom and in virtual patient.

As with a Markus ion-chamber, exit dose contributed by primary photons can be measured with OSL with or without back scatter material added and it was found that this does not affect the measurement results significantly.

The total dose to a point in a patient or phantom is the sum of the contributions from the primary photons and secondary scattered photons. The influence of the primary photons on the exit dose are not changed when field size changes. So the influences on the exit dose measurement must come from the contributions of the secondary scattered photons. The exit dose measurement's results found that as back scatter material thickness decreases the response (that can be expressed by reduction ratios) to the chamber or to the OSLD also decreases. That means that measured exit dose readings (through reduction ratio) have a dependence on field size, in other words, the reduction ratios become increasingly more negative as field size increases. Without additional back scatter material behind the chamber or OSLD there is much less change in chamber or OSLD readings even for the larger field sizes demonstrating again that the major contributions to exit dose are mostly from secondary scattered photons.

The secondary scattered photons' influence can be measured by changing the field size and the shape. OSL results show overall reduction from field size 3x3cm^2 to 15x15cm^2 with a good agreement with the Markus ion-chamber results, which show overall reduction ratios at the full back scatter condition within 1.5% for field sizes less than 10x10cm^2 and up to 3% with the field sizes of 20x20cm^2. OSL results are similar: as the back scatter thickness decreases there are less contributions from secondary scattered photons for larger field sizes.

With 10MV x-rays the readings show a lower reduction ratio compared to 6 MV x-rays for both the Markus chamber and OSL. This is due to lower back scatter from higher energy 10MV than that from 6MV x-rays.

Compared to the clinical TMR data OSL results are 1% lower at the full backscatter condition, 2% at the 1cm, and 3.5% at a no additional back scatter condition. The difference between the results without backscatter to those with full backscatter is 2.5%, and 1.5% different to the data with 1cm backscatter. The OSL data in phantom 4 with a tissue insert RED of 1.53, which is considered to be equivalent to hard bone, show a maximum 6.0% reduction in depth dose value compared to the no backscatter condition. This result has good agreement to that of the Markus chamber; 5%.

OSLs show slightly lower reduction ratios in comparison with TMR values. This difference is about the same as the Markus measurements compared with depth dose values.

In conclusion, OSLD can be used for exit dose measurements in showing some reduction with changes in backscatter thickness compared to clinical TMR value with full backscatter. With a 0.5cm~1.0cm back scatter thickness added, compared to the full backscatter condition, the difference between OSL and TMR values is within 2% for normal soft tissue inserts, and 4% for a high density tissue insert after tissue equivalent thickness correction. OSLs can also be used in air alone, with a difference of 3.5% between OSL and TMR values for normal soft tissue inserts and 6% for high density tissue inserts. This result gives one confidence that OSL can be used as a exit dosimetry tool as this uncertainty is well within ICRU report 24 recommendations. Accurate OSL use however requires a comprehensive quality control (QC) process in order to meet this requirement.

Chapter 10 Conclusions and Recommendations

This study investigated the potential of Optically Stimulated Luminescence (OSL) for treatment unit and patient Quality Assurance (QA) using a commercial OSL dosimetry system developed by Landauer (Landauer Inc., Glenwood, IL). This OSL system includes Al_2O_3:C based InLight™ dosimeters (OSLD) and an InLight™ MicroStar™ reader system.

OSL is a radiation measurement technique that uses the ability of OSL materials for storing radiation and then releasing that energy as light when stimulated with a light source having an appropriate wavelength. OSL commonly refers to the luminescence of an irradiated insulator or semiconductor when exposed to light. OSL is similar to thermo-simulated-luminescence, as used in the more common thermoluminescent dosimeters (TLD), except that electrons trapped in defects can be stimulated to generate luminescent emission by laser light rather than by thermal means.

OSL however offers some advantages over thermoluminescence (TL) dosimetry. The OSLDs are unique in that they can take the form of a flexible film which can be cut into different shapes and sizes to conform to the measurement conditions. OSL readings can be repeated several times after a single radiation exposure with a low degree of variation in each reading. OSL material can be re-used by overlaying additional radiation doses over previous ones without the need for optical annealing until a saturation dose is reached (before departure from the linearity or saturation in dose response). As with TLD's, OSL material may be reused by using a carefully managed optical annealing process, although there are indications that the repeatability of measurements diminishes rapidly after five or more radiation-annealing cycles.

OSL sensitivity is potentially higher than TL and it does not need thermal quenching (Bøtter-Jensen *et al*. 1991;Duller 1993; Murry *et al*., 1997; Murray and Wintle 1998;Duller *et al*, 1999). OSL dose can be read repeatedly from the same dosimeter and can be corrected by using a pre-determined decay constant (Duller 1993; Murray and Wintle 1998). Readings can be made from a single grain of an OSL detector by using a focused laser beam. OSL responds to a similar range of radiation energies as TL, but is more sensitive to visible light than a Thermoluminescent Dosimeter (TLD).

The purpose of this research was to test the Landauer Al_2O_3:C based InLight™ dosimeters (OSLD) and the InLight™ MicroStar™ reader system based OSL system in order to: 1) evaluate the general stability and reliability of this MicroStar™ reader, 2) to evaluate OSL dosimetric characteristics in megavoltage beam radiotherapy, 3) to explore the possibilities of using OSL as a dosimetry tool to verify both point dose and dose distributions by evaluating OSLs when used with a clinical IMRT plan in a phantom and 4) to explore the possibilities of using OSL as a dosimetry tool for skin exit dose measurements (exit dosimetry) using homogeneous and heterogeneous phantoms.

1: Evaluation of the general stability and reliability of the Landauer MicroStar™ OSL reader:

The evaluation of the stability and reliability of the Landauer OSL system used in this study included testing OSL reader performance, OSL dosimeter (OSLD) reproducibility, random fluctuations of repeated readings and the consequences of random OSLD orientation errors. The studies showed that after one OSLD irradiation the MicroStar reader can show some variation. For this reasons multiple readings should be obtained from the same OSLD as multiple readings reduce the deviation to an acceptable value. Single dot dosimeters should be snapped into the adapter correctly as a wrong orientation can cause a 11% error.

2: Evaluation of the dosimetric characteristics of OSL when used in megavoltage beam radiotherapy

The evaluation of this OSL system for use with megavoltage beam radiotherapy included assessing the response of individual OSLDs to various beam qualities, their dose-response curve linearity, dose dynamic range, directional/angular dependence, incremental exposure dose characteristics, reproducibility, read-out time dependence and post-irradiation dependence. The optimum annealing process and light source as well as OSL fading and reusability was also determined.

In the typical radiotherapy energy range, OSL dosimetry provides a wide dose response range, good dose linearity and reproducibility. There is an almost energy independent linear dose-response shown for both electron and photon beams. For 6 MV and 10 MV photon beams the standard deviation in OSL response is 2.0%, whilst there is 5.0%

deviation among electron beam energies from 6 MeV to 14MeV. Dose-response curves are linear up to 800 cGy with maximum deviations of 2.0% from linearity. For doses below 600 cGy deviations are less than 1.5%. There is an insignificant difference of less than 0.5% for doses up to 200 cGy, which is the generally clinically relevant dose range for one fraction of radiotherapy. Directional/angular variation is ±0.7%, which varies randomly over gantry angles of 0, 30, 45, and 90 degrees.

Incremental exposure / accumulated dose dose-response curves show a slightly higher variation (3.0%) than that of single exposures (2.0%) up to 800 cGy, but are still suitable for tracking patient dose over the whole treatment course. This enables OSLDs to be used repeatedly for dose measurement without using an intermediate optical annealing process. However, this may increase the noise level.

Sensitivity of OSLDs vary between various dosimeters; about 7.0% for unscreened OSLDs and 2.0% for screened OSLDs. A simple optical annealing procedure can be used with either a fluorescent light source or incandescent light source, while the later one is more effective. However, the optical annealing procedure is not able to erase the previous measurement readings completely. Over 3 cycles of: irradiation–reading–optical annealing, there is almost a 10% increase in dose response, making the accurate measurement of the residual signal after optical annealing vital before reusing the OSL dosimeter.

3) Evaluation of OSL viability as a dosimetry tool to verify both point dose and dose distributions, for example, when used for clinical IMRT:

This OSL system was evaluated as a dosimetry tool to verify point dose and dose distributions of a clinical IMRT plan by using a custom spherical phantom and three selected clinical IMRT plans (nasopharynx, prostate and lung). The cases chosen were: a nasopharynx case with multiple critical organs at risk (OAR) around the target; a prostate case simulating the sharper fall-off of isodose at target-volume boundary and a lung case to test OSLD response with higher beam energies (10 MV). The OSL measurement results were compared with those calculated by a TPS. Overall OSL measurements varied from TPS calculations by up to 5% in high dose regions, and may more than 5% in a high dose

gradient regions. However, the difference between TPS and OSL measurements were mostly caused by setup errors: dose variations contributed by setup error in the three selected clinical cases were up to 0.06Gy of a 1Gy fraction compared to the planed dose in the high dose gradient distribution region.

4) Evaluation of OSL use as a dosimetry tool for skin exit dose measurements (exit dosimetry):

This investigation aimed to compare the results of an existing de-facto standard in exit dosimetry, the Markus ion chamber, with those of OSL. The study included three steps: 1) use of a Markus ion-chamber to measure skin exit dose and factors that may affect it, 2) OSLD measurements following similar experiment procedures to those used with the Markus ion-chamber and 3) comparison of the measurement results from the Markus ion chamber and those of the OSLDs.

The results from the Markus ion chamber show that backscatter thickness does not affect measurement results significantly. The reduction ratio is within -3% on average for non-backscatter conditions compared to that of a full backscatter condition. There is a small influence of different field sizes; a 20x20 cm^2 field size reduces dose by 1.5% compared to 3x3cm^2 . Beam qualities have a ±1% effect and a heterogeneity correction, ±0.5%. Due to physical limitations of the PTW Markus Ion-chamber a minimum back scatter thickness of 1.4cm cannot be removed as it is part of the chamber's construction. However, for more accurate dosimetry, ensuring sufficient backscatter should be considered.

The OSLD calibration result shows slightly higher dose response compared to that of clinical depth dose in full backscatter but like the Markus ion chamber OSLDs also show reduction with changes in backscatter thickness. The reduction ratio is within -6% on average for a no-backscatter condition, and within -2% on average for 0.5 cm backscatter, compared to the full backscatter condition. Field size changes from 3x3cm^2 to 15x15 cm^2 reduce dose by 1.5%, and heterogeneity corrections, ±2.0%. With a back scatter thickness of 0.5cm, there is no significant difference between 6 and 10MV. There is

little energy dependence of OSLDs as the overall reduction ratio for both energies is within -1.0%. The average difference for all measurements between OSLD and Markus ion-chamber measurements is within 1%.

Dose response in skin exit dose measurements within the radiotherapy beam energy range is very important as the energy's spectrum is even more complex due to the fact that backscattered photons have a lower energy spectrum, which may be responsible for the dose response changes. Dose response at the low energies present in the scattered radiation varies with several factors including the primary photon flux, shape of the exit side skin surface and the thickness of back scatter materials added.

The evaluation of OSL system stability, reliability, dosimetry characteristics and performance in the megavoltage range, even when compared to current commonly used QA equipment such as ion-chamber, diode (array) and TLDs, provides confidence in the Landauer OSL system. Studies of OSL use for IMRT plan dose verifications performed in both phantoms and virtual patients (simulated by using a phantom with tissue equivalent material inserts) give us similar confidence that OSL can be used as a clinical dosimetry tool for patient specific QA, and augment or replace current commonly used devices such as ion-chambers, diodes (array) or film. Skin exit dose measurements (exit dosimetry) in homogeneous and heterogeneous phantoms indicate this OSL system can be used as a clinical dosimetry tool for linear accelerator machine QA. However, it should be noted that these quantitative comparisons were highly dependent on the control dose or calibration of the OSLDs. It should also be noted that although OSLs can be used to measure dose distributions in a high dose gradient region as a point dosimetry tool, OSLDs have certain limitations in this situation.

Simple operation, the possibility of repeated readouts without losing a significant amount of the signal, and the possibility to accumulate dose are additional bonuses of OSL use.

In conclusion, the research work shows that OSL dosimetry can be an alternative dosimetry technique for use in radiotherapy especially for patient specific QA, including skin dose measurement, IMRT plan checks, and linear accelerator QA. Because reference dose calibrations may directly influence dose measurement results, carefully setting up the reference point is extremely important when taking

reference readings (A practical guide for using the InLight^{TM} OSL dosimetry system for radiotherapy dosimetry is summarized in Appendix A). In addition, many clinical scenarios, in particular in-vivo dosimetry, produce more complex beam qualities that are often not known. Further work should also consider combining these tests with Monte Carlo calculations.

It is hoped that the results from this experimental work will lead to the use of two dimensional (2D) OSL film-like material and an associated readout system. Routine use of 2D OSL for dose imaging would have big advantages in measuring 2D dose distributions, especially in the high dose gradient region. 2D OSL could also be used for patient imaging, for example, as part of image guided radiotherapy (IGRT). Therefore it is believed that future efforts could also focus on developing a high accuracy readout system.

Reference

Ahnesjö A. and Aspradakis M.M, (1999) Dose calculations for external photon beams in radiotherapy. Phys. Med. Biol. 44:R99–R155.

Aitken MJ (1998) An introduction to optical dating, Oxford University Press, Oxford.

Akselrod MS, Kortov VS, Kravetsky DJ and Gotlib VI (1990) Highly sensitive thermoluminescent anion-defect α-Al_2O_3:C single crystal detectors. Radiat. Prot. Dosim. 33:119–122.

Akselrod MS, Kortov VS and Gorelova EA. (1993) Preparation and properties of α-Al_2O_3:C, Radiat. Prot. Dosim. 47:159-164.

Akselrod MS, Lucas AC, Polf JC andMcKeever SWS. (1998a) Optically stimulated luminescence of Al_2O_3. Radiat. Meas. 29:391-399.

Akselrod MS, Agersnap Larsen N, Whitely V, and McKeever SWS. (1998b) Thermal quenching of F-center luminescence in Al_2O_3:C. Int. J. Radiat. Oncol. Biol. Phys. 84(6):3364-3373.

Akselrod MS and McKeever SWS.(1999), A radiation dosimetry method using pulsed optically stimulated luminescence. Radiat. Prot. Dosim. 81(3):167-176.

Akselrod MS, Agersnap Larsen N and McKeever SWS. (2000) A procedure for the distinction between static and dynamic radiation exposures of personal radiation badges using pulsed optically stimulated luminescence. Radiat Meas. 32:215-225.

Akselrod A and Akselrod MS. (2002) Correlations between OSL and the distribution of TL traps in Al_2O_3:C. Radiat. Prot. Dosim. 100:217-220.

Akselrod MS, Bøtter-Jensen L and McKeever SWS. (2007) Optically stimulated luminescence and its use in medical dosimetry. Radiat Meas. 41:S78 –S99

Alecu R, Alecu M and Ochran TG. (1998) A method to improve the effectiveness of diode in vivo dosimetry. Med. Phys. 25(5):746-749.

Albert L, Defez D, Porcheron D, Fau P, Gassa F, Dusseau L, Fesquet J, and Gasiot J. (1997) Dose mapping system based on laser heating thermoluminescent plates. In Discussion and comparison with results about Gamma-Knife SFPM congress,

Nice.

Andersen CE, Aznar MC, Bøtter-Jensen L, Bäck SAJ, Mattsson S, and Medin J. (2003). Development of optical fibre luminescence techniques for RT in-vivo dosimetry in radiotherapy. Paper presented at the IAEA symposium on standards and codes of practice in medical radiation dosimetry. Vienna, November 25-28, 2(x)2 (IAEA-CN-96-118).

Andersen CE, Marckmann CJ, Aznar MC, Bøtter-Jensen L, Kjær-Kristoffersen F and Medin J. (2006) An algorithm for real-time dosimetry in intensity-modulated radiation therapy using the radioluminescence signal from Al_2O_3:C. Radiat. Prot. Dosim. 120:7–13.

Anderser CE, Edmund JM, Damkjæra SMS, and Greilich S. (2008) Temperature coefficients for in vivo RL and OSL dosimetry using Al_2O_3:C. Radiat. Meas. 43:948-953.

Anderse CE, Edmund JM, Damkjær SMS and Greilich S, (2008) Temperature coefficients for in vivo RL and OSL dosimetry using Al_2O_3:C. Radiat. Meas. 43:948-953.

Antonov-Romanovskii V.V, Kcium-Marcus I.F, Poroshina M. S, and Trapeznikova A. Z. (1956) Conference of the Academy of Sciences if the USSR on the Peaceful Uses of Atomic Energy, Moscow, 1955. USAEC Report AEC-tr-2435 (Pt.1):239.

Aznar MC, Andersen CE Bøtter-Jensen L, Bäck SAJ, Mattsson S, Kjær-Kristoffersen F, and Medin J. (2004) Real-time optical-fibre luminescence dosimetry for radiotherapy: physical characteristics and applications in photon beams. Phys. Med. Biol. 49:1655-1669.

Bailiff IK, and Clark RJ. (1999) A preliminary study of the fast time-resolved luminescence in Al_2O_3:C. Radiat. Prot. Dosim. 84:457-460.

Banks PW, Brand S, Jaros M. (1980) Optical cross sections associated with deep levels in semiconductors. J. Phys. C_Sol Stat. Phys. 13:6167-6180.

Beddar AS, Mackie TR, and Attix FH. (1992a) Cerenkov light generated in optical fibres and other light pipes irradiated by electrons beams. Phys. Med. Biol. 37:925–935.

Beddar AS, Mackie TR and Attix FH.(1992b) Water -equivalent plastic scintillation detectors for high energy beam dosimetry: I. Physical characteristics and theoretical considerations. Phys. Med. Biol. 37(10):1883–1900.

Beteille D, Setzkorn R, Prevost H, Dusseau L, Fesquet J, Gasiot J, Muraro S, Delard R, Dubois JB, Ailleres N, and Missous O.(1996), Laser heating of thermoluminescence plates: application to intraoperative radiotherapy. Med. Phys. 23(8):1421-1424.

Benoit D, Vaillé J-R, Ravotti F, Garcia P, and Dusseau L. (2007) Optically Stimulated Luminescence Dosimetry, 1st Workshop on Instrumentation for Charged Particle Therapy - May 9th 2007, London, UK

Benton ER and Benton EV. (2001) Space radiation dosimetry in low-earth orbit and beyond. Nucl Instr Meth. B. 184:255-294

Bernal and Bogard, (2004), Protocols for Thermoluminescence and Optically Stimulated luminescence Research at DOSAR, ORNL/TM-2004/193.

Beteille D, Setzkorn R, Prevost H, Dusseau L, Fesquet J, and Gasiot J. (1996) Laser heating of thermoluminescence plate: application to intraoperative radiotherapy, Med. Phys. 23(8):1421–1424.

Blakemore JS, and Rahimi S, (1984) Models for mid-gap states in GaAs: Semiconductors and Semimetals. 20, Academic Press. Orlando:233-261.

Blanco S, Lopez-Bote MA, and Desco M. (1987) Quality assurance in radiation therapy: Systematic evaluation of errors during the treatment execution. Radiother. Oncol.. 8(3):253–261.

Bloemen-van Gurp E, Mijnheer BJ, Verschueren TAM, Lambin P. (2007) Total body irradiation, toward optimal individual delivery: dose evaluation with metal oxide field effect transistors, thermoluminescence detectors, and a treatment planning system. Int. J. Radiat Oncol Biol. Phys. 69(4):1297-1304.

Boellaard R, van Herk M, and Mijnheer BJ. (1997) A convolution model to convert transmission dose images to exit dose distributions. Med. Phys.24(2):189-199.

Boellaard R, van Herk M, and Mijnheer BJ. (1997) A convolution model to convert transmission dose images to exit dose distributions. Med. Phys. 24(2):189-199.

Boyer A, Biggs P, Galivin J, Klein E, LoSasso T, Low D, Mah K, Yu C (2001). Basic applications of multileaf collimators. AAPM Report No. 72.American Association of Physicists in Medicine publication.

Bortolot VJ. (2000) A new modular high capacity OSL reader system. Radiat Meas. 32:751-757.

Butson MJ, Yu PKN, and Metcalfe PE. (1998) Measurements of off-axis and peripheral skin dose using radiochromic film. Phys. Med. Biol. 43:2647-2650.

Bøtter-Jensen L. Ditlevsen C, and Mejdahl V. (1991) Combined OSL (infrared) and TL studies of feldspars. Nucl. Tracks. Radiat. Meas. 20: 549-553.

Bøtter-Jensen L, and McKeever SWS. (1996a) Optically stimulated luminescence dosimetry using natural and synthetic materials. Radiat. Prot. Dosim. 65:273-280/

Bøtter-Jensen L, Markey BG, Poolton NRJ, and Jungner H. (1996b) Luminescence properties of porcelain ceramics relevant to retrospective radiation dosimetry. Radiat. Prot. Dosim. 65:369-372.

Bøtter-Jensen L, Agersnap Larsen N, Markey BG. and McKeever SWS, (1997), Al_2O_3:C as a sensitive OSL dosimeter for rapid assessment of environmental photon dose rates, 'Radiat Meas. ', 27(2):295–298.

Bøtter-Jensen L, Banerjee D, Jungner H, and Murray AS. (1999) Retrospective assessment of environmental dose rates using optically stimulated luminescence from Al_2O_3:C and quartz. Radiat. Prot. Dosim. 84:537-542.

Bøtter-Jensen L, Bulur E, Duller GAT and Murray AS. (2000) Advances in luminescence instrument systems. Radiat Meas. 32:523-528.

Bøtter-Jensen L, Bulur E, Murry AS, and Poolton NRJ. (2002) Enhancements in luminescence measurement techniques. Radiat. Prot. Dosim. 101:119-124.

Bøtter-Jensen L, Andersen CE, Duller GAT, and Murray AS. (2003) Developments in radiation, stimulation and observation facilities in luminescence measurements. Radiat Meas. 37:535-541.

Bøtter-Jensen L, McKeever SWS and Wintle AG. (2003) Optical Stimulated Luminescence Dosimetry.

Bøtter-Jensen L, Thomsen KJ, and Jain M. (2009) Review of optically stimulated luminescence (OSL) instrumental developments for retrospective dosimetry, Radiat Meas. Article in Press.

Brăuulich P, Schăfer D, and Scharmann A. (1967) A simple model for thermoluminescence and thermally stimulated conductivity of inorganic photoconducting phosphors and experiments pertaining to infra-red stimulated luminescence. Proceedings of the First International Conference on Luminescence Dosimetry. Stanford, June 1965, USAEC:57-73.

Brahme A. (1984) Dosimetric precision requirements in radiation therapy. Acta Radiological Oncology. 23(5):379–391.

Briot E, Dutreix A. and Bridier A. (1990) Dosimetry for total body irradiation. Radiother. Oncol.18:supplement 1:16-29.

Budzanowski M, Bilski P, Bøtter-Jensen L, Delgado A, Olko P, Sáez-Vergara JC, and Waligorski MPR. (1996) Comparison of LiF:Mg, Cu,P (MCP-N, GR-200A) and α-Al_2O_3:C TL detectors in short-term measurements of natural radiation. Radiat. Prot. Dosim. 66:157-160.

Bulur E, (1996) An alternative technique for optically stimulated luminescence (OSL) experiment. Radiat Meas. 26:701-709.

Bulur E, Goksu H.Y, and Wahl W. (1998) Infrared(IR) stimulated luminescence from α-Al_2O_3:C. Radiat Meas. 29:625-638.

Bulur E. (2000) A simple transformation for converting CW-OSL curves to LM-OSL curves. Radiat Meas. 32:141-145.

Bulur E, Bøtter-Jensen L, and Murray AS. (2001) LM-OSL signals from some insulators: an analysis of the dependency of the de-trapping probability on stimulation light intensity. Radiat Meas. 33:715-719.

Chen R. (2001) Advantages and disadvantages in the utilisation of thermoluminescence (TL) for radiation dosimetry , IRPA Regional Congress on Radiation Protection in Central Europe Dubrovnik, Croatia, May 20-25.

Chen Y and Evans BD. (1987) A model of lattice defects in sapphire. IEEE Transactions on Nuclear Science. NS-34(6):1709-1712.

Ciocca M. Orecchia R, Caribaldi C, Rondi E, Luini A, Gatti G, Intra M, Veronesi P, Lazzari R, Tosi G, Veronesi U. (2003) In vivo dosimetry using radiochromic films during intraoperative electron beam radiation therapy in early-stage breast cancer. Radiother. Oncol. 69:285-289.

Colyott LE, Akselrod MS and McKeever SWS. (1996), Photo transferred thermoluminescence in α-Al_2O_3:C. Radiat. Prot. Dosim. 65:263-266.

Colyott LE, McKeever SWS, Akselrod MS. (1999) An integrating UVB dosimeter system. Radiat. Prot. Dosim. 85:309-312.

Cygler J, Soubra M, Szanto J. Mackay GF and Thompson I. (1995) Application of MOSFET dosimetry system in TBI and HDR treatments. Med. Phys. 22:1541.

Ditlevsen C. and Huntley DJ. (1994) Optical excitation of trapped charges in quartz, potassium feldspars and mixed silicates: the dependence on photon energy. Radiat. Meas. 23: 675-682.

Duller GAT. and Bøtter-Jensen L. (1993) Luminescence from potassium feldspars stimulated by infrared and green light. Radiat. Prot. Dosim. 47:683-688.

Duller GAT, Bøtter-Jensen L, Kohsiek P and Murray AS. (1999) A high sensitivity optically stimulated luminescence scanning system for measurement of single sand-sized grains. Radiat. Prot. Dosim. 84:325-330.

Dusseau L, Polge G, Albert, L, Magnac Y, Bessiere JC, Fesquet J, and Gasiot J. (1998) Irradiated Integrated Circuits Dose-Attenuation Mapping Using Optically Stimulated Phosphors for Packaging Dosimetry. IEEE Transactions on Nuclear Science. 45:2695-2699

Dusseau L, Ranchoux G, Polge G, Plattard D, Saigne F, Bessiere JC, Fesquet J, and Gasiot J. (1999) High Energy Electron Dose-Mapping Using Optically Stimulated Luminescent Films, IEEE Transactions on Nuclear Science. 46:1757-1761.

Dusseau L, Polge G, Mathias S, Vaille J.R, Germanicus R, Broadhead R, Camanzi B, Glaser M, Saigne F, Fesquet J. andGasiot J. (2001) High Energy Particle Irradiation of Optically Stimulated Luminescent Films at CERN. IEEE Transactions on Nuclear Science. 48(6):2056-2060.

Dyk JW, Galvin JM, Glasgow GP and Podgorsak EB.(1986) AAPM Report No. 17 (TG-29) .The physical aspects of total and half body irradiation. American Association of Physicists in Medicine publication.

Edmund J.M, Andersen C.E, Marchmann C.J, Aznar M.C, Akselrod M.S, and Bøtter-Jensen L, (2006), 'Radiat. Prot. Dosim.', 119:368-374.

Engstrom PE, Haraldsson P, Landberg T, Hansen HS, Engelholm SA, Nystrom H. (2005) In vivo dose verification of IMRT treated head and neck cancer patients. Acta Ontological. 44:572-578.

Edward S. Yang. (1988) Microelectronic Devices. Chapters 2 and 3, New York: McGraw-Hill, Inc. 1988.

Erfurt G, Krbetschek MR, Trautmann T, and Stolz W. (2000) Radioluminescence (RL) behaviour of Al_2O_3:C-potential for dosimetric applications. Radiat Meas. 32:735–739.

Evans BD and Stapelbroek M. (1978) Optical properties of F^+-properties in crystalline Al_2O_3. Physical Review B: Condensed matter. 18:7089-7098.

Essers M, Lanson JH, and Mijnheer BJ. (1993) In vivo dosimetry during conformal therapy of prostatic cancer. Radiother. Oncol. 29(2):271–279.

Essers M, Lanson JH, Leunens G, Schnabel T, Mijnheer B.J, (1995) The accuracy of CT-based inhomogeneity corrections and in vivo dosimetry for the treatment of lung cancer. Radiother. Oncol. 37:199–208.

Essers M, Boellaard R, Van Herk M, Lanson H, and Mijnheer B. (1996) Transmission dosimetry with a liquid-filled electronic portal imaging device. Int. J. Radiat. Oncol. Biol. Phys. 34(4):931-941.

Essers M, and Mijnheer BJ, (1999) In vivo dosimetry during external photon beam radiotherapy. Int. J. Radiat. Oncol. Biol. Phys. 43(2):245–259.

Eveling JN, Morgan AM, Pitchford WG, (1998) Commissioning a p-type silicon diode for use in clinical electron beams, Med. Phys. 26(1):100-107.

Fairbanks EJ and DeWerd LA. (1993) Thermoluminescent characteristics of LiF:Mg, Ti from three manufacturers. Med. Phys. 20:729-73.

Fiorino C, del Vecchio A, Cattaneo GM, Fusca M, Longobardi B, Signorotto P, and Calandrino R, (1993) Exit dose measurements by portal film dosimetry, Radiother. Oncol. 29:336-340.

Fraass B, Doppke K, Hunt M, Kutcher G, Stern R, and van Dyke J.(1998) American Association of Physicists in Medicine Radiation Therapy Committee Task Group 53: Quality assurance for clinical radiotherapy treatment planning. Med. Phys. 25:1773-1829.

Gagon WF and Horton JL. (1979) Physical factors affecting absorbed dose to the skin from cobalt-60 gamma rays and 25-MV x-rays. Med. Phys. 6(4):285-290.

Gaza R, McKeever SMS, Akselord MS, Akselord A, Underwood T, Yoder C, Anderson CE, Aznar MC, Marckmann CJ. and Bøtter-Jensen L. (2004) A fibre-dosimetry method based on OSL from Al_2O_3:C for radiotherapy applications. Radiat Meas. 38:809-812.

Geise RA and McCullough EC. (1977) The use of CT scanners in megavoltage photon-beam therapy planning. Radiology.124:133-141.

Gladstone DJ and Chin LM. (1991) Automated data collection and analysis system for MOSFET radiation detectors. Med. Phys.18:542-548.

Gimadova TL, Bessonova TS, Tale IA, Avvakumova LA, and Bodyachevsky SV. (1990) On the thermoluminescence mechanism of non-doped corundum monocrystals with defect structure. Radiat. Prot. Dosim. 33:47-50.

Greig JR, Miller RW, and Okunieff P. (1996) An approach to dose measurement for total body irradiation. Int. J. Radiat. Oncol. Biol. Phys. 36(2):463-468.

Grimmeiss HG and Ledebo L-A. (1975a) Photo-ionisation of deep impurity levels in semiconductors with non-parabolic bands, J. Phys. C: Sol. Stat. Phys. 8:2615-2626.

Grimmeiss HG and Ledebo L-A. (1975b) Spectral distribution of photoionization cross sections by photoconductivity measurements. Int. J. Radiat. Oncol. Biol. Phys. 46(5):2155-2162.

Hamers HP, Johansson KA, Venselaar JLM, de Brouwer P, Hansson U. and Moudi C. (1991) Entrance and exit TL-dosimetry in conservative treatment of breast cancer, a pilot study for the EORTC-radiotherapy Cooperative Group. Radiother.

Oncol. 22(4):280-284.

Hansen VN, Evans PM, and Swindell W. (1996) The application of transit dosimetry to precision radiotherapy. Med. Phys. 23(5):713–721.

Heijmen BJM, Pasma KL, Kroonwijk M, Althoft VGM, de Boer JCJ, Visser AG, and Huizenga H, (1995) Portal dose measurement in radiotherapy using an electronic portal imaging device (EPID). Phys. Med. Biol. 40:1943–1955.

Henson PW and Fox RA. (1984) The electron density of bone for inhomogeneity correction in radiotherapy planning using CT numbers, Phys. Med. Biol. ,29(4), 351-359.

Heydarian M, Hoban PW and Beddoe AH. (1996), A comparison of dosimetry techniques in stereotactic radiosurgery. Phys. Med. Biol. 41:93–100.

Higgins PD, Alaei P, Gerbi BJ and Dusenbery KE. (2003) In vivo diode dosimetry for routine quality assurance in IMRT. Med. Phys. 30:3118-3123.

Howell RW, Ferenci MS, Hertel NE, and Fullerton GD. (2005) Investigation of secondary neutron dose for 18 MV dynamic MLC IMRT delivery. Med. Phys. 32:786-793.

Horowitz YS, Oster L, and Margaliot M (2008) Some dosimetric characteristics of the temperature TL in LiF:Mg, Ti (TLD-100). Rad. Meas. 43:203-207.

Hu B, Wang Y and Zealey W. (2009) Performance of Al_2O_3:C optically stimulated luminescence dosimeters for clinical radiation therapy applications. Australasia. Phys. Eng. Sci. Med. 32(4):226-232.

Huntley DJ, Godfrey-Smith DI and Thewalt MLW. (1985) Optical dating of sediments. Nature. 313:105-107.

Huntley DJ, Short MA, Dunphy A. (1996) Deep traps in quartz and their use for optical dating. Can. J. Phys. 74:81-91.

Huston AL, Justus BL, Falkenstein PL, Miller RW, Ning H and Altemus R. (2001) Remote optical fiber dosimetry. Nucl Instr Meth. B. 184:55–67.

Huston AL, Justus BL, Falkenstein PL, Miller RW, Ning H, and Altemus R. (2002)

Optically stimulated luminescent glass optical fibre dosimeter. Radiat Prot. Dosim. 101:23-26.

Hutt G, Jaek I, Tchonka J. (1988) Optical dating: K-feldspars optical response stimulation spectra. Quat. Sci. Rev. 7:381-385.

Huyskens D, Van Dam J, and Dutreix A, (1994) Mid-plane dose determination using in vivo dose measurements in combination with portal imaging. Phys. Med. Biol. 39:1089-1101.

ICRU Publication 24, 1976, Determination of Absorbed Dose in a Patient Irradiated by Beams of X or Gamma Rays in Radiotherapy Procedures.

Idri K, Santoro L, Charpiot E, Herault J, Costa A, Ailleres N, Delard R, Vaille JR, Fesquet J, and Dusseau L.(2004) Quality Control of Intensity Modulated Radiation Therapy With Optically Stimulated Luminescent Films. IEEE Transactions on Nuclear Science. 51(6):3638-3641.

Intensity Modulated Radiation Therapy Collaborative Working Group (IMRTCWG), (2001) Intensity-Modulated radiotherapy: current status and issues of interest. Int. J.Ratiation Oncology Biol. Phys., Vol.51(4):880-914

Izak-Biran T, Moscovitch M. (1996) Light-induced TL and Light-induced fading of TL in α:Al_2O_3:C. Radiat Meas. 26(2):259-264.

Jaek I, Hutt G, and Streltsov A. (1999) Study of deep traps in alkali feldspars and quartz by the optically stimulated afterglow. Radiat. Prot. Dosim. 84:467-470.

Jeraj R, Keall P.J. and Siebers JV. (2002) The effect of dose calculation accuracy on inverse treatment planning. Phys. Med. Biol. 47:391–407. Med. Phys. 37(1):132-140.

Juristic PA. (2007) Characterization of optically stimulated luminescent dosimeters, OSLDs, for clinical dosimetric measurements. Med. Phys.34(12):4594-4604.

Juristic PA. (2010) Changes in optically stimulated luminescent dosimeter (OSLD) dosimetric characteristics with accumulated dose.

Karzmark CJ. et al. (1987) Total skin electron therapy technique and dosimetry. American Association of Physicists in Medicine by the American Institute of Physics

(AAPM) report 23.

Keall PJ, Mageras GS, Balter JM, Emery RS, Forster KM, Jiang SB, Kapatoes JM, Kubo HD, Low DA, Murphy MJ, Murray BR, Ramsey CR, van Herk MB, Vedam SS, Wong JW, and Yorke E. (2006) The management of respiratory motion in radiation oncology report of AAPM Task Group 76. Med. Phys.33(10):3874-3900.

Kirby MC and Williams PC. (1995) The use of an electronic portal imaging device for exit dosimetry and quality control measurements. Int. J. Radiation Oncology Bio. Phys. 31(3):593-603.

Kitis G, Papadopoulos JG, Charalambous S, Tuyn JWN. (1994) The influence of heating rate on the response and trapping parameters of α-Al_2O_3:C.Radia. Prot. Dosim. 55:83-190.

Klein EE, Hanley J, Bayouth J, Yin FF, Simon W, Dresser S, Serago C, Aguirre F, Ma L, Arjomandy B, Liu C, et al. (2009) Task Group 142 report: Quality assurance of medical accelerators. Med. Phys.36(9):4197-4212.

Kortov VS, Milman II, Kirpa VI, Lesz J. (1994) Some features of α-Al_2O_3:C dosimetric thermoluminescent crystals. Radiat. Prot. Dosim. 55:279-283.

Knöös T, Ahlgren L and Nilsson M. (1986) Comparison of measured and calculated absorbed doses from tangential irradiation of the breast. Radiother. Oncol. 7(1):81-88.

Kortov VS, Milman II, Kirpa VI, Lesz J. (1994) Some features of α-Al_2O_3 dosimetric thermoluminescent crystals. Radiat. Prot. Dosim. 55 (4):279-283.

Kron T, Elliot A, Wong T, Showell G, Clubb B, and Metcalfe P.(1993a) X-ray surface dose measurement using TLD extrapolation. Med. Phys. 20(3):703-711.

Kron T, Buston M, Wong T, Metcalfe P. (1993b) Readout thermoluminescence dosimetry chips using contact planchet heater. Australas. Phys. Eng. Sci. Med. 16:137-142.

KronT. (1995) Thermoluminescence dosimetry and its applications in medicine. Part 2. History and applications. Australas. Phys. Eng. Sci. Med. 18: l-25.

Kron T, Ostwald PM, Hamilton CS and Denham JW. (1996) TLD Extrapolation

measurements for entrance and exit dose in radiotherapy. Radiat. Prot. Dosim. 66(1-4):323-336.

Kroonwijk M, Pasma K.L, Quint S, Koper PCM, Visser AG, Heijmen BJM. (1998) In vivo dosimetry for prostate cancer patients using an electronic portal imaging device (EPID); demonstration of internal organ motion. Radiother. Oncol.49:125-132.

Kuhns CK, Agersnap Larsen N, McKeever SWS. (2000), Characteristics of LM-OSL from several different types of quartz. 'Radiat Meas. ', 32:413-418.

Kutch GJ, Coia L, Gillin M, Hanson W, et al. (1994), Comprehensive QA for radiation oncology. American Association of Physicists in Medicine (AAPM) publication.

Lambert GD, Liversage WE, Hirst AM and Doughty D. (1983) Exit dose studies in megavoltage phantom therapy. British Journal of Radiology. 56:329-334.

Lanson JH, Essers M, Uiterwaal GJ, Kroes G, and Mijnheer BJ. (1995) In-vivo dosimetry: An essential part of a quality assurance programme of conformal radiotherapy. Radiother. Oncol. 37:S53.

Landsberg PT.(1991) Recombination in semiconductors. Cambridge University Press, Cambridge.

Laub WU, Kaulich TW and Nusslin F. (1999) A diamond detector in the dosimetry of high energy electron and photon beams. Phys. Med. Biol. 44:2183–2192.

Lee L. Le QT, Xing L. (2008) Retrospective IMRT dose reconstruction based on cone-beam CT and MLC log-file. Int J Radiat Oncol Biol Phys. 70:634-644.

Leunens G, Verstraete J, Van Dam J, Dutreix A. and van der Schueren E. (1994) Experience of in-vivo dosimetry investigations in Leuven. In "Radiation dose in radiotherapy from prescription to delivery. IAEA Report TECDOC-734, 283-289.

Leunens G, Verstraete J, Van Dam J, Dutreix A. and van der Schueren E. (1994) Experience of in-vivo dosimetry investigations in Leuven. In "Radiation dose in radiotherapy from prescription to delivery. IAEA Report TECDOC-734, 283-289.

Leunens G, Van Dam J, Dutreix A, and van der Schueren E. (1990) Quality assurance in radiotherapy by in vivo dosimetry. 2. Determination of the target absorbed dose. Radiother. Oncol. 19(1):73-87.

Leunens G, Verstraete J, Van den Bogaert W, Dutreix A, and van der Schueren E. (1992) Human errors in data transfer during the preparation and delivery of radiation treatment affecting the final result: “garbage in, garbage out”. Radiother. Oncol.. 23:217–222.

Ling CC, Burman C, Chui CS, Kutcher GJ, Leibel SA, LoSasso T, Mohan R, Bortfeld T, Reinstein L, Spirou S, Wang XH, Wu Q, Zelefsky M, Fuks Z. (1996) Conformal radiation treatment of prostate cancer using inversely-planned intensity-modulated photon beams produced with dynamic multileaf collimation. Int J Radiat Oncol Biol Phys. 35:721–730

Loncol T, Greffe JL, Vynckier S, Scalliet P. (1996) Entrance and exit dose measurements with semiconductors and thermoluminescent dosimeters: a comparison of methods and in vivo results, Radiother. Oncol. 41:179–187.

LoSasso T, Chui CS Ling CC. (1998) Physical and dosimetric aspects of a multileaf collimation system used in the dynamic mode for implementing intensity modulated radiotherapy. Med. Phys. 25:1919-1927.

LoSasso T, Chui C-S, Ling C. (2001) Comprehensive quality assurance for the delivery of intensity modulated radiotherapy with a multileaf collimator used in the dynamic mode. Med. Phys. 28:2209-2219.

Low DA, Chao KSC, Mutic S, Gerber RL, Perez CA, Purdy JA. (1998a) Quality assurance of serial tomotherapy for head and neck patient treatments. ‘Int. J. Radiat Oncol Biol. Phys. , 42:681-692.

Low DA, Mutic S, Gerber RL, Bosch WR, Perez CA, Purdy JA. (1998b) Quantitative dosimetric verification of an IMRT planning and delivery system. Radiother. Oncol. 49:305-316.

Low DA, Mutic S, Dempsey JF, Markman J, Goddu SM, Purdy JA. (1999) Abutment region dosimetry for serial tomotherapy. Int. J. Radiation Oncol Biol. Phys. 45:193-203.

Low DA. (2002) Seminars in Radiation Oncology. 12(3):219-228

Lucovsky G. (1964) On the photoionization of deep impurity centres in semiconductors. Solid State Communication. 3:299-302.

Magne S, Auger L, Bordy JM, de Carlan L. Isambert A, Bridier A. Ferdinand P, and Barthe J. (2008) Multichannel dosimeter and Al_2O_3:C optically stimulated luminescence fibre sensors for use in radiation therapy: evaluation with electron beams. Radiat. Prot. Dosim. 131(1):93-99.

Marckmann CJ, Andersen CE, Aznar MC, Bøtter-Jensen L. (2006) Optical fibre dosimeter system for clinical application based on radioluminescence and optically stimulated luminescence from Al_2O_3:C. Radiat. Prot. Dosim.128:28-32.

Marinello G, Barthe J, Pollack J, and Portal G, (1992) "PCL" a new automatic fast reader suitable for in vivo dosimetry , Radiother. Oncol. 25(1):63-66.

Markey BG, Colyott LE, and McKeever SWS. (1995), Time-resolved optically stimulated luminescence from α-Al_2O_3:C. Radiat Meas. 24:457-463.

Markey BG, McKeever SWS, Akselrod MS and Bøtter-Jensen L. (1996) The temperature dependence of optically stimulated luminescence from α-Al_2O_3. Radiat. Prot. Dosim. 65, 185-189.

Marinello G, Barrié AM. and Le Bourgeois JP. (1982) Measurement and calculation of lung dose in total body irradiations performed with cobalt 60. J. Eur. Radiother. 3:174-182.

McDermott LN, Wendling M, van Asselen B, Stroom, J, Snoke JJ, van Herk M, and Mijnheer BJ.(2006) Clinical experience with EPID dosimetry for prostate IMRT pre-treatment dose verification. Med. Phys. 33(10):3921-3930.

McDermott LN, Wendling M, Nijkamp J, Mans A, Snoke J-J, Mijnheer BJ, van Herk M. (2008) 3D in vivo dose verification of entire hypo-fractionated IMRT treatments using an EPID and cone-beam CT. Radiother. Oncol. 86:35-42.

McKeever, SWS. (1985) Thermoluminescence of solids. Cambridge university press.

McKeever, SWS, Moscovitch, M, Townsend PD. (1995) Thermoluminescence Dosimetry Materials: Properties and Uses. Nuclear Technology Publishing, Ashford, UK.

McKeever SWS, Akselrod MS, and Markey BG. (1996) Pulsed optically stimulated luminescence dosimetry using α-Al_2O_3:C. Radiat. Prot. Dosim. 65:267-272.

McKeever SWS, Bøtter-Jensen L. Agersnap Larsen N, Duller GAA. (1997a) Temperature dependence of OSL decay curves: Experimental and theoretical aspects. Radiat Meas. 27(2):161-170.

McKeever SWS, Agersnap Larsen N, Bøtter-Jensen L, and Mejdahl V. (1997b) OSL sensitivity changes during single aliquot procedures: computer simulations. Radiat Meas. 27(2):75-82.

McKeever SWS, Akselrod MS, Colyott LE, Agersnap Larsen N, Polf J.C, Whitely V. (1999a) Characterisation of Al_2O_3 for use in thermally and optically stimulated luminescence dosimetry. Radiat. Prot. Dosim. 84:163-168.

McKeever SWS and Akselrod MS. (1999b) Radiation dosimetry using pulsed optically stimulated luminescence of Al_2O_3:C. Radiat. Prot. Dosim. 84:317-320.

McKeever SWS and Moscovitch M. (2003) On the advantages and disadvantages of optically stimulated luminescence dosimetry and thermoluminescence dosimetry. Radiat. Prot. Dosim. 104(3):263-270.

McGhee P, Humphreys S and Dunscombe P. (1993) An efficient approach to routine TL dosimetry. Medical Dosimetry. 18:187-191.

McLaughlin WL and others (1989), Dosimetry for radiation processing, 'Taylor and Francis', Philadelphia, pp 163

Meeks SL, Paulino AC, Pennington EC, Simon JH, Skwarchuk MW, Buatti JM, (2002) In vivo determination of extra-target doses received from serial tomotherapy. Radiother. Oncol. 63:217-222.

Miften M, Gayou O, Reitz B, and Fuhrer R, (2007) IMRT planning and delivery incorporating daily dose from mega-voltage cone-beam computed tomography imaging. Med. Phys. 34(10):3760-3767.

Mijnheer B, Batternann J and Wambersie A. (1987) Waht degree of accuracy is required and can be achieved in photon and neutron therapy, Radiother. Oncol. 8: 237-252.

Mijnheer B. (1994) Possibilities and limitations of in-vivo dosimetry. In "Radiation dose in radiotherapy from prescription to delivery", IAEA Report TECDOC-734, 259-266.

Mijnheer B. (2008) State of the art of in vivo dosimetry. Radiat. Prot. Dosim.. 131:117-122.

Millers D. and Murphy MK. (2007) Technical performance of the Luxel Al_2O_3:C Optically Stimulated Luminescence Dosimeter Element at Radiation Oncology and Nuclear Accident Dose Levels . Radiat. Prot. Dosim. 123(4):435-442.

Molnar G, Benabdesselam M, Borossay J, Lapraz D, Iacconi P, Kortov VS, Surdo AI. (2001) Photoluminescence and thermoluminescence of titanium ions in sapphire crystals. Radiat Meas. 33:663-667.

Morton EJ, Swindell W, Lewis DG, Evans PM. (1991) A linear array, scintillation crystal-photodiode detector for megavoltage imaging. Med. Phys. 18:681–691.

Moscovitch M, Tawil RA, Svinkin M. (1993) Light induced fading in α-Al_2O_3:C. Radiat. Prot. Dosim. 47:251-253.

Moscovitch M, (1999), Personal dosimetry using LiF:Mg, Cu, P. 'Radiat. Prot. Dosim.', 85:49-56.

Mosleh-Shirazi MA, Evans PM, Swindell W, Symonds-Tayler JR, Webb S, Partridge M. (1998) Rapid portal imaging with a high-efficiency, large field-of-view detector. Med. Phys. 25:2333–46.

Munzenrider JE, Pilepich M, Rene-Ferrero JB, Tchakarova I, and Carter BL. (1977), Cancer. 40:177-179.

Murphy MJ, Balter J, Balter S, BenComo JA, Das IJ, Jiang SB, Ma CM, Olivera GH, ROdebaugh RF, Ruchala KJ, Shirato H, and Yin FF. (2007) The management of imaging dose during image-guide radiotherapy: report of AAPM Task Group 75. Med Phys 34(10):4041-4063.

Murray AS, Roberts RG, and Wintle AG. (1997) Equivalent dose measurement using a single aliquot of quartz. Radiat Meas. 27(2):171-184.

Murray AS and Wintle AG, (1998) Factors controlling the shape of the OSL decay curve in quartz. Radiat Meas. 29(1):65-79.

Nijsten SM, Mijnheer BJ, Dekker AL, Lambin P, Minken AW. (2007) Routine individualised patient dosimetry using electronic portal imaging devices. Radiother

Oncol. 83:65–75.

Nilsson B and Scrcini S. (1989) Surface dose measurements in clinical photon beams. Acta nOncol. 28:537-904.

Noel A, Aletti P, Bey P, and Malissard L. (1995) Detection of errors in individual patients in radiotherapy by systematic in-vivo dosimetry. Radiother. Oncol. 34:144–151.

O'Connor, J.E, The variation of scattered X-rays with density in an irradiated body.

Oster L, Weiss D, Kristianpoller N, (1994), A study of photo stimulated thermoluminescence in C-doped α-Al_2O_3 crystals. Journal of Physics D: Applied Physics. 27:1732-1736.

Ostwald PM, Kron T, Hamilton CS and Denham JW. (1995) Clinical use of carbon-loaded thermoluminescent dosimeters for skin dose determination. Int. J. Radiat. Oncol. Biol. Phys. 33: 943-950.

Pagonis V, Chen R, and Lawless JL. (2008), A quantitative kinetic model for Al_2O_3:C: TL response to UV-illumination. Radiat Meas. 43:175-179.

Parker RP, Hobday PA, and Cassell KJ. (1979), The direct use of CT numbers in radiotherapy dosage calculations for inhomogeneous media. Phys. Med. Biol. 24:802-809.

Pasma KL, Dirkx MLP, Kroonwijk M, Visser AG, Heijmen BJ. (1999) Dosimetric verification of intensity modulated beams produced with dynamic multileaf collimation using an electronic portal imaging device. Med. Phys. 26:2373–2378.

Peet DJ and Pryor MD. (1999) Evaluation of a MOSFET radiation sensor for the measurement of entrance surface dose in diagnostic radiology. The British Journal of Radiology. 72:562–568.

Pelenyov VE, Kortov VS and Milman II. (2001) The interaction of deep traps in anion-defective α-Al_2O_3:C. Radiat Meas. 33:629-631.

Perks C.A, Le Roy G. and Prugnaud B. (2007) Introduction of the InLight Monitoring Service. Radiat. Prot. Dosim. 125:220-223

Piermattei A, Fidanzio A, Azario L, Grimaldi L, D'Onofrio G, Cilla S, Balducci M, Gambacorta M.A, Napoku N.D, Cellini N.Stimato G. (2006) In vivo dosimetry by an aSi-based EPID. Med. Phys. 33:4414–22.

Pogatshnik GJ, Chen Y, and Evans BD. (1987) A model of lattice defects in sapphire. IEEE Transaction on Nuclear Science NS-34(6):1709-1712

Polge G, Dusseau L, Matias S, Gensanne D, Plattard D, Fesquet J, Gasiot J, McNulty PJ, Davis M, Tortora M, Iborra-Brassart N, Porcheron D, Dubois JB, Ailleres N, Delard R. (2000), Applications to Radiotherapy of a Dose-mapping System Base on the Optically Stimulated luminescence, IEEE Medical Imaging Conference, Lyon, France:1947-1951.

Poolton NRJ, Bøtter-Jensen L, Ypma PJM, Johnsen O. (1994) Influence of crystal structure on the optically stimulated luminescence properties of feldspars. Radiat Meas. 23:551-554.

Poolton NRJ, Bøtter-Jensen L, Johnsen O. (1995a) Influence on donor electron energies of the chemical composition of K, Na and Ca aluminosilicates. Journal of Physics: Condensed Matter. 7:4751-4762.

Poolton NRJ, Bøtter-Jensen L, and Johnsen O. (1995b) Thermo-optical properties of optically stimulated luminescence in feldspars. Radiat Meas. 24(4):531-534.

Poolton NRJ, Wallinga J, Murray AS, Bulur E, Bøtter-Jensen L. (2002a) Electrons in feldspar I: on the wave function of electrons trapped at simple lattice defects. Phys. Chem. Minerals. 29:210-216.

Poolton NRJ, Ozanyan KB, Wallinga J, Murray AS, Bøtter-Jensen L. (2002b) Electron in feldspar II: a consideration of the influence of conduction band-tail states on luminescence processes. Phys. Chem. Minerals. 29:217-225.

Ramani R, Russel S and O'Brien P. (1997) Clinical dosimetry using MOSFETs. Int. J. Radiat. Oncol. Biol. Phys. 37(4):956-964.

Ridley R K. (1988) Quantum Processes in semiconductors, Clarendon Press, Oxford.

Rikner G and Grusell E. (1987) General specifications for silicon semiconductors for use in radiation dosimetry. 32(9):1109-1117.

Rizzotti A, Compri C and Garusi GF. (1985) Dose evaluation to patients irradiated by 60Co beam by means of direct measurement on the incident and on the exit surfaces. Radiother. Oncol. 3(3):279-283.

Roy O, Magne S, Gaucher JC, Albert L, Dusseau L, Bessiere JC, Ferdinand P. (1997) All optical fiber sensor based on optically stimulated luminescence for radiation detection. In: Presented at the 12th International Conference on Optical Fiber Sensors OFS'97, Williamsburg, Virginia, USA, October 28–31.

Robert F. Pierret.(2002) Advanced Semiconductor Fundamentals. 2nd Ed, New York: Prentice Hall

Sanderson DCW and Clark RJ. (1994) Pulsed photostimulated luminescence of alkali feldspars. Radiat Meas. 23:633-639.

Sanboren EN and Beard EL. (1967) Sulphides of strontium, calcium, and magnesium in infra-red stimulated luminescence dosimetry. In Luminescence Dosimetry. U.S. Atomic Energy Commission. ed. F.H. Attix, pp.183-193.

Saw CB, Ayyangar KM, Thompson RB, Zhen WZ and Enke CA. (2001a) Commissioning of Peacock System for intensity-modulated radiation therapy. Medical Dosimetry. 26(1):55-64

Saw CB, Ayyangar KM, Zhen W, Thompson RB, and Enke CA. (2001b) Quality assurance procedures for the Peacock system. Medical Dosimetry. 26(1):83-90.

Scalchi P, Francescon P and Rajaguru P. (2005) Characterization of a new MOSFET detector configuration for in vivo skin dosimetry. Med Phy. 32(6):1571-1578.

Schembri V. and Heijmen BJM. (2007) Optically stimulated luminescence (OSL) of carbon-doped aluminium oxide (Al_20_3:C) for film dosimetry in radiotherapy. Med. Phys. 34(6):2113-2118.

Schulman JH. Solid state dosimeters for Radiat Meas. In: Marley WG, Morgan KZ, eds. Progress in nuclear energy. Series XII Health Physics Vol I. New York: Pergamon Press; 1959:150-159

Seco J. and Evans PM. (2006) Assessing the effect of electron density in photon dose calculations. Med. Phys, 33(2):540-552.

Shi J, Simon WE, Zhu TC. (2003) Modelling the instantaneous dose rate dependence of radiation diode detectors. Med. Phys. 30(9): 2509-2519.

Soubra M and Cygler J. (1994) Evaluation of a dual bias dual metal oxide-silicon semiconductor field effect transistor detector as radiation dosimeter. Med. Phys. 21(4):567–572.

Spooner NA. (1994) On the optical dating signal from quartz. Radiat Meas. 23(2-3):593-600.

Springis M, Kulis P, Veipals A, and Tale I. (1995) Photo-and thermo stimulated processes in α-Al_2O_3:C. Radiat Meas. 24:453-456.

Summers GP. (1984) Thermoluminescence in signal crystal α-Al_2O_3. Radiat. Prot. Dosim.8:69-80.

Suzuki A and Ito M. (2001) Characteristics of OSL dosimeters. JAERT-Tech 2000-089, Japan Atomic Energy Research Institute. February

Symonds-Tayler JR, Partridge M, Evans PM. (1997) An electronic portal imaging device for transit dosimetry. Phys. Med. Biol. 42:2273–2283.

Tale I, Piters TM, Barboza-Flores M, Perez-Salas R, Aceves R, and Springis M. (1996) Optical properties of complex anion vacancy centres and photo-excited electronic processes in anion defective α-Al_2O_3. Radiat. Prot. Dosim. 65:235-238.

Thomas SJ and Palmer N. (1989) The use of carbon-loaded thermoluminescent dosimeters for the measurement of surface doses in megavoltage x-ray beams, Med. Phys.16(6):902-904.

Thomas SJ. (1999) Relative electron density calibration of CT scanners for radiotherapy treatment planning. The British Journal of Radiology. 72:781-786.

Thomas MDR. and Warrington AP. (2006) Gafchromic RTQA film for routine quality assurance of high-energy photon beams. Phys. Med. Biol. 51:1439-1447.

Trinkler I, Bøtter-Jensen L, Christensen P, and Berzina B. (2000) Studies of aluminium nitride ceramics for application in UV dosimetry. Radiat. Prot. Dosim. 92(4):299-306.

Tsai JS, Wazer DE, Ling MN, et al, (1998), Dosimetric verification of the dynamic intensity-modulated radiation therapy of 92 patients. Int. J. Radiat. Oncol. Biol. Phys. 40(5):1213-1230.

Tung CJ, Wang HC, Lo SH, Wu JM, and Wang CJ. (2004) In vivo dosimetry for external photon treatments of head and neck cancers by diodes and TLDs. Radiat. Prot. Dosim. 111(1):45-50.

Van Bree NAM, Van Battum LJ, Huizenga H and Mijnheer BJ. (1994) Results of quality control of breast cancer irradiations in the Netherlands. In "Radiation dose in radiotherapy from prescription to delivery", IAEA Report TECDOC-734, 251-256.

Van Dam J, Vaerman C, Blanckaert N, Leunens G, Dutreix A, and Van Der Schueren E. (1992) Are port films reliable for in vivo exit dose measurements? Radiother. Oncol. 25:67-72

van Dam J and Marinello G. (2006) Methods for in vivo dosimetry in external radiotherapy. ESTRO publication.

Van Dyk J, Galvin JM, Glasgow GP and Podgorsak EB. (1986) The physical aspects of total and half body photon irradiation. American Association of Physicists in Medicine by the American Institute of Physics (AAPM) report 17.

van Elmpt W, McDermott L, Nijsten S, Wendling M, Lambin P, Mijnheer B. (2008) A literature review of electronic portal imaging for radiotherapy dosimetry. Radiother. Oncol. 88:289–309.

van Elmpt W, Nijsten S, Pettt S, Mijnheer B, Lambin P, and Dekker A. (2009) 3D in vivo dosimetry using megavoltage cone-beam CT and EPID dosimetry. Int. J. Radiat Oncol Biol. Phys. 73(5):1580-1587.

Van Esch A, Bohsung J, Sorvari P, Tenhunen M, Paiusco M, Iori M, Engstrom P, Nystrom H, Huyksens DP. (2002) Acceptance tests and quality control (QC) procedures for the clinical implementation of intensity modulated radiotherapy (IMRT) using inverse planning and the sliding window technique: experience from five radiotherapy departments. Radiother. Oncol. 65:53–70.

van Zijtveld M, Dirkx M.L, de Boer HCJ, and Heijmen BHM. (2007a) 3D dose reconstruction for clinical evaluation of IMRT pre-treatment verification with an EPID.

Radiother Oncol. 82:201-207.

van Zijtveld M, Dirkx M.L. and Heijmen BHM. (2007b) Correction of conebeam CT values using a planning CT for derivation of the “dose of the day“. Radiother Oncol. 85:195-200.

Viamonte A, da Rosa LAR, Buckley LA, Cherpak A. and Cygler JE. (2008), Radiotherapy dosimetry using a commercial OSL system. Med. Phys. 35(4):1261-1266.

Walker FD, Colyott LE, Agersnap Larsen N, McKeever SWS. (1996) The wavelength dependence of light-induced fading of thermoluminescence from α-Al_2O_3:C. Radiat Meas. 26(5):711-718.

Wang L, Yorke E, Desobry G, and Chui CS. (2002) Dosimetric advantage of using 6 MV over 15 MV photons in conformal therapy of lung cancer: Monte Carlo studies in patient geometries. J Appl Clin Med Phys 3:15-59.

Weaver RD, Gerbi BJ and Dusenbery KE. (1995). Evaluation of dose variation during total skin electron irradiation using thermoluminescent-cent dosimeters. Journal of applied clinical Med. Phys. 33(2):475-478.

Weltens C, van Dam J, Leunens G, Dutreix A, and van der Schueren E. (1994) Reliability of clinical port films for measuring dose inhomogeneities in radiotherapy for head and neck tumours. Radiother. Oncol. 30(2):167-170.

Wheeler GCWS. (1988) Optically stimulated phosphorescence and optically transferred TL as a tool for dating. Quaternary Sci. 7:407-410.

Whitley VH and McKeever SWS. (2000), Photoionization of deep centres in Al_2O_3. Journal of applied clinical Med. Phys. 87:249-256.

Whitley VH and Mckeever SWS. (2001) Linearly modulated photoconductivity and linearly modulated optically stimulated luminescence measurements on Al_2O_3:C. Journal of applied physics. 90(12):6073-6083.

White PJ, Zwicher RD, and Huang DT. (1996) Comparison of dose homogeneity effects due to electron equilibrium loss in lung for 6 MV and 18 MV photons. Int J Radiat Oncol Biol Phys 34:1141-1146.

Wierzbicki JG and Waid DS. (1998) Large discrepancies between calculated D_{max} and diode readings for small field sizes and small SSDs of 15 MV photon beams. Med. Phys. 25(2):245-246.

Wintle AG. (1993) Recent developments in optical dating of sediments. Radiat. Prot. Dosim. 47(1):627-635.

Wood JJ and Mayles WP. (1995) Factors affecting the precision of TLD dose measurements using an automatic TLD reader. Phys. Med. Biol. 40:309-313.

Yang W. (2005) Digital film dosimetry in radiotherapy and the development of analytical applications software. PhD thesis.

Yin F-F, Schell MC, and Rubin P. (1994) Input/output characteristics of a matrix ion-chamber electronic portal imaging device. Med. Phys. 21(9):1447–1454.

Yoder RC and Salasky MR. (1997) A dosimetry system based on delayed optically stimulated luminescence. Health physics. 72:S18-S19.

Yoker E, Alecu R, Ding L, et al. (2005) AAPM report No. 87 (TG-62).Diode in vivo dosimetry for patients receiving external beam radiation therapy. American Association of Physicists in Medicine publication.

Yu CX, Jaffray DA, Wong JW. (1998) The effects of intra-fraction organ motion on the delivery of dynamic intensity modulation. Phys. Med.Biol. 43:91-104.

Yukihara EG, Whitley VH, McKeever SWS, Akselrod AE and Akselrod MS. (2004), Effect of high-dose irradiation on the optically stimulated luminescence of Al_2O_3:C, Radiat Meas. 38:317-330.

Yukihara EG, Yoshimura EM, Lindstrom TD, Ahmad S, Taylor KK, and Mardirossian G. (2005) High-precision dosimetry for radiotherapy using the optically stimulated luminescence technique and thin Al_2O_3:C dosimeters. Phys. Med. Biol. 50:5619-5628.

Yukihara EG, Mardirossian G, Mirzasadeghi M, Guduru S, and Ahmad S. (2008a) Evaluation of Al_2O_3:C optically stimulated luminescence (OSL) dosimeters for passive dosimetry of high-energy photon and electron beams in radiotherapy. Med. Phys. 35:260-269

Yukihara EG. and McKeever SWS. (2008b), Optically stimulated luminescence (OSL) dosimetry in medicine. Phys. Med. Biol. 53:R351-R379.

Zhu Y, Jiang X-Q and Van Dyk J. (1995) Portal dosimetry using a liquid ion chamber matrix: Dose response studies. Med. Phys. 22(7):1101–1106.

Appendix A: A Guide for OSL Dosimetry Radiotherapy Protocol Design

A.1 Sample handing

- OSLs are very sensitive to the light. An OSL dosimeter should be stored in a dark environment.
- The InLight™ dosimeter is based on a thin layer of carbon-doped aluminium oxide Al_2O_3:C powder deposited onto a clear polyester film. Each dosimeter element is a disc of 0.3 mm thick and 7 mm in diameter. Each slide of an InLight™ dosimeter is designed for storing the detector elements in a light-tight case using metal and plastic filters to protect the detectors from radiation. The InLight™ dot dosimeter has only the plastic case to protect it from light.
- Film type OSL can be carried by hand, but soiled hands need to avoided during cutting, reading and optical annealing. For small cut OSL films mechanical tweezers may should to used to assist in handling. OSL film is very sensitive to the physical damage; user need to careful to avoid bending the OSL.
- When using the InLight™ dot dosimeter it must be snapped into an adapter with the sensitivity code and serial number must face the front of the adapter.
- When using an InLight™ dosimeter remove the case during the irradiation. The case of an InLight™ dosimeter could filter the radiation causing measurement errors.

A.2 Setting up a new MicroStar reader

- Read and follow the instruction manual
- Test the reader and create separate control charts for DRK, CAL and LED standards and plot the established average value for each standard
- Calibrate the reader. Both the weak beam (High Dose) and the strong LED beam (Low Dose) need to be calibrated.
- Measure the control dose group. Measure a group of standard dosimeters exposed to the beam quality and range of doses you expect to need to read.

The manufacturer's control dose group OSLD can be used as control dose in environment dosimetry or diagnostic x-rays. For radiotherapy applications the control dose OSLD group should be irradiated to typical doses and beam qualities expected to be used in the clinic.

- Control dose: The MicroStar reader can use the default control dose for calibration. The default control dose is the average reading to dose converted value for all blank dosimeters following the method described in the manual. The "Use control dose for calibration" function can be disabled, which allows the user to define their own control dose. This is commonly useful for radiotherapy dosimetry.
- Dosimeter readout: If the default control dose is used, the readouts are shown as a dose in the selected units. If the default control dose is not used the readouts need to be converted to dose based on the user defined control dose.
- Look for a drift of readings with use

A.3 Routine use of the reader

1. Check the reader periodically and make sure the counts fall within the following parameters as recommended by the manufacturer:

- DRK is less than 30
- CAL within ± 10% of the established average value for the specific reader
- LED within ± 10% of the established average value for the specific reader

2. Recalibrate the reader when:

- It is moved between sites
- after repair or maintenance
- if there is a change in the type of dosimeter used
- if there is a change in the range of expected exposures

3. Check the control dose at regular intervals

4. Regularly check the movement of the Measurement Position Dial to make sure it works smoothly.

5. Establish a Quality Control Program

A.4 What to Consider when performing calibration of OSLDs with a user supplied radiation source

- Exposure OSLDs using a proper equivalent depth to maintain electron equilibrium
- Exposing OSLDs using different beam energies can improve the accuracy
- Use a sufficient number of dosimeters
- The sensitivity of OSLDs may vary by manufacture and batch
- Record radiation history of OSLDs, avoid the incremental dose (accumulated dose) over a linear range
- Reproducibility of all experimental conditions
- After an exposure multiple readings (Maximum 10 times) of each OSLD and averaging the result is recommended. The manufacture states that each reading of the dosimeter depletes some of the signal (less than about 0.2% per reading) and that background radiation exposure will increase the dose on calibration dosimeters.
- Annealing may or may not be required. If you use the annealing process the OSLD sensitivity needs to be reconsidered and re-measured.

A.5 Improving accuracy and precision

- Store OSL dosimeters in a dark environment
- Making multiple readings (maximum 10 times) and averaging the result is recommended for each irradiation measurement
- Using OSLDs for same manufacture's production batch for each measurement will improve accuracy and precision
- OSL dosimeters measure point dose. The position of the dosimeter is important.

A.6 OSL use in therapeutic radiology

- Can be used for skin dose and exit dose measurement in in-vivo dosimetry. Adding appropriate back scatter material will improve the accuracy.

- Can be used in a phantom as a point measurement tool for 3D-CRT and IMRT plan checks.
- Can be used for other applications in which TLDs are involved, for example, for Diagnostic X-rays.

Appendix B Original data for Markus Experiment in Exit dose dosimetry

Table B.1: Markus Experiment 1 results(1): raw reading (nC) of a measurement point at isocentre in a homogeneous slab phantom using a PTW Markus Ion-chamber through various back scatter thicknesses. The add-on physical back scatter thickness varies from 5.5cm to 0cm, and then with Markus Ion-chamber only. 100MU was delivered. Standard deviations of 3 repeated readings were added. (Data matching Figure 9.8)

(1): 6MV-X, RED=1.08, Units are nC

Add-on back scatter Physical Thickness (cm)	Square Field Size (cm^2) at isocentre				
	3x3	5x5	10x10	15x15	20x20
5.5	0.6030±0.0004	0.6407±0.0002	0.6918±0.0001	0.7171±0.0002	0.7324±0.0002
4.5	0.6029±0.0002	0.6406±0.0002	0.6914±0.0003	0.7164±0.0001	0.7319±0.0002
3.5	0.6023±0.0002	0.6400±0.0000	0.6903±0.0000	0.7143±0.0001	0.7302±0.0002
2.5	0.6024±0.0002	0.6394±0.0001	0.6894±0.0002	0.7131±0.0000	0.7277±0.0001
1.5	0.6015±0.0002	0.6384±0.0001	0.6873±0.0001	0.7106±0.0001	0.7246±0.0002
0.5	0.6013±0.0001	0.6377±0.0002	0.6859±0.0001	0.7078±0.0001	0.7211±0.0002
0	0.6004±0.0002	0.6367±0.0002	0.6837±0.0001	0.7047±0.0002	0.7177±0.0002
chamber only	0.6002±0.0002	0.6343±0.0002	0.6780±0.0001	0.6971±0.0002	0.7089±0.0003

(2): 10MV-X, RED=1.08, Units are nC

Add-on back scatter Physical Thickness (cm)	Square Field Size (cm^2) at isocentre				
	3x3	5x5	10x10	15x15	20x20
5.5	0.6467±0.0003	0.6883±0.0001	0.7355±0.0003	0.7572±0.0001	0.7719±0.0002
4.5	0.6467±0.0002	0.6883±0.0002	0.7352±0.0001	0.7571±0.0002	0.7713±0.0002
3.5	0.6467±0.0001	0.6879±0.0002	0.7346±0.0002	0.7557±0.0000	0.7700±0.0002
2.5	0.6461±0.0002	0.6875±0.0001	0.7345±0.0000	0.7550±0.0001	0.7689±0.0001
1.5	0.6455±0.0001	0.6863±0.0002	0.7332±0.0001	0.7529±0.0002	0.7661±0.0002
0.5	0.6455±0.0002	0.6857±0.0001	0.7313±0.0003	0.7519±0.0002	0.7643±0.0001
0	0.6451±0.0003	0.6848±0.0001	0.7288±0.0001	0.7488±0.0002	0.7609±0.0003
chamber only	0.6451±0.0002	0.6833±0.0001	0.7250±0.0004	0.7430±0.0002	0.7543±0.0003

Table B.2: Markus Experiment 1 results(2): Percentage difference from a build down thickness of 5.5 cm(as reference) to various back scatter thicknesses. The data were based on the raw readings from Table 10.1. The add-on back scatter physical thickness changes from 5.5cm to 0cm, then the Markus Ion-chamber in air only. Standard deviations in percentage of 3 repeated readings were added. (Data matching Figure 9.9)

A: 6MV-X, RED=1.08, Unit is ratio

Add-on back scatter Physical Thickness (cm)	Squared field size (cm^2) at isocentre				
	3x3	**5x5**	**10x10**	**15x15**	**20x20**
5.5	0.00%±0.04%	0.00%±0.02%	0.00%±0.01%	0.00%±0.02%	0.00%±0.02%
4.5	-0.02%±0.02%	-0.02%±0.02%	-0.06%±0.03%	-0.10%±0.01%	-0.07%±0.02%
3.5	-0.12%±0.02%	-0.11%±0.00%	-0.22%±0.00%	-0.39%±0.01%	-0.30%±0.02%
2.5	-0.10%±0.02%	-0.20%±0.01%	-0.35%±0.02%	-0.56%±0.00%	-0.64%±0.01%
1.5	-0.25%±0.02%	-0.36%±0.01%	-0.65%±0.01%	-0.91%±0.01%	-1.06%±0.02%
0.5	-0.28%±0.01%	-0.46%±0.02%	-0.86%±0.01%	-1.29%±0.01%	-1.54%±0.02%
0	-0.43%±0.02%	-0.62%±0.02%	-1.18%±0.01%	-1.73%±0.02%	-2.01%±0.02%
chamber only	-0.46%±0.02%	-0.99%±0.02%	-2.00%±0.01%	-2.79%±0.01%	-3.21%±0.03%

B: 10MV-X, RED=1.08, Unit is ratio

Add-on back scatter Physical Thickness (cm)	Squared field size (cm^2) at isocentre				
	3x3	**5x5**	**10x10**	**15x15**	**20x20**
5.5	0.00%±0.03%	0.00%±0.01%	0.00%±0.03%	0.00%±0.01%	0.00%±0.01%
4.5	0.00%±0.02%	0.00%±0.02%	-0.04%±0.01%	-0.01%±0.02%	-0.08%±0.02%
3.5	0.00%±0.01%	-0.06%±0.02%	-0.12%±0.02%	-0.20%±0.00%	-0.25%±0.02%
2.5	-0.10%±0.02%	-0.11%±0.01%	-0.14%±0.00%	-0.29%±0.01%	-0.39%±0.01%
1.5	-0.19%±0.01%	-0.29%±0.02%	-0.31%±0.01%	-0.57%±0.02%	-0.75%±0.02%
0.5	-0.19%±0.02%	-0.37%±0.01%	-0.57%±0.03%	-0.70%±0.02%	-0.99%±0.01%
0	-0.26%±0.03%	-0.51%±0.01%	-0.92%±0.01%	-1.11%±0.02%	-1.43%±0.03%
chamber only	-0.26%±0.03%	-0.73%±0.01%	-1.43%±0.04%	-1.88%±0.02%	-2.28%±0.03%

Table B.3: Markus Experiment 2 results (1): homogeneous phantom 1 with a RED of 1.08 was delivered 100MU under 6MV x-ray irradiation. Measurement points were taken at exit surface and the isocentre was at target centre of the phantom. The add-on physical back scatter thickness changed from 5.5cm to 0cm, then the Markus Ion-chamber in air only. Standard deviation of repeated readings was added for each OSL measurement. (Data matching Figure 9.12)

A: The raw reading (nC). Standard deviations of 3 repeated readings were added.

Backscatter Physical Thickness (cm)	Square field size (cm^2) at isocentre (Square field size (cm^2) at measurement point)				
	3x3 (3.27x3.27)	5x5 (5.45x5.45)	10x10 (10.90x10.90)	15x15 (16.35x16.35)	20x20 (21.80x21.80)
5.5	0.2709±0.0000	0.2975±0.0001	0.3460±0.0000	0.3761±0.0001	0.3954±0.0001
4.5	0.2715±0.0001	0.2980±0.0000	0.3465±0.0000	0.3766±0.000	0.3959±0.0002
3.5	0.2714±0.0000	0.2981±0.0002	0.3464±0.0000	0.3761±0.0000	0.3953±0.0001
2.5	0.2715±0.0001	0.2980±0.0001	0.3458±0.0001	0.3756±0.0001	0.3944±0.0001
1.5	0.2711±0.0000	0.2978±0.0001	0.3452±0.0001	0.3744±0.0002	0.3927±0.0000
0.5	0.2708±0.0000	0.2968±0.0000	0.3442±0.0001	0.3727±0.0001	0.3908±0.0001
0	0.2705±0.0002	0.2962±0.0001	0.3423±0.0001	0.3698±0.0001	0.3878±0.0000
Chamber only	0.2705±0.0002	0.2957±0.0001	0.3405±0.0001	0.3673±0.0002	0.3842±0.0002

B: The reduction ratio using the 5.5cm thickness. Standard deviations as a percentage of 3 repeated readings were added. Units are a percentage ratio.

Backscatter Physical Thickness (cm)	Square field size (cm^2) at isocentre (Square field size (cm^2) at measurement point)				
	3x3 (3.27x3.27)	5x5 (5.45x5.45)	10x10 (10.90x10.90)	15x15 (16.35x16.35)	20x20 (21.80x21.80)
5.5 as reference	0.00%±0.01%	0.00%±0.01%	0.00%±0.00%	0.00%±0.01%	0.00%±0.01%
4.5	0.24%±0.01%	0.17%±0.00%	0.14%±0.00%	0.15%±0.00%	0.15%±0.02%
3.5	0.19%±0.00%	0.21%±0.02%	0.12%±0.00%	0.01%±0.00%	-0.03%±0.01%
2.5	0.21%±0.01%	0.15%±0.01%	-0.07%±0.01%	-0.13%±0.01%	-0.25%±0.01%
1.5	0.08%±0.00%	0.08%±0.01%	-0.23%±0.01%	-0.45%±0.02%	-0.67%±0.00%
0.5	-0.03%±0.00%	-0.24%±0.00%	-0.53%±0.01%	-0.89%±0.01%	-1.15%±0.01%
0	-0.13%±0.02%	-0.43%±0.01%	-1.06%±0.01%	-1.66%±0.01%	-1.91%±0.00%
Chamber only	-0.16%±0.02%	-0.62%±0.01%	-1.59%±0.01%	-2.34%±0.02%	-2.83%±0.02%

Table B.4: Markus Experiment 2 results (2): phantom 4 with tissue sample of RED 1.53 inserted was delivered 100MU under 6MV x-ray irradiation. Measurement points were at exit surface and isocentre was at target centre of the phantom. The add-on physical back scatter thickness changes from 5.5cm to 0cm, then the Markus Ion-chamber in air only. Standard deviation of repeated readings was added for each OSL measurement. The add-on physical back scatter thickness changes from 5.5cm to 0cm, then the Markus Ion-chamber exposed in air. 100MU was delivered. (Data matching Figure 9.13)

A: The raw reading (nC). Standard deviations of 3 repeated readings were added.

Backscatter Physical Thickness (cm)	**Square field size (cm^2) at isocentre (Square field size (cm^2) at measurement point)**				
	3x3 (3.27x3.27)	**5x5 (5.45x5.45)**	**10x10 (10.90x10.90)**	**15x15 (16.35x16.35)**	**20x20 (21.80x21.80)**
5.5	0.2204±0.0001	0.2451±0.0001	0.2897±0.0001	0.3192±0.0001	0.3378±0.0001
4.5	0.2203±0.0002	0.2449±0.0001	0.2896±0.0000	0.3187±0.0001	0.3371±0.0001
3.5	0.2203±0.0001	0.2447±0.0000	0.2893±0.0001	0.3181±0.0002	0.3363±0.0001
2.5	0.2206±0.0000	0.2449±0.0001	0.2890±0.0000	0.3176±0.0001	0.3355±0.0000
1.5	0.2204±0.0001	0.2449±0.0001	0.2884±0.0000	0.3168±0.0001	0.3346±0.0001
0.5	0.2202±0.0001	0.2449±0.0000	0.2881±0.0001	0.3158±0.0000	0.3332±0.0001
0	0.2200±0.0000	0.2448±0.0001	0.2878±0.0001	0.3150±0.0000	0.3322±0.0000
Chamber only	0.2199±0.0000	0.2436±0.0001	0.2849±0.0002	0.3107±0.0000	0.3269±0.0001

B: The reduction ratio to the 5.5cm thickness. Standard deviations in percentage of 3 repeated readings were added. The units are a percentage ratio.

Backscatter Physical Thickness (cm)	**Square field size (cm^2) at isocentre (Square field size (cm^2) at measurement point)**				
	3x3 (3.27x3.27)	**5x5 (5.45x5.45)**	**10x10 (10.90x10.90)**	**15x15 (16.35x16.35)**	**20x20 (21.80x21.80)**
5.5 as reference	0.00%±0.01%	0.00%±0.01%	0.00%±0.01%	0.00%±0.01%	0.00%±0.01%
4.5	-0.05%±0.02%	-0.08%±0.01%	-0.03%±0.00%	-0.16%±0.01%	-0.21%±0.01%
3.5	-0.05%±0.01%	-0.16%±0.00%	-0.14%±0.01%	-0.34%±0.02%	-0.44%±0.00%
2.5	0.07%±0.01%	-0.08%±0.01%	-0.24%±0.01%	-0.50%±0.01%	-0.68%±0.01%
1.5	-0.02%±0.01%	-0.10%±0.01%	-0.45%±0.01%	-0.75%±0.01%	-0.95%±0.01%
0.5	-0.10%±0.00%	-0.10%±0.02%	-0.56%±0.01%	-1.07%±0.01%	-1.35%±0.01%
0	-0.18%±0.02%	-0.14%±0.01%	-0.67%±0.00%	-1.32%±0.01%	-1.67%±0.01%
Chamber only	-0.21%±0.01%	-0.60%±0.01%	-1.67%±0.01%	-2.65%±0.03%	-3.24%±0.03%

Table B.5: Markus Experiment 2 results (3): phantom 3 with tissue sample of RED 0.97 inserted was delivered 100MU under 6MV x-ray irradiation. Measurement points were at exit surface and isocentre was at target centre of the phantom. The add-on physical back scatter thickness changes from 5.5cm to 0cm, then the Markus Ion-chamber only. Standard deviation of repeated readings was added for each OSL measurement. (Data matching Figure 9.14)

A: The raw reading (nC). Standard deviations of 3 repeated readings were added.

Builddown Physical Thickness (cm)	**Square field size (cm^2) at isocentre (Square field size (cm^2) at measurement point)**				
	3x3 (3.27x3.27)	**5x5 (5.45x5.45)**	**10x10 (10.90x10.90)**	**15x15 (16.35x16.35)**	**20x20 (21.80x21.80)**
5.5	0.2805±0.0002	0.3075±0.0001	0.3566±0.0000	0.3869±0.0001	0.4060±0.0001
4.5	0.2810±0.0001	0.3076±0.0002	0.3566±0.0001	0.3871±0.0002	0.4060±0.0001
3.5	0.2808±0.0001	0.3079±0.0001	0.3564±0.0000	0.3866±0.0001	0.4053±0.0001
2.5	0.2809±0.0001	0.3078±0.0000	0.3562±0.0001	0.3859±0.0002	0.4047±0.0001
1.5	0.2807±0.0001	0.3077±0.0001	0.3553±0.0001	0.3851±0.0001	0.4033±0.0001
0.5	0.2808±0.0001	0.3073±0.0002	0.3546±0.0001	0.3832±0.0001	0.4014±0.0001
0	0.2804±0.0000	0.3062±0.0001	0.3530±0.0000	0.3814±0.0001	0.3995±0.0001
Chamber only	0.2800±0.0002	0.3052±0.0001	0.3507±0.0001	0.3780±0.0003	0.3949±0.0003

B: The reduction ratio to the 5.5cm thickness. Standard deviations in percentage of 3 repeated readings were added. The unit is a percentage ratio.

Builddown Physical Thickness (cm)	**Square field size (cm^2) at isocentre (Square field size (cm^2) at measurement point)**				
	3x3 (3.27x3.27)	**5x5 (5.45x5.45)**	**10x10 (10.90x10.90)**	**15x15 (16.35x16.35)**	**20x20 (21.80x21.80)**
5.5 as reference	0.00%±0.02%	0.00%±0.01%	0.00%±0.00%	0.00%±0.01%	0.00%±0.01%
4.5	0.18%±0.01%	0.03%±0.02%	0.00%±0.01%	0.05%±0.02%	0.00%±0.01%
3.5	0.11%±0.01%	0.13%±0.01%	-0.06%±0.00%	-0.08%±0.01%	-0.17%±0.01%
2.5	0.14%±0.01%	0.10%±0.00%	-0.11%±0.01%	-0.26%±0.02%	-0.32%±0.01%
1.5	0.07%±0.01%	0.07%±0.01%	-0.36%±0.01%	-0.47%±0.01%	-0.67%±0.01%
0.5	0.11%±0.00%	-0.07%±0.02%	-0.56%±0.01%	-0.96%±0.01%	-1.13%±0.01%
0	-0.03%±0.02%	-0.43%±0.01%	-1.00%±0.00%	-1.43%±0.01%	-1.60%±0.01%
Chamber only	-0.18%±0.01%	-0.75%±0.01%	-1.65%±0.01%	-2.30%±0.03%	-2.73%±0.03%

Table B.6: Markus Experiment 2 results (4): phantom 2 with tissue sample of RED 0.22 inserted was delivered under 6MV x-ray irradiation. Measurement points were at exit surface and isocentre was at target centre of the phantom. The add-on physical back scatter thickness changes from 5.5cm to 0cm, then the Markus Ion-chamber only. Standard deviation of repeated readings was added for each OSL measurement. (Data matching Figure 9.15)

A: The raw reading (nC). Standard deviations of 3 repeated readings were added.

Builddown Physical Thickness (cm)	Square field size (cm^2) at isocentre (Square field size (cm^2) at measurement point)				
	3x3 (3.27x3.27)	5x5 (5.45x5.45)	10x10 (10.90x10.90)	15x15 (16.35x16.35)	20x20 (21.80x21.80)
5.5	0.3297±0.0001	0.3578±0.0001	0.4104±0.0002	0.4418±0.0001	0.4612±0.0001
4.5	0.3296±0.0001	0.3576±0.0001	0.4103±0.0001	0.4417±0.0001	0.4610±0.0001
3.5	0.3297±0.0002	0.3574±0.0000	0.4099±0.0002	0.4410±0.0001	0.4602±0.0000
2.5	0.3295±0.0000	0.3573±0.0001	0.4096±0.0000	0.4405±0.0002	0.4595±0.0001
1.5	0.3298±0.0001	0.3572±0.0002	0.4089±0.0001	0.4394±0.0001	0.4582±0.0000
0.5	0.3299±0.0000	0.3569±0.0000	0.4080±0.0000	0.4379±0.0000	0.4562±0.0001
0	0.3295±0.0001	0.3564±0.0000	0.4070±0.0000	0.4365±0.0000	0.4548±0.0001
Chamber only	0.3288±0.0001	0.3551±0.0001	0.4040±0.0001	0.4323±0.0001	0.4497±0.0002

B: The reduction ratio to the 5.5cm thickness. Standard deviations in percentage of 3 repeated readings were added. Unit is a percentage ratio.

Builddown Physical Thickness (cm)	Square field size (cm^2) at isocentre (Square field size (cm^2) at measurement point)				
	3x3 (3.27x3.27)	5x5 (5.45x5.45)	10x10 (10.90x10.90)	15x15 (16.35x16.35)	20x20 (21.80x21.80)
5.5 as reference	0.00%±0.01%	0.00%±0.01%	0.00%±0.02%	0.00%±0.01%	0.00%±0.01%
4.5	-0.03%±0.01%	-0.06%±0.01%	-0.02%±0.01%	-0.02%±0.01%	-0.04%±0.01%
3.5	0.00%±0.02%	-0.11%±0.00%	-0.11%±0.02%	-0.18%±0.01%	-0.22%±0.00%
2.5	-0.06%±0.01%	-0.14%±0.01%	-0.19%±0.00%	-0.29%±0.01%	-0.37%±0.00%
1.5	0.02%±0.01%	-0.18%±0.01%	-0.37%±0.00%	-0.55%±0.01%	-0.65%±0.01%
0.5	0.06%±0.01%	-0.26%±0.00%	-0.57%±0.01%	-0.89%±0.01%	-1.08%±0.02%
0	-0.08%±0.00%	-0.41%±0.01%	-0.82%±0.01%	-1.21%±0.00%	-1.39%±0.01%
Chamber only	-0.27%±0.01%	-0.76%±0.01%	-1.55%±0.03%	-2.14%±0.01%	-2.50%±0.01%

Table B.7: Markus Experiment 2 results (5): homogeneous phantom 1 with a RED of 1.08 was delivered 100MU under 10MV x-ray.. Measurement points were taken at exit surface and the isocentre was at target centre of the phantom. The add-on physical back scatter thickness changed from 5.5cm to 0cm, then the Markus Ion-chamber only. Standard deviation of repeated readings was added for each OSL measurement. (Data matching Figure 9.16)

A: The raw reading (nC). Standard deviations of 3 repeated readings were added.

Builddown Physical Thickness (cm)	**Square field size (cm^2) at isocentre (Square field size (cm^2) at measurement point)**				
	3x3 (3.27x3.27)	**5x5 (5.45x5.45)**	**10x10 (10.90x10.90)**	**15x15 (16.35x16.35)**	**20x20 (21.80x21.80)**
5.5	0.3417±0.0002	0.3732±0.0001	0.4206±0.0002	0.4474±0.0001	0.4646±0.0002
4.5	0.3421±0.0000	0.3733±0.0001	0.4207±0.0001	0.4475±0.0002	0.4644±0.0003
3.5	0.3421±0.0001	0.3734±0.0001	0.4204±0.0001	0.4475±0.0000	0.4645±0.0000
2.5	0.3421±0.0000	0.3734±0.0001	0.4202±0.0001	0.4464±0.0003	0.4636±0.0001
1.5	0.3415±0.0001	0.3724±0.0002	0.4186±0.0001	0.4448±0.0001	0.4616±0.0002
0.5	0.3412±0.0002	0.3721±0.0001	0.4174±0.0000	0.4432±0.0000	0.4602±0.0001
0	0.3407±0.0001	0.3707±0.0004	0.4162±0.0004	0.4414±0.0001	0.4577±0.0001
Chamber only	0.3407±0.0000	0.3705±0.0001	0.4152±0.0001	0.4396±0.0002	0.4552±0.0002

B: The reduction ratio to the 5.5cm thickness. Standard deviations in percentage of 3 repeated readings were added. Units are a percentage ratio.

Builddown Physical Thickness (cm)	**Squared field size (cm^2) at isocentre (Square field size (cm^2) at measurement point)**				
	3x3 (3.27x3.27)	**5x5 (5.45x5.45)**	**10x10 (10.90x10.90)**	**15x15 (16.35x16.35)**	**20x20 (21.80x21.80)**
5.5 as reference	0.00%±0.02%	0.00%±0.01%	0.00%±0.02%	0.00%±0.01%	0.00%±0.02%
4.5	0.11%±0.00%	0.01%±0.01%	0.01%±0.01%	0.00%±0.02%	-0.05%±0.03%
3.5	0.09%±0.01%	0.04%±0.01%	-0.05%±0.01%	0.01%±0.00%	-0.02%±0.00%
2.5	0.11%±0.00%	0.04%±0.01%	-0.11%±0.01%	-0.23%±0.03%	-0.23%±0.01%
1.5	-0.08%±0.01%	-0.20%±0.02%	-0.47%±0.01%	-0.59%±0.01%	-0.66%±0.02%
0.5	-0.15%±0.02%	-0.30%±0.01%	-0.76%±0.00%	-0.95%±0.00%	-0.96%±0.02%
0	-0.30%±0.01%	-0.68%±0.04%	-1.05%±0.04%	-1.36%±0.01%	-1.49%±0.01%
Chamber only	-0.30%±0.00%	-0.74%±0.01%	-1.28%±0.01%	-1.76%±0.02%	-2.04%±0.02%

Table B.8: Markus Experiment 2 results (6): phantom 4 with tissue sample of RED 1.53 inserted was delivered under 10MV x-ray irradiation 100MU. Measurement points were at exit surface and isocentre was at target centre of the phantom. The add-on physical back scatter thickness changes from 5.5cm to 0cm, then the Markus Ion-chamber only. Standard deviation of repeated readings was added for each OSL measurement. (Data matching Figure 9.17)

A: The raw reading (nC). Standard deviations of 3 repeated readings were added.

Backscatter Physical Thickness (cm)	Square field size (cm^2) at isocentre (Square field size (cm^2) at measurement point)				
	3x3 (3.27x3.27)	5x5 (5.45x5.45)	10x10 (10.90x10.90)	15x15 (16.35x16.35)	20x20 (21.80x21.80)
5.5	0.2884±0.0001	0.3180±0.0001	0.3616±0.0001	0.3876±0.0001	0.4034±0.0001
4.5	0.2885±0.0001	0.3181±0.0002	0.3613±0.0001	0.3869±0.0001	0.4025±0.0001
3.5	0.2885±0.0002	0.3178±0.0001	0.3609±0.0001	0.3867±0.0002	0.4027±0.0001
2.5	0.2884±0.0001	0.3178±0.0001	0.3606±0.0001	0.3860±0.0001	0.4017±0.0002
1.5	0.2884±0.0002	0.3178±0.0002	0.3595±0.0001	0.3846±0.0000	0.4009±0.0000
0.5	0.2882 ±0.0001	0.3174±0.0002	0.3587±0.0002	0.3833±0.0001	0.3984±0.0002
0	0.2876±0.0001	0.3169±0.0001	0.3579±0.0001	0.3825±0.0001	0.3964±0.0003
Chamber only	0.2869±0.0001	0.3160±0.0002	0.3570±0.0000	0.3804±0.0002	0.3949±0.0002

B: The reduction ratio to the 5.5cm thickness. Standard deviations in percentage of 3 repeated readings were added. Unit is percentage ratio.

Backscatter Physical Thickness (cm)	Square field size (cm^2) at isocentre (Square field size (cm^2) at measurement point)				
	3x3 (3.27x3.27)	5x5 (5.45x5.45)	10x10 (10.90x10.90)	15x15 (16.35x16.35)	20x20 (21.80x21.80)
5.5	0.00% ±0.01%	0.00%±0.01%	0.00%±0.01%	0.00%±0.01%	0.00%±0.01%
4.5	0.03%±0.01%	0.03%±0.02%	-0.08%±0.01%	-0.18%±0.01%	-0.22%±0.01%
3.5	0.03%±0.02%	-0.06%±0.01%	-0.19%±0.01%	-0.23%±0.02%	-0.17%±0.01%
2.5	-0.01%±0.01%	-0.06%±0.01%	-0.27%±0.01%	-0.41%±0.01%	-0.42%±0.02%
1.5	0.00%±0.02%	-0.05%±0.02%	-0.58%±0.01%	-0.77%±0.00%	-0.62%±0.00%
0.5	-0.06%±0.01%	-0.18%±0.02%	-0.80%±0.02%	-1.11%±0.01%	-1.23%±0.02%
0	-0.27%±0.01%	-0.34%±0.01%	-1.02%±0.01%	-1.33%±0.01%	-1.74%±0.03%
In Air	-0.52%±0.01%	-0.64%±0.02%	-1.26%±0.00%	-1.87%±0.02%	-2.12%±0.02%

Table B.9: Markus Experiment 2 results (7): phantom 3 with tissue sample of RED 0.97 inserted was delivered under 10MV x-ray. Measurement points were at exit surface and isocentre was at target centre of the phantom. The add-on physical back scatter thickness changes from 5.5cm to 0cm, then the Markus Ion-chamber only. Standard deviation of repeated readings of each OSL was added. (Data matching Figure 9.18)

A: The raw reading (nC). Standard deviations of 3 repeated readings were added.

Backscatter Physical Thickness (cm)	**Square field size (cm^2) at isocentre (Square field size (cm^2) at measurement point)**				
	3x3 (3.27x3.27)	**5x5 (5.45x5.45)**	**10x10 (10.90x10.90)**	**15x15 (16.35x16.35)**	**20x20 (21.80x21.80)**
5.5	0.3497±0.0002	0.3820±0.0001	0.4297±0.0001	0.4570±0.0002	0.4738±0.0001
4.5	0.3495±0.0003	0.3822±0.0003	0.4297±0.0000	0.4568±0.0001	0.4729±0.0002
3.5	0.3499±0.0001	0.3821±0.0001	0.4294±0.0001	0.4562±0.0002	0.4727±0.0001
2.5	0.3502±0.0002	0.3820±0.0002	0.4290±0.0002	0.4559±0.0001	0.4719±0.0001
1.5	0.3499±0.0001	0.3819±0.0001	0.4285±0.0002	0.4551±0.0000	0.4713±0.0000
0.5	0.3500±0.0001	0.3817±0.0000	0.4279±0.0001	0.4542±0.0001	0.4703±0.0001
0	0.3500±0.0003	0.3816±0.0001	0.4269±0.0003	0.4534±0.0001	0.4693±0.0001
Chamber only	0.3495±0.0001	0.3800±0.0001	0.4248±0.0001	0.4498±0.0003	0.4641±0.0002

B: The reduction ratio to the 5.5cm thickness. Standard deviations in percentage of 3 repeated readings were added. Units are a percentage ratio.

Backscatter Physical Thickness (cm)	**Square field size (cm^2) at isocentre (Square field size (cm^2) at measurement point)**				
	3x3 (3.27x3.27)	**5x5 (5.45x5.45)**	**10x10 (10.90x10.90)**	**15x15 (16.35x16.35)**	**20x20 (21.80x21.80)**
5.5	0.00%±0.02%	0.00%±0.01%	0.00%±0.01%	0.00%±0.02%	0.00%±0.01%
4.5	-0.06%±0.03%	0.05%±0.03%	0.00%±0.00%	-0.04%±0.01%	-0.19%±0.02%
3.5	0.06%±0.01%	0.03%±0.01%	-0.07%±0.01%	-0.18%±0.02%	-0.23%±0.01%
2.5	0.14%±0.02%	0.00%±0.02%	-0.16%±0.02%	-0.24%±0.01%	-0.40%±0.01%
1.5	0.06%±0.01%	-0.03%±0.01%	-0.28%±0.02%	-0.42%±0.00%	-0.53%±0.00%
0.5	0.09%±0.01%	-0.08%±0.00%	-0.42%±0.01%	-0.61%±0.01%	-0.74%±0.01%
0	0.09%±0.03%	-0.10%±0.01%	-0.65%±0.03%	-0.80%±0.01%	-0.96%±0.01%
Chamber only	-0.06%±0.01%	-0.52%±0.01%	-1.14%±0.01%	-1.58%±0.03%	-2.05%±0.02%

Table B.10: Markus Experiment 2 results (8): phantom 2 with tissue sample of RED 0.22 inserted was delivered 100MU under 10MV x-ray. Measurement points were at exit surface and isocentre was at target centre of the phantom. The add-on physical back scatter thickness changes from 5.5cm to 0cm, then the Markus Ion-chamber only. Standard deviation of repeated readings of each OSL was added. (Data matching Figure 9.19)

A: The raw reading (nC). Standard deviations of 3 repeated readings were added.

Backscatter Physical Thickness (cm)	Square field size (cm^2) at isocentre (Square field size (cm^2) at measurement point)				
	3x3 (3.27x3.27)	5x5 (5.45x5.45)	10x10 (10.90x10.90)	15x15 (16.35x16.35)	20x20 (21.80x21.80)
5.5	0.3926±0.0001	0.4261±0.0001	0.4771±0.0001	0.5055±0.0003	0.5222±0.0002
4.5	0.3927±0.0001	0.4258±0.0000	0.4767±0.0001	0.5052±0.0001	0.5227±0.0001
3.5	0.3922±0.0002	0.4256±0.0001	0.4763±0.0000	0.5051±0.0001	0.5213±0.0002
2.5	0.3925±0.0001	0.4256±0.0001	0.4764±0.0001	0.5044±0.0002	0.5213±0.0001
1.5	0.3923±0.0001	0.4257±0.0001	0.4761±0.0000	0.5037±0.0001	0.5202±0.0004
0.5	0.3923±0.0001	0.4256±0.0002	0.4758±0.0003	0.5030±0.0000	0.5193±0.0002
0	0.3922±0.0001	0.4251±0.0000	0.4747±0.0002	0.5014±0.0003	0.5176±0.0003
Chamber only	0.3916±0.0001	0.4232±0.0001	0.4718±0.0001	0.4975±0.0003	0.5131±0.0002

B: The reduction ratio to the 5.5cm thickness. Standard deviations in percentage of 3 repeated readings were added. Units are a percentage ratio.

Backscatter Physical Thickness (cm)	Square field size (cm^2) at isocentre (Square field size (cm^2) at measurement point)				
	3x3 (3.27x3.27)	5x5 (5.45x5.45)	10x10 (10.90x10.90)	15x15 (16.35x16.35)	20x20 (21.80x21.80)
5.5	0.00%±0.01%	0.00%±0.01%	0.00%±0.01%	0.00%±0.03%	0.00%±0.02%
4.5	0.03%±0.01%	-0.07%±0.00%	-0.08%±0.01%	-0.06%±0.01%	0.00%±0.01%
3.5	-0.10%±0.02%	-0.12%±0.01%	-0.17%±0.00%	-0.08%±0.01%	-0.17%±0.02%
2.5	-0.03%±0.01%	-0.12%±0.01%	-0.15%±0.01%	-0.22%±0.02%	-0.17%±0.01%
1.5	-0.07%±0.04%	-0.09%±0.01%	-0.21%±0.00%	-0.37%±0.01%	-0.39%±0.01%
0.5	-0.07%±0.01%	-0.13%±0.02%	-0.28%±0.03%	-0.49%±0.00%	-0.56%±0.02%
0	-0.11%±0.01%	-0.23%±0.00%	-0.51%±0.02%	-0.81%±0.03%	-0.88%±0.03%
Chamber only	-0.25%±0.01%	-0.67%±0.01%	-1.10%±0.01%	-1.58%±0.03%	-1.74%±0.02%

Table B.11: Markus Experiment 2 results (9): The summary of the reduction ratios of various thicknesses to that of full back scatter (back scatter =5.5cm) in average of four phantom combinations (phantom 1 to 4). The add-on physical back scatter thickness changes from 5.5cm to 0cm, then the Markus Ion- chamber in air only. The raw readings of back scatter thickness in 5.5cm are set as reference. 100MU was delivered with 6MV and 10MV x-rays. To be mentioned that the standard deviation of repeated readings were not list due to less than 0.05%. (Data matching Figure 9.20)

A: The raw reading (nC). Standard deviations of 3 repeated readings were added.

Backscatter Physical Thickness (cm)	**Square field size (cm^2) at isocentre (Square field size (cm^2) at measurement point)**				
	3x3 (3.27x3.27)	**5x5 (5.45x5.45)**	**10x10 (10.90x10.90)**	**15x15 (16.35x16.35)**	**20x20 (21.80x21.80)**
4.5	0.09%±0.15%	0.02%±0.11%	-0.05%±0.19%	-0.01%±0.15%	-0.03%±0.15%
3.5	0.06%±0.11%	0.02%±0.18%	-0.12%±0.22%	-0.17%±0.20%	-0.21%±0.17%
2.5	0.09%±0.12%	0.01%±0.14%	-0.23%±0.19%	-0.34%±0.24%	-0.41%±0.19%
1.5	0.04%±0.05%	-0.03%±0.13%	-0.43%±0.18%	-0.60%±0.23%	-0.73%±0.14%
0.5	0.01%±0.09%	-0.16%±0.10%	-0.63%±0.16%	-1.02%±0.22%	-1.18%±0.12%
0	-0.11%±0.06%	-0.35%±0.14%	-0.96%±0.20%	-1.49%±0.22%	-1.64%±0.21%
Chamber only	-0.20%±0.05%	-0.68%±0.08%	-1.69%±0.11%	-2.50%±0.50%	-2.83%±0.31%
Maximum SD	**±0.15%**	**±0.18%**	**±0.22%**	**±0.50%**	**±0.31%**

B: The reduction ratio to the 5.5cm thickness. Standard deviations in percentage of 3 repeated readings were added. Units are a percentage ratio.

Backscatter Physical Thickness (cm)	**Square field size (cm^2) at isocentre (Square field size (cm^2) at measurement point)**				
	3x3 (3.27x3.27)	**5x5 (5.45x5.45)**	**10x10 (10.90x10.90)**	**15x15 (16.35x16.35)**	**20x20 (21.80x21.80)**
4.5	0.03%±0.07%	0.00%±0.05%	-0.04%±0.05%	-0.07%±0.08%	-0.12%±0.11%
3.5	0.02%±0.09%	-0.02%±0.08%	-0.12%±0.07%	-0.12%±0.11%	-0.15%±0.09%
2.5	0.05%±0.08%	-0.02%±0.08%	-0.17%±0.07%	-0.28%±0.09%	-0.31%±0.12%
1.5	-0.02%±0.06%	-0.14%±0.08%	-0.39%±0.17%	-0.54%±0.19%	-0.55%±0.12%
0.5	-0.05%±0.10%	-0.23%±0.09%	-0.56%±0.25%	-0.79%±0.29%	-0.87%±0.29%
0	-0.15%±0.18%	-0.48%±0.23%	-0.81%±0.27%	-1.08%±0.31%	-1.27%±0.42%
Chamber only	-0.28%±0.19%	-0.70%±0.05%	-1.20%±0.09%	-1.70%±0.14%	-1.98%±0.17%
Maximum SD	**±0.19%**	**±0.23%**	**±0.27%**	**±0.31%**	**±0.42%**

Table B.12: Markus Experiment 3 results (1): The raw reading (nC) of phantom 2, 3 and 4 with three tissue samples (RED =0.22, 0.97 and 1.53, respectively) inserted. 100MU was delivered using 6MV x-rays. The isocentre was set to measurement points which at the exit surface of the phantoms. The add-on physical back scatter thicknesses were 5.5cm, 0.5cm and then the Markus Ion- chamber only (represented by In Air here). (Data matching Figure 9.22)

Square Field (cm x cm) at SAD/SCD=100	**Phantom 2 (RED=0.22) Equivalent thickness 14.58cm**			**Phantom 3 (RED=0.97) Equivalent thickness 18.88cm**			**Phantom 4 (RED=1.53) Equivalent thickness 22.24cm**		
Back scatter (cm)	**5.5**	**0.5**	**In Air**	**5.5**	**0.5**	**In Air**	**5.5**	**0.5**	**In Air**
3x3	0.3953	0.3951	0.3954	0.3323	0.3319	0.3332	0.2629	0.2615	0.2624
4x4	0.4124	0.4121	0.4109	0.3487	0.3478	0.3485	0.2778	0.2766	0.2767
5x5	0.4275	0.4267	0.4243	0.3629	0.3617	0.3618	0.2911	0.2897	0.2894
6x6	0.4412	0.4398	0.4372	0.3759	0.3744	0.3739	0.3032	0.3010	0.3006
7x7	0.4545	0.4529	0.4496	0.3882	0.3863	0.3857	0.3138	0.3116	0.3106
8x8	0.4668	0.4646	0.4611	0.3993	0.3971	0.3960	0.3240	0.3216	0.3199
9x9	0.4776	0.4750	0.4713	0.4095	0.4071	0.4054	0.3333	0.3305	0.3286
10x10	0.4876	0.4846	0.4803	0.4189	0.4160	0.4142	0.3421	0.3387	0.3367
11x11	0.4968	0.4933	0.4887	0.4273	0.4239	0.4217	0.3499	0.3464	0.3438
12x12	0.5052	0.5015	0.4965	0.4353	0.4318	0.4288	0.3575	0.3535	0.3504
13x13	0.5127	0.5086	0.5031	0.4424	0.4384	0.4352	0.3642	0.3601	0.3566
14x14	0.5193	0.5148	0.5090	0.4491	0.4450	0.4412	0.3707	0.3660	0.3625
15x15	0.5259	0.5209	0.5150	0.4554	0.4506	0.4467	0.3769	0.3718	0.3678
16x16	0.5321	0.5269	0.5203	0.4613	0.4562	0.4516	0.3824	0.3769	0.3728
17x17	0.5375	0.5321	0.5253	0.4668	0.4613	0.4567	0.3876	0.3818	0.3774
18x18	0.5427	0.5370	0.5296	0.4715	0.4658	0.4605	0.3923	0.3862	0.3814
19x19	0.5469	0.5411	0.5335	0.4762	0.4702	0.4648	0.3963	0.3903	0.3852
20x20	0.5507	0.5451	0.5373	0.4800	0.4738	0.4680	0.4002	0.3939	0.3885

Table B.13: Markus Experiment 3 results (2): The reduction ratio (%) of phantom 2, 3, and 4 with three tissue samples (RED =0.22, 0.97 and 1.53, respectively) inserted. 100MU was delivered using 6MV x-rays. The isocentre was set to measurement points which at the exit surface of the phantoms. The add-on physical back scatter thicknesses were 5.5cm, 0.5cm and then the Markus Ion- chamber only (represented by In Air here). (Data matching Figure 9.23)

Square Field (cm x cm) at SAD/SCD=100	**Phantom 2 (RED=0.22) Equivalent thickness 14.58cm**		**Phantom 3 (RED=0.97) Equivalent thickness 18.88cm**		**Phantom 4 (RED=1.53) Equivalent thickness 22.24cm**	
Back scatter (cm)	**0.5**	**In Air**	**0.5**	**In Air**	**0.5**	**In Air**
3x3	-0.04%	0.03%	-0.12%	0.27%	-0.53%	-0.19%
4x4	-0.08%	-0.36%	-0.36%	-0.06%	-0.43%	-0.40%
5x5	-0.19%	-0.75%	-0.33%	-0.30%	-0.48%	-0.58%
6x6	-0.32%	-0.91%	-0.40%	-0.53%	-0.71%	-0.84%
7x7	-0.35%	-1.08%	-0.49%	-0.64%	-0.70%	-0.70%
8x8	-0.47%	-1.22%	-0.55%	-0.83%	-0.74%	-1.27%
9x9	-0.54%	-1.32%	-0.60%	-1.00%	-0.84%	-1.41%
10x10	-0.62%	-1.50%	-0.69%	-1.12%	-0.99%	-1.58%
11x11	-0.70%	-1.63%	-0.80%	-1.31%	-1.00%	-1.74%
12x12	-0.73%	-1.72%	-0.80%	-1.49%	-1.11%	-1.97%
13x13	-0.80%	-1.87%	-0.90%	-1.63%	-1.13%	-2.09%
14x14	-0.87%	-1.98%	-0.91%	-1.76%	-1.27%	-2.21%
15x15	-0.95%	-2.07%	-1.05%	-1.91%	-1.35%	-2.41%
16x16	-0.98%	-2.22%	-1.11%	-2.10%	-1.44%	-2.51%
17x17	-1.00%	-2.27%	-1.18%	-2.16%	-1.50%	-2.63%
18x18	-1.04%	-2.40%	-1.21%	-2.33%	-1.55%	-2.78%
19x19	-1.06%	-2.45%	-1.26%	-2.39%	-1.51%	-2.81%
20x20	-1.02%	-2.44%	-1.29%	-2.50%	-1.57%	-2.93%

Table B.14: Markus Experiment 4results (1): The raw data (nC) of phantom 2 with tissue material RED of 0.22 inserted. 100MU was delivered using 6MV and 10MV x-rays. The isocentre was set to measurement points which at the exit surface of the phantoms. The add-on physical back scatter thicknesses were 5.5cm, 0.5cm and then the Markus Ion-chamber only (represented by 'In Air' here). (Data matching Figure 9.24)

Square Field (cm x cm) at SAD/SCD=100	**6MV**			**10MV**		
Back scatter (cm)	**5.5**	**0.5**	**In Air**	**5.5**	**0.5**	**In Air**
3x3	0.3953	0.3951	0.3954	0.4739	0.4749	0.4755
4x4	0.4124	0.4121	0.4109	0.4961	0.4957	0.4957
5x5	0.4275	0.4267	0.4243	0.5121	0.5110	0.5109
6x6	0.4412	0.4398	0.4372	0.5262	0.5250	0.5244
7x7	0.4545	0.4529	0.4496	0.5388	0.5374	0.5369
8x8	0.4668	0.4646	0.4611	0.5509	0.5493	0.5485
9x9	0.4776	0.4750	0.4713	0.5613	0.5592	0.5584
10x10	0.4876	0.4846	0.4803	0.5704	0.5680	0.5669
11x11	0.4968	0.4933	0.4887	0.5790	0.5762	0.5750
12x12	0.5052	0.5015	0.4965	0.5862	0.5832	0.5816
13x13	0.5127	0.5086	0.5031	0.5932	0.5901	0.5881
14x14	0.5193	0.5148	0.5090	0.5990	0.5953	0.5936
15x15	0.5259	0.5209	0.5150	0.6053	0.6012	0.5991
16x16	0.5321	0.5269	0.5203	0.6106	0.6062	0.6040
17x17	0.5375	0.5321	0.5253	0.6152	0.6105	0.6081
18x18	0.5427	0.5370	0.5296	0.6196	0.6147	0.6121
19x19	0.5469	0.5411	0.5335	0.6232	0.6183	0.6154
20x20	0.5507	0.5451	0.5373	0.6267	0.6215	0.6182

Table B.15: Markus Experiment 4 results (2): The reduction ratio (%) of phantom 2 with tissue material RED of 0.22 inserted. 100MU was delivered using 6MV and 10MV x-rays. The isocentre was set to measurement points which at the exit surface of the phantoms. The add-on physical back scatter thicknesses were 5.5cm, 0.5cm and then the Markus Ion-chamber only (represented by 'In Air' here). Back scatter of 5.5cm raw reading was set as a reference for comparison. (Data matching Figure 9.25)

Square Field (cm x cm) at SAD/SCD=100	**6MV**		**10MV**	
Back scatter (cm)	**0.5**	**In Air**	**0.5**	**In Air**
3x3	-0.04%	0.03%	0.21%	0.34%
4x4	-0.08%	-0.36%	-0.09%	-0.08%
5x5	-0.19%	-0.75%	-0.21%	-0.22%
6x6	-0.32%	-0.91%	-0.22%	-0.33%
7x7	-0.35%	-1.08%	-0.26%	-0.36%
8x8	-0.47%	-1.22%	-0.29%	-0.44%
9x9	-0.54%	-1.32%	-0.37%	-0.51%
10x10	-0.62%	-1.50%	-0.42%	-0.61%
11x11	-0.70%	-1.63%	-0.47%	-0.68%
12x12	-0.73%	-1.72%	-0.51%	-0.78%
13x13	-0.80%	-1.87%	-0.52%	-0.86%
14x14	-0.87%	-1.98%	-0.62%	-0.90%
15x15	-0.95%	-2.07%	-0.69%	-1.02%
16x16	-0.98%	-2.22%	-0.73%	-1.08%
17x17	-1.00%	-2.27%	-0.76%	-1.15%
18x18	-1.04%	-2.40%	-0.79%	-1.21%
19x19	-1.06%	-2.45%	-0.79%	-1.25%
20x20	-1.02%	-2.44%	-0.83%	-1.36%
Min Difference	**-0.04%**	**0.03%**	**-0.09%**	**-0.08%**
Max Difference	**-1.06%**	**-2.45%**	**-0.83%**	**-1.36%**

Table B.16: Markus Experiment 5 results (1): Verification measurement data in phantom 2 with equivalent thickness of 14.58cm. Full backscatter (5.5cm) was added to PTW Markus ion-chamber. All the measured data were delivered using 100MU of 6MV x-rays. Raw data (1), raw data at the dmax of 6MV (2) were measured. Correction factors (4) were calculated using a effective SSD method based on relative RED to water calculated in Chapter 9. TMR (d=18) data were set as reference. Others were calculated based on the equations described in the table. (Data matching Figure 9.26)

	(1)	(2)	(3)	(4)	(5)	(6)	(7)	(8)
FSZ at isocentre	**Raw data**	**Raw data at dmax**	**Data Normalized to dmax** (1)/(2)	**Correction Factor (CF)**	**Data After CF Correction** (3)/(4)	**Ref TMR (d=18)**	**Difference** (5) – (6)	**Diff (%)** (7)/100
3x3	0.3953	0.6892	0.5736	1.1577	0.49543	0.4995	-0.0041	**-0.41%**
4x4	0.4124	0.7049	0.5850	1.1586	0.50496	0.5094	-0.0045	**-0.45%**
5x5	0.4275	0.7171	0.5962	1.1586	0.51454	0.5192	-0.0047	**-0.47%**
6x6	0.4412	0.7273	0.6066	1.1566	0.52449	0.5301	-0.0056	**-0.56%**
7x7	0.4545	0.7366	0.6170	1.1532	0.53505	0.5396	-0.0045	**-0.45%**
8x8	0.4668	0.7447	0.6268	1.1514	0.54441	0.5490	-0.0046	**-0.46%**
9x9	0.4776	0.7513	0.6357	1.1521	0.55177	0.5575	-0.0057	**-0.57%**
10x10	0.4876	0.7568	0.6443	1.1495	0.56050	0.5652	-0.0047	**-0.47%**
11x11	0.4968	0.7618	0.6521	1.1469	0.56861	0.5725	-0.0039	**-0.39%**
12x12	0.5052	0.7665	0.6591	1.1442	0.57604	0.5792	-0.0031	**-0.31%**
13x13	0.5127	0.7705	0.6654	1.1417	0.58283	0.5852	-0.0024	**-0.24%**
14x14	0.5193	0.7737	0.6712	1.1394	0.58907	0.5912	-0.0021	**-0.21%**
15x15	0.5259	0.7775	0.6764	1.1371	0.59485	0.5974	-0.0025	**-0.25%**
16x16	0.5321	0.7809	0.6814	1.135	0.60035	0.6043	-0.0039	**-0.39%**
17x17	0.5375	0.7836	0.6859	1.1322	0.60584	0.6110	-0.0051	**-0.51%**
18x18	0.5427	0.7868	0.6898	1.1283	0.61132	0.6166	-0.0053	**-0.53%**
19x19	0.5469	0.7884	0.6937	1.1271	0.61546	0.6200	-0.0045	**-0.45%**
20x20	0.5507	0.7907	0.6965	1.1261	0.61848	0.6234	-0.0049	**-0.49%**
Minimum difference								**-0.21%**
Maximum difference								**-0.57%**

Table B.17: Markus Experiment 5 results (2): Verification measurement data in phantom 2 with equivalent thickness of 14.58cm. No additional backscatter was added to PTW Markus ion-chamber. All the measured data were delivered using 100MU of 6MV x-rays. Raw data (1), raw data at dmax of 6MV (2) were measured. Correction factors (4) were calculated using a effective SSD method based on relative RED to water calculated in Chapter 9. TMR (d=18) data were set as reference. Others were calculated based on the equations described in the table. (Data matching Figure 9.26)

	(1)	(2)	(3)	(4)	(5)	(6)	(7)	(8)
FSZ at isocentre	**Raw data**	**Raw data at dmax**	**Data Normalized to dmax** (1)/(2)	**Correction Factor (CF)**	**Data After CF Correction** (3)/(4)	**Ref TMR (d=18)**	**Difference** (5) – (6)	**Diff (%)** (7)/100
3x3	0.3954	0.6892	0.5737	1.1577	0.4956	0.4995	-0.0040	**-0.40%**
4x4	0.4109	0.7049	0.5829	1.1586	0.5031	0.5094	-0.0063	**-0.63%**
5x5	0.4243	0.7171	0.5917	1.1586	0.5107	0.5192	-0.0085	**-0.85%**
6x6	0.4372	0.7273	0.6011	1.1566	0.5197	0.5301	-0.0103	**-1.03%**
7x7	0.4496	0.7366	0.6104	1.1532	0.5293	0.5396	-0.0103	**-1.03%**
8x8	0.4611	0.7447	0.6192	1.1514	0.5378	0.5490	-0.0112	**-1.12%**
9x9	0.4713	0.7513	0.6273	1.1521	0.5445	0.5575	-0.0130	**-1.30%**
10x10	0.4803	0.7568	0.6346	1.1495	0.5521	0.5652	-0.0130	**-1.30%**
11x11	0.4887	0.7618	0.6415	1.1469	0.5593	0.5725	-0.0131	**-1.31%**
12x12	0.4965	0.7665	0.6477	1.1442	0.5661	0.5792	-0.0131	**-1.31%**
13x13	0.5031	0.7705	0.6530	1.1417	0.5719	0.5852	-0.0133	**-1.33%**
14x14	0.509	0.7737	0.6579	1.1394	0.5774	0.5912	-0.0138	**-1.38%**
15x15	0.515	0.7775	0.6624	1.1371	0.5825	0.5974	-0.0149	**-1.49%**
16x16	0.5203	0.7809	0.6663	1.135	0.5870	0.6043	-0.0173	**-1.73%**
17x17	0.5253	0.7836	0.6704	1.1322	0.5921	0.6110	-0.0189	**-1.89%**
18x18	0.5296	0.7868	0.6731	1.1283	0.5966	0.6166	-0.0200	**-2.00%**
19x19	0.5335	0.7884	0.6767	1.1271	0.6004	0.6200	-0.0196	**-1.96%**
20x20	0.5373	0.7907	0.6795	1.1261	0.6034	0.6234	-0.0200	**-2.00%**
Minimum difference								**-0.40%**
Maximum difference								**-2.00%**

Table B.18: Markus Experiment 5 results (3): Verification measurement data in phantom 3 with equivalent thickness of 18.88cm. Full backscatter (5.5cm) was added for PTW Markus ion-chamber. All the measured data were delivered 100MU with 6MV x-ray. Raw data (1), raw data at dmax of 6MV (2) were measured. Correction factors (4) were calculated using effective SSD method based on relative RED to water calculated in Chapter 9. TMR (d=18) data were set as reference. Others were calculated based on the equations described in the table. (Data matching Figure 9.26)

	(1)	(2)	(3)	(4)	(5)	(6)	(7)	(8)
FSZ at isocentre	**Raw data**	**Raw data at dmax**	**Normalized to dmax** (1)/(2)	**Correction Factor**	**After CF Correction** (3)/(4)	**TMR (d=18)**	**Difference** (5) – (6)	**Diff (%)**
3x3	0.3324	0.6892	0.4822	0.9633	0.5005	0.4995	0.0012	**0.12%**
4x4	0.3437	0.7049	0.4947	0.9654	0.5124	0.5094	-0.0044	**-0.44%**
5x5	0.3577	0.7171	0.5061	0.9680	0.5228	0.5192	-0.0039	**-0.39%**
6x6	0.3703	0.7273	0.5168	0.9664	0.5348	0.5301	-0.0033	**-0.33%**
7x7	0.3827	0.7366	0.5270	0.9651	0.5461	0.5396	-0.0013	**-0.13%**
8x8	0.3936	0.7447	0.5362	0.9689	0.5534	0.549	-0.0035	**-0.35%**
9x9	0.4036	0.7513	0.5451	0.9689	0.5626	0.5575	-0.0030	**-0.30%**
10x10	0.4128	0.7568	0.5535	0.9686	0.5715	0.5652	-0.0020	**-0.20%**
11x11	0.4214	0.7618	0.5609	0.9710	0.5777	0.5725	-0.0028	**-0.28%**
12x12	0.4292	0.7665	0.5679	0.9730	0.5837	0.5792	-0.0037	**-0.37%**
13x13	0.4363	0.7705	0.5742	0.9722	0.5906	0.5852	-0.0028	**-0.28%**
14x14	0.4426	0.7737	0.5805	0.9714	0.5976	0.5912	-0.0023	**-0.23%**
15x15	0.4493	0.7775	0.5857	0.9708	0.6033	0.5974	-0.0021	**-0.21%**
16x16	0.4548	0.7809	0.5907	0.9700	0.6090	0.6043	-0.0039	**-0.39%**
17x17	0.4598	0.7836	0.5957	0.9694	0.6145	0.611	-0.0057	**-0.57%**
18x18	0.4646	0.7868	0.5993	0.9694	0.6182	0.6166	-0.0074	**-0.74%**
19x19	0.469	0.7884	0.6040	0.9706	0.6223	0.6200	-0.0071	**-0.71%**
20x20	0.4729	0.7907	0.6071	0.9718	0.6247	0.6234	-0.0079	**-0.79%**
							Minimum difference	**0.12%**
							Maximum difference	**-0.79%**

Table B.19: Markus Experiment 5 results (4): Verification measurement data in phantom 3 with equivalent thickness of 18.88cm. No additional back scatter was added for PTW Markus ion-chamber. All the measured data were delivered using 100MU of 6MV x-rays. Raw data (1), raw data at dmax of 6MV (2) were measured. Correction factors (4) were calculated using effective SSD method based on relative RED to water calculated in Chapter 9. TMR (d=18) data were set as reference. Others were calculated based on the equations described in the table. (Data matching Figure 9.26)

	(1)	(2)	(3)	(4)	(5)	(6)	(7)	(8)
FSZ at isocentre	**Raw data**	**Raw data at dmax**	**Normalized to dmax** (1)/(2)	**Correction Factor**	**After CF Correction** (3)/(4)	**TMR (d=18)**	**Difference** (5) – (6)	**Diff (%)** (7)/100
3x3	0.3332	0.6892	0.4835	0.9633	0.5019	0.4995	0.0024	**0.24%**
4x4	0.3485	0.7049	0.4944	0.9654	0.5121	0.5094	0.0027	**0.27%**
5x5	0.3618	0.7171	0.5045	0.9680	0.5212	0.5192	0.0020	**0.20%**
6x6	0.3739	0.7273	0.5141	0.9664	0.5320	0.5301	0.0019	**0.19%**
7x7	0.3857	0.7366	0.5236	0.9651	0.5426	0.5396	0.0030	**0.30%**
8x8	0.396	0.7447	0.5318	0.9689	0.5488	0.549	-0.0002	**-0.02%**
9x9	0.4054	0.7513	0.5396	0.9689	0.5569	0.5575	-0.0006	**-0.06%**
10x10	0.4142	0.7568	0.5473	0.9686	0.5651	0.5652	-0.0001	**-0.01%**
11x11	0.4217	0.7618	0.5536	0.9710	0.5701	0.5725	-0.0024	**-0.24%**
12x12	0.4288	0.7665	0.5594	0.9730	0.5750	0.5792	-0.0042	**-0.42%**
13x13	0.4352	0.7705	0.5648	0.9722	0.5810	0.5852	-0.0042	**-0.42%**
14x14	0.4412	0.7737	0.5702	0.9714	0.5871	0.5912	-0.0041	**-0.41%**
15x15	0.4467	0.7775	0.5745	0.9708	0.5918	0.5974	-0.0056	**-0.56%**
16x16	0.4516	0.7809	0.5783	0.9700	0.5962	0.6043	-0.0081	**-0.81%**
17x17	0.4567	0.7836	0.5828	0.9694	0.6012	0.611	-0.0098	**-0.98%**
18x18	0.4605	0.7868	0.5853	0.9694	0.6038	0.6166	-0.0128	**-1.28%**
19x19	0.4648	0.7884	0.5895	0.9706	0.6074	0.62	-0.0126	**-1.26%**
20x20	0.468	0.7907	0.5919	0.9718	0.6091	0.6234	-0.0143	**-1.43%**
							Minimum difference	**-0.02%**
							Maximum difference	**-1.43%**

Table B.20: Markus Experiment 5 results (5): Verification measurement data in phantom 4 with equivalent thickness of 22.24cm. Full backscatter (5.5cm) was added for PTW Markus ion-chamber. All the measured data were delivered using 100MU of 6MV x-rays. Raw data (1), raw data at dmax (2) were measured. Correction factors (4) were calculated using effective SSD method based on relative RED to water calculated in Chapter 9. TMR (d=18) data were set as reference. Others were calculated based on the equations described in the table. (Data matching Figure 9.26)

	(1)	(2)	(3)	(4)	(5)	(6)	(7)	(8)
FSZ at isocentre	**Raw data No add-on back scatter**	**Raw data at dmax**	**Normalized to dmax** (1)/(2)	**Correction Factor**	**After CF Correction** (3)/(4)	**TMR (d=18)**	**Difference** (5) – (6)	**Diff (%)**
3x3	0.2629	0.6892	0.3815	0.8226	0.4637	0.4995	-0.0358	**-3.58%**
4x4	0.2778	0.7049	0.3941	0.8266	0.4768	0.5094	-0.0326	**-3.26%**
5x5	0.2911	0.7171	0.4059	0.8311	0.4884	0.5192	-0.0308	**-3.08%**
6x6	0.3032	0.7273	0.4168	0.8271	0.5039	0.5301	-0.0262	**-2.62%**
7x7	0.3138	0.7366	0.4260	0.8291	0.5138	0.5396	-0.0258	**-2.58%**
8x8	0.3240	0.7447	0.4351	0.8327	0.5225	0.549	-0.0265	**-2.65%**
9x9	0.3333	0.7513	0.4436	0.8358	0.5308	0.5575	-0.0267	**-2.67%**
10x10	0.3421	0.7568	0.4520	0.837	0.5401	0.5652	-0.0251	**-2.51%**
11x11	0.3499	0.7618	0.4593	0.8387	0.5476	0.5725	-0.0249	**-2.49%**
12x12	0.3575	0.7665	0.4663	0.8406	0.5548	0.5792	-0.0244	**-2.44%**
13x13	0.3642	0.7705	0.4727	0.8421	0.5613	0.5852	-0.0239	**-2.39%**
14x14	0.3707	0.7737	0.4791	0.8435	0.5680	0.5912	-0.0232	**-2.32%**
15x15	0.3769	0.7775	0.4848	0.8449	0.5737	0.5974	-0.0237	**-2.37%**
16x16	0.3824	0.7809	0.4897	0.8464	0.5786	0.6043	-0.0257	**-2.57%**
17x17	0.3876	0.7836	0.4946	0.8477	0.5835	0.611	-0.0275	**-2.75%**
18x18	0.3923	0.7868	0.4986	0.8503	0.5864	0.6166	-0.0302	**-3.02%**
19x19	0.3963	0.7884	0.5027	0.8531	0.5892	0.62	-0.0308	**-3.08%**
20x20	0.4002	0.7907	0.5061	0.8543	0.5925	0.6234	-0.0309	**-3.09%**
							Minimum difference	**-2.32%**
							Maximum difference	**-3.58%**

Table B.21: Markus Experiment 5 results (6): Verification measurement data in phantom 4 with equivalent thickness of 22.24cm. No additional back scatter was added for PTW Markus ion-chamber. All the measured data were delivered using 100MU of 6MV x-rays. Raw data (1), raw data at dmax (2) were measured. Correction factors (4) were calculated using effective SSD method based on relative RED to water calculated in Chapter 9. TMR (d=18) data were set as reference. Others were calculated based on the equations described in the table. (Data matching Figure 9.26)

	(1)	(2)	(3)	(4)	(5)	(6)	(7)	(8)
FSZ at isocentre	**Raw data No add-on back scatter**	**Raw data at dmax**	**Normalized to dmax**	**Correction Factor**	**After CF Correction**	**TMR (d=18)**	**Difference**	**Diff (%)**
			(1)/(2)		(3)/(4)		(5) – (6)	(7)/100
3x3	0.2624	0.6892	0.3807	0.8226	0.4628	0.4995	-0.0367	**-3.67%**
4x4	0.2767	0.7049	0.3925	0.8266	0.4749	0.5094	-0.0345	**-3.45%**
5x5	0.2894	0.7171	0.4036	0.8311	0.4856	0.5192	-0.0336	**-3.36%**
6x6	0.3006	0.7273	0.4133	0.8271	0.4997	0.5301	-0.0304	**-3.04%**
7x7	0.3106	0.7366	0.4217	0.8291	0.5086	0.5396	-0.0310	**-3.10%**
8x8	0.3199	0.7447	0.4296	0.8327	0.5159	0.549	-0.0331	**-3.31%**
9x9	0.3286	0.7513	0.4374	0.8358	0.5233	0.5575	-0.0342	**-3.42%**
10x10	0.3367	0.7568	0.4449	0.837	0.5315	0.5652	-0.0337	**-3.37%**
11x11	0.3438	0.7618	0.4513	0.8387	0.5381	0.5725	-0.0344	**-3.44%**
12x12	0.3504	0.7665	0.4571	0.8406	0.5438	0.5792	-0.0354	**-3.54%**
13x13	0.3566	0.7705	0.4628	0.8421	0.5496	0.5852	-0.0356	**-3.56%**
14x14	0.3625	0.7737	0.4685	0.8435	0.5555	0.5912	-0.0357	**-3.57%**
15x15	0.3678	0.7775	0.4731	0.8449	0.5599	0.5974	-0.0375	**-3.75%**
16x16	0.3728	0.7809	0.4774	0.8464	0.5640	0.6043	-0.0403	**-4.03%**
17x17	0.3774	0.7836	0.4816	0.8477	0.5682	0.611	-0.0428	**-4.28%**
18x18	0.3814	0.7868	0.4847	0.8503	0.5701	0.6166	-0.0465	**-4.65%**
19x19	0.3852	0.7884	0.4886	0.8531	0.5727	0.62	-0.0473	**-4.73%**
20x20	0.3885	0.7907	0.4913	0.8543	0.5751	0.6234	-0.0483	**-4.83%**
							Minimum difference	**-3.04%**
							Maximum difference	**-4.83%**

Table B.22 Markus Experiment 6 results (1): A. Raw readings of phantom 2B under 6MV x-ray irradiation. B.Raw readings of phantom 2S under 6MV x-ray irradiation. Measurement points were at exit surface and isocentre was at target centre of the phantom. The add-on physical back scatter thickness changes from 5.5cm to 0cm, then the Markus Ion-chamber exposed in air. 100MU was delivered. (Data matching Figure 9.29)

A: . Raw readings of phantom 2B under 6MV x-ray irradiation

Backscatter Physical Thickness (cm)	**Square field size (cm^2) at isocentre (Square field size (cm^2) at measurement point)**				
	3x3 (3.27x3.27)	**5x5 (5.45x5.45)**	**10x10 (10.90x10.90)**	**15x15 (16.35x16.35)**	**20x20 (21.80x21.80)**
5.5	0.3320	0.3591	0.4110	0.4435	0.4629
4.5	0.3322	0.3592	0.4111	0.4429	0.4627
3.5	0.3315	0.3587	0.4102	0.4416	0.4615
2.5	0.3299	0.3561	0.4065	0.4378	0.4573
1.5	0.3297	0.3573	0.4080	0.4392	0.4584
0.5	0.3299	0.3574	0.4077	0.4381	0.4565
0	0.3309	0.3571	0.4067	0.4363	0.4550
Chamber only	0.3304	0.3560	0.4036	0.4324	0.4497

B. Raw readings of phantom 2S under 6MV x-ray irradiation

Back scatter Physical Thickness (cm)	**Square field size (cm^2) at isocentre (Square field size (cm^2) at measurement point)**				
	3x3 (3.27x3.27)	**5x5 (5.45x5.45)**	**10x10 (10.90x10.90)**	**15x15 (16.35x16.35)**	**20x20 (21.80x21.80)**
5.5	0.3236	0.3522	0.4026	0.4332	0.4531
4.5	0.3237	0.3523	0.4029	0.4336	0.4528
3.5	0.3239	0.3521	0.4023	0.4327	0.4519
2.5	0.3238	0.3521	0.4019	0.4322	0.4513
1.5	0.3237	0.3519	0.4012	0.4311	0.4496
0.5	0.3239	0.3514	0.4004	0.4295	0.4478
0	0.3236	0.3503	0.3988	0.4283	0.4461
Chamber only	0.3235	0.3496	0.3965	0.4239	0.4411

Table B.23 Markus Experiment 6 results (2): A. Raw readings of phantom 2B under 10MV x-ray irradiation. B.Raw readings of phantom 2S under 10MV x-ray irradiation. Measurement points were at exit surface and isocentre was at target centre of the phantom. The add-on physical back scatter thickness changes from 5.5cm to 0cm, then the Markus Ion-chamber exposed in air. 100MU was delivered. (Data matching Figure 9.30)

A: . Raw readings of phantom 2B under 10 MV x-ray irradiation

Back scatter Physical Thickness (cm)	**Square field size (cm^2) at isocentre (Square field size (cm^2) at measurement point)**				
	3x3 (3.27x3.27)	**5x5 (5.45x5.45)**	**10x10 (10.90x10.90)**	**15x15 (16.35x16.35)**	**20x20 (21.80x21.80)**
5.5	0.3990	0.4299	0.4801	0.5091	0.5264
4.5	0.3985	0.4295	0.4796	0.5089	0.5261
3.5	0.3980	0.4289	0.4787	0.5073	0.5246
2.5	0.3961	0.4266	0.4755	0.5041	0.5215
1.5	0.3954	0.4277	0.4773	0.5053	0.5222
0.5	0.3953	0.4275	0.4763	0.5041	0.5212
0	0.3969	0.4278	0.4759	0.5029	0.5197
Chamber only	0.3965	0.4254	0.4727	0.4997	0.5153

B: . Raw readings of phantom 2S under 10MV x-ray irradiation

Back scatter	**Square field size (cm^2) at isocentre (Square field size (cm^2) at measurement point)**				
Physical Thickness (cm)	**3x3 (3.27x3.27)**	**5x5 (5.45x5.45)**	**10x10 (10.90x10.90)**	**15x15 (16.35x16.35)**	**20x20 (21.80x21.80)**
5.5	0.3893	0.4221	0.4725	0.5005	0.5174
4.5	0.3889	0.4223	0.4714	0.4997	0.5165
3.5	0.3887	0.4217	0.4709	0.4987	0.5160
2.5	0.3887	0.4217	0.4708	0.4982	0.5150
1.5	0.3884	0.4213	0.4704	0.4975	0.5147
0.5	0.3885	0.4212	0.4694	0.4963	0.5132
0	0.3882	0.4209	0.4693	0.4959	0.5118
Chamber only	0.3882	0.4206	0.4670	0.4923	0.5076

Table B.24: Markus Experiment 6 results (3): Percentage difference of phantom 2B to phantom 2 under 6MV x-ray irradiation. Measurement points were at exit surface and isocentre was at target centre of the phantom. The add-on physical back scatter thickness changes from 5.5cm to 0cm, then the Markus Ion-chamber exposed in air. 100MU was delivered. (Data matching Figure 9.31)

Back scatter	Square field size (cm^2) at isocentre (Square field size (cm^2) at measurement point)				
Physical Thickness (cm)	3x3 (3.27x3.27)	5x5 (5.45x5.45)	10x10 (10.90x10.90)	15x15 (16.35x16.35)	20x20 (21.80x21.80)
5.5	0.70%	0.35%	-0.16%	0.37%	0.36%
4.5	0.79%	0.45%	0.19%	0.26%	0.37%
3.5	0.55%	0.36%	0.07%	0.14%	0.28%
2.5	0.12%	-0.34%	-0.76%	-0.61%	-0.48%
1.5	-0.02%	0.04%	-0.21%	-0.03%	0.04%
0.5	0.00%	0.15%	-0.08%	0.05%	0.06%
0	0.44%	0.21%	-0.07%	-0.03%	0.04%
Chamber only	0.49%	0.26%	-0.10%	0.02%	0.01%
Mean±SD	**0.38%±0.31%**	**0.19%±0.25%**	**-0.14%±0.28%**	**0.02%±0.29%**	**0.09%±0.27%**

Table B.25: Markus Experiment 6 results (4): Percentage difference of phantom 2S to phantom 2 under 6MV x-ray irradiation. Measurement points were at exit surface and isocentre was at target centre of the phantom. The add-on physical back scatter thickness changes from 5.5cm to 0cm, then the Markus Ion-chamber exposed in air. 100MU was delivered. (Data matching Figure 9.31)

Back scatter Physical Thickness (cm)	Square field size (cm^2) at isocentre (Square field size (cm^2) at measurement point)				
	3x3 (3.27x3.27)	5x5 (5.45x5.45)	10x10 (10.90x10.90)	15x15 (16.35x16.35)	20x20 (21.80x21.80)
5.5	-1.85%	-1.58%	-2.19%	-1.95%	-1.76%
4.5	-1.79%	-1.48%	-1.80%	-1.83%	-1.78%
3.5	-1.76%	-1.48%	-1.85%	-1.88%	-1.80%
2.5	-1.73%	-1.46%	-1.88%	-1.88%	-1.78%
1.5	-1.83%	-1.48%	-1.87%	-1.88%	-1.88%
0.5	-1.82%	-1.53%	-1.87%	-1.91%	-1.85%
0	-1.78%	-1.70%	-2.01%	-1.87%	-1.91%
Chamber only	-1.63%	-1.54%	-1.86%	-1.95%	-1.91%
Mean±SD	**-1.77%±0.07%**	**-1.53%±0.08%**	**-1.92%±0.12%**	**-1.89%±0.04%**	**-1.83%±0.06%**

Table B.27 Markus Experiment 6 results (5): Percentage difference of phantom 2B to phantom 2 under 10MV x-ray irradiation. Measurement points were at exit surface and isocentre was at target centre of the phantom. The add-on physical back scatter thickness changes from 5.5cm to 0cm, then the Markus Ion-chamber exposed in air. 100MU was delivered. (Data matching Figure 9.31)

Back scatter	Square field size (cm^2) at isocentre (Square field size (cm^2) at measurement point)				
Physical Thickness (cm)	3x3 (3.27x3.27)	5x5 (5.45x5.45)	10x10 (10.90x10.90)	15x15 (16.35x16.35)	20x20 (21.80x21.80)
5.5	1.62%	0.88%	0.63%	0.71%	0.81%
4.5	1.46%	0.86%	0.61%	0.73%	0.76%
3.5	1.48%	0.78%	0.49%	0.44%	0.63%
2.5	0.92%	0.23%	-0.19%	-0.06%	0.04%
1.5	0.79%	0.47%	0.25%	0.33%	0.39%
0.5	0.76%	0.45%	0.11%	0.22%	0.37%
0	1.19%	0.64%	0.26%	0.30%	0.41%
Chamber only	1.24%	0.51%	0.18%	0.44%	0.42%
Mean±SD	**1.18%±0.33%**	**0.60%±0.23%**	**0.29%±0.28%**	**0.39%±0.26%**	**0.48%±0.25%**

Table B.28 Markus Experiment 6 results (6): Percentage difference of phantom 2S to phantom 2 under 10MV x-ray irradiation. Measurement points were at exit surface and isocentre was at target centre of the phantom. The add-on physical back scatter thickness changes from 5.5cm to 0cm, then the Markus Ion-chamber exposed in air. 100MU was delivered. (Data matching Figure 9.31)

Back scatter Physical Thickness (cm)	Square field size (cm^2) at isocentre (Square field size (cm^2) at measurement point)				
	3x3 (3.27x3.27)	5x5 (5.45x5.45)	10x10 (10.90x10.90)	15x15 (16.35x16.35)	20x20 (21.80x21.80)
5.5	-0.85%	-0.94%	-0.97%	-0.99%	-0.92%
4.5	-0.97%	-0.82%	-1.11%	-1.09%	-1.09%
3.5	-0.89%	-0.92%	-1.13%	-1.27%	-1.02%
2.5	-0.97%	-0.92%	-1.18%	-1.23%	-1.21%
1.5	-1.00%	-1.03%	-1.20%	-1.22%	-1.05%
0.5	-0.97%	-1.03%	-1.34%	-1.33%	-1.17%
0	-1.01%	-0.99%	-1.13%	-1.10%	-1.12%
Chamber only	-0.88%	-0.62%	-1.02%	-1.05%	-1.08%
Mean±SD	**-0.94%±0.06%**	**-0.91%±0.13%**	**-1.14%±0.11%**	**-1.16%±0.12%**	**-1.08%±0.09%**